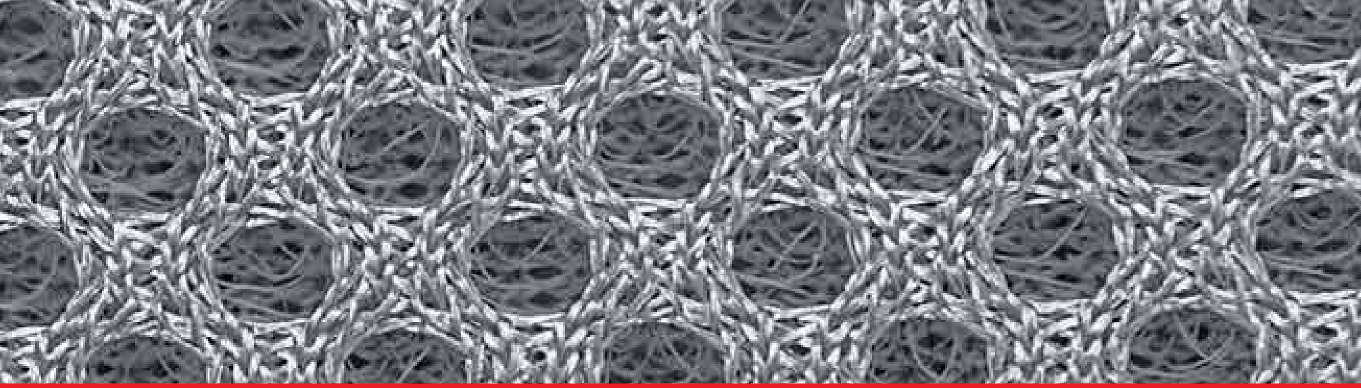

IntechOpen

Advanced Surface Engineering Research

Edited by Mohammad Asaduzzaman Chowdhury

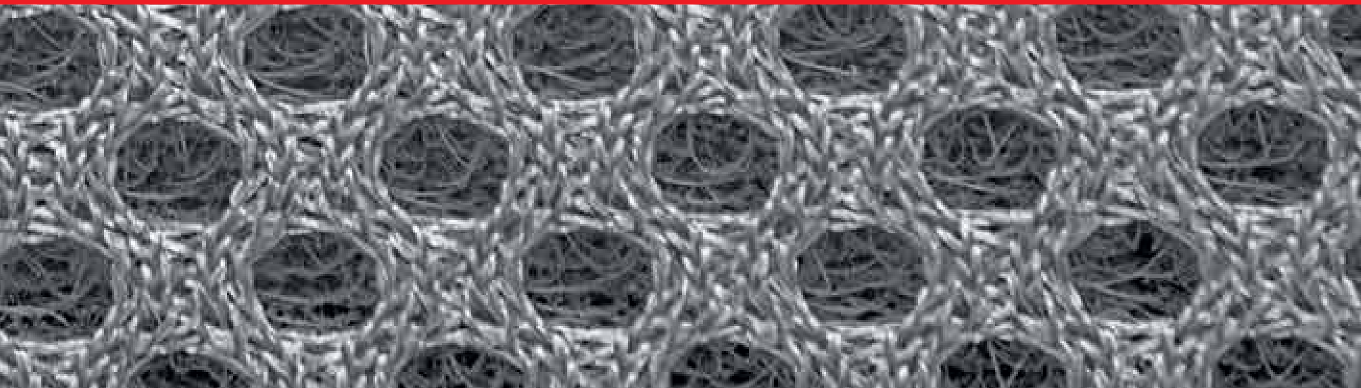

ADVANCED SURFACE ENGINEERING RESEARCH

Edited by **Mohammad Asaduzzaman Chowdhury**

Advanced Surface Engineering Research
http://dx.doi.org/10.5772/intechopen.75772
Edited by Mohammad Asaduzzaman Chowdhury

Contributors

Ann Zammit, Petrică Vizureanu, Manuela Cristina Perju, Dragos Cristian Achitei, Carmen Nejneru, Yiran Fan, Geoff D. Fowler, Daniel Sola, Jose I. Peña, Roto Roto, Alexander R. Cholach, Nicolae Enaki, Ion N. Mihailescu, Gianina-Florentina Popescu-Pelin, Maria Badiceanu, Marina Turcanu, Sergiu Bizgan, Carmen-Georgeta Ristoscu, Andrei Nistreanu, Viorica Tonu, Tatiana Paslari, Elena Starodub, Aurelia Profir, Jose Antonio Garcia, Pedro J. Rivero, Iban Quintana, Rocio Ortiz, Rafael J. Rodriguez, Maria Marinescu, Ludmila Otilia Cinteza, Stefan Valkov, Peter Petrov, Maria Ormanova

© The Editor(s) and the Author(s) 2018
The rights of the editor(s) and the author(s) have been asserted in accordance with the Copyright, Designs and Patents Act 1988. All rights to the book as a whole are reserved by INTECHOPEN LIMITED. The book as a whole (compilation) cannot be reproduced, distributed or used for commercial or non-commercial purposes without INTECHOPEN LIMITED's written permission. Enquiries concerning the use of the book should be directed to INTECHOPEN LIMITED rights and permissions department (permissions@intechopen.com).
Violations are liable to prosecution under the governing Copyright Law.

Individual chapters of this publication are distributed under the terms of the Creative Commons Attribution 3.0 Unported License which permits commercial use, distribution and reproduction of the individual chapters, provided the original author(s) and source publication are appropriately acknowledged. If so indicated, certain images may not be included under the Creative Commons license. In such cases users will need to obtain permission from the license holder to reproduce the material. More details and guidelines concerning content reuse and adaptation can be foundat http://www.intechopen.com/copyright-policy.html.

Notice

Statements and opinions expressed in the chapters are these of the individual contributors and not necessarily those of the editors or publisher. No responsibility is accepted for the accuracy of information contained in the published chapters. The publisher assumes no responsibility for any damage or injury to persons or property arising out of the use of any materials, instructions, methods or ideas contained in the book.

First published in London, United Kingdom, 2018 by IntechOpen
eBook (PDF) Published by IntechOpen, 2019
IntechOpen is the global imprint of INTECHOPEN LIMITED, registered in England and Wales, registration number: 11086078, The Shard, 25th floor, 32 London Bridge Street
London, SE19SG – United Kingdom
Printed in Croatia

British Library Cataloguing-in-Publication Data
A catalogue record for this book is available from the British Library

Additional hard and PDF copies can be obtained from orders@intechopen.com

Advanced Surface Engineering Research
Edited by Mohammad Asaduzzaman Chowdhury

p. cm.

Print ISBN 978-1-78984-339-2

Online ISBN 978-1-78984-340-8

eBook (PDF) ISBN 978-1-83881-827-2

Meet the editor

Mohammad Asaduzzaman Chowdhury is a professor of mechanical engineering at Dhaka University of Engineering and Technology, Gazipur, Bangladesh. His research interests are engineering tribology, surface engineering, coating technology, polymer and composite materials, metals and alloys, erosive wear of different materials, material fabrication, characterization of materials, self-energy generating materials, atomic transfer mechanisms, etc. Currently, he is working as an editorial board member of a large number of international reputed journals, and as an editor and reviewer of many ISI and Scopus Indexed international journals and books. He has also published many research and review papers in refereed international journals and conference proceedings. He is also working as a consultant, advisor, and expert member of many government and autonomous organizations. His teaching and research experience covers 20 years. He is involved with different cultural and social activities, and is engaged in writing articles, stories, lyrics, and poems in different newspapers and relevant media.

Contents

Preface

Advanced surface engineering fertilizes the high-throughput chemical and physical engineering phenomenon in relation to magnetic, electrical, electronic, optical, and thermal controls, as well as surface areas, excessive gas exchange, and protective coatings. Smart surface technology provides an interlayer model that prevents the entry of substances without affecting the properties of neighboring layers.

Advanced surface engineering research provides the motivation for research aimed at developing a fundamental understanding of the nature and consequences of the interaction between materials at the atomic scale. This book guides the rational design of material for technological application.

The chapter **"Synthesis and nonlinear studies on selected organic compounds in nanostructured thin films"** discusses nonlinear optical properties of new synthesized derivatives evaluated in relation with the chemical structure by using *density functional theory* molecular modeling.

The chapter "**Shot peening of austempered ductile iron"** looks into the effect of shot peening on austempered ductile iron (ADI) in more detail and delves into a case study that was carried out to analyze the bending fatigue resistance and tribological characteristics of Cu–Ni-alloyed ADI.

The chapter **"Advanced electro-spark deposition process on metallic alloys"** studies the material base–surface multilayer system for various types of depositions (increasing the wear resistance of Fe–C alloy parts), whose compatibility with the substrate provides high-quality parts.

The chapter "**Surface manufacturing of materials by high energy fluxes"** aims to summarize the topics related to the application of a surface treatment by high-energy fluxes (i.e. electron and laser beams) for developing new multifunctional materials, as well as modifying their surface properties.

The chapter "**The potential of pyrolytic biomass as a sustainable bio-filler for styrene-butadiene rubber"** explains the significant potential of pyrolytic biomass char for use as a sustainable carbon black replacement filler for rubber materials. The manufacture of rubber filler is not only energy consuming, contributing significantly to global CO_2 emissions, but uses non-renewable feedstock in production making it unsustainable.

The chapter "**Ultrafast laser inscription of buried waveguides in W-TCP bioactive eutectic glasses"** reviews the fundamentals of the ultrafast laser inscription technique to produce optical waveguides inside dielectric materials such as crystals and glasses. Next, as an example, the application of this technique is revised to create buried waveguides inside bioactive glasses and specifically inside wollastonite-tricalcium phosphate eutectic glasses.

The chapter **"Surface modification of Fe_3O_4 as magnetic adsorbents for recovery of precious metals"** looks comprehensively at the preparation, characterization, and use of the magnetic core–shell modified with functional groups as magnetic adsorbent. After adsorption, the materials together with the ions can be recovered by use of a magnet before further separation and purification.

The chapter **"Hidden resources of a coordinated XPS and DFT studies**" electronic configuration of chemically bound atoms at the surface or in the bulk of a solid, and contains the traps for the energy absorption provided by valence band transitions. The core-level excitation of any origin is coupled with those traps forming a multichannel route for energy dissipation. The chapter shows tracing over the channels by means of X-ray photoelectron spectroscopy (XPS) and density functional theory (DFT).

The chapter proposes an effective way of decontamination using optical metamaterials like photonic crystals consisting of glass microspheres or granulated quartz with various geometries. Efficient decontamination using the evanescent zone of metamaterials opens a new perspective in pathogen decontamination.

The chapter "**Efficient microbial decontamination of translucent liquids and gases using optical metamaterials"** proposes different topological structures of metamaterials to enlarge the contact surface of ultraviolet radiation with polluted translucent fluids.

The chapter "**Advanced surface treatments for improving the biocompatibility of prosthesis and medical implants"** presents an updated review of the most used surface engineering technologies for biomaterials, such as novel PVD coatings, ion implantation, and other plasma spray treatments, as well as a critical review of the characterization techniques. This study is completed with an insight into the future of the field.

I am very much grateful to my university (**Dhaka University of Engineering and Technology, Gazipur) for creating the opportunities to do this work.**

I wish to give my heartfelt and sincere thanks to Eng. Bengir Ahmed Shuvho for his continuous technical and valuable support to complete the book successfully. I appreciate and acknowledge his contributions in the review process of all the chapters. I am immensely grateful to Author Service Manager Ms. Dolores Kuzelj and IntechOpen publisher, UK. I also gratefully acknowledge the authors for their worthy contributions to write an application-based chapter for this book. I learnt a lot about editing this book from **Professor Dr. Mohammed Alauddin, Honorable Vice Chancellor of Dhaka University of Engineering and Technology, Gazipur.** Hopefully, this book will be used as a state of the art for creating the basis of fundamental and applied research. Students of different renowned universities will also benefit from this book.

My special thanks go to my wife Anisa Akhtar, my son Ayan, and my daughter Afsheen, who have been forbearing during the year when I spent long days and nights conducting research and keeping up with the literature and preparation of this book.

Professor Dr. Mohammad Asaduzzaman Chowdhury
Dhaka University of Engineering and Technology (DUET)
Gazipur, Bangladesh

Chapter 1

Synthesis and Nonlinear Studies on Selected Organic Compounds in Nanostructured Thin Films

Ludmila-Otilia Cinteza and Maria Marinescu

Additional information is available at the end of the chapter

http://dx.doi.org/10.5772/intechopen.79522

Abstract

Organic compounds based on ferrocene, pyrazolone, and octahydroacridine exhibit high interest due to their unusual structure, with potential practical applications due to their special optical properties. Nonlinear optical (NLO) properties of some new synthesized derivatives are evaluated in relationship with the chemical structure by using DFT molecular modeling. In condensed state, ferrocene and other organic molecules were found in a staggered arrangement (D5d) as a nonpolar molecule, but the eclipsed (D5h) and twisted (D5) forms exhibit SHG capabilities. The molecular polarizability (α), first-order hyperpolarizabilities (β_{tot}), dipole (μ_{tot}), and quadrupole (Q) moments were computed. The NLO efficiency was assessed by the relationship between high (β_{tot}) and low HOMO-LUMO energy gap. The nonlinear optical properties of some new synthesized compounds were evaluated in thin films with nanometric morphology obtained using various methods: Langmuir-Blodgett (LB) thin films, sol-gel deposition, and layer-by-layer deposition.

Keywords: nonlinear optics, thin films, nanostructures, hybrid materials
Langmuir-Blodgett film, layer by layer

1. Introduction

Nonlinear optics has become a vibrant field of research since the optical second-harmonic generation (SHG) was first observed in the early 1960s [1]. A better understanding was achieved on the origin of nonlinear optical (NLO) phenomena and the structure-property relationships of NLO chromophores in the late 1970s when various tools were developed to accurately measure and calculate hyperpolarizabilities [2]. Organic NLO materials, which can be modulated and processed readily, are of much contemporary interest because of their potential applications in modulation of optical signals, medicine, spectroscopic and electrochemical sensing, microfabrication and imaging, laser technology, data storage, and telecommunication [3]. Recent studies were focused on the synthesis of the organic molecules with special geometry and certain electronic molecular parameters to possess nonlinear optical (NLO) properties [3–24]. The demand of substances with NLO properties for numerous industrial applications has resulted in many articles reporting the manufacture of various novel molecules, with highly active chromophores and superior optical activity. However, it remains the issue of processing these materials, as long as the specific optical properties have to be preserved, together with new requirements added, such as chemical stability, mechanical strength, etc. The main materials used as host for the embedding of chromophores and fabrication methods are discussed. The influence of parameters (such as chemical structure of the host material, synthesis conditions, and external stimuli) on the optical and electrical properties of the final product is also evidenced.

2. Synthesis of compounds with NLO properties

Recent literature shows some classes of organic compounds suitable for applications for molecular switches that possess certain characteristics, such as high molecular hyperpolarizability coefficients (β), special geometry, and in most cases small HOMO-LUMO energy gaps [25–27]. In the following sections, we will refer to the recent synthesis of several classes of organic compounds possessing the abovementioned characteristics.

2.1. Alkyne compounds

Ryhding et al. synthesized by Sonogashira Pd-catalyzed cross-coupling reactions a series of new oligo(*p*-phenyleneethynylene) **1–4** (Scheme 1) [28]. Miao et al. successfully synthesized a series of novel donor-acceptor chromophores **5–8** in an excellent yield by metal-free [2 + 2] click chemistry. These compounds possessed energy-level modulation of the organic π-conjugated aniline derivatives (see **Figure 1**) [29].

The new derivatives **9–10** were obtained by Michinobu et al. in quantitative yield (96–100%) by [2 + 2] cycloaddition between tetracyanoethylene- and dimethylanilino-substituted alkynes, followed by electrocyclic ring opening of the initially formed cyclobutenes [30].

2.2. Push-pull derivatives as NLO chromophores

The organic molecules which contain a couple, donor (D)-acceptor (A) (or "push-pull" system), connected to a system which contributes to the delocalization of the π-electrons make the *classic structures* with optical response due to large hyperpolarizabilities that arise from a combination of strong electron-donating groups (e.g., $\mathbf{-}NR_2$, $\mathbf{-}OR$) and strong electron-withdrawing groups (e.g., $\mathbf{-}NO_2$, $\mathbf{-}CN$), positioned at the opposite ends of a conjugated system (see **Figure 2**) [16, 23, 31, 32]. Therefore, the synthesis of the classic structures occupies a central place even in the current research.

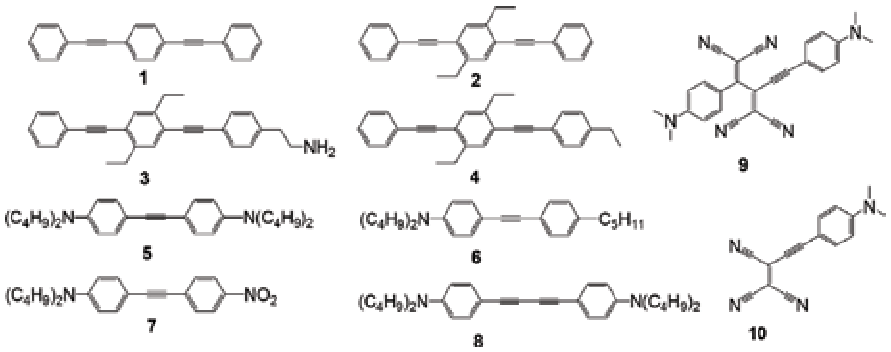

Figure 1. Alkyne compounds with NLO properties [28–30].

Figure 2. Organic structures that contain a couple: donor-acceptor or a "push-pull" system [32].

There are several classes of organic compounds in this category, from which some representatives will be presented.

2.2.1. Push-pull dyes

Arylazo-5-alkoxy-2,2′-bithiophene-conjugated dyes **11**, synthesized through a combination of the Friedel-Crafts and the Lawesson reactions by Raposo et al., have been proven as promising NLO chromophores (see **Figure 2**). Compounds **11** exhibit high molecular nonlinearities, as their values are 13–16 times higher than that of the well-known 4-nitroaniline (PNA) and the corresponding β_0 values are 2.5 to 4 times higher than that of PNA (see **Figure 3**) [33].

Kleinpeter et al. demonstrated that compounds **12** possessed excellent values of molecular hyperpolarizability β_0; therefore, they can be considered as candidates for nonlinear optical (NLO) applications [34]. A series of pyrazole-5-ones **13**, synthesized by azo-coupling reactions, which present only hydrazo tautomers with a planar structure, responsible for their nonlinear optical properties were discussed in terms of NLO parameters by Marinescu et al. [32]. Herein, the NLO efficiency of compounds was assessed by the relationship between high β_{tot} and low HOMO-LUMO energy gap. Also, these compounds can function as ligands for erbium complexes, which possessed solvatochromic properties and have NLO material characteristics [35]. Zajac et al. reported that the synthesis of benzothiazole dyes **17** and their NLO properties was investigated [36]. Formulation of 2-heteroaryl-benzothiazoles by Vilsmeier-Haack reaction gives the corresponding carbaldehydes, which subsequently underwent a Wittig reaction providing target compounds in good yields [36].

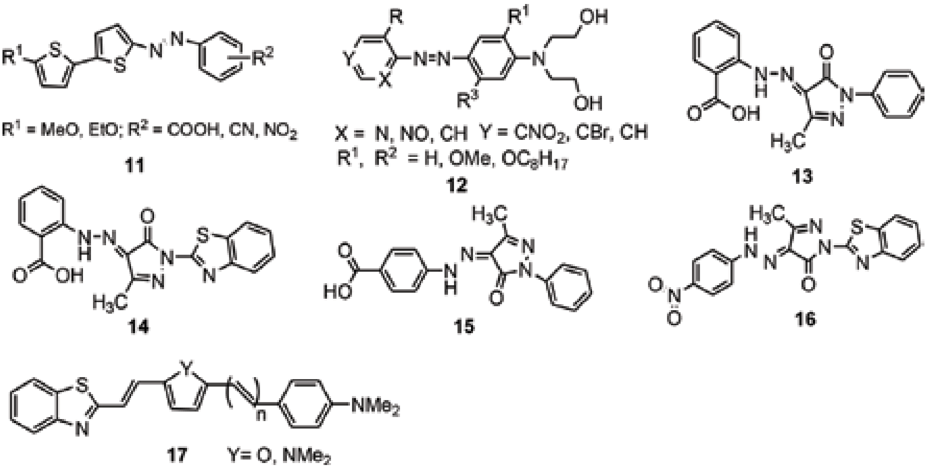

Figure 3. Push-pull dyes as NLO chromophores [33–36].

2.2.2. Push-pull structures from different classes of heterocyclic compounds

Push-pull molecular structures based on angular benzobisthiazolium acceptor were synthesized by Cibova et al. A comparison of selected spectral and nonlinear optical properties of the prepared compounds shows that compound **18** possess the best NLO properties (see **Figure 4**) [37]. Hebbar et al. describe the synthesis of various push-pull molecules **19–20** with a central pyrazine unit connected to a hexatriene chain terminated by various *p*-substituted phenyl groups. The compounds were synthesized by a Negishi coupling reaction followed by Wittig and Wadsworth-Emmons reactions [38]. Cho et al. synthesized new efficient push-pull organic semiconductors comprising of the bis(9,9-dimethyl-9H-fluoren-2-yl)aniline donor and the various acceptors such as NO_2, 4-dicyanomethylene-6-*tert*-butyl-4H-pyran, and 2-dicyanomethylene-3-cyano-5-dimethyl-2,5-dihydrofuran, which were linked with bithiophene or vinyl bithiophene *p*-conjugation bridges, were synthesized, and their photovoltaic characteristics were investigated in solution-processed small molecule organic solar cells (SMOSCs) [39].

The compounds **21–23** were readily prepared through Knoevenagel condensation reaction with 5-bromo-5′-nitro-2,2′-bithiophene, 2-(2-*tert*-butyl-6-methyl-4*H*-pyran-4-ylidene) malononitrile, and 2-(3-cyano-4,5,5-trimethyl-5H-furan-2-ylidene)malononitrile, respectively, and a palladium-catalyzed Suzuki coupling reaction with 2-bromo-5-nitrothiophene using phase-transfer catalyst. Shi et al. synthesized boron dipyrromethene **24** derivative bearing an electron-donating 4-(dimethylamino)phenylethynyl group and an electron-withdrawing 4-nitrophenylethynyl group in the opposite two and six positions by Knoevenagel condensation followed by sequential Sonogashira coupling reactions and the second-order nonlinear optical properties of this compound has been studied [40]. Farat et al. synthesized novel xanthene push-pull chromophores and luminophores **25–26** and show these structures as the more pronounced vibrational bands in the luminescence spectra, which indicate the more rigid structure of these molecules in the excited state [41]. Malytskyi et al. synthesized thiophene-based push-pull chromophores **27–28**

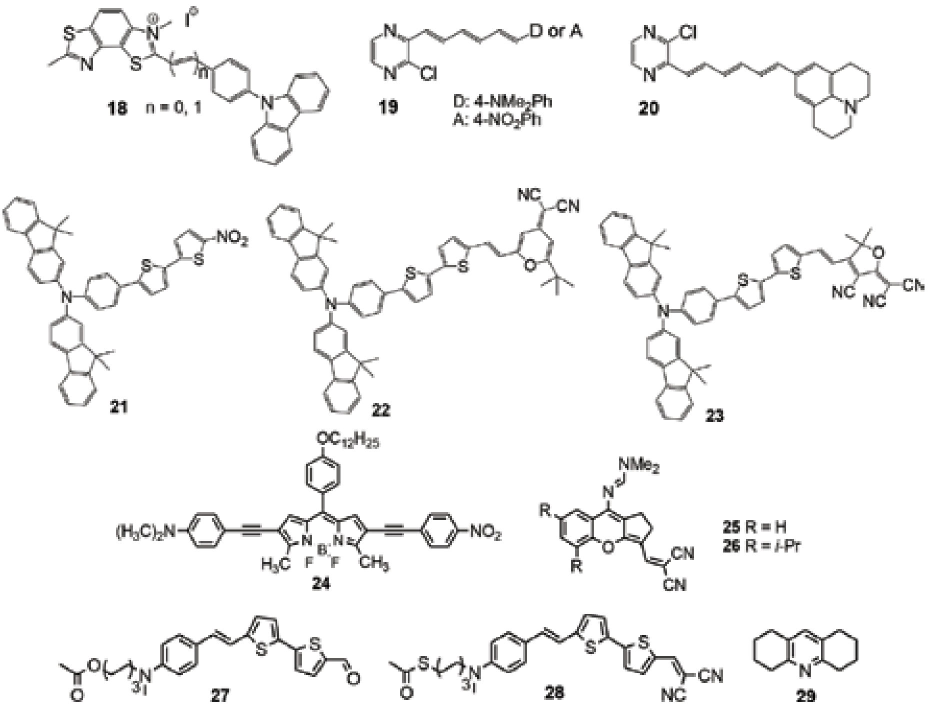

Figure 4. Push-pull molecules as NLO chromophores [37–43].

for tuning the electrical and optical properties of surfaces with controlled self-assembled monolayer (SAM) formation [42]. Ion et al. reported for smooth/compact 1,2,3,4,5,6,7,8-octahydroacridine **29** thin films grown by matrix-assisted pulsed laser evaporation (MAPLE) the presence of the SHG (second-harmonic generation) signal related to the conformational asymmetry of the OHA molecule and therefore the nonlinear optical applications of it [43].

2.3. Thienyl compounds as NLO materials

Thiophenes are among the most studied heterocyclic spacers for D-π-A systems due to their relatively low resonance energies and have allowed the preparation of chromophores with high stabilities and nonlinearities [44]. Raposo et al. reported the synthesis of formyl-substituted 1-alkyl(aryl)-2-(2′-thienyl)pyrroles **30–32** as versatile building blocks for NLO materials, by functionalization of the pyrrole or thiophene ring of thienylpyrroles using different methods: Vilsmeier formylation or metalation followed by reaction with DMF (see **Figure 5**) [45]. Batista et al. reported the synthesis of new chromophores with second-order nonlinearities containing thienylpyrrolyl and benzothiazolyl moieties. The solvatochromic behavior of the compounds was investigated, and the hyperpolarizabilities β of derivatives **33–35** were measured using hyper-Rayleigh scattering [46]. A series of thienylpyrrolyl π-conjugated systems attached to functionalized benzimidazole heterocycles **36–37** were developed by Batista et al. [47]. These chromophores possess excellent solvatochromic properties and good molecular optical nonlinearities. Herbivo et al. reported the synthesis of a series of formyl-substituted

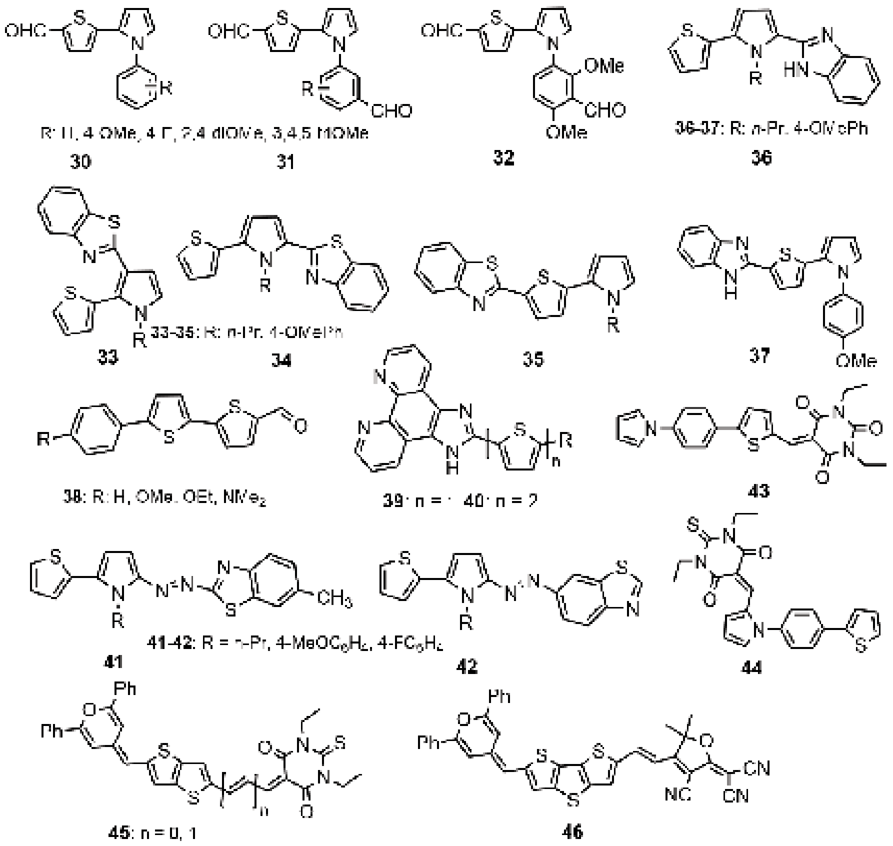

Figure 5. Structures of thienyl compounds with nonlinear optical properties [44–51].

5-aryl-2,2′-bithiophenes **38** using two different methods: Vilsmeier-Haack-Arnold reaction and through Suzuki coupling as precursors for NLO materials [48]. Batista et al. synthesized that chromophores possess an (oligo)thienyl *p*-conjugated system attached to an imidazo-phenanthroline moiety by condensation of phenanthroline-5,6-dione with formyl-thiophene derivatives in the presence of ammonium acetate in glacial acetic acid. Compounds **39–40** possess good values of β hyperpolarizabilities and solvatochromic properties [49]. Raposo et al. reported the synthesis of the two series of donor-acceptor conjugated heterocyclic azo-thienylpyrrole system **41–42**. The compounds **41** have the largest first-order hyperpolarizabilities (β = 460–660 10^{-30} esu, T convention) [50]. Castro et al. designed two series of novel push-pull 1-(4-(thiophen-2-yl)phenyl)-1H-pyrroles **43–44** to explore the consequence of using different electron-accepting moieties linked to the thiophene at the arylthiophene bridge or to the pyrrole heterocycle, which plays the role of donor group. Thiobarbituric acid derivative **5b** functionalized in the thiophene ring exhibits the largest first-order hyperpolarizability (β =2480 × 10^{-30} esu) [51]. Marco et al. synthesized two series of compounds bearing dithienothiophene or thienothiophene as π-conjugated spacer **45–46** with high second-order molecular nonlinearity [44].

2.4. Ferrocene derivatives

Ferrocene (**47**), or *bis*-cyclopentadienyl iron, is a sandwich-like compound known since 1951 when Pauson and Kealy reacted cyclopentadienyl magnesium bromide with anhydrous ferric chloride (see **Figure 6**) [52, 53]. Ferrocene, in bulk or as thin films, is one of the most studied metallocenes. Ferrocene found itself applications not only in a multitude of areas, from chemical synthesis and engineering, e.g., materials chemistry (catalyst in carbon nanotechnology, precursor material, ligand and scaffolding, fuel additives, etc.), and pharmaceutics (anticancer and other drugs), but also in theoretical and basic research [54–57]. Matei et al. present results on the morphology and optical properties of ferrocene thin films grown by a nonconventional laser-assisted technique, films that were further used in two-photon absorption investigations, evidencing that the compound has low-to-medium SHG capabilities [58]. Constantinescu et al. studied nonlinear optical applications of ferrocene carboxaldehyde **48** thin films grown by matrix-assisted pulsed laser evaporation (MAPLE) [59]. Two-photon absorption investigations reveal that the ferrocene carboxaldehyde thin films deposited by MAPLE have second-harmonic generation capabilities improved compared to simple ferrocene, opening the path toward applications in optoelectronics.

Yang et al. synthesized two electron-donating π-acceptor (D-π-A) chromospheres **49–50**, with ferrocene as the electron donor and pyridinium as the electron acceptor, and investigated the nonlinear optical absorption (NOA) properties in the solution state by the Z-scan technique [60].

Both compounds exhibited reverse saturable absorption (RSA) and optical limiting effect under nanosecond pulse irradiation. Matei et al. synthesized 4-(ferrocenylmethylimino)-2-hydroxy-benzoic **51** acid using a Schiff reaction and deposited thin films of it with controlled thickness by matrix-assisted pulsed laser evaporation (MAPLE), on quartz and silicon substrates, with the aim of evaluating the nonlinear optical properties for potential optoelectronic applications. Second-harmonic generation signals were weak due to the relatively short time of

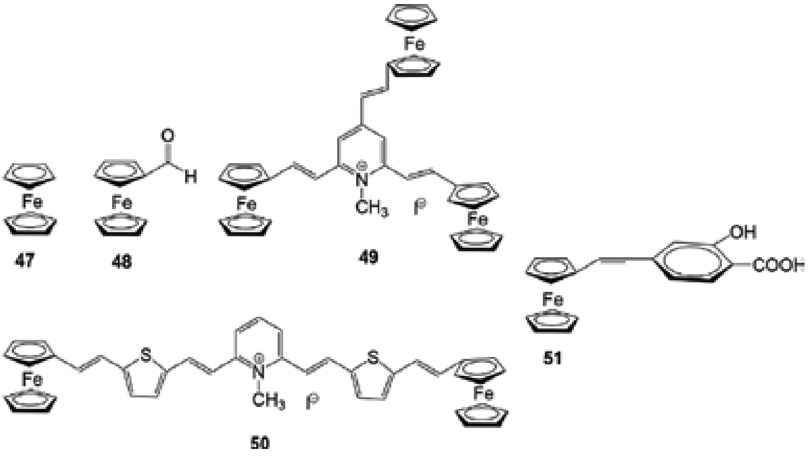

Figure 6. Ferrocene derivatives with nonlinear optical properties [52–60].

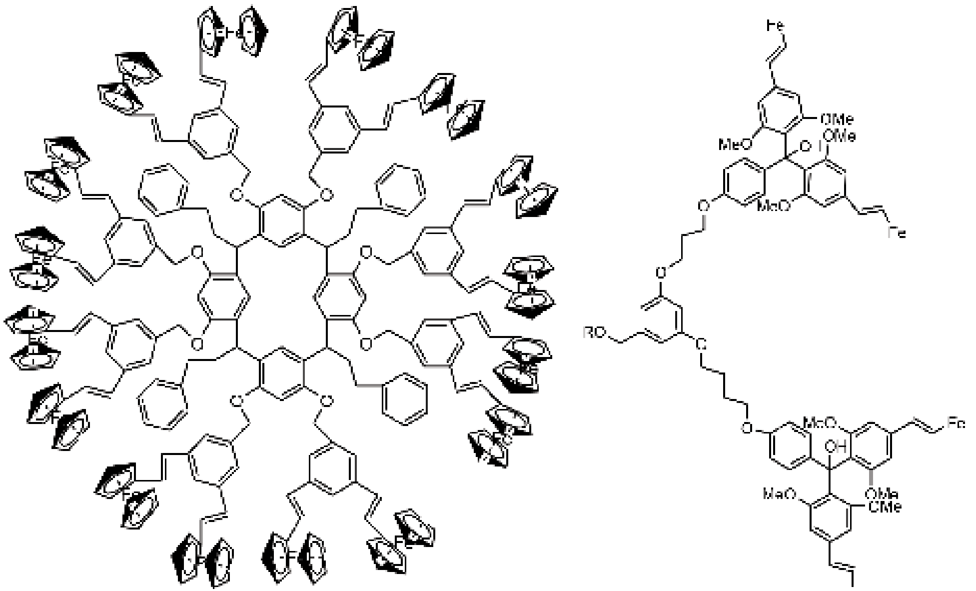

52

53: R: H. TBS

Figure 7. Ferrocene dendrimers with nonlinear optical properties [62, 63].

recording [61]. Lijanova et al. synthesized dendrimers **52** with ferrocenyl-ended groups joined by vinyl moieties (see **Figure 7**) [62].

The synthesis of the dendrimers with vinyl ferrocene was carried out applying the convergent Frechet approach that consists of three steps: (1) the synthesis of the two conjugated dendrons, (2) the selective formation of resorcinarenes bearing three different solubilizing groups, and (3) the alkylation of the dendrons to the resorcinarenes. Under this order, dendrons containing ferrocenylvinyl groups were prepared starting from a Heck reaction coupling of 3,5-dibromobenzaldehyde with vinyl ferrocene in dimethylformamide/triethylamine (1:0.25) using palladium acetate as catalyst. The $\chi^{(3)}$ values estimated from the THG Maker fringe technique for ferrocenyl-ended resorcinarene dendrimers dispersed in thin solid films are of the order of 10^{-12} esu.

Villalonga-Barber et al. synthesized new dodecaferrocenyl dendrimer **53** using sixfold Huisgen cycloaddition. Each dendron containing four ferrocenyl groups has been synthesized by conventional synthetic methods in good yields [63]. The cyclic voltammetry studies revealed that they all undergo a reversible single-electron transfer process. The absorptions at around 450 nm for the ferrocene-containing carbinols **52** are due to ferrocene d-d bands.

3. Fabrication of thin films with NLO properties

For most practical uses, substances with NLO properties are incorporated into a host material to ensure good dispersibility and stability. Thus, in most of the cases, polymers are used, usually with electrical and optical properties to improve the performance of the hybrid system. The polymeric derivatives applicable as matrices are the ones with high thermal stability and optical transparency. A large variety of polymers were tested as host matrix, such as polymethyl methacrylates, polyether ketones, polyimides, and polycarbonates. The most used material is polymethyl methacrylate, due to its intrinsic optical properties, stability, functionalization possibilities, and processability. Another material used as the host for NLO substances is silica matrix, which has important advantages: the facility and flexibility of syntheses as well as the possibility of processing them as thin films. Ji et al. [64, 65] report the successful embedding of Disperse Red 1 as chromophore in a silica glass prepared by using sol-gel synthesis. The silicate precursor was a new derivative 1,4 phenylene bis(4-trimethoxysilyl ethyl benzoate), with a structure that allows uniform dispersion and accommodates the chromophore molecules in the cross-linked polymeric matrix (see **Figure 8**).

The hybrid film is fabricated by in situ poling and sol-gel synthesis. The final material exhibits an efficient NLO behavior, with a very good thermal stability (the SHG signal is stable until 120°C, and the half decay temperature is 170°C.

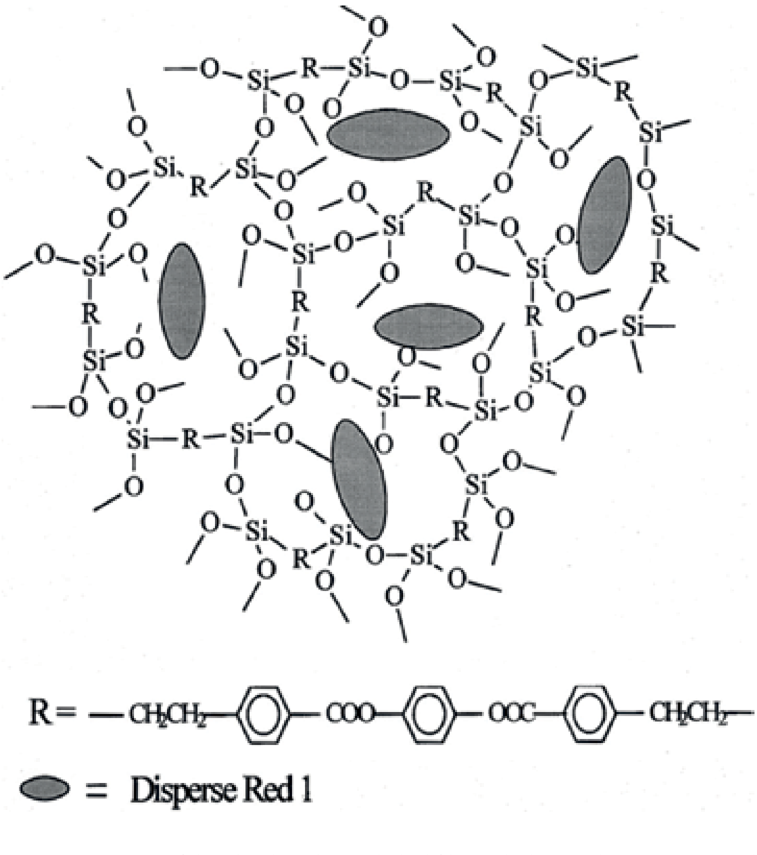

Figure 8. Schematic representation of the silica-based cross-linked film with chromophore Disperse Red 1 (adapted with the permission from reference [64]).

Another advantage of silica as host material is the possibility to prepare polymer-silica hybrid matrix that combines the best properties from both substances. An interpenetrating polymer-silica matrix was prepared [66] from polymerization of γ-methacrylpropyl)-silsesquioxane and an allyl glycidyl ether modified chromophore (Disperse Orange 3 (DO3)). The high degree of cross-link density and order leads to enhancement of the nonresonant second-order nonlinearity in the film obtained. Unfortunately, the process is very difficult and laborious, since the incorporation of the NLO chromophore in the polymer-silica network is a three-step synthesis: (i) functionalization of DO3 with glycidyl ether, (ii) synthesis of monomer (γ-methacrylpropyl)-silsesquioxane using hydrolytic condensation of commercially available silane derivative, and (iii) the preparation of NLO embedded matrix through the free radical polymerization of modified chromophore and methacrylpropyl compound and the simultaneous cross-linking of the network [66].

The AFM images of the DO3-doped methacrylate-silica film before and after poling demonstrate that the poling process allows a better orientational order of the chromophore molecules (see **Figure 9**).

This material exhibits a very good temporal stability of the chromophore orientation in the interpenetrated hybrid polymer-silica matrix, together with superior NLO properties.

Silica material mentioned above could also provide the sites to adjust covalent bonding of the chromophores. Recently, Laskowska et al. [67] reported the fabrication of NLO thin films from a novel functionalized mesoporous silica material as host matrix. To show the efficiency of the concept in tuning the NLO behavior from the morphology of the silica matrix, a very simple optically active compound is proposed, a dipolar copper propyl phosphonate fragment. The copper-containing functional groups are covalently linked to the silica wall inside the pore of the matrix. The structure of the proposed material is presented schematically in **Figure 10**.

The host matrix consists in mesoporous silica thin films with 2D hexagonally distributed nanometric pores. The suitable morphological characteristics of the silica material, with

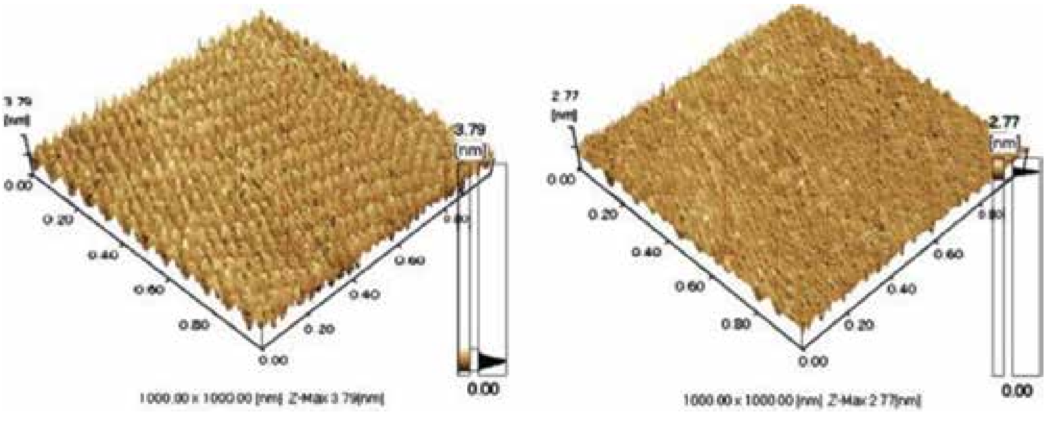

Figure 9. The AFM images of the film before and after poling 2 h at 150°C (reproduced with permission from reference [66]).

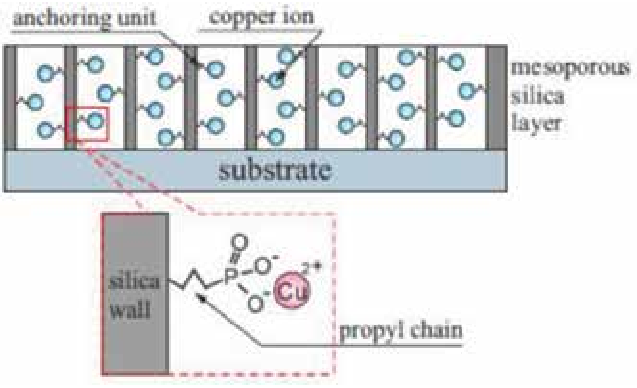

Figure 10. Schematic representation of the structure of mesoporous silica thin layer with Cu^{2+} propyl phosphonate chromophore bonded into pores (adapted with the permission from reference [67]).

hexagonal pores, regularly 2D distributed and aligned perpendicularly to the substrate, provide large specific area for easy access to the pore interior and lead to a high loading of the active chromophore. Moreover, the optical active moieties are very uniformly distributed.

Since the SHG signal obtained depends on the concentration of the NLO fragments, the material with tunable NLO response could be obtained by adjusting the functionalization degree from the synthesis parameters.

4. The arrangement of chromophores in polymeric host matrix

The macromolecular host matrix encapsulates the chromophores either dispersed or attached on the polymeric chain. In both cases, the most important issue that appears is the proper arrangement of NLO active molecules. The common procedure to obtain the required noncentrosymmetric arrangement for the dipolar push-pull chromophores embedded in a polymeric matrix is based on electric field poling process. It consists in the application of the electric field across the material, when heating the system to the glass transition temperature (Tg) of the polymer.

When photosensitive dyes are encapsulated, for example, azo-derivatives, light can be used in order to replace the heating procedure (photoassisted poling). This method is a choice when temperature-sensitive NLO molecules are involved, enabling poling process preformed at temperatures well below Tg. A large variety of azo-derivatives have been poled using this method (1).

Other guest molecules may be covalently bonded to the polymer chain, but the chemistry involved in the attachment of the chromophore to the macromolecule still remains a major challenge. Severe conditions in synthesis and processing employed to prepare most of side-chain NLO polymers (polymers with grafted chromophore as side chain) limit their practical application. The use of these polymer-based materials generates several film properties required for photonic applications, such as thermal and chemical stability, high loading of the active molecule, and stability of the chromophore orientation [68]. Highly cross-linking of side-chain polymers enhances the stability of the thin film together with the chromophore moiety arrangement.

Another covalent bonded variant is main-chain NLO polymer, with chromophores linked in the backbone at either end of the chromophore or linked at both ends of the chromophores, to form the polymer backbone. The dye fragment can be processed in various configurations: a head-to-tail (isoregic), head-to-head (syndioregic), or in random head-to-tail and head-to-head configurations (aregic) (2) [69].

4.1. Langmuir-Blodgett films

The most efficient way to obtain the arrangement of the large dye molecules is to take advantage from their intrinsic self-assembling ability. Hydrophobically modified chemicals that exhibit NLO properties can be efficiently organized as 2D structure using the Langmuir-Blodgett technique. Formation of the coherent and stable Langmuir film at liquid-air interface is mandatory for the further step, the transfer on solid substrate. The self-assembling properties of the NLO compounds could be tuned by chemical modification of the chromophore with various groups with suitable hydrophobicity, but the chemical modification will also influence the optical properties.

Tang et al. [70] report a study on the influence of the terminal group of the modified amphiphilic azobenzene chromophore on the Langmuir-Blodgett monolayer and multilayer formation. The azobenzene NLO derivative was modified with various electron acceptor groups (acetyl, nitro, and cyano), and the self-assembling behavior of the resulted compounds was investigated, to produce monolayers and multilayers deposited onto hydrophobically treated quartz substrate.

The experimental data confirm the molecular modeling conclusion that the packing of modified azobenzene molecules at the water-air interface and the transfer of the film are both due to the equilibrium of non-covalent interactions in the aggregates, dipol-dipol and π-π stacking interactions, respectively. The packing density and the electronic coupling vary strongly with the chemical structure of the functional group (see **Figure 11**).

The possibility to control the internal morphology and stability of the film through the balance of non-covalent interactions leads to the preparation of highly ordered multilayered film with large second-order susceptibility.

Most of the NLO chromophores could not be chemically modified to achieve suitable properties for spreading as Langmuir monolayers at the air-liquid or liquid-liquid interfaces; thus, the formation of Langmuir-Blodgett film is restricted to compound with a required degree of amphiphilicity. At the same time, many NLO materials processed by using Langmuir-Blodgett technique exhibit poor mechanical stability and limited surface area for deposition. A more sophisticated method to ensure the orientation of the chromophore molecules in the polymeric host network is to produce self-assembled thin film with the aid of film-forming matrix.

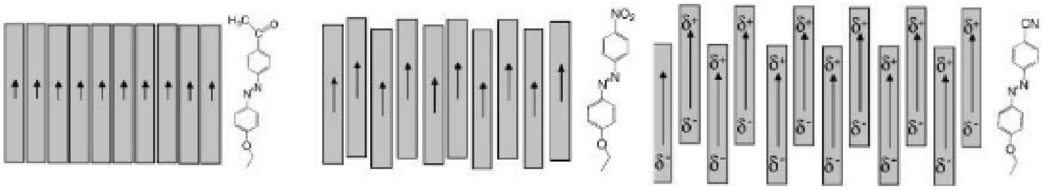

Figure 11. The representation of monolayer structure with various packing densities for azobenzene NLO compounds bearing acetyl, nitro, and cyano groups (adapted with the permission from reference [70]).

Usually, Langmuir-Blodgett films are obtained from Langmuir film deposited at the air-water interfaces with the well-known orientation of the molecule with the hydrophobic groups in air and hydrophilic ones immersed in water.

The driving forces of coherent monolayer formation are the hydrophobic interactions between the nonpolar parts and the interaction between the polar groups and the water subphase. Wang et al. [71] propose an unconventional method to prepare NLO LB films based on the molecular electrostatic interaction of hydrogen bonding in a chromophore modified with urea. The new synthesized optic active compound is 1-(10′-[(10-nitro)-6,7-azobenzenl]-ether-decyl)-3-(tetracosa-12,14-diynyl)urea (NAEDTDU), which exhibits an unusual packing behavior at air-water interface as it is proven by the Π-A isotherm (see **Figure 12**).

The recorded specific molecular area of NAEDTDU is 35 Å^2/molecule, smaller than the molecular area of the usual urea-containing derivatives in Langmuir film (50 Å^2/molecule).

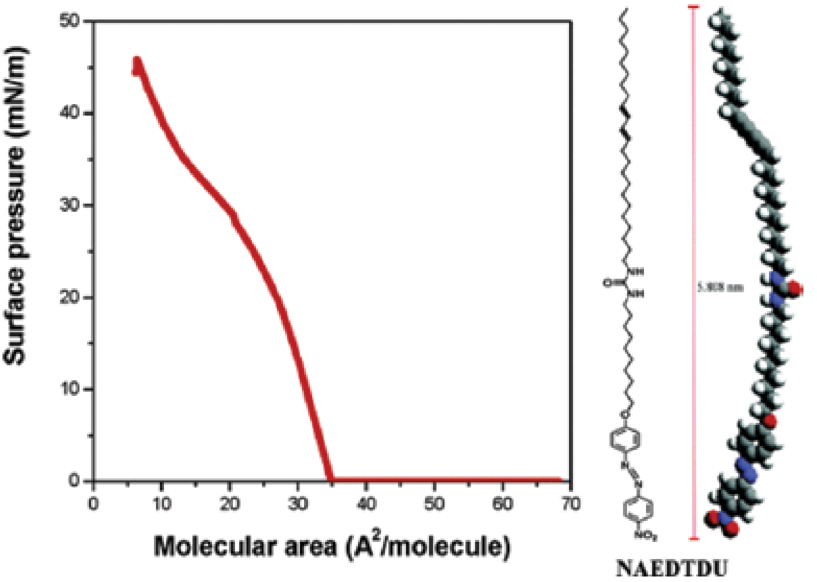

Figure 12. Π-A isotherm of Langmuir film of NAEDTDU (adapted with the permission from reference [71]).

When assuming a traditional orientation of NAEDTDU molecule in the monolayer, with the urea polar group in the water subphase and both hydrophobic alkyl chain and nitro-azobenzene group in air, the molecular modeling suggests specific surface area larger than 50 $Å^2$/molecule. To obtain the observed 35 $Å^2$/molecule value, it is presumable that the nitro group of chromophore molecule lies on the air-water interface. Langmuir NAEDTDU monolayer can be transferred onto a hydrophobically modified quartz and silicon substrates using conventional vertical upward dipping technique and produces Langmuir-Blodgett multilayers. In this nontraditional LB monolayer, a peculiar aggregation of the chromophore molecules is suggested, i.e., the formation of a stable and linear network based on the hydrogen bonding between the urea groups.

The noncentrosymmetric arrangement of the NAEDTDU molecule in LB films generates relatively large intensities of SHG signal recorded. The thermal stability of SHG activity of LB multilayers was improved after photopolymerization of diacetylene moieties in film, due to the restriction of the movement of the chromophores and stabilization of their ordered orientation.

4.2. Layer-by-layer deposited thin films

The layer-by-layer (LbL) method to produce thin films is a versatile and convenient technique for the fabrication of thin films, based on the electrostatic attraction between the materials in different layers successively deposited. The most relevant advantage of LbL technique is represented by the precise control of the composition and thickness of the final film, which can be easily tuned from the chemical structure of the polyelectrolytes and deposition parameters. Acentric supramolecular architecture, as essential requirement for preservation of NLO properties, is a challenge to be achieved from chromophores and polyelectrolytes in LbL film technique. The conventional LbL technique should be adjusted in order to ensure the density and stability of the optic active molecules in the obtained film, with particular attention to be paid to the orientation of chromophore [72].

Facile fabrication of a second-order nonlinear optical films with superior properties and stability was reported [73] using a surface sol-gel synthesis of ZrO_2 layers and subsequent layer-by-layer (LbL) deposition of the nonlinear optical (NLO)-active azobenzene-containing polyanion and poly(diallyldimethylammonium chloride). The resulted material is an organic/inorganic hybrid multilayer film with noncentrosymmetrically orientated azobenzene chromophores. The specific orientation of the NLO-active azobenzene chromophores is produced by the strong repulsive interactions between the negatively charged ZrO_2 and the sulfonate groups of the sulfonate-modified azobenzene chromophore.

The SHG signal could be increased by increasing the number of deposition cycles and also with the increase of the azobenzene graft ratio in the polyion. Wang et al. [74] proposed a method to fabricate an organic/inorganic hybrid NLO film by electric field-induced layer-by-layer deposition technique. The compound used to produce alternative layers is a new synthesized polycation from aromatic diazo group linked silicon and a chromophore molecule 2-({4-[4-(2-carboxy-2-cyano-vinyl)-phenylazo]-phenyl}-methyl-amino)-ethyl acid (DRCB) as anion.

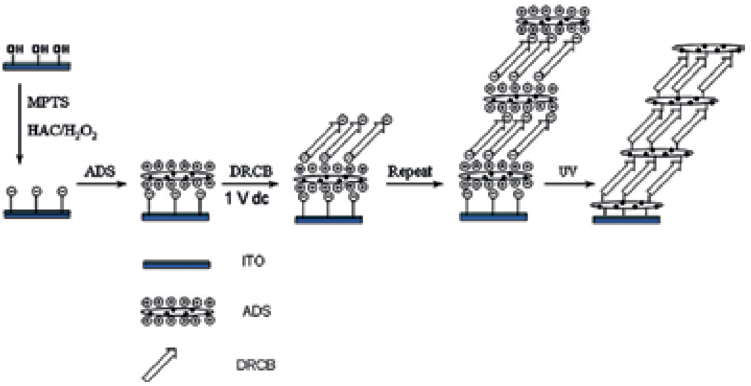

Figure 13. The structure of the ADS-DRBC hybrid thin film (adapted with the permission from reference [74]).

Using electric field in assembling process, the oriented adsorption of chromophores is facilitated, and the density of oriented optic active molecules increases. The preparation of the hybrid film using LbL deposition of aromatic diazonium salt-linked silicon sol (ADS) and DRCB chromophore on ITO glass previously functionalized with (3-mercaptopropyl)-trimethoxysilane (MTPS) is presented in **Figure 13**.

The UV irradiation of deposited multilayered films results in transformation of the electrostatic interaction between layers in covalent bonds, leading to a significant increase of the thermal and chemical stability of the final material. The architecture assembles with the aid of the electric field ensuring a high degree of molecular orientation of chromophores; thus, large second-harmonic generation signal of the LbL film was observed.

5. Theoretical modeling

In order to rational design the host-guest material, molecular dynamic simulation is used for quantum chemical calculation. The structures of considered molecules are simulated by using molecular dynamics, and relevant electrical properties, such as polarizability α and β, could be computed with density functional theory (DFT). For example, Makowska-Janusik (3) reports the investigation of the influence of polymeric matrix on the NLO properties of the pyrazoloquinoline derivatives in poly(methyl methacrylate) matrix. According to the chemical structure of the chromophore molecules, the best description of the pyrazoloquinolines-PMMA systems could be obtained by using various approaches, such as point-dipole or distributed molecular response models, with good concordance with the experimental data. Molecular simulation is also performed in order to elucidate the origin of the NLO behavior in composite materials, since in experimental approach it is not possible to separate the contributions of each component. The molecular modeling methods can provide explanations about the nature of the guest-host interaction based on the separate different contribution of the components to the optical properties.

A particular kind of host-guest material exhibiting NLO properties is obtained by using semiconducting nanoparticles (quantum dots) as optical active materials. The interface phenomena play an important role in tuning the NLO properties of these materials.

An innovative approach is reported by Britton et al. [75], to significantly increase the nonlinear properties when combining in the polymeric matrix a low symmetry phthalocyanine derivative with CdSe/CdS quantum dots. The new synthesized metal-free chromophore 2,3-bis[2′-(2″-hydroxyethoxy)ethoxy]-9,10,16,17,23,24-hexa-*n*-butoxyphthalocyanine exhibits by itself an unusual electric properties due to the high dissymmetry of electronic density in the molecule. The addition of CdSe/CdS quantum dots to the phthalocyanine in chloroform solution produces a negligible effect on the values of the imaginary component of the third-order optical susceptibility and nonlinear absorption coefficient β_{eff}. However, when the dye is embedded into a polycarbonate matrix, a twofold increase of the abovementioned optical properties is recorded, while the incorporation of both phthalocyanine and CdSe quantum dots into the polymeric film produces a three-times increase of the third-order optical susceptibility compared to the chloroform solution of the dye. The chromophore molecules and CdSe/CdS nanoparticles are in close proximity when they are locked together in the polymeric film; thus, the heavy atom effect could manifest, resulting in a significant improvement of NLO properties.

6. Conclusion

The synthesis of the most important classes of the organic compounds, alkyne, dye, heterocycle, thienyl, and ferrocene compounds, was presented. A lot of important reactions, like Sonogashira, Suzuki, Heck, Huisgen, Wadsworth-Emmons, Vilsmeier-Haack-Arnold, Wittig, etc., were employed for the synthesis of the new compounds with nonlinear optical applications. The synthesis of the new molecules possessing privileged structures, with a couple donor-acceptor or "push-pull" molecules, was the purpose of the last decades. Besides, new unorthodox structures, which do not possess this system, but with very good NLO properties and very good SHG signal, were reported, and the number of these increase every year. The most important parameters in the characterization of the new NLO organic compounds are the HOMO-LUMO energy gap and the first-order hyperpolarizability β_{tot}. Small energy gaps and high hyperpolarizabilities define the best compounds with nonlinear optical applications.

Thin films were fabricated by incorporating substances with NLO properties in a large variety of polymers to improve the performance of the resulted hybrid system. Polymethyl methacrylate is the most used polymer, but silica matrix is preferred. Also, Disperse Red 1 in a silica glass allows uniform dispersion and arrangement of the chromophore molecules in the cross-linked polymeric matrix. The new hybrid films are fabricated by sol-gel synthesis. The morphology of the silica matrix is very important for a good NLO behavior. Each class of organic compounds possesses a specific method for the fabrication of the thin films in order to increase their NLO properties. Thus, azo-photosensitives dyes are encapsulated. Noncentrosymmetric arrangement for the dipolar push-pull chromophores embedded in a polymeric matrix is obtained when heating the system to the glass transition temperature (T)g of the polymer. Langmuir-Blodgett films, which exhibit better NLO properties, are obtained from Langmuir film deposited at the air-water interfaces with the well-known orientation of the molecule with the hydrophobic groups in air and hydrophilic ones immersed in water. A convenient technique for the fabrication of thin films is the layer-by-layer (LbL) method which presents the advantage of the precise control of the composition and thickness of the final film. Both theoretical modeling and experimental approach should be addressed, in order to find the best matching between the host and guest material. In addition, the influence of the surface and film formation method should be considered, with a particular attention to the thermo- or photosensitive chromophores.

Conflict of interest

The authors have no conflict of interest to declare.

List of abbreviations

SHG	Second-harmonic generation
HOMO-LUMO gap	The difference between the energy of the highest occupied molecular orbital and the lowest unoccupied molecular orbital (eV)
α	Molecular polarizability (esu·D)
β_{tot}	First-order hyperpolarizability (esu·D)
μ_{tot}	Dipole moment (D)
Q	Quadrupole moment (D)
Tg	Glass transition temperature (°C)
LbL	Layer-by-layer deposition technique

Author details

Ludmila-Otilia Cinteza[1] and Maria Marinescu[2]*

*Address all correspondence to: maria7marinescu@yahoo.com

1 Faculty of Chemistry, Department of Physical Chemistry, University of Bucharest, Bucharest, Romania

2 Faculty of Chemistry, Department of Organic Chemistry, Biochemistry and Catalysis, University of Bucharest, Bucharest, Romania

References

[1] Delaire JA, Nakatani K. Linear and nonlinear optical properties of photochromic molecules and materials. Chemical Reviews. 2000;**100**:1817-1846

[2] Yesodha SK, Sadashiva Pillai CK, Tsutsumi N. Stable polymeric materials for nonlinear optics: A review based on azobenzene systems. Progress in Polymer Science. 2004;**29**:45-74

[3] Makowska-Janusik M. Influence of the polymeric matrix on the NLO molecular response in guest-host materials. Nonlinear Optical and Quantum Electronics. 2007;**37**:75-85

[4] Liu X, Yang Z, Wang D, Cao H. Molecular structures and second-order nonlinear optical properties of ionic organic crystal materials. Crystals. 2016;**6**:158-165

[5] Wazzan N, Safi Z. DFT calculations of the tautomerization and NLO properties of 5-amino-7-(pyrrolidin-1-yl)-2,4,4-trimethyl-1,4-dihydro-1,6-naphthyridine-8-carbonitrile (APNC). Journal of Molecular Structure. 2017;**1143**:397-404

[6] Wang T, Wang X, Zhang J, Wang C, Shao J, Jiang Z, et al. Synthesis, structure and third-order optical nonlinearities of hyperbranched metal phthalocyanines containing imide units. Dyes and Pigments. 2018;**154**:75-81

[7] Pegu D, Deb J, Saha SK, Paul MK, Sarkar U. Molecular structure, chemical reactivity, nonlinear optical activity and vibrational spectroscopic studies on 6-(4-n-heptyloxybenzyoloxy)-2-hydroxybenzylidene)amino)-2H-chromen-2-one: A combined density functional theory and experimental approach. Journal of Molecular Structure. 2018;**1160**:167-176

[8] Liu J, Ykang M, Gao W, Fedorchuk AA, Kityk IV. Synthesis and nonlinear optical properties of novel conjugated small molecules based on indole donor. Journal of Molecular Structure. 2018;**1165**:223-227

[9] Akchurin IO, Yakhutina AI, Bochkov AY, Solovjova NP, Medvedev MG, Traven VF. Novel push-pull fluorescent dyes—7-(diethylamino)furo- and thieno[3,2-c]coumarins derivatives: Structure, electronic spectra and TD-DFT study. Journal of Molecular Structure. 2018;**1160**:215-221

[10] Ghiasuddin AM, Adeel M, Khalid M, Tahir MN, Khan MU. A combined experimental and computational study of 3-bromo-5-(2,5-difluorophenyl) pyridine and 3,5-bis(naphthalen-1-yl)pyridine: Insight into the synthesis, spectroscopic, single crystal XRD, electronic, nonlinear optical and biological properties. Journal of Molecular Structure. 2018;**1160**:129-141

[11] Sangeetha KG, Aravindakshan KK, Safna Hussan KP. Insight into the theoretical and experimental studies of 1-phenyl-3-methyl-4-benzoyl-5-pyrazolone N(4)-methyl-N(4)-phenylthiosemicarbazone—A potential NLO material. Journal of Molecular Structure. 2017;**1150**:135-145

[12] Bragiel P, Radkowska I, Belka R, Marciniak B, Bak Z. Structural, spectroscopic and NLO features of 4-chloro-1-naphthol. Journal of Molecular Structure. 2018;**1154**:27-38

[13] Katariya SB, Patil D, Rhyman L, Alswaidan IA, Ramasami P, Sekar N. Triphenylamine-based fluorescent NLO phores with ICT characteristics: Solvatochromic and theoretical study. Journal of Molecular Structure. 2018;**1150**:493-506

[14] Drozd M, Daszkiewicz M. A synthesis, X-ray crystallographic and vibrational studies of guanidinium *o*-nitrobenzoate hydrate. New NLO crystal in guanidinium nitrobenzoate family. Journal of Molecular Structure. 2018;**1161**:383-392

[15] Sangeetha K, Guru Prasad L, Mathammal L. Structural elucidation and physicochemical properties of an organic NLO crystal: 4-Nitrotoluene-2-sulphonic acid dihydrate. Journal of Molecular Structure. 2018;**1155**:598-609

[16] Szukalski A, Sahraoui B, Kulyk B, Lazar CA, Manea AM, Mysliwiec J. Chemical structure *versus* second-order nonlinear optical response of the push–pull type pyrazoline-based chromophores. RSC Advances. 2017;**2017**:9941-9947

[17] Yhang YX, Wang YH. Nonlinear optical properties of metal nanoparticles: A review. RSC Advances. 2017;**2017**:45129-45144

[18] Han P, Wang D, Gao H, Zhang J, Xing Y, Yang Z, et al. Third-order nonlinear optical properties of cyanine dyes with click chemistry modification. Dyes and Pigments. 2018;**149**:8-15

[19] Fernandesa SSM, Herbivo C, Aires-de-Sousa J, Comel A, Belsley M, Raposo MMM. Theoretical and experimental studies of aryl-bithiophene based push-pull π-conjugated heterocyclic systems bearing cyanoacetic or rhodanine-3-acetic acid acceptors for SHG nonlinear optical applications. Dyes and Pigments. 2018;**149**:566-573

[20] Čibová A, Martinická A, Magdolen P, Zahradník P, Cigáň M, Uherek M, et al. Dicationic and monocationic benzobisthiazolium salts as potential NLO chromophores. Dyes and Pigments. 2018;**149**:597-611

[21] Xu H, Wan N, Zhang X, Li Z, Deng G. Monolithic NLO chromophores with different pendant groups and matrix-assisted-poling effect: Synthesis and characterization. Dyes and Pigments. 2018;**157**:230-237

[22] Fominykh OD, Kalinin AA, Sharipova SM, Sharipova AV, Burganov TI, Smirnov MA, et al. Composite materials containing chromophores with 3,7-(di)vinylquinoxalinone π-electron bridge doped into PMMA: Atomistic modeling and measurements of quadratic nonlinear optical activity. Dyes and Pigments. 2018;**158**:131-141

[23] Durand RJ, Achelle S, Gauthier S, Cabon N, Ducamp M, Kahlal S. Incorporation of a ferrocene unit in the π-conjugated structure of donor-linker-acceptor (D-π-A) chromophores for nonlinear optics (NLO). Dyes and Pigments. 2018;**155**:68-74

[24] Erande Y, Kothavale S, Sreenath MC, Chitrambalam S, Joe IH, Sekar N. Triphenylamine derived coumarin chalcones and their red emitting OBO difluoride complexes: Synthesis, photophysical and NLO property study. Dyes and Pigments. 2018;**148**:474-491

[25] Pandith AH, Islam N. Electron transport and NLO properties of substituted aryldimesityl boranes: A DFT study. Lisesivdin SB, editor. PLoS ONE. 2014;**9**:e114125

[26] Hasan T, Mehdi SH, Ghalib RM, Singh PK, Misra N. An investigation on structural, vibrational and nonlinear optical behavior of 4b,9b-dihydroxy-7,8-dihydro-4bH-Indeno [1,2-b] Benzofuran-9,10(6H,9bH)-dione: A DFT study. Journal of Chemical Sciences. 2015; **127**:2217-2223

[27] Goud NR, Zhang X, Bredas JL, Coropceanu V, Matzger AJ. Discovery of nonlinear optical materials by function-based screening of multi-component solids. Chem. 2018;**4**:150-161

[28] Ryhding T, Suhr Kirketerp M-B, Kadhane U, Lykkegaard MK, Panja S, Nielsen SB, et al. Upon the intrinsic optical properties of oligo(p-phenyleneethynylene)s (OPEs). Synthesis of OPE3 for experimental gas-phase absorption studies. Tetrahedron. 2008;**64**(50): 11475-11479

[29] Wang D, Zhang W, Xing Y, Gao H, Wang X, Zhao Y, et al. Energy-level modulation of organic alkynes by click chemistry. Tetrahedron. 2013;**69**:895-901

[30] Ostroverkhova O, editor. Handbook of Organic Materials for Optical and (Opto)Electronic Devices: Properties and Applications. Oxford: Woodhead Publ; 2013. 804 p. (Woodhead publishing series in electronic and optical materials)

[31] Yadav P, Anand T, Moram SSB, Bhattacharya S, Sankar M, Rao SV. Synthesis and femtosecond third order nonlinear optical properties of push-pull trans-A2B-corroles. Dyes and Pigments. 2017;**143**:324-330

[32] Marinescu M, Emandi A, Marton G, Cinteza LO, Constantinescu C. Structural studies and optical nonlinear response of some pyrazole-5-ones. Nanoscience Nanotechnology Letters. 2015;**7**:846-854

[33] Raposo MMM, Ferreira AMFP, Belsley M, Moura JCVP. 5′-Alkoxy-2,2′-bithiophene azo dyes: A novel promising series of NLO-chromophores. Tetrahedron. 2008;**64**:5878-5884

[34] Kleinpeter E, Koch A, Mikhova B, Stamboliyska BA, Kolev TM. Quantification of the push–pull character of the isophorone chromophore as a measure of molecular hyperpolarizability for NLO applications. Tetrahedron Letters. 2008;**49**:1323-1327

[35] Emandi A, Vasiliu IC, Marinescu M. Solvatochromic properties of azo pyrazolone ligands in coordinative compounds with erbium. Nanoscience Nanotechnology Letters. 2013;**5**: 487-492

[36] Zajac M, Hrobárik P, Magdolen P, Foltínová P, Zahradník P. Donor–π-acceptor benzothiazole-derived dyes with extended heteroaryl-containing conjugated system: Synthesis, DFT study and antimicrobial activity. Tetrahedron. 2008;**64**:10605-10618

[37] Čibová A, Magdolen P, Fülöpová A, Kožíšek J, Cigáň M, Zahradník P. Push–pull molecular structures based on angular benzobisthiazolium acceptor: Synthesis, photophysical properties and theoretical studies. Tetrahedron. 2015;**71**:315-323

[38] Hebbar N, Ramondenc Y, Plé G, Dupas G, Plé N. Push–pull structures with a pyrazine core and hexatriene chain: Synthesis and light-emitting properties. Tetrahedron. 2009;**65**: 4190-4200

[39] Cho N, Kim J, Song K, Lee JK, Ko J. Synthesis and characterization of push–pull organic semiconductors with various acceptors for solution-processed small molecule organic solar cells. Tetrahedron. 2012;**68**:4029-4036

[40] Shi W-J, Lo P-C, Singh A, Ledoux-Rak I, Ng DKP. Synthesis and second-order NLO properties of push-pull BODIPY derivatives. Tetrahedron. 2012;**68**:8712-8718

[41] Farat OK, Farat SA, Ananyev IV, Okovytyy SI, Tatarets AL, Markov VI. Novel xanthene push-pull chromophores and luminophores: Synthesis and study of their spectral properties. Tetrahedron. 2017;**73**:7159-7168

[42] Malytskyi V, Gadenne V, Ksari Y, Patrone L, Raimundo J-M. Synthesis and characterization of thiophene-based push-pull chromophores for tuning the electrical and optical properties of surfaces with controlled SAM formation. Tetrahedron. 2017;**73**:5738-5744

[43] Ion V, Matei A, Constantinescu C, Ionita I, Marinescu M, Dinescu M, et al. Octahydroacridine thin films grown by matrix-assisted pulsed laser evaporation for NLO applications. Material Science in Semiconductor Processing. 2015;**36**:78-83

[44] Marco AB, Andreu R, Franco S, Garín J, Orduna J, Villacampa B, et al. Efficient second-order nonlinear optical chromophores based on dithienothiophene and thienothiophene bridges. Tetrahedron. 2013;**69**:3919-3926

[45] Raposo MMM, Sousa AMRC, Fonseca AMC, Kirsch G. Synthesis of formyl-thienylpyrroles: Versatile building blocks for NLO materials. Tetrahedron. 2006;**62**:3493-3501

[46] Batista RMF, Costa SPG, Malheiro EL, Belsley M, Raposo MMM. Synthesis and characterization of new thienylpyrrolyl-benzothiazoles as efficient and thermally stable nonlinear optical chromophores. Tetrahedron. 2007;**63**:4258-4265

[47] Batista RMF, Costa SPG, Belsley M, Raposo MMM. Synthesis and second-order nonlinear optical properties of new chromophores containing benzimidazole, thiophene, and pyrrole heterocycles. Tetrahedron. 2007;**63**:9842-9849

[48] Herbivo C, Comel A, Kirsch G, Raposo MMM. Synthesis of 5-aryl-5′-formyl-2,2′-bithiophenes as new precursors for nonlinear optical (NLO) materials. Tetrahedron. 2009;**65**:2079-2086

[49] Genin E, Hugues V, Clermont G, Herbivo C, Castro MCR, Comel A. Fluorescence and two-photon absorption of push–pull aryl(bi)thiophenes: Structure–property relationships. Photochemical & Photobiological Sciences. 2012;**11**:1756-1766

[50] Raposo MMM, Castro MCR, Fonseca AMC, Schellenberg P, Belsley M. Design, synthesis and characterization of the electrochemical, nonlinear optical properties, and theoretical studies of novel thienylpyrrole azo dyes bearing benzothiazole acceptor groups. Tetrahedron. 2011;**67**:5189-5198

[51] Castro MCR, Belsley M, Fonseca AMC, Raposo MMM. Synthesis and characterization of novel second-order NLO-chromophores bearing pyrrole as an electron donor group. Tetrahedron. 2012;**68**:8147-8155

[52] Pauson PL. Ferrocene—How it all began. Journal of Organometallic Chemistry. 2001; **637–639**:3-6

[53] Matei A, Constantinescu C, Ion V, Mitu B, Ionita I, Dinescu M, et al. Ferrocene, an old molecule with a bright future: Thin films grown by matrix-assisted pulsed laser evaporation for nonlinear optical applications. Journal of Organometallic Chemistry. 2014;**751**:638-643

[54] Werner H. At least 60 years of ferrocene: The discovery and rediscovery of the sandwich complexes. Angewandte Chemie International Eddition. 2012;**51**:6052-6058

[55] Enlow JO, Jiang H, Grant JT, Eyink K, Su W, Bunning TJ. Plasma polymerized ferrocene films. Polymer. 2008;**49**:4042-4045

[56] Rubbiani R, Blacque O, Gasser G. Sedaxicenes: Potential new antifungal ferrocene-based agents? Dalton Transactions. 2016;**45**:6619-6626

[57] Altaf AA, Khan N, Lal B, Badshah A. Synthesis, characterization and DNA-intercalation studies of two ferrocene-based Fe-Sn heterobimetallic compounds, and crystal structure of trimethyltin (p-ferrocenyl)benzoate. Journal of Coordination Chemistry. 2017;**70**:3523-3540

[58] Matei A, Constantinescu C, Ion V, Mitu B, Ionita I, Dinescu M, et al. Ferrocene, an old molecule with bright future: Thin films grown by matrix-assisted pulsed laser evaporation for nonlinear optical applications. The Journal of Organic Chemistry. 2014;**751**:638-643

[59] Constantinescu C, Matei A, Ion V, Mitu B, Ionita I, Dinescu M, et al. Ferrocene carboxaldehyde thin films grown by matrix-assisted pulsed laser evaporation for nonlinear optical applications. Applied Surface Science. 2014;**302**:83-86

[60] Yang F, Xu X-L, Gong Y-H, Qiu W-W, Sun Z-R, Zhou J-W, et al. Synthesis and nonlinear optical absorption properties of two new conjugated ferrocene-bridge-pyridinium compounds. Tetrahedron. 2007;**63**:9188-9194

[61] Matei A, Marinescu M, Constantinescu C, Ion V, Mitu B, Ionita I, et al. Nonlinear optical studies on 4-(ferrocenylmethylimino)-2-hydroxy-benzoic acid thin films deposited by MAPLE. Applied Surface Science. 2016;**374**:206-212

[62] Victorovna-Lijanova I, Reyes-Valderrama MI, Maldonado J-L, Ramos-Ortiz G, Tatiana K, Martínez-García M. Synthesis and cubic nonlinear optical behavior of phenyl and ferrocenyl-ended resorcinarene-based dendrimers. Tetrahedron. 2008;**64**:4460-4467

[63] Villalonga-Barber C, Vallianatou K, Georgakopoulos S, Steele BR, Micha-Screttas M, Levin E, et al. Synthesis, characterisation, electronic spectra and electrochemical investigation of ferrocenyl-terminated dendrimers. Tetrahedron. 2013;**69**:3885-3895

[64] Ji S, Li Z, Zhou X, Cao M, Dai D, Zhang R, et al. Silica-based hybrid nonlinear optical chromophore-trapping film prepared by sol-gel polymerization. Polymers for Advanced Technologies. 2003;**14**:254-259

[65] Zongo S, Kerasodou AP, Sone BT, Diallo A, Mthunzi P, Iliopoulus K. Nonlinear optical properties of poly(methyl methacrylate) thin films doped with Bixa Orellana dye. Applied Surface Science. 2015;**340**:72-77

[66] Wang D, Chen X, Zhang X, Wang W, Liu Y, Hu L. Fabrication of nonlinear optical films based on methacrylate/silica hybrid matrix. Current Applied Physics. 2009;**9**(3):S170-S173

[67] Laskowska M, Kityk I, Dulski M, Jędryka J, Wojciechowski A, Jelonkiewicz J, et al. Functionalized mesoporous silica thin films as a tunable nonlinear optical material. Nanoscale. 2017;**9**:12110-12123

[68] Muller K, Bugnicourt E, Latoore M, Jorda M, Sanz YE, Lagaron JM, et al. Review on the processing and properties of polymer nanocomposites and nanocoatings and their applications in the packaging, automotive and solar energy fields. Nanomaterials. 2017;**7**:2-47

[69] Colpaert M, Banerjee S, Ladmiral V, Ono T, Ameduri B. Synthesis and properties of poly (trifluoroethylene) via a persistent radical mediated polymerization of trifluoroethylene. Polymer Chemistry. 2018;**9**:894-903

[70] Tang Z, Johal MS, Scudder P, Caculitan N, Magyar RJ, Tretiak S, et al. Study of the noncovalent interactions in Langmuir–Blodgett films: An interplay between $\pi-\pi$ and dipole–dipole interactions. Thin Solid Films. 2007;**516**:58-66

[71] Wang Y, Wang C, Wang X, Guo Y, Xie B, Cui Z, et al. Hydrogen-bonding fabrication of NLO Langmuir−Blodgett films with nontraditional molecular architecture and unique thermal stability. Chemistry of Materials. 2005;**17**:1265-1268

[72] Yan Y, Yuan Y, Wang B, Gopalan V, Giebink NC. Sub-wavelength modulation of $X^{(2)}$ optical nonlinearity in organic thin films. Nature Communications. 2017;**8**:14269

[73] Kang E-H, Bu T, Jin P, Sun J, Yang Y, Shen J. Layer-by-layer deposited organic/inorganic hybrid multilayer films containing noncentrosymmetrically orientated azobenzene chromophores. Langmuir. 2007;**23**:7594-7601

[74] Wang S, Zhao L, Zhang X, Shi Z, Cui Z, Yang Y. Electric-field-induced layer-by-layer fabrication of inorganic–organic hybrid second-order nonlinear optical films. Journal of Colloid and Interface Science. 2009;**336**:470-476

[75] Britton J, Martynov AG, Oluwole DO, Gorbunova YG, Tsivadze AY, Nyokong T. Improvement of nonlinear optical properties of phthalocyanine bearing diethyleneglycole chains: Influence of symmetry lowering vs. heavy atom effect. Journal of Porphyrins and Phthalocyanines. 2016;**20**:1296-1305

Chapter 2

Shot Peening of Austempered Ductile Iron

Ann Zammit

Additional information is available at the end of the chapter

http://dx.doi.org/10.5772/intechopen.79316

Abstract

Austempered ductile iron (ADI) is a type of heat-treated cast iron, which offers numerous positive advantages including: good combination of mechanical properties and damping characteristics, lower density than steel and the possibility of casting components into near-net shape. However, surface engineering techniques are necessary to extend the use and prolong the lifetime of ADI engineering components. One such treatment for improving the bending fatigue strength of ADI is shot peening. This treatment creates compressive residual stresses and high dislocation densities at the surface of the treated components. However, the shot peening process is not always beneficial in improving the tribological characteristics of ADI. Its behaviour depends on the type of wear mechanism, applied loads, lubrication, heat treatment process parameters and the resulting surface finish of the components. This chapter will look into the effect of shot peening on ADI in more detail and will delve into a case study, which was carried out to analyse the bending fatigue resistance and tribological characteristics of Cu-Ni-alloyed ADI.

Keywords: cast iron, austempered ductile iron, graphite nodules, upper ausferrite, shot peening, bending fatigue, tribology, surface engineering

1. Introduction

Compared to other ferrous materials, austempered ductile iron (ADI) has marked economic advantages such as low melting temperature, low shrinkage, excellent castability, good machinability and high damping capacity. Its versatility and wide range of properties make it widely used in the transportation industries, defence, heavy machinery, agricultural machinery and for general engineering applications. ADI can compete with steel on considerations of strength, for a given level of ductility. However, some alloyed and hardened steels exhibit better properties than ADI, and the use of ADI is limited when extreme tensile strength is required. As a raw material, ADI is cheaper than steel. It also has a lower manufacturing cost due to the possibility of casting the components to near-net shape. The cost and weight of ADI per unit of yield strength can compete with cast and forged aluminium, and forged steel. ADI exhibits higher damping characteristics than steel, leading to lower noise emission and less vibrations. The presence of graphite in ADI dampens vibrations 40% faster than in steel gears, and it also results in a 10% reduction in density compared to steel.

ADI is a type of cast iron, more commonly referred to as ductile iron, having an austempering heat treatment process applied to it. It is made up of graphite nodules in a matrix of acicular ferrite and retained austenite frequently referred to as ausferrite (**Figure 1**). Optimum properties are obtained when the chemical alloy composition, solidification micro-structure and heat treatment parameters are carefully controlled. The austempering heat treatment cycle (**Figure 2**) consists of first austenitising the ductile iron to temperatures between 850 and 1000°C, followed by quenching in a salt or oil bath. The bath is maintained between 230 and 450°C, a temperature above the martensite start temperature M_s and left there for sufficient time to transform the austenite to ausferrite. This is followed by cooling to room temperature.

The mechanical properties of ADI depend on the parameters of the austempering process, which determine the morphology of the ferrite, the volume fraction of retained austenite, the carbon content in the retained austenite, and the presence or absence of martensite and iron carbides in the austenite or ferrite. In general, the tensile strength of ADI varies from around 1500 MPa with a corresponding 1% elongation, to lower tensile strengths (900–1200 MPa) and higher corresponding elongations of up to 12%. The former group of ADIs is produced at lower austempering temperatures of 230–330°C and exhibits high hardness (~50–54 HRC), but limited ductility. These are used for applications requiring high resistance to contact stress. ADIs having lower tensile strength, which are produced at higher austempering temperatures of 350–400°C, have lower hardness ranging from around 23 to 34 HRC, but have high toughness and ductility [3]. This range of ADIs consist of structures with greater amounts of

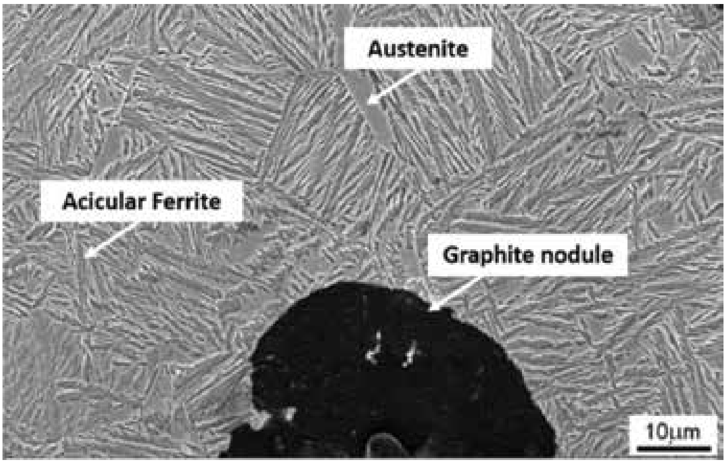

Figure 1. Typical micro-structure of ADI (austenitised at 900°C for 2 hours, austempered at 360°C for 1 hour) [1].

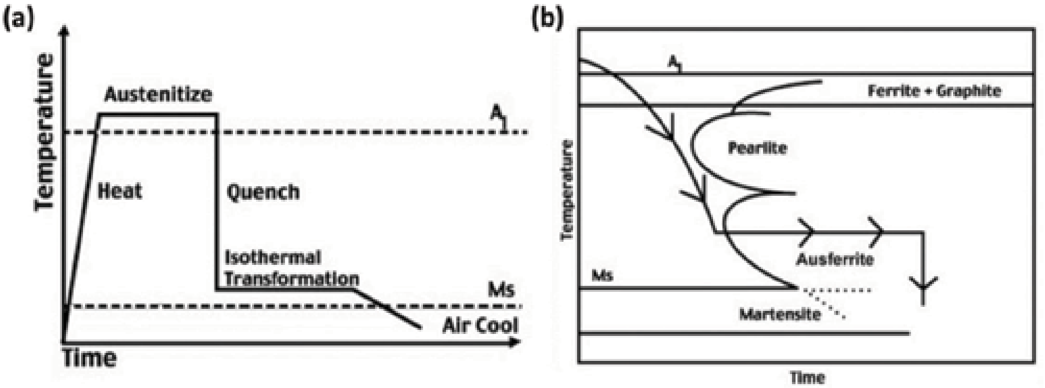

Figure 2. (a) Temperature-time plot for a typical austempering treatment and (b) austempering treatment superimposed on an isothermal transformation diagram [2].

austenite (V_γ), having high carbon content (C_γ) and provide a bending fatigue strength in the region between 200 and 500 MPa as reported in various studies carried out on both alloyed and unalloyed ADI [4–8].

When ADI engineering components require high toughness and ductility at the core of the component coupled with high bending fatigue strength and good tribological characteristics at the surface, the ADI can be first austempered in the higher temperature range of 350–400°C to obtain upper ausferrite. It is subsequently engineered to improve the surface properties and obtain the fatigue and tribological characteristics required by the intended application, using processes such as shot peening.

2. Shot peening

Shot peening (SP) is a conventional mechanical surface treatment during which the surface of a material is bombarded by spherical media (called *shot*) arriving at high velocity and under controlled conditions. During SP, shots are accelerated towards the surface using air pressure and a nozzle or a centrifugal wheel. Shots impart forces that form a dimple by plastic deformation and radial stretching of the material. The numerous dimples on the surface create several of such plastically deformed hemispheres, while the elastically stressed region tries to recover to the fully unloaded state. These inhomogeneous elastic-plastic deformations induce high residual compressive stress and high dislocation densities in the surface and to a depth of circa 120–500 μm [9]. Their magnitude is a function of the mechanical properties of the target material and is at least equal to half the yield strength of the material being peened [10].

The essential parameters of the SP process can be classified into three groups: shot (shape, hardness and size), workpiece (hardness, chemical composition, crystal structure, geometry) and flow parameters (shot velocity, impact angle, mass flow rate, peening time, coverage). These parameters need to be carefully controlled in order to achieve a uniform distribution of compressive stresses on the surface of a component.

The induced compressive layer and work hardening increase the resistance to crack initiation and propagation, which in turn prolongs components' lifetime. In fact, SP has been used for years to extend the bending fatigue life of various engineering components in the transport industry, mainly for automobile and aircraft parts. Such components include gears, axles, springs, connecting rods, crankshafts, I-beams in heavy duty applications, compressors, turbine rotors and shafts. SP can be applied to the whole component, or just confined to parts of the component that are expected to be highly stressed. For example, in gears, one can SP the entire gear tooth or alternatively focus the SP only at the tooth root fillets, which are exposed to the highest stress.

Although SP is not a new process, it is still very popular and has evolved considerably in the late twentieth and early twenty-first centuries. A great deal of research has been carried out to study the effects of SP on the materials being treated, including metallurgical, mechanical, and geometrical effects and also the effects of SP on the mechanical properties, tribological characteristics and corrosion resistance of a wide range of metals and alloys [11]. Recently, advanced surface modification technologies show the use of variants of the traditional SP process, four of which are shown in this issue, namely ultrasonic SP, severe SP (SSP), surface mechanical attrition treatment (SMAT) and duplex SP. Other variants of SP can be found in literature, including laser shock peening (LSP), micro-peening, cavitation shotless peening and ball or roller burnishing.

3. Shot peening of ADI

The high strains applied by the high-pressure impact of the shots on the surface of ADI are higher than the yield strength of the material, and both the ferrite and the austenite undergo plastic deformation. The ferrite work hardens with an increase in the dislocation density, while the austenite has the ability to cold work and to locally transform into martensite at high plastic deformation. The transformation induced plasticity (TRIP) phenomenon has been studied by various researchers [12, 13] and shown to depend on the carbon content in the austenite, its size and morphology and distribution within the structure.

As a result of work hardening and phase transformation, the hardness at the surface following SP of ADI increases by approximately 40–60% [11, 14–19]. Apart from an increase in the surface hardness, SP also results in the creation of compressive residual stresses of around 700–1000 MPa [15–19]. The residual compressive stresses caused by SP increases the dislocation density hindering dislocation motion. The stress-induced austenite to martensite transformation also results in volume expansion further creating local compressive stresses.

3.1. Influence of shot peening on bending fatigue strength of ADI

Shot peening is known to improve the bending fatigue properties of ADI [14, 15, 20, 21]. The improvement of bending fatigue resistance following SP is due to the formation of a compressed layer beneath the surface of the SP component. Cracks tend not to initiate or propagate in surfaces upon which a compressive force is acting. The induced compressive stresses shift crack nucleation to the sub-surface and hinders fatigue crack propagation at the surface. Apart from hardening the surface, SP also eliminates microscopic defects, machining marks and grinding defects. This also increases the bending fatigue strength. However, Uematsu et al. [22] showed that SP cast iron containing spheroidal vanadium carbides (VCs), dispersed in a martensitic matrix, did not eliminate large casting voids. These voids and clusters of VCs served as sources of crack initiation, and hence SP did not improve the bending fatigue strength in this particular case.

3.2. Influence of shot peening on tribological characteristics of ADI

Wear of materials is a complex phenomenon, and depends on the running conditions and the properties of the tribopair materials. SP should be beneficial in reducing wear rates because of the high hardness due to work hardening, stress-induced austenite to martensite transformation, and residual compressive stresses at the surface [10, 23, 24]. Compressive stresses prevent micro-cracks from forming, thus inhibiting pitting or spalling. Kobayashi and Hasegawa [25] showed this to be true for carburised steel gears. This was attributed to the compressive stress suppressing cracking and delaying crack growth. Champaigne [10] and Townsend and Zaretsky [26] reported an improvement in the contact fatigue life of SP steel gears of around 1.5 times. In another study, Townsend [27] reported that a higher peening intensity (0.38–0.43 mmA) resulted in higher compressive stresses, and hence lead to a 10% rolling contact fatigue life (*L10*) of 2.15 times that of the carburised gears peened with an intensity of 0.18–0.23 mmA. Adamović et al. [28] investigated the sliding wear characteristics of ground and SP steel under boundary lubrication, and reported a slight decrease in coefficient of friction and a 30% increase in the wear resistance after SP.

The effect of the rough SP surfaces on the tribological behaviour has been reported in a number of articles. The dimpled surface is sometimes considered to be favourable in lubricated contact, which acts as reservoirs that aid in the retention of the lubricant and maintaining a full film thickness between meshing teeth. Better lubrication reduces fretting, noise, spalling, scuffing and the operating temperature by reducing friction. That said, Vaxevanidis et al. [29] still reported improved sliding wear resistance of SP tool steel tested under dry conditions. A higher coefficient of friction was reported at the beginning of the test, but as the test progressed, this decreased to a lower value than that of specimens, which were not SP. This can be attributed to flattening of the rough surfaces during the wear test.

In contrast, studies by other researchers show no improvement in the tribological characteristics of surfaces after SP [30–32]. The reason given is that surface roughening counterbalances the positive effects of compressive stresses and hardening caused by SP.

Very few works have been conducted to study the tribological behaviour of SP ADI [30, 31]. Work by Sharma [31] showed that at a given load, the contact fatigue life of SP Mo-Ni ADI austempered at 230°C is 35–45% lower than that of carburised steel. The author attributed this to the rougher surface and a lower hardness of the SP ADI when compared to carburised steel. Lubricated rolling contact fatigue tests carried out by Ohba et al. [30] showed that SP Cu-alloyed ADI exhibited similar wear rates to corresponding as-austempered specimens.

This was attributed to surface roughening, which counterbalances the positive effects of compressive stresses and hardening caused by SP.

3.3. Case study: shot peening of Cu-Ni-alloyed ADI

This section is related to a study, which was conducted to address the inconsistencies related to the tribological characteristics of SP ADI. A Cu-Ni-alloyed ADI having the composition shown in **Table 1** was used for this study [16–19]. Ductile iron samples were first austenitised at a temperature of 900°C for 2 hours and subsequently austempered at 360°C for 1 hour. Following the austempering process, this material had an upper ausferrite matrix with an yield strength of 737 MPa, a tensile strength of 1012 MPa and an elongation of 7%. SP was done up to full coverage with S330 steel shots and with an Almen intensity of 0.38 mmA. The stand-off distance was 90 mm, while the angle of impingement was set at 90°. The surface roughness R_a following SP was measured to be 3.1 μm.

As indicated in Section 2, SP of austempered ductile iron results in strain-induced phase transformation from the face-centred cubic (FCC) austenite to body centred tetragonal (BCT) martensite. This can be observed in the X-ray diffraction pattern presented in **Figure 3**. The top pattern, which is for the SP specimen, does not show any of the austenite peaks present in the as-austempered ductile iron (bottom pattern in **Figure 3**), suggesting that only ferrite and martensite peaks are present and that the strain induced during SP has transformed the austenite to martensite. Similar findings are commonly reported in ferrous alloys having retained austenite present in the initial micro-structure before SP [14, 15, 23, 33].

The SP-induced work hardening and phase transformation result in an increase of the surface hardness of 43% from 370 to 535 HV (**Figure 4(a)**) and decreases steadily towards the interior of the specimen. This is in agreement with results reported in literature, where the typical hardness increase following SP of ADI is in the range of 40–60% [14, 15]. The depth of the SP layer was measured from the hardness-depth profile (**Figure 4(a)**) and is approximately 400 μm. The maximum compressive stress occurring at the SP surface has a value of 975 MPa (**Figure 4(b)**), which is 67% greater than the yield strength of the material. Similar values of compressive stress for the Cu-Mn ductile iron austempered at 380°C were reported by Ebenau et al. [15].

3.3.1. Bending fatigue resistance of shot-peened Cu-Ni ADI

As a result of SP, both the mean bending fatigue strength and the fatigue life of the Cu-Ni ADI were increased [18]. **Figure 5** shows the S-N curve for both the as-austempered and SP condition. It can be noted that the fatigue strength increased by approximately 60%, that is from 250 to 390 MPa. The improvement in fatigue life of around 35% was noted at all stress levels. On

Element	**C**	**Si**	**Cu**	**Ni**	**Mn**	**P**	**Mg**	**Al**	**S**	**Fe**
Wt.%	3.26	2.36	1.63	1.58	0.24	0.011	0.057	0.024	0.006	Bal.

Table 1. Chemical composition of the Cu-Ni-alloyed ductile iron.

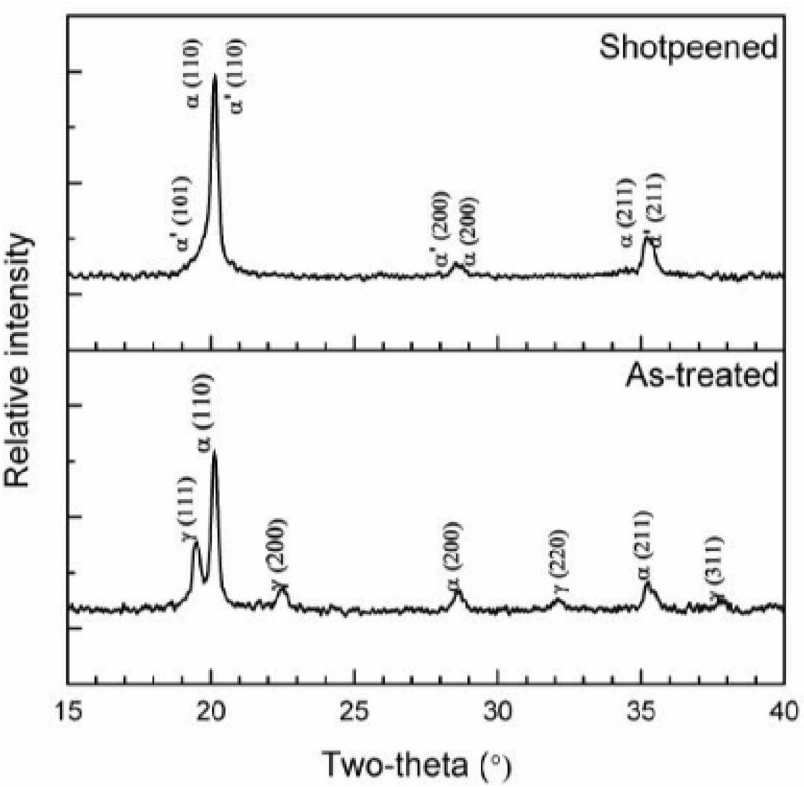

Figure 3. X-ray diffraction patterns of polished as-treated and shot-peened ADI (S330, intensity = 0.38 mmA) [18].

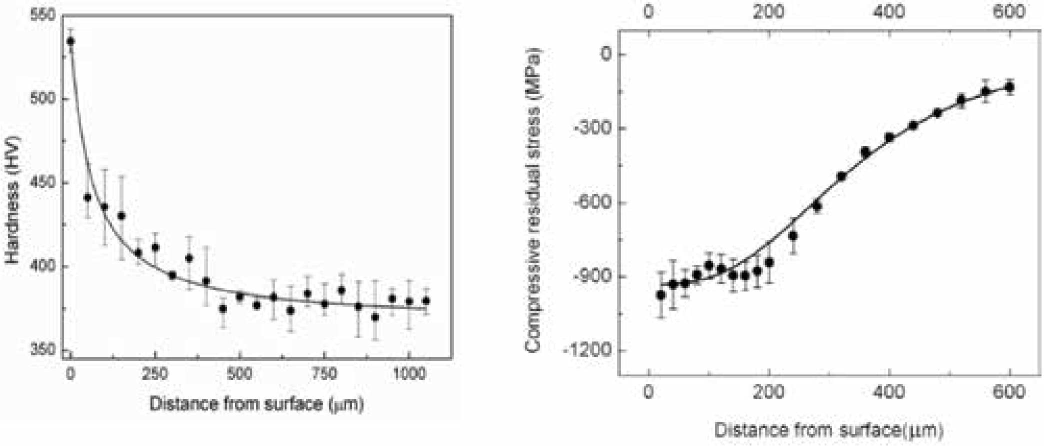

(a)

(b)

Figure 4. (a) Micro-hardness-depth profile of shot-peened ADI (S330, intensity = 0.38 mmA) and (b) residual stress-depth profile of shot-peened ADI (S330, intensity = 0.38 mmA) [18].

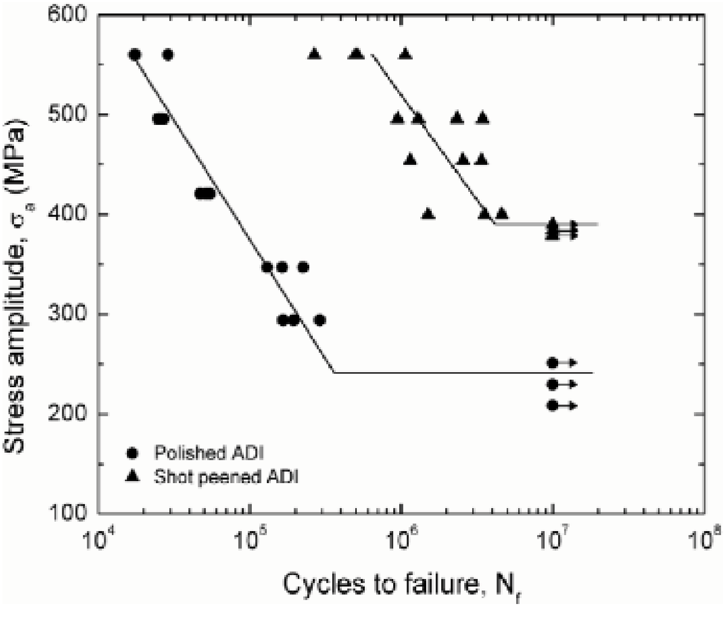

Figure 5. S-N curves for polished as-austempered ductile iron and SP ADI specimens [18].

the one hand, the results obtained for SP ADI (390 MPa) are similar to those obtained in other studies conducted by Mhaede et al. [34] and Ochi et al. [35] for unalloyed ADI, and by Benam et al. [14] for Cu-Ni-alloyed ADI. On the other hand, however, Ebenau et al. [15] reported values of 560 MPa when carrying out bending fatigue tests on SP Cu-Mn ADI austempered at 380°C. Surprisingly, these high values were obtained using the same S330 shots used in the present investigation: similar peening pressure of 3 bar and with recorded maximum residual compressive stress of 700 MPa. These results could potentially be explained in terms of differences in chemical compositions or heterogeneity in micro-structures.

The fatigue ratio, which is the ratio of the fatigue limit to the tensile strength, is 0.31 and 0.39 for the polished and SP specimens, respectively. This ratio is in agreement with British Cast Iron Research Association (BCIRA) reports that quote a fatigue ratio of 0.37 for austempered irons with tensile strengths in the range of 900–1000 N/mm^2 [36]. Johansson et al. [37] obtained higher endurance ratios of around 0.44, which were obtained in irons with tensile strengths in the range of 1000–1200 N/mm^2 produced by austempering between 350 and 375°C.

When comparing the bending fatigue strength obtained for the ADI in the present study to that for the carburised steel, it can be noted that the performance of carburised steel is far superior. Bending fatigue strengths of between 850 and 1500 MPa have been reported in a number of studies. This can be attributed to the harder surfaces (approximately 700 HV) and the deeper carburised layers (approximately 1.2 mm).

The crack propagation deflected along the graphite-matrix interface is shown in a cross section of a fractured specimen in **Figure 6**, which indicates a relatively weak interface between graphite nodules and the matrix. **Figure 7** also shows nodule debonding from one of the fractured

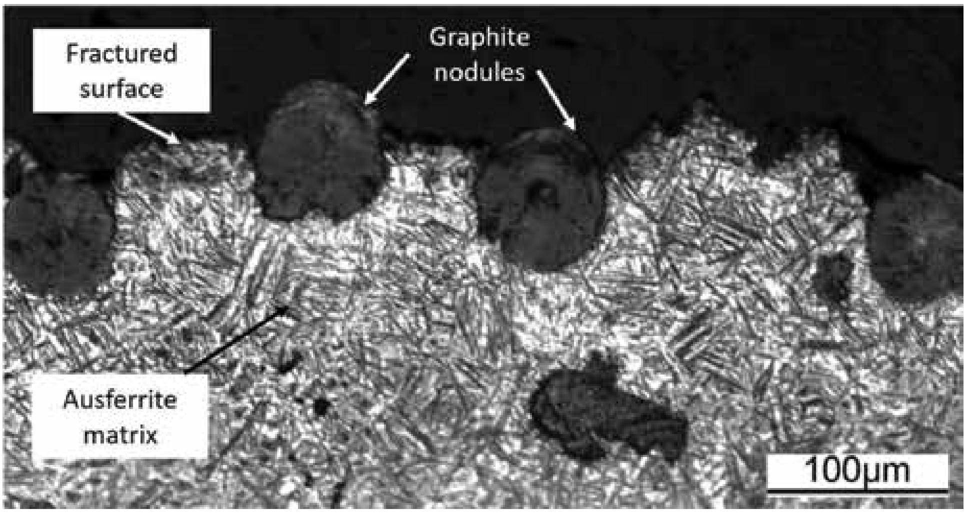

Figure 6. Crack propagation along graphite-matrix interface for a shot-peened ADI specimen [18].

surfaces. When traversing between graphite nodules, cracks were seen to pass through the lath of austenite and ferrite or through the austenite/ferrite interface, these being paths of least resistance. Similar results were also reported by Voigt [38] and Tayanç et al. [39]. Therefore, if nodules are sometimes considered as defects, the high toughness of stable austenite makes up for this negative effect. Crack propagation is also affected by the high toughness and ductility of the ausferritic micro-structure, making it a strong crack arrester. This structure absorbs the energy of the advancing crack during fracture, arresting the crack or deflecting it. In addition, ausferrite can strain harden during cyclic loading, providing high plastic deformation, which further hinders crack growth. Tanaka et al. [40] measured the hardness of upper ausferritic matrix after being subjected to different number of cycles during bending fatigue tests. The hardness of the matrix increased with longer number of cycles. Apart from strengthening by plastic deformation, unstable austenite can transform to martensite as the crack advances. The accompanying volume change, resulting in a compressed zone ahead of the crack tip, may retard crack growth, if not arrest it completely.

The extent to which the nodules can affect the fatigue behaviour of ADI depends on the nodularity where a high nodularity provides a better continuity of the matrix with less stress raisers. Furthermore, the nodule size, count and distribution are of equal importance. A high count, a smaller diameter and evenly distributed nodules decrease intercellular micro-segregation of elements. This results in an increase in the fracture toughness and fatigue resistance of ADI.

3.3.2. Dry sliding wear resistance of shot-peened Cu-Ni ADI

Dry sliding wear tests were carried out on the Cu-Ni ADI using a conventional pin-on-disk tribometer using two different applied pressures, 2.5 and 10 MPa [16]. **Figure 8** shows the wear factor *K* of the as-austempered DI and SP ADI specimens as a function of sliding distance. It can be noted that there is no difference between the wear rates for the two surface

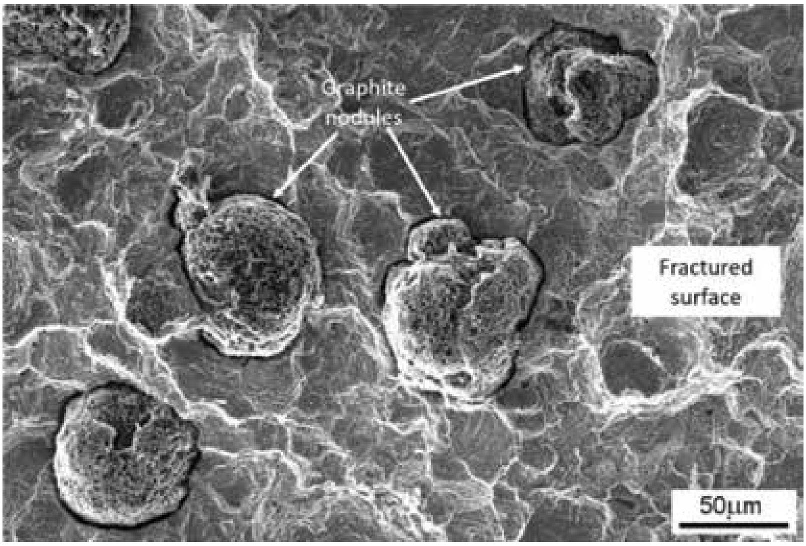

Figure 7. Graphite nodules attached to one of the fractured surfaces of an as-austempered DI specimen [18].

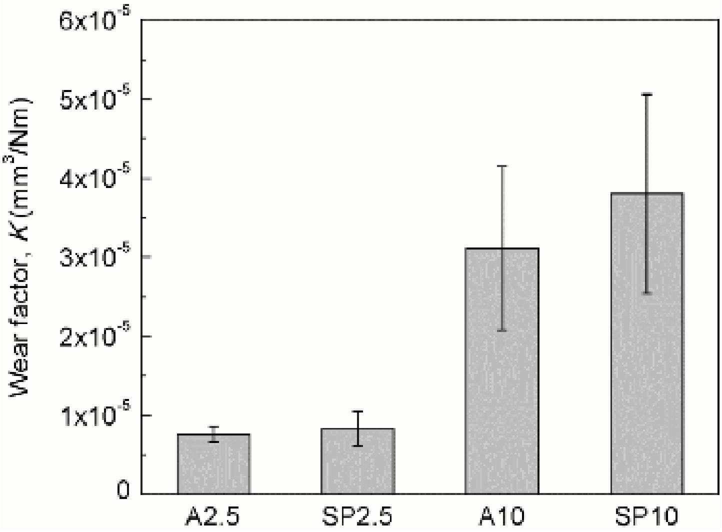

Figure 8. Wear factors of as-austempered ductile iron (A) and shot-peened ADI (SP) samples [16].

conditions: as-austempered DI and SP ADI specimens at the two applied loads. This indicates that SP did not result in an improvement in the dry sliding wear resistance. This suggests that a higher original hardness (535 HV for SP specimens compared to 370 HV for as-austempered specimens) does not necessarily result in better wear resistance. It may be argued, however, that the potential improvement resulting from an increase in hardness is being counterbalanced by the increased surface roughness caused by SP.

The micro-hardness-depth profiles taken on cross sections of the worn specimens are shown in **Figure 9(a)**, while **Figure 9(b)** compares the surface hardness at both applied pressures of specimens before and after the wear tests. At a low applied pressure of 2.5 MPa, the micro-hardness of the worn surface of as-austempered specimens was measured to be around 19% higher than that of the bulk. The thickness of this hardened layer is around 100 μm and is due to strain hardening of the ausferritic matrix at the surface region, which predominates over any frictional heating effect. As a result of this plastic deformation, the material is stronger and causes surface flow and the micro-structure to distort, as shown in **Figure 10(a)**.

It can be noted that the hardness of SP specimens decreases from 535 to 450 HV (**Figure 9**) after testing at the lower applied pressure of 2.5 MPa. This is probably due to the removal of part of the SP layer during the wear test, or tempering of the martensite, which was formed during the SP process.

On the other hand, the surface micro-hardness of specimens tested at the higher load is over 600 HV (**Figure 9**). This indicates a phase transformation to a high hardness phase. Micrographs show that a white non-etchable phase is present at the surface of the specimens tested with the higher load (**Figure 10(b)**). When the two surfaces slide over each other, most of the work done against friction is converted into heat, causing a general rise in temperature, as well as localised temperature spikes where an asperity makes contact with the mating surface. The resulting rise in temperature may modify the mechanical and metallurgical properties of the sliding surfaces, causing them to oxidise, or possibly melt. This high temperature transforms the ausferrite to austenite and can result in carbon diffusion from the nodules into the austenite and hence increasing the hardenability of the pin. Consequently, the critical cooling rate is lowered, resulting in the formation of untempered martensite at a slow cooling rate upon cooling of the pin and disk after the test is stopped. It is also possible that the austenite being produced due to the high temperatures reached at the asperities is rapidly cooled as heat is conducted into the underlying bulk material when the tip of the asperity breaks during sliding. As a result, the austenite transforms to martensite during testing.

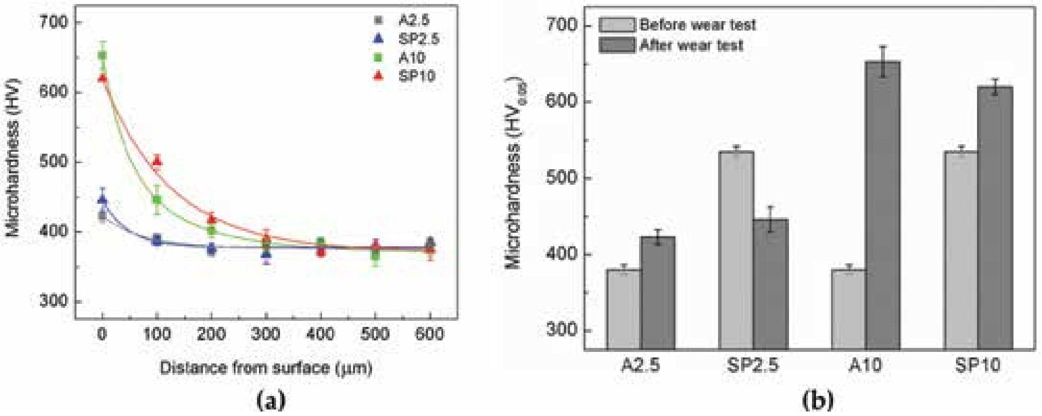

Figure 9. (a) Micro-hardness-depth profiles of cross sections of worn specimens and (b) surface hardness before and after dry sliding wear tests [16].

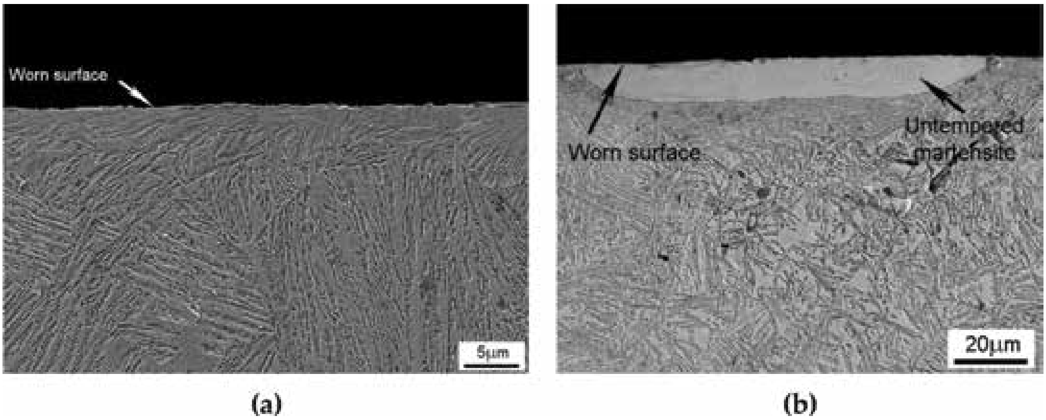

Figure 10. Micro-structure just below the worn surface of a specimen tested at an applied pressure of (a) 2.5 and (b) 10 MPa [16].

Fordyce et al. [41] also observed this white non-etchable layer during the unlubricated sliding wear of austempered spheroidal cast iron but not of as-cast spheroidal iron. Straffelini et al. [42] explained how the wear rate of ADI at high sliding speeds of 1.5–2.6 m/s was dominated by the formation and cracking of this white layer formed on the sliding surface. Sharma [31] has also shown that high loads applied during wear testing may transform the metastable austenite to martensite.

The presence of graphite nodules has a major influence on the wear rate of ADI as superficial graphite is smeared over the surface and aids in lubricating the surfaces in sliding contact. Graphite naturally has an inherent lubricating ability, being able to smear over the contacting surfaces. This lowers the friction coefficient and prevents metallic contact, hence reducing the adhesive bonding between the surfaces and material loss due to wear. Due to this, ADI components, for example railcar wheels, are sometimes run dry without the need of lubrication. Cracks have a tendency of passing through the graphite-matrix interface, this being the path of least resistance. On the other hand, a nodule may arrest crack propagation. Whether or not a crack is arrested or assisted to propagate as it reaches a graphite nodule would depend on the angle of approach. It follows that graphite nodules influence the propagation path.

3.3.3. Scuffing resistance of shot-peened Cu-Ni ADI

Figure 11(a) shows that during starved lubricated sliding wear tests, the SP Cu-Ni ADI (SP) specimens exhibited a higher scuffing wear resistance than corresponding as-austempered (A) specimens [43]. SP specimens survived 21 × 10^3 cycles, while the as-austempered specimens endured 2.3 × 10^3 cycles before failure. The improved scuffing performance due to SP might seem anomalous, since rough surfaces generally create low values of the specific film thickness λ and induce scuffing. However, the superposition of indentations arising from the SP process can be considered as an advantage in starved lubricated moving parts. These act as oil reservoirs by dragging the oil into them and generating a load-carrying hydrodynamic pressure. This decreases the pressure from the sliding surfaces, leading to longer lives for the

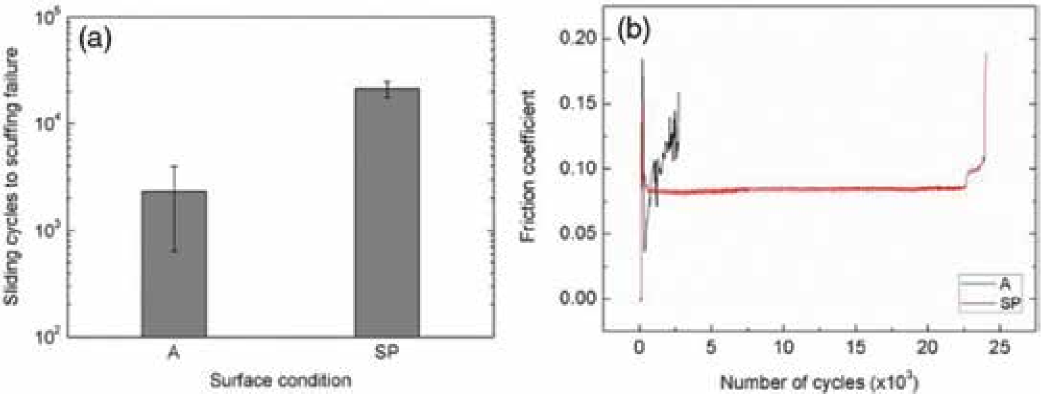

Figure 11. (a) Number of sliding cycles to scuffing failure for as-austempered (A) ADI and shot-peened (SP) ADI specimens and (b) friction coefficient evolution for lubricated sliding wear tests involving the as-austempered ADI and shot-peened ADI specimens [43].

SP specimens. On the other hand, the larger number of smaller asperities for the ground as-austempered specimens leads to a larger real area of contact upon application of the normal force and the presence of a very thin oil film. As a result, the number of sliding cycles to failure decreases due to plastic flow of the softer ADI specimens and micro-fracture of the asperities. This highlights the importance of the surface topography in asperity-asperity contact during sliding of components.

The higher scuffing resistance of the SP specimens could also be attributed to the high compressive stresses present in these specimens. It has been explained in previous sections that compressive stresses create a resistance to crack propagation and flaking of the surface. This was also attested by Adamović et al. [28], who reported a 30% improvement in the wear resistance of steels after SP.

Additionally, the SP specimens exhibit a lower value of coefficient friction at 0.08, when compared to that measured for their counterpart as-austempered specimens. This can be seen from the friction coefficient data of the lubricated sliding wear tests presented in **Figure 11(b)**. The coefficient of friction for the as-austempered specimens is seen to increase progressively as the test progresses. This is attributable to the larger number of small asperities of the as-austempered pin in contact with the disk. In contrast, the local traction at asperity contacts is reduced in the dimpled SP specimens, again as a result of the oil pockets on the surface. It is known that at lower levels of friction, the surface traction forces and sub-surface shear forces between two interacting bodies might not be sufficient to initiate crack growth and delamination. Hence, the lower friction for the SP specimens leads to longer number of cycles before the onset of failure. A lower coefficient of friction than that produced by ground surfaces was also reported for SP steel specimens [28] and for dented steel surfaces [44] under starved lubrication conditions.

The higher hardness of the SP specimens (~535 HV) should have also contributed to the improved scuffing resistance. The benefit of a high hardness in wear tests carried out under starved lubrication conditions was also mentioned by Adamović et al. [28]. In fact, the hardness of mating surfaces is a crucial factor in avoiding scuffing.

It was also noted that the graphite nodules play a part in determining the scuffing resistance. In fact, as seen in **Figure 12** cracks emanate or stop at the nodules. This observation is similar to that mentioned earlier during bending fatigue [18] and dry sliding wear of ADI [16].

3.3.4. Rolling contact fatigue resistance of shot-peened Cu-Ni ADI

As-austempered and SP Cu-Ni ADI specimens were tested up to pitting failure using a cone-three ball tribosystem at an applied stress of 2.56 GPa [19]. **Figure 13** presents the Weibull probability plot for the tests, showing the percentage of specimens that will fail up to a specific number of cycles. The cumulative distribution function (CDF) is shown on the y-axis, while the number of rolling cycles to contact fatigue is shown on the x-axis. In this plot, the data points represent the number of cycles to failure of the ADI specimens.

Figure 13(b) shows the average contact fatigue lives for the as-austempered DI and SP specimens. Results show that the average contact fatigue life of SP specimens decreased by 72% when compared to the performance of the as-austempered specimens. Similarly, Sharma et al. [31] reported that SP lowered the contact fatigue life of ADI by 60%. Also, Vrbka et al. [46] report an 82% decrease in life of steel specimens following rolling contact fatigue tests. In the current study, austempering at 360°C resulted in a hardness of 370 HV, while SP increased the surface hardness to approximately 530 HV. Based only on hardness, one would expect an improvement in the contact fatigue resistance. Also, the residual compressive stresses present in SP layers (**Figure 4(b)**) should effectively reduce the maximum shear stress inside the Hertzian contact field, delaying crack nucleation and propagation.

However, the surfaces of the SP specimens have a higher surface roughness (*Ra* = 3.1 μm) than the counterpart as-austempered specimens (*Ra* = 0.4 μm). This leads to an extremely low

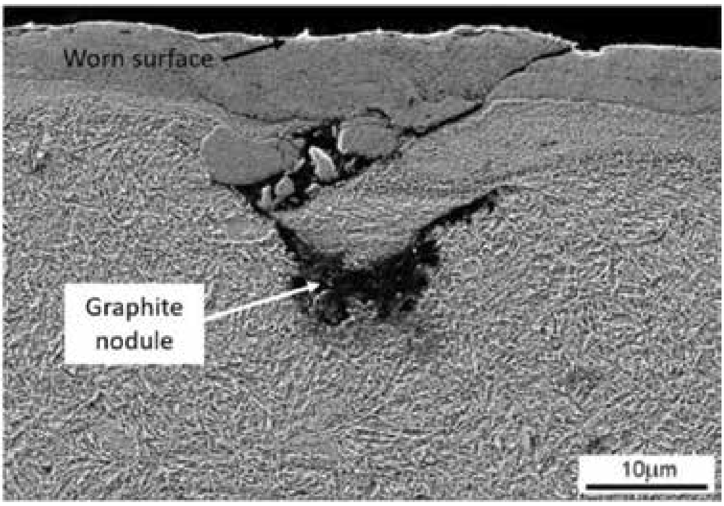

Figure 12. Micro-graph showing the influence of graphite nodules on crack initiation and/or propagation [43].

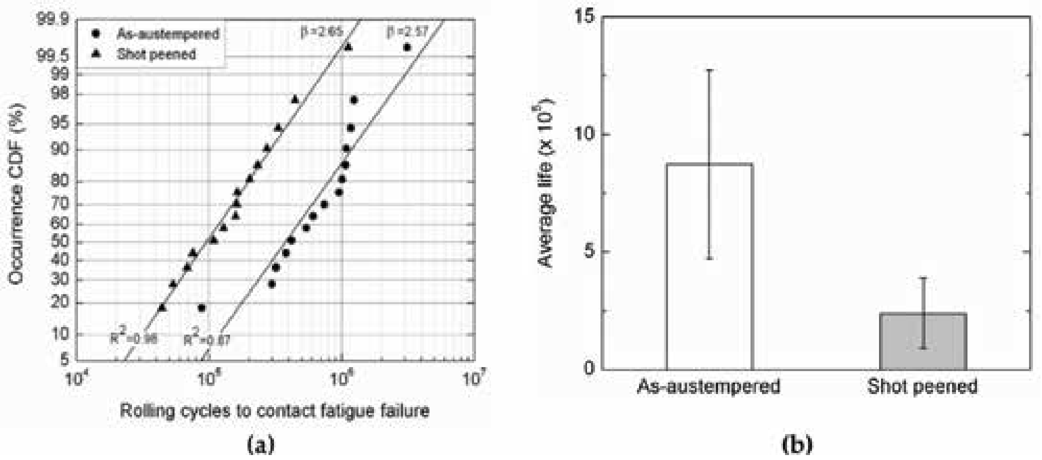

Figure 13. (a) Weibull probability plot for data obtained from rolling contact fatigue tests and (b) L10, L50, characteristic (η) fatigue lives for as-austempered and shot-peened ADI specimens [19, 45].

value of the specific film thickness λ of 0.05, which contrast with a corresponding value of 2.81 for the as-austempered specimens. A value of λ smaller than 0.4 denotes that a boundary lubricated condition exists, implying that peaks of the asperities of the SP specimens are penetrating the lubricant film. Contact, therefore, occurs between the asperities of the SP ADI cones and balls. Metal-to-metal contact is unavoidable and nearly all the load is supported by the asperities, defying the principal purpose of lubrication. Contact fatigue failure starts from the surface as a result of a presumably high coefficient of friction.

This might seem anomalous after having shown that under starved lubricated sliding wear, the dimples forming the rough surface of the SP specimens act as lubricant reservoirs, aiding in keeping the lubricant between the surfaces and serving to delay failure. One may have expected this positive attribute to apply also for the rolling tests. However, with the application of larger quantity of lubricant, smoother surfaces of the as-austempered samples proved to be more beneficial as it resulted in the formation of a full lubricating film. One should note that in contrast, all the specimens in the starved lubricated sliding wear tests were tested under boundary lubricated conditions. These results are in agreement with Zhai et al. [44] who report that the effect of surface dents is favourable under poorly lubricated conditions, but adverse under a well-lubricated environment. This means that the influence of dimpled surfaces on the tribological characteristics of the material depends on the lubrication regime.

For rough SP surfaces to operate in a fully lubricated condition, the minimum film thickness should be thicker than the combined surface roughness of the two interacting components. A thicker film is obtained by increasing the operating speed, the oil viscosity or the relative radius of curvature of the surfaces in contact. The elastic properties of the gear teeth and the applied load have relatively small influences on the lubricant film thickness. Increasing the load will only increase the elastic flattening (the width of the Hertzian contact band) and the contact area, without changing the geometry of the inlet region. Apart from the benefits of a thicker film, improving the performance of SP surfaces might be due to lower surface roughness. This can be achieved by either using shots having a smaller diameter, or by grinding/polishing the surface after SP. In fact, rolling contact fatigue tests carried out by Ohba et al. [30] showed nearly equal fatigue lives for ground as-austempered DI and SP ADI using shots with a diameter of 0.1 mm. On the other hand, Vrbka et al. [46] report a deterioration in the rolling contact fatigue resistance of steel despite the use of shots having smaller diameters of 0.07 and 0.11 mm. One notes that shots used in the present study had diameters in the range of 0.85–1.2 mm. Results in this study [46] were improved when testing specimens, which were polished after SP, thus creating relatively smoother surfaces, in which the asperities did not protrude the lubricant film. However, grinding or polishing of SP surfaces might be challenging since extra care must be taken so as not to remove the SP layer and hence eliminate the beneficial effects, which result from SP (high hardness and compressive stresses at the surface).

4. Conclusion

The work presented in this chapter has hopefully contributed to a better understanding of the mechanical behaviour and tribological characteristics of both as-austempered ductile iron (ADI) and shot-peened (SP) ADI. A case study was presented in which bending fatigue tests and three different tribological tests were carried out on Cu-Ni-alloyed ADI. The major conclusions of can be summarised as follows:

1. After SP, a good balance between surface roughness, high surface hardness and hardened depth was obtained. Austenite transformed to martensite by the TRansformation Induced Plasticity (TRIP) phenomenon and the surface hardness increased by about 43% to a value of approximately 535 HV; the depth of the SP layer was approximately 400 μm, residual compressive stresses had a maximum value of 975 MPa and the surface roughness increased from 0.4 to 3.1 μm.

2. Rotating bending fatigue tests revealed that SP improved the bending fatigue strength of the Cu-Ni ADI by around 60% from 250 to 390 MPa. This was attributed to the induced compressive stresses that shift crack nucleation to the sub-surface and hinders fatigue crack propagation.

3. Dry lubricated sliding wear tests showed that SP did not result in an improvement in the dry sliding wear resistance of Cu-Ni ADI. The potential advantages resulting from the higher hardness at the surface, stress-induced austenite to martensite transformation and the residual compressive stresses of the SP specimens are counteracted by the induced surface roughness.

4. Starved lubricated sliding wear tests showed that SP resulted in an 800% improvement in the scuffing wear resistance of the ADI. The lower resistance to scuffing attested by the as-austempered specimens was attributed to plastic flow and micro-fracture of asperities. On the other hand, the superposition of indentations arising from the SP process acted as oil reservoirs and hence reduced surface traction forces. The higher scuffing resistance of the SP specimens was also partly attributed to the high hardness and high compressive stresses present in the surface of these specimens.

5. Lubricated rolling contact fatigue tests revealed that SP resulted in a 72% decrease in the average contact fatigue life when compared to the resulting fatigue life obtained by the as-austempered specimens. This was attributed to the rough surfaces of SP specimens, which in turn caused a low specific film thickness, leading to rolling in the boundary lubrication regime. In contrast, rolling of the polished as-austempered specimens was conducted in the presence of a full lubricant film, which is the ideal lubrication regime of components under rolling contact.

The SP process is constantly maturing, and many questions still remain open as the industry is continuously on the search for process improvements that improve and extent the service lifetime of components. For example, the improvement in surface roughness has improved the tribological characteristics, the ability to create textured nanostructured surface layers and also new equipment and techniques to characterise the treated surfaces [11].

Acknowledgements

The authors would like to acknowledge the positive impact of ERDF funding and the purchase of the testing equipment through the project: Developing an Interdisciplinary Material Testing and Rapid Prototyping R&D Facility (Ref. no. 012).

Author details

Ann Zammit

Address all correspondence to: ann.zammit@um.edu.mt

Department of Metallurgy and Materials Engineering, University of Malta, Msida, Malta

References

[1] Zammit A. Tribological and mechanical characteristics of surface modified austempered ductile iron [PhD thesis]. University of Malta; 2014

[2] Borui Casting International Ltd. Austempering Process for Ductile Iron [Internet]. Available from: http://www.metals-china.com/austempering-process-for-ductile-iron-austempered-ductile-iron.html [Accessed: 17-05-2018]

[3] Harding RA. The production, properties and automotive applications of austempered ductile iron. Kovove Materialy. 2007;**45**:1-16

[4] Shanmugam P, Rao PP, Udupa KR, Venkataraman N. Effect of microstructure on the fatigue strength of an austempered ductile iron. Journal of Materials Science. 1994; **29**:4933-4940. DOI: 10.1007/BF00356546

[5] Bahmani M, Elliott R, Varahram N. The relationship between fatigue strength and microstructure in an austempered Cu–Ni–Mn–Mo alloyed ductile iron. Journal of Materials Science. 1997;**32**:5383-5388. DOI: 10.1023/A:1018631314765

[6] Lin CK, Wei JY. High-cycle fatigue of austempered ductile irons in various-sized Y-block castings. Materials Transactions (JIM). 1997;**38**:682-691. DOI: 10.2320/matertrans1989.38.682

[7] Lin CK, Hung TP. Influence of microstructure on the fatigue properties of austempered ductile irons—II. Low-cycle fatigue. International Journal of Fatigue. 1996;**18**:309-320. DOI: 10.1016/0142-1123(95)00108-5

[8] Benam AS. Effect of shot peening on the high-cycle fatigue behavior of high-strength cast iron with nodular graphite. Metal Science and Heat Treatment. 2017;**58**:568-571. DOI: 10.1007/s11041-017-0056-6

[9] Schulze V. Characteristics of surface layers produced by shot peening. In: Proceedings of the 8th International Conference on Shot Peening; 2002; Garmisch-Partenkirchen, Germany. 2002. p. 145

[10] Champaigne J. Shot peening overview. Metal Improvement Company. 2001

[11] Zammit A. Editorial: Special issue on shot peening. Surface Engineering. 2017;**33**:649-650. DOI: 10.1080/02670844.2017.1338552

[12] Myszka D. Austenite-martensite transformation in austempered ductile iron. Archives of Metallurgy and Materials. 2007;**52**:475-480

[13] Daber S, Rao PP. Formation of strain-induced martensite in austempered ductile iron. Journal of Materials Science. 2008;**43**:357-367. DOI: 10.1007/s10853-007-2258-6

[14] Benam AS, Yazdani S, Avishan B. Effect of shot peening process on fatigue behavior of an alloyed austempered ductile iron. China Foundry. 2011;**8**:325-330

[15] Ebenau A, Lohe D, Vohringer O, Macherauch E. Influence of shot peening on the microstructure and the bending fatigue strength of bainitic-austenitic nodular cast iron. In: Proceedings of the ICSP-4; Tokyo, Japan. 1990. pp. 389-398

[16] Zammit A, Abela S, Wagner L, Mhaede M, Grech M. Tribological behavior of shot peened Cu-Ni austempered ductile iron. Wear. 2013;**302**:829-836. DOI: 10.1016/j.wear.2012.12.027

[17] Zammit A, Hopkins L, Betts JC, Grech M. Austenite transformation in austempered ductile iron. In: Materials Science and Engineering (MSE 2008); Nuremberg, Germany. 2008

[18] Zammit A, Mhaede M, Grech M, Abela S, Wagner L. Influence of shot peening on the fatigue life of Cu-Ni austempered ductile iron. Materials Science and Engineering: A. 2012;**545**:78-85. DOI: 10.1016/j.msea.2012.02.092

[19] Zammit A, Abela S, Michalczewski R, Wagner L, Mhaede M, Wan R, Grech M. Influence of shot peening on the rolling contact fatigue resistance of Cu-Ni austempered ductile iron. In: Proceedings of the ICSP-12; Goslar, Germany. 2014. pp. 38-73

[20] Ezoe S, Hashimoto M, Asano I, Tanno Y. Effects of shot peening and heat treatment on endurance limits of austempered ductile cast iron gears. In: Proceedings of the ICSP-6; San Francisco, California, USA. 1996. pp. 14-23

[21] Johansson M. Austenitic-bainitic ductile iron. Transactions of the American Fisheries Society. 1977;**85**:117-122

[22] Uematsu Y, Kakiuchi T, Tokaji K, Nishigaki K, Ogasawara M. Effects of shot peening on fatigue behavior in high speed steel and cast iron with spheroidal vanadium carbides dispersed within martensitic-matrix microstructure. Materials Science and Engineering: A. 2013;**561**:386-393. DOI: 10.1016/j.msea.2012.10.045

[23] Kirk D. Residual stresses and retained austenite in shot peened steels. In: Proceedings of the ICSP-1; Paris, France. 2013. pp. 271-278

[24] Blackmore PA, Harding RA. The effects of metallurgical process variables on the properties of ADI. Journal of Heat Treating. 1984;**3**:310-325

[25] Kobayashi M, Hasegawa K. Effect of shot peening on the pitting fatigue strength of carburised gears. In: Proceedings of the ICSP-4; Tokyo, Japan. 1990. pp. 465-476

[26] Townsend DP, Zaretsky EV. Effect of shot peening on surface fatigue life of carburized and hardened AISI 9310 spur gears. NASA Technical Paper, 2047. 1982. pp. 5-12

[27] Townsend DP. Improvement in surface fatigue life of hardened gears by high-intensity shot peening. NASA Tech Report 91-C-042. 1992

[28] Adamovic D, Babic M, Jeremic B. Shot peening influence on tribological characteristics of surfaces. In: ICSP-7; Warsaw, Poland. 1999. pp. 350-358

[29] Vaxevanidis NM, Manolakos DE, Koutsomichalis A, Petropoulos G, Panagotas A, Sideris I, Mourlas A, Antoniou SS. The effect of shot peening on surface integrity and tribological behaviour of tool steels. In: AITC-AIT; Parma, Italy. 2006

[30] Ohba H, Matsuyama S, Yamamoto T. Effect of shot peening treatment on rolling contact fatigue properties of austempered ductile iron. Tribology Transactions. 2002;**45**:576-582

[31] Sharma VK. Roller contact fatigue study of austempered ductile iron. Journal of Heat Treating. 1984;**3**:326-334

[32] Peyrac C, Flavenot J. Optimisation of carburising and shot peening, in order to improve both bending and contact fatigue behaviour for gear applications. In: Proceedings of the ICSP-9; Paris, France. 2005

[33] Watanabe Y, Hasegawa N, Namiki K, Hatano A. The influence of broken shots on peening effect of hard shot peening. In: Proceedings of the ICSP-4; Tokyo, Japan. 1990

[34] Mhaede MH, Ibrahim KM, Wollmann M, Wagner L. Enhancing fatigue performance of ductile Iron by austempering and mechanical surface treatments. In: Proceedings of Arabcast. 2008

[35] Ochi Y, Masaki K, Matsumura T, Sekino T. Effect of shot-peening treatment on high cycle fatigue property of ductile cast iron. International Journal of Fatigue. 2001;**23**:441-448. DOI: 10.1016/S0142-1123(00)00110-9

[36] Gilbert GNJ. An introduction to the Mechanical Properties of Nodular (SG) Cast Irons. Alvechurch, Birmingham: BCIRA; 1986

[37] Johansson M, Vesanen A, Rettig H. Austenitic-bainitic cast iron with spheroidal graphite as construction material for gears. Antriebstechnik (BCIRA Translation T1507). 1976;**15**:593-600

[38] Voigt RC. Microstructural analysis of austempered ductile cast iron using the scanning electron microscope. Transactions of the American Fisheries Society. 1983;**83-89**:253-262

[39] Tayanc M, Aztekin K, Bayram A. The effect of matrix structure on the fatigue behaviour of austempered ductile iron. Materials and Design. 2007;**28**:797-803

[40] Tanaka Y, Yang Z, Miyamoto K. Evaluation of fatigue limit of spheroidal graphite cast iron. Materials Transactions (JIM). 1995;**36**:749-756

[41] Fordyce EP, Allen C. The dry sliding wear behaviour of an austempered spheroidal cast iron. Wear. 1990;**135**:265-278. DOI: 10.1016/0043-1648(90)90030-E

[42] Straffelini G, Pellizzari M, Maines L. Effect of sliding speed and contact pressure on the oxidative wear of austempered ductile iron. Wear. 2011;**270**:714-719. DOI: 10.1016/j.wear.2011.02.004

[43] Zammit A, Abela S, Wagner L, Mhaede M, Wan R, Grech M. The effect of shot peening on the scuffing resistance of Cu-Ni austempered ductile iron. Surface and Coatings Technology. 2016;**308**:213-219. DOI: 10.1016/j.surfcoat.2016.06.089

[44] Zhai X, Chang L, Hoeprich MR, Nixon HP. On mechanisms of fatigue life enhancement by surface dents in heavily loaded rolling line contacts. Tribology Transactions. 1997;**40**:708-714. DOI: 10.1080/10402009708983712

[45] Zammit A, Abela S, Michalczewski R, Kalbarczyk M, Wagner L, Mhaede M, Wan R, Grech M. Rolling contact fatigue resistance of shot peened austempered ductile iron. Tribologia. 2014;**4**:137-147

[46] Vrbka M, Křupka I, Svoboda P, Šperka P, Návrat T, Hartl M, Nohava J. Effect of shot peening on rolling contact fatigue and lubricant film thickness within mixed lubricated non-conformal rolling/sliding contacts. Tribology International. 2011;**44**:1726-1735. DOI: 10.1016/j.triboint.2011.06.019

Advanced Electro-Spark Deposition Process on Metallic Alloys

Petrică Vizureanu, Manuela-Cristina Perju,
Dragoş-Cristian Achiței and Carmen Nejneru

Additional information is available at the end of the chapter

http://dx.doi.org/10.5772/intechopen.79450

Abstract

This chapter will study the material base-surface multilayer system for various types of depositions (increasing the wear resistance of Fe-C alloy parts) whose compatibility with the substrate provides high-quality parts. Thus, this system of layers can be applied on both the new and worn parts, being able to recondition and reintroduce in an intensive exploitation regime any parts with complex configuration operating in dynamic conditions. Deposited layers will be obtained using electro-spark deposition (ESD) process, which is a technology that uses electrical energy stored in a capacitor to initialize an electrical spark between the cathode and the anode. The high temperature generated by the electrical spark leads to partial melting of substrate and mixing of it with the material of the electrode. Between the two electric sparks, the amount of the molten metal solidifies to form the surface layer. The ESD is a very well used process for materials manufacturing in many industrial sectors.

Keywords: deposition, microstructure, hardness, mass transfer, spark

1. Introduction

Scientific aim of this chapter fits the theme of the widely known under the name of engineered surfaces and seeks to make contributions in what is defined as thin-layer deposition or by combined methods. It is known that in such cases systems are characterized by contradictory layer-substrate properties and system design requires operating limit. The method of analysis clearly relates the design of the system material base-surface multilayer so that it responds well to its functional role in the efficient use of materials and also affordable. The literature shows the diversity of the applicability domain of the electro-spark deposition process and the variety of filler materials and basic materials used. There are also a multitude of purposes of use: in obtaining amorphous layers, in obtaining epitaxial layers, layers with special physical, chemical, and mechanical properties (corrosion resistance, wear resistance, fatigue resistance, and shock resistance) [1–4].

It is noted that the main reasons that cause system need to replace some parts in the industry are the destruction of surface layer by corrosion, wear, fatigue, and mechanical shock. The properties of metallic materials have been improved [5, 6], in order to increase the adhesion of deposits to the base material layer using the layer of composite material by means of electro-spark deposition process.

Currently, electro-spark deposition process is gaining more ground to thin film deposition with various metallic materials, which gives the surface characteristics of hardness and high wear resistance [7–16]. Most studies have focused on the analysis of the mechanical properties of the material base-surface multilayer system and mass transfer behavior to obtain required properties and to control as much as possible the thickness of the deposited layer. But there are unsolved issues that deserve the attention of a detailed study. Going to these relevant issues in industrial practice, research conducted in different countries, like Japan, China, [17–19], and Ireland [20] had highlighted a number of concern technologies knowledge and fundamental character and experimental studies leading to improve properties of surface layers obtained using the method with pulsed electrical discharges. The wear, fatigue, and corrosion phenomena are the most aggressive factors that lead to scrapping one part. From this, situation results the high importance for the physical-chemical research of the phenomenon that takes place into these superficial layers in connection with coating technologies [21, 22]. One of the methods to process the materials is electro-spark deposition method that can allow to coat complex shaped and reduced dimension parts by extracting material from the surface of the part or developing coating layers by applying the compact material electrodes or by introducing into working area of powders or mix of powders. It is necessary that the surface layers have a good adherence to the part and especially a good connection to the sublayer. In some surface areas, high hardness layers are formed. Most studies are focused on chemical, physical, and mechanical properties of deposited layer and on mass transfer behavior, to obtain the properties imposed and to control as much as possible the coating layer thickness.

Compared with laser ablation technology, CVD, PVD, etc., the ESD method is technologically much easier to execute and requires no vacuum chamber or additional devices. The deposition can be done both automatically and manually, allowing a wide range of surface adjustments and ease of correcting surface quality.

2. ESD process description

The technology can be defined as a micro-pulsed welding technique that allows deposition of one "electrode material" on a metallic sublayer; mass transport is made in high current intensity and in short time periods. ESD method implies heat and mass transfer phenomena. Basically, multiple phenomena involve such as heating to incandescence, melting, and eventually evaporating of the electrode material. There is a stream of electrons, ions, and neutral fast atoms in the electric field between the electrodes. Electric field is concentrated on a microportion of the piece where metal melting bath forms. Microalloying between base material and electrode melt generates the formation of nitrides, carbides, carbonitrides, and plasma through air decomposition (nitrogen and active oxygen). All these phenomena and others successively describe the formation of the hardened superficial layer through deposition.

The process of electro-spark deposition on the material surfaces is based on the electro-erosion phenomenon and the polar transfer of the anode (electrode) material to the cathode (metallic part) during the electrical discharge in pulses between the anode and the cathode, discharge which occurs in a gaseous medium. Unlike conventional electro-erosion machining, a pulsed rectifying current with reversed polarity is used at pulse electrical discharge. In this case, the impulse electric discharge process has the air as the gaseous medium. In the deposition technology, the electrode performs a vibratory motion. Due to the polar effect, the predominant transfer of the anode material (electrode) to the cathode (the piece) ensures the formation of the superficial layer with well-defined physic and chemical properties. Upon completion of the discharge, at a very low temperature range, cathode anode removal begins, an action that ends with the electrical circuit break, after which the process is resumed. As a result of the transfer of material and thermal changes from the discharge zone, in the process of superficial discharge of metallic materials with electric sparks, the surface layer of the cathode changes its structure and chemical composition. The characteristics of this layer may vary greatly depending on the electrode material, the composition of the medium between the electrodes, the impulse discharge parameters, and other conditions of the cathode layer formation [23]. Between two sparks, the low quantity of melted metal solidifies, developing a protective layer.

Electrical and working principle of the pulse electric discharge process is shown in **Figure 1**.

The electrical scheme represents a generator, the cathode coupled part, and the electrode as the anode, which is used to form the superficial layers on the part. The surface processing begins with the proximity of the sample electrode and at the critical breaking distance triggering the electrical discharge by impulses, which is often continuous and ends only at the contact of the electrodes. After penetrating the gap between the electrodes, due to the energy accumulated in the C_p capacitor, at the contact surface of the electrodes, strong heated area (local melting and evaporation outbreaks) occurs that causes the electrical erosion of the electrodes (the piece and the electrode itself). The essence deposition using the pulsed electrical discharge method lies in the complexity of physical phenomena which are occurring during the technological process. Discharge parameter regimes (voltage, current, and pulse time)

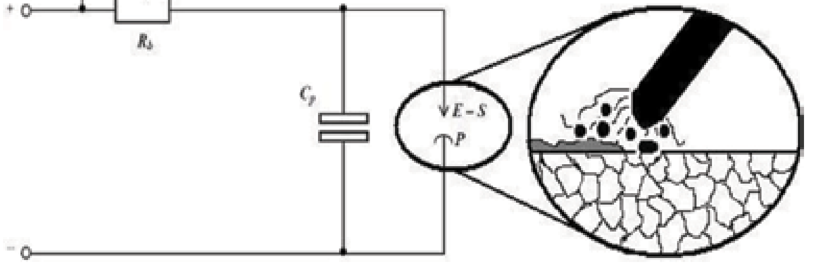

Figure 1. Surface processing using electro-spark deposition method: wiring diagram for the processing device: C_p, condenser; R_b, variable resistance; E-S, electrode connected to the anode; and P, part connected to the cathode.

depend on the physical and chemical properties of the electric and working circuit (device-electrode-base material). In this context, we can say that the parameters depend on the type of electrode deposition, and its melting temperature, the thermal conductivity, chemical reactivity of the anode elements, diffusivity, density, electrical resistance, thermal inertia, flow ability, and parameter temperature dependence.

Among the basic features of the impulse electric discharge method, which also include advantages, can be mentioned: lack of special preparation of the surface to be processed; the deposited layer, due to the high solidification/cooling speed, obtains amorphous-specific properties; the deposited layer does not usually require subsequent finishing; apply easily to the surface of complex parts; the deposition can be done in strictly indicated places; the deposited layer has good adhesion to the support; the possibility of using as electrode both pure metals and their alloys; the possibility of deposition using metal-ceramic materials and hard fusible compounds; lack of heating of the sample in the process of deposition and implicitly of the collateral effects; the effect of pollution is minimal and completely eliminates the use of toxic nonmetallic compounds such as cyanide in the coating process; the necessary equipment is relatively simple, and the technology has costs mainly generated by the quality of the additive materials [23].

Procedure's advantage is that heat density of the piece is minimum maintaining chemical composition and the properties of basic material. The thin layer system hardened through impulse electric discharge method is splitted into: an exterior layer with a strongly modified structure at the surface and an interior layer (diffusion layer) with the properties corresponding to basic material and added material. The hardened layer presents cracks that are advantageous to the lubrication process (during exploitation) by protecting basic material of excessive wear.

An inadequate diffusion is a risk factor for obtaining thin films, their long-term stability, and security in service. This can be solved by applying a heat treatment or thermochemical treatment afterwards. This may cause high electrode consumption due to its elongation and tear, due to the rapid dissipation of heat developed to part contact area, while the heat dissipated in the electrode is made slower, this being due to the large mass difference between the piece and the electrode. This problem can be solved by choosing an optimum working regime using appropriate parameters. Deposited layer characteristics are controlled process parameters: spark energy, discharge voltage, spark duration, inductance, frequency, temperature, number of passes, pressure on the end electrode (filler) on the surface of the base material, linear speed horizontal electrode, etc. The difficulty of the problem, in some cases, to the incompatibility between the filler material is characterized by special properties and support.

For this reason, there is a need for multiple layers: the first layer deposited actually providing the support anchoring surface layer.

2.1. Mass transfer

The mass transfer intensity and coating parameters can vary depending on the electrode material nature and basic material nature. Energetic transfer is depending on the physical and chemical characteristics (specific heat, density conductivity, and thermal transfer coefficient), on the atomic number, and on the value of the elements that are in the cathode, anode, and work environment composition. The electro-spark deposition can be viewed evolutionarily, over time, by the steps required to form the layer, that is, the proximity of the electrodes, the penetration of the gaseous zone between the electrode and the base material, and also the creation of a thermal flux that has the effect of melting the areas limiting the flow to both the cathode and the anode; creation of a plasma area surrounding the energy and mass transfer field, an area that favors chemical activities, due to the formation of strong reactivity ions [24]. But, the same deposition can also be seen in terms of evolution in space by studying the structure of the areas that make up the deposition system. The deposition areas can be divided according to their position and role in the operation, as follows: anode electrode area (area of the filler material); deposition flow area; part deposited material area; and cathodic area of the base material.

Electrode anodic area. Priming arc between the two electrodes has the first effect, a thermal flux that leads to electrode top melting (**Figure 2a**).

Because of the temperature parabolic variations, the electrode material will melt, so the top of the electrode will take an interior shape like the thermal field. During coating, the initial thermal flux separates, and warm small areas are developed inside the cone. Inside the cone appears small bumps because small warm areas are migrating inside, and the material melting from inside is done depending on local thermal peaks. Tungsten electrode peak pictures show that the cone peak coating is deeper (**Figure 2b**). Electro-erosion energetic flux is creating a small top cone, with high differentiated and with a visible and deep crater. Crater side surface is soft, less involved in coating and plasmatic cinematic processes of the treatment.

Flux area. It is the area with the higher dynamism, here is forming the electrical, thermal, and plasmatic flux, with active elements development: atoms, ions, and electrons. This is influencing

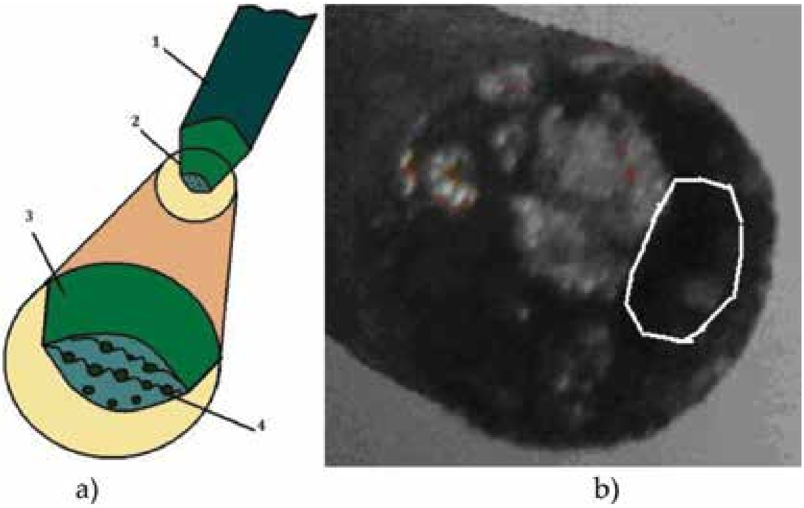

Figure 2. (a) Maximum and minimum of local mass transfer; (1) electrode; (2) attack zone; (3) enlarged attack zone for highlighting the formations at the interior cone base; (4) maximum and minimum local thermal areas developed during mass transfer; (b) tungsten electrode peak used in this experiment.

the character and the quality of the coating. In the flux area (**Figure 3**), are developing, beside high thermal, electrical fields and added material witch strikes with high force. This material is solid (particles) or liquid (drops). Depending on the electrode type, we will have mainly one of the two up-mentioned forms: nickel and titanium have in their flux, mainly, melted material drops, and tungsten, because of high melting temperature created inside the flux, specially extracted particles.

Material deposition area. The area of the deposited material is important because it gives information about the surface characteristics. The amount of melted and deposited material on the surface depends on various parameters, such as: pulse current frequency, gap size, electrode material properties, average intensity, pulse power, etc. Studying the part surface microgeometry modification using the development of the waves on the surface of the liquid metal in the impulse discharge conditions, author Topală (**Figure 4**) writes that the phenomenon is accompanied by the appearance of craters on the surfaces of electrodes [25].

In fact, three types of craters have been recorded, all of them having the shape of a spherical calotte (**Figure 5**): (i) a smooth profile with good flow properties (low relative melting temperature such as Ni and Ti); (ii) a rugged profile, specific for the fragile material electrodes, which

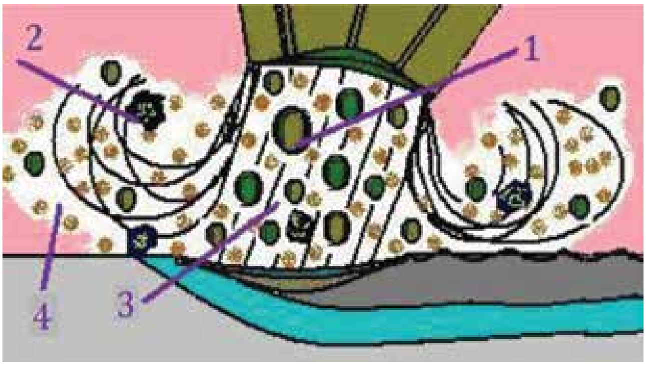

Figure 3. Flux elements; (1) liquid added material (drops); (2) extracted added material (particles); (3) thermal flux—heat jet; and (4) plasma (developed by gases decomposition and nitrogen, oxygen, and carbon active atoms.

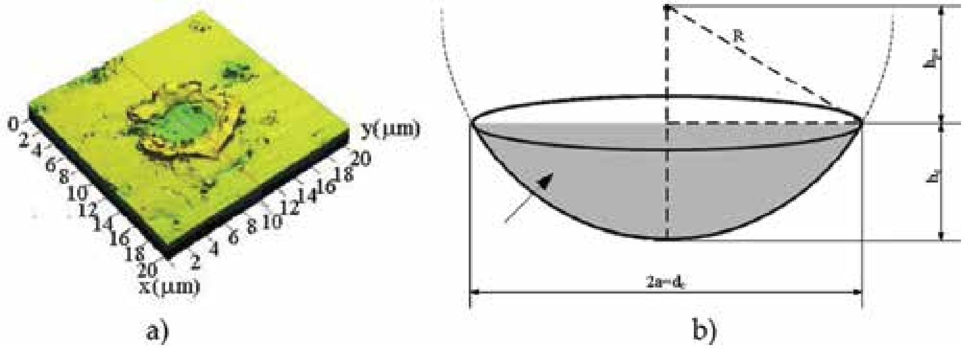

Figure 4. (a) General view of a deposition erosion crater; (b) the spherical calotte is an idealized form of the crater.

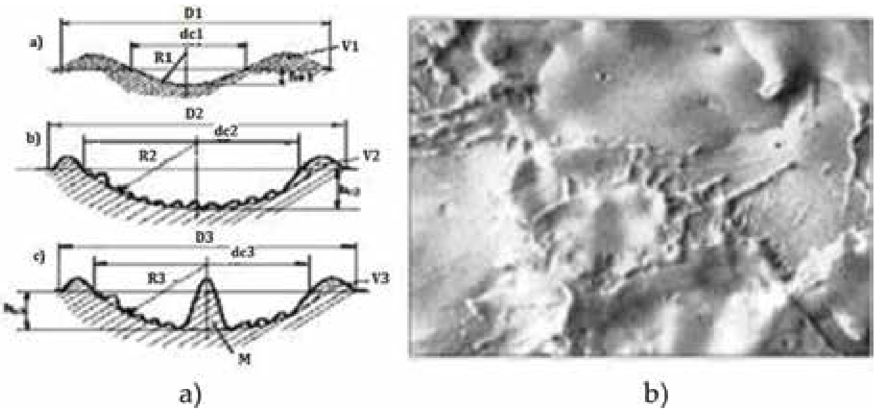

Figure 5. (a) Types of craters obtained by dimensional processing by electroerosion (D_1, D_2, and D_3—the diameter of the craters together with the wave; $d_{c1,}$ d_{c2}, and d_{c3}—the diameters of three types of craters; $h_{c1,}$ h_{c2}, and h_{c3}—The depth of the craters; M—meniscus; and V—wave); (b) the waveform of the deposition surface.

break out during deposition and do not melt easily (due to very high melting temperature, for example, tungsten); and (iii) a middle meniscus, characteristic for materials that solidify at a high rate (high melting temperature, when the "drop" touches the cold part, solidification begins).

The forces that compete to create surface geometry are the ion beam pressure force and the metal vapor reaction force, due to the static pressure of the metal vapors in the crates. It has been noticed that the height of the meniscus depends on the following factors: discharge energy, discharge time, electrode material, and application of the electric field to the gap.

Base material area. This area is important to the necessary consistency with the addition material, so that the small bonding area that ensures the adhesion of the layer is as strong as possible.

2.2. Surface morphology

The hardening of the surface of a piece by the ESD method requires knowledge of the properties of both the basic material (physical and chemical properties) and the deposition material. When heterogeneous multilayer layers are depositing, the base layer must be metallurgically compatible with the adduct and have good adhesion properties and near by physical properties (coefficient of expansion, conductivity, diffusivity, electrical resistance, melting point, and vaporization). The exterior layers must have the characteristics required to operate the part (wear resistance, dynamic shock, corrosion resistance, abrasion resistance, hardness, etc.). In the case of an intermediate layer, the deposited layer and the surface layer must be connected.

Tests were made with the Elitron 22A type machine (**Figure 6**). The device parameters listed in the machine's technical manual are: the power consumed (kVA)—0.5; productivities (cm^2/min)—4; working voltage (V)—220; working regimes (r), amplitude of vibration (A)—(A1 = 0.04 mm, A2 = 0.06 mm, A3 = 0.08 mm, A4 = 0.1 mm, A5 = 0.12 mm, A6 = 0.14 mm, A7 = 0.16 mm, A8 = 0.18 mm, and A9 = 0.2 mm); mass (kg)—21 [26]. The Elitron 22A instrument used in the experiments has nine amplitude and six work modes.

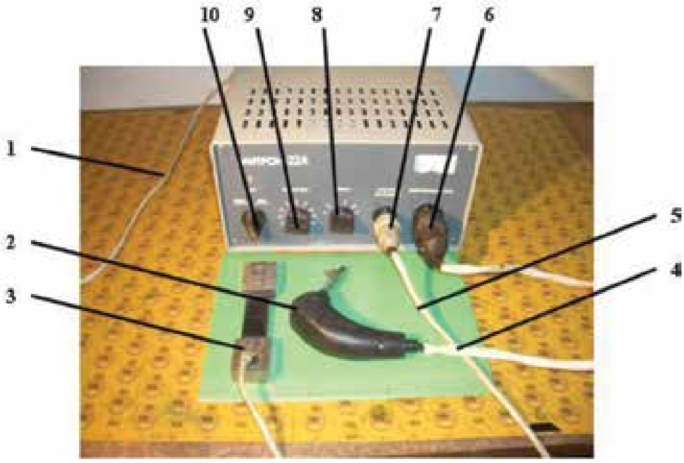

Figure 6. Components of the Elitron 22A pulse electric pulse deposition device: (1) power supply cord; (2) electrode support; (3) piece support; (4) electrode support cable; (5) piece support cable; (6) and (7) connecting sockets; (8) adjustment knob (intensity); (9) vibration amplitude adjustment knob; and (10) stop-start button.

As a base material for the coating, ferritic-pearlitic cast iron was used, which chemical composition is presented in **Table 1**. The chemical composition determined by means of Foundry Master spectrometer.

Justifying the choice of the base material is given by the advantages of choosing this material in textile industry machines and installations (cams, friction skates, and gears in looms). Gray cast iron is a material with a good thermal shock resistance and does not require lubrication. Expanding and contraction coefficients are low and have the property to absorb easily apparent tensions during work by means that graphite from the matrix is creating discontinuities that can absorb vibrations and shock exposure.

Electrodes used for deposition are Ti, TiC, W, and WC. The surfaces of the deposition drops were analyzed by means of electron scanning microscope (SEM).

2.3. Analysis of deposition drops

In the pulsed electric discharge deposition process, in addition to particular importance for the mass, transfer workflow parameters and physicochemical characteristics of the whole area, a great contribution to the achievement of appropriate structures is the type of deposition, and in particular adhesion and microalloying for the drop. As long as the connected metal layers are obtained using this technology, the coating properties are dependent by the chemical reactions at the interface. Since a coating obtained by depositing consists of multiple single drops,

Element	C	Si	Mn	P	Cr	Ni	Cu
Percentage, %	3.97	2.87	0.25	0.06	0.28	0.12	0.17

Table 1. Chemical composition of base material.

formed in a dependent rotary movement order of the electrode is important to study the deposition "drops" generation and also the characteristics for the uni-impulse drops. At the same time, the interface chemical reactions lead to the formation of varied compounds, also influencing the coating properties. The drop represents the part exterior shape after the treatment, because the layer is formed by a lot of drops, some of them remelted by the subsequent crossing. The flattening of the "drops" sputtered on the substrate is one of the most important processes occurring in coatings using electric arc. The layer structure will determine the coating structure and therefore, adhesion and coating properties. Therefore, attention was paid to the study of "drops" by experimental observations.

Analysis of the "droplet" shape using a titanium electrode. It is noticed that the Ti electrode does not only achieve a smooth deposition of the "droplet," but also the process is much more dynamic, the deposition takes place at a certain speed, and the strike impulse creates micro-depression surface, which subsequently, upon the fall of a new "droplet", leads to a microalloying with the subsequent in depth layer (it is at most 20 μm) (**Figure 7**).

The map of the surface elements of the titanium shell (Ti) on the ferrite-perlite substrate is shown in **Figure 8**.

Uniform distribution of the elements can be observed, indicating the complete alloying process between the base and the substrate. The Ti was distributed in the melting zone on the cast iron substrate and by diffusion in area interface. New phases have been formed in the coating layer due to the chemical reaction during the deposition process. Note the titanium distribution in **Figure 8b**.

Thus, due to the high temperature conditions, the following reaction takes place: Ti + C = TiC. The "drop" striking energy on the metal surface is added to the thermal energy and plasma energy that is formed during the deposition. Thus, optimum conditions are created for the formation of highly intermetallic compounds or chemical compounds. Another particular aspect is that Ti compact droplets are distributed at the edge of the droplet rather than the center, this being possible due to the splashing dynamics. An advantage of the

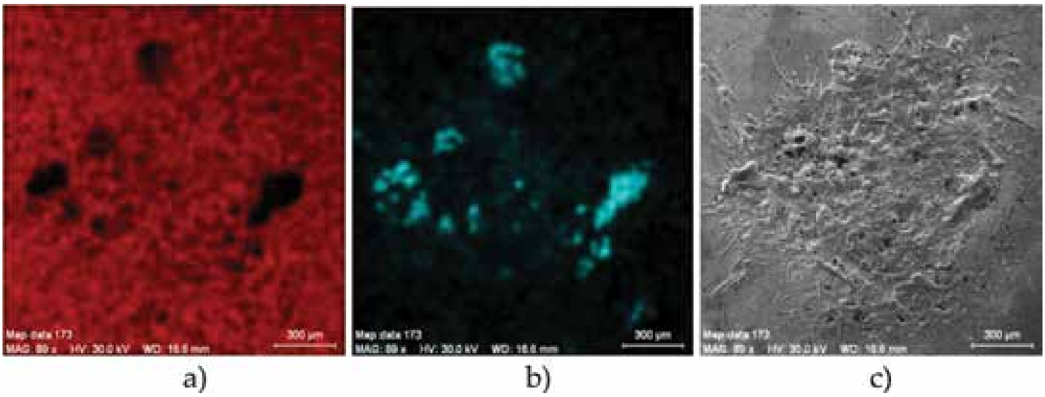

Figure 7. Distribution of Fe and Ti elements; (a) SE_Fe; (b) SE_Ti; and (c) the "drop" by Ti, SE image giving information about surface relief.

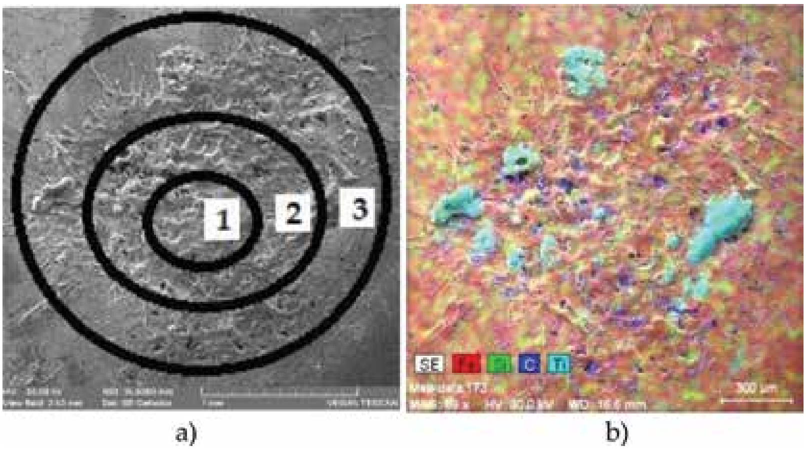

Figure 8. (a) Area distribution of the drop; (b) elemental distribution of the "drop."

melting and solidification dynamics specific to Ti is that there are no large and visible cracks, and the layer is relatively compact.

A disadvantage of the dynamics of the phenomenon is that the roughness of the piece is quite high. Studying the BSE (Back Scattered Electrons) image shows the phase difference by the appearance of dark areas and bright areas, when the surface of the base material contains ferrite grains (light color) with darker vermicular areas (carbon), areas found in higher quantity in the center of the "droplet" (carbon forms titanium chemical compound due to chemical activity of carbon in the plasma). The black areas are made up of Ti droplets. The "droplet" area can be divided into three regions characterized by both the variation of the deposition form and the variation of the deposition element content.

The first region (**Figure 8a**) represents the center of the "droplet" that received the highest energy impulse in the deposition motion, where the temperature was the maximum, and a melting of the substrate took place. In this area, we do not actually encounter Ti in the form of a microdrop, but just accidentally by slashing. In this area, chemical compounds obtained through the reactions between Ti and the substrate elements predominate, facilitated by the energy released in the area.

The second region represents the immediate vicinity area, in the form of an annular shape, and which is a transition zone to the edges of the "droplet". In this area, Ti is found in the form of a compact micromelt, as well as microalloying compounds due to the dynamics of the melting bath and migrating from the center to the outside.

In the third zone, which is the periphery of the "droplet," melted and solidified splashes of Ti are predominant; also drops from the melted substrate pulled away the formation site due to the splashing motion. Also, due to the splashing, bumps are formed by microelevation formation right on the edge of the "drop," while in the center, there are flattened areas with a certain concavity.

The spreading zone is quite large because Ti and its chemical compounds melt at relatively low temperatures and are in a liquid form, a relatively long time (order of seconds). Due to the fluidity of the drop elements and the fact that the expansion coefficient of the substrate and the drop is almost the same, no visible cracks appear, **Figure 9**.

The outside droplet pores found, the third scattering zone, are derived from the presence of chemically absorbed gases at the surface of the part, or gases from the metal bath reaction.

2.4. Titanium deposition on a cast iron layer

From micrographs made by scanning electron microscope shall be observed that Ti deposition on cast iron electrode creates a relatively compact layer with limited bumps and obvious cracks. Titanium shall be uniformly deposited both highlighted in **Table 2** by its high percentage and the EDX analysis (**Figure 10**), when is observed the distribution of the titanium deposition on almost the entire surface.

Titanium coatings are compact, as the atomic number of Ti (22) is much closer to that of Fe (26), which means that their atomic radius difference is very small. This makes it easy to transfer the titanium on the substrate. The outer layer of iron underwent a partial melting allowing for titanium microalloying, but mainly the layer is thin, micro interrupted.

Alloying titanium base material is achieved in a smaller extent because of high melting titanium temperature (1800°C) making titanium to quickly solidify once reached the surface. Thus, it explains the presence of areas with excess deposited material (compact undissolved titanium areas into "drop" metal bath and stuck to the surface). At Ti deposition on gray cast

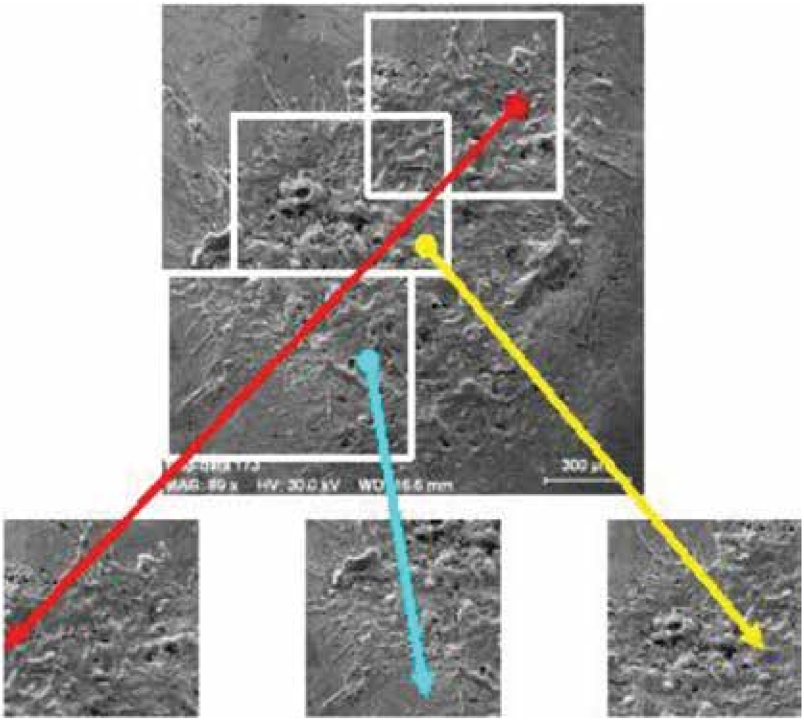

Figure 9. Enlarged areas in the SEM image are for highlighting the extent of spreading of the melted area.

Element	Volume percent, (%)	Atomic percent, (%)
Titanium	76.56	77.64
Iron	22.36	19.44
Carbon	0.46	1.89
Silicon	0.44	0.76
Phosphorus	0.16	0.27

Table 2. Chemical composition for Ti deposition on cast iron.

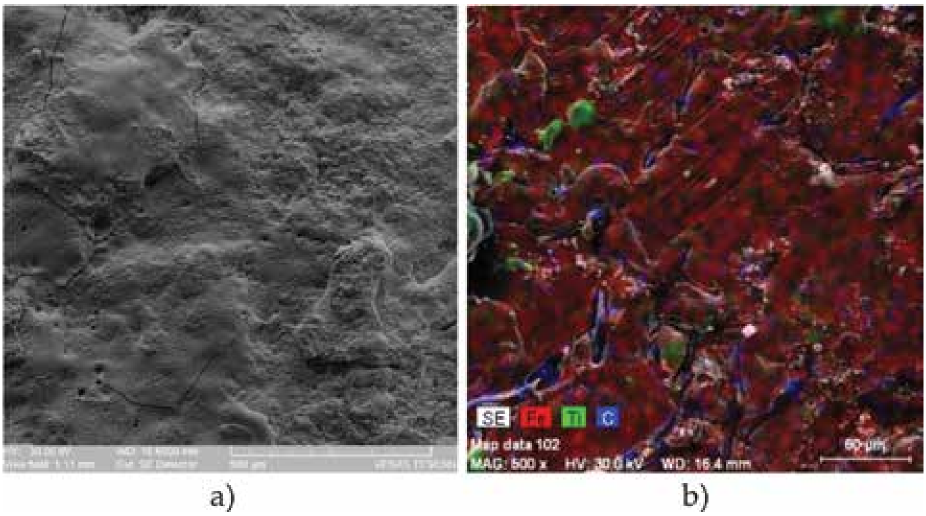

Figure 10. (a) SEM microstructure; single layer Ti deposition on cast iron, SE, 500 µm scale; (b) elements distribution by EDX analysis, 60 µm.

iron, the graphite slides do not melt and dissolve in the microzones of the deposition drops. Due to this, the lamellas absorb the heat and release it gradually, keeping the surface warm for a long time, resulting in a more complete distribution of Ti deposited on the surface.

2.5. One-way deposition and two-way deposition using Ti electrode

In one-way deposition, the deposits with Ti electrode (**Figure 11a**) are compact, due to the atomic number of Ti which is closer to Fe meaning that the difference of atomic radius is very small. This makes titanium transfer easily from interface to substrate. The exterior layer of the ferritic-pearlitic iron stands a partial melting, which made possible titanium micro alloying.

It achieved a thin layer with discontinuous micro zones, without material withdrawals. Titanium has good coating qualities when base material is ferritic-pearlitic iron. The images and the chemical composition of the layer are achieved by means of electronic scanning microscope.

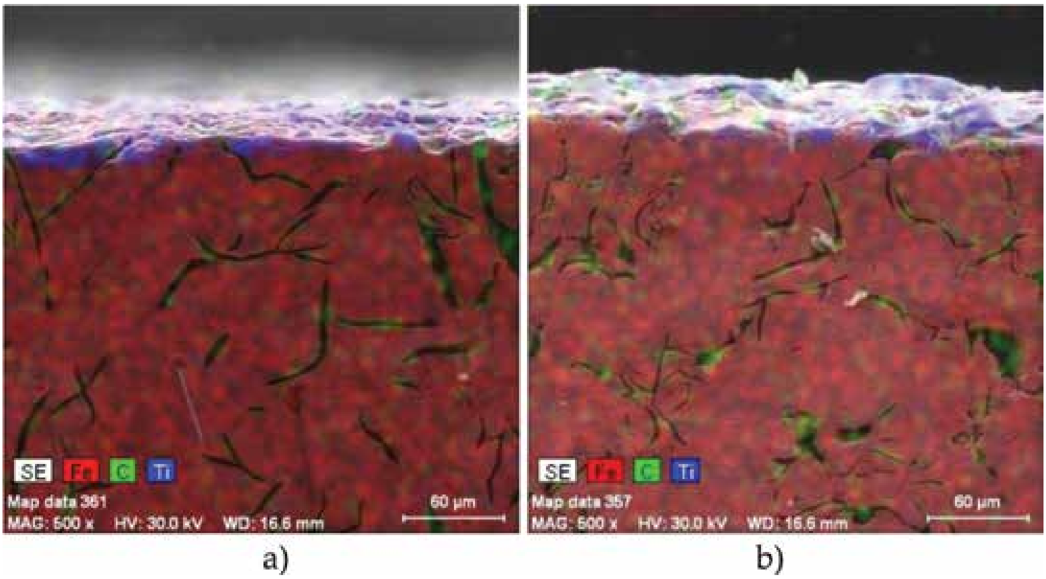

Figure 11. (a) Distribution of Fe, C, and Ti elements for one-way deposition, 500X; (b) distribution of Fe, C, and Ti elements for two-way deposition, 500X.

In **Figure 11b**, notices zones with microcracks due to the increase of the superficial layer and to the fact substrate is colder than in one-way deposition, so that the cracks are less pronounced. It is also possible that the cracks are only in the first layer and do not get into the second layer.

In **Table 3**, it is given the chemical composition of the deposit layer with Ti electrode, one-way deposition. The chemical composition of the deposit layer with Ti electrode, two-way deposition, presents in **Table 4**. Element distribution presents common repartition areas of Fe, C, and Ti, indicating the presence of intermetallic compounds within alloying bath. Microzones with cementite can be seen in the microstructure due to the energy application of the thermal flow and due to the powerful temperature gradient at cooling (the exterior layer cools down quickly). Cooling takes place due to air contact and to the small thickness of the layer (some tens of microns).

The layer thickness, (**Figure 12a**), Ti deposited (one-way deposition) varies between 24.75 and 30.63 μm, indicating a good uniformity of deposition with very small deviations from the flatness of the surface and a low roughness.

When analyzing the layer thickness (two layers of titanium, **Figure 12b**), it is observed, by examining electron micrographs, that the outer layer of Ti two-way deposition creates a surface as smooth as depositing a Ti layer. The thickness of Ti layer by deposition of two passes is uniform and varies between 36.52 and 47.72 μm.

Blanking, titanium deposition (**Figure 13a**) is a thin layer with good adhesion because the rupture is smooth, without exfoliation. The breakage of the layer is similar to a fragile crack due to the higher hardness of the coating over the base material. Analyzing the micrographs

Element	Iron	Carbon	Titanium	Silicon
Percentage, %	88.32	7.25	2.41	1.99

Table 3. Chemical composition of one-way deposition of Ti layer.

Element	Iron	Carbon	Titanium	Silicon
Percentage, %	58.82	35.59	3.58	1.99

Table 4. Chemical composition of two-way Ti layer.

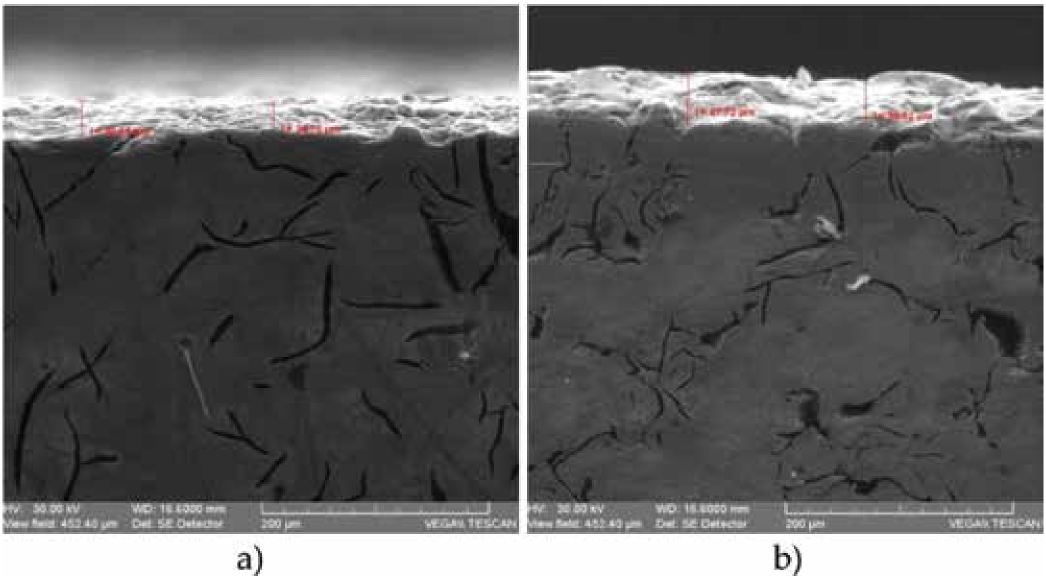

Figure 12. (a) Thickness value for depositing one-way deposition Ti layer; (b) thickness for deposition of Ti two-way layer.

obtained in the electronic scanning microscope for two-layer titanium casting test specimen (**Figure 13b**), the deposition and compactness of the layer were observed.

The deposition of titanium in the quartz has a characteristic form of breakage due to the high hardness of the deposited area.

2.6. Ti/W/TiC deposition analysis

Heterogeneous triple deposition begins by depositing a titanium layer on the surface of the base because it has good adhesion, depositing relatively compact, no gaps, no strong oxide layers, and no massive roughing on the surface of the sample. Titanium has the property of being a good support for mechanical and thermal shocks. The second layer is a tungsten electrode, which is a hard material with a very high melting temperature that creates deposition craters and areas of material gaps but improves the hardness of the deposited layer. Titanium

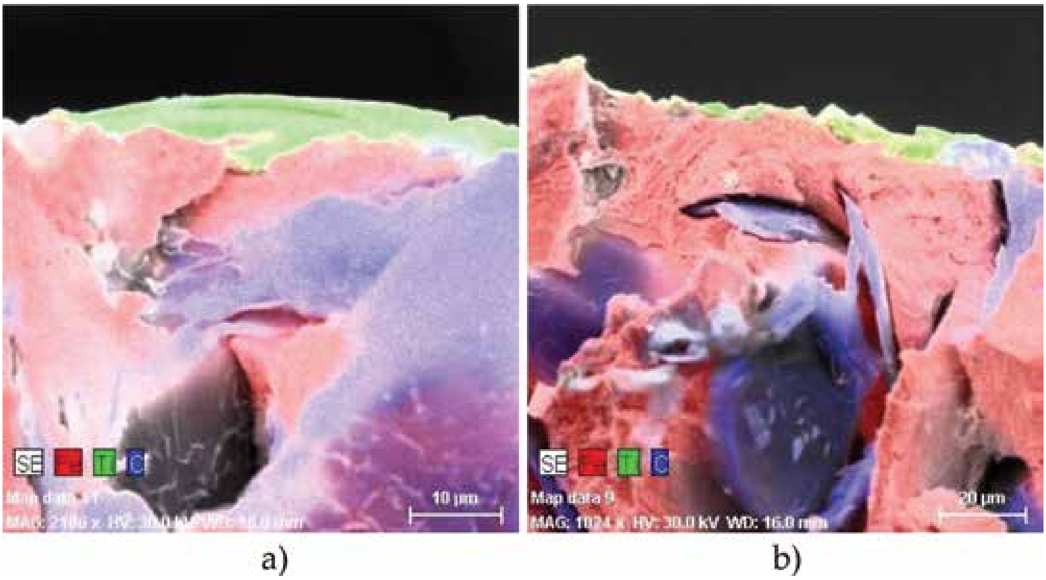

Figure 13. Distribution of elements in the crack; (a) simple Ti deposition: Ti, Fe, and C; (b) deposition Ti double layer: Ti, Fe, and C.

carbide alleviates the defects introduced by tungsten by smoothing out surface roughness and covering areas with crackers and squeezing of the material.

Studying the EDX analysis is observed in the presence of a 32.42% of tungsten and just 13% titanium (**Table 5**) [27].

A layer thickness analysis was made. It is observed that the triple layer has a relatively even thickness, and the variation of the thickness is proportional with the roughness of the surface. The thickness of the layer varies between 172 and 119 µm (**Figure 14**), meaning that is a relatively thick layer. The surface layer can be grinded, after that also the thickness is relatively high [27].

In the fracture, the combination of triple base deposition material presents as a fragile rupture due to the high hardness of the deposited layer. It is noticed that the deposition has not separated, which shows a microalloy with the large diffusion area that creates the adhesion between the deposited layer and the base material.

This ensures the deposited layer a hybrid structure with amorphous feature, containing a layer with deposition elements dissolved in high concentration in basic matrix on a smaller distance than 100 µm [27].

2.7. XPS analysis for the sample with WC/TiC/W deposition

The analyses were done on multi-layer depositions, namely, tungsten carbide—as the first interface and titanium carbide—as the second interface and tungsten exterior layer (WC/TiC/W), being made with PHI 5000 Versa Probe-XPS X-ray photoelectron spectrometer. The determination of energetic maximum (energetic peaks) gives indications on the chemical compounds

Element	Iron	Carbon	Tungsten	Titanium
Percentage, %	49.82	4.67	32.41	13.07

Table 5. Chemical composition of the Ti/W/TiC layer.

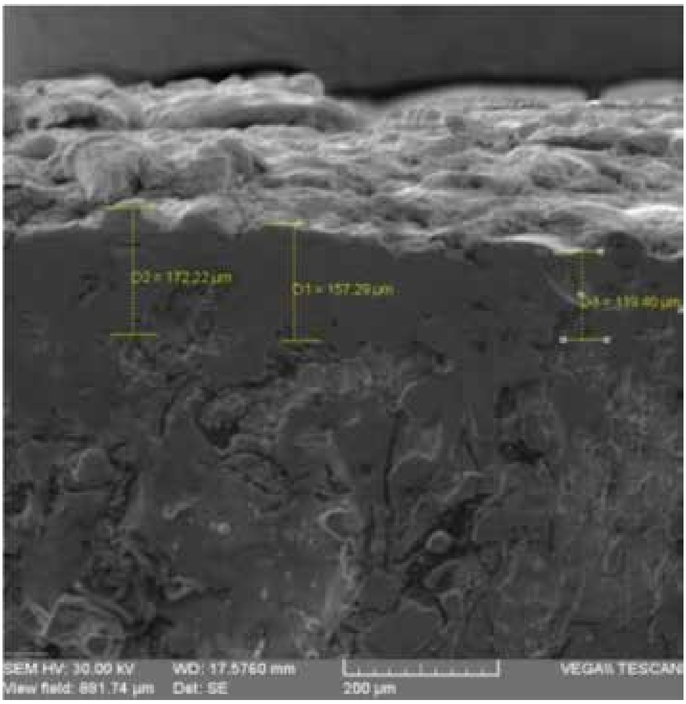

Figure 14. Deposition layer thickness Ti/W/TiC; 200 μm.

of that element in the energy area corresponding to the photoelectronic spectrum of kinetic energy. For the sample with WC/TiC/W deposition are presented two graphs generated at different radiation times, the first at 16.01 minutes (**Figure 15a**) and the second at 32.01 minutes (**Figure 15b**). Exposure time was increased to remove the effects of contamination because elements such as Si, P, and Ni appear in small percentages, being elements that occur through absorption on surface during deposition or later on. In general, graphs notice the presence of the chemical elements on the surface as well as the orbitals of each element such as C1s—28.6%, Fe2p3—22.4%, Ti2p—8.1%, and W4f—6.5% and from the atmosphere O1s—30.6% and N1s—3.1% [28].

The graph with local maxima is presented showing chemical elements and bonds in the energetic range of 0–1200 eV. For each chemical element, the energetic bonds were studied such as the chemical compounds appeared in the layer and so enlarged areas in the energetic scale realized.

- for C1s between 274 and 296 eV. In the area maxima peaks discovered that correspond to the following compounds CO_2, CO_3, TiCN, TiC, WC. Local energetic maximum areas are listed in **Table 6** for each chemical compound in whose composition carbon enters.

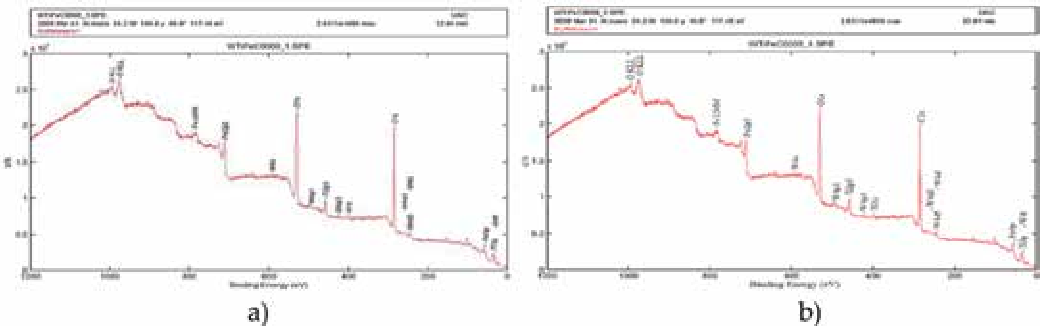

Figure 15. General graph obtained at radiation time for WC/TiC/W deposition at duration of: (a) 16.01 minutes; (b) 32.01 minutes.

Chemical compound	**CO_2**	**CO_3**	**TiCN**	**C**	**TiC**	**WC**
Energetic maximum (eV)	291.6	290.2	288.7	285.1	281.2	281.1

Table 6. Local energetic maximum areas for each compound.

- for O1s with the energetic band between 522 and 544 eV local extremes decompose appropriate to the following oxides Fe_2O_4, TiO_2, TiNO, WO_3, Ti_2O_4. Local energetic maximum areas are listed in **Table 7** for each chemical compound in whose composition oxygen enters.
- for Fe2p3, **Table 8**, with the energetic band between 700 and 740 eV, it notices local maxima in the energetic range of the following chemical compounds Fe_2O_3, FeOOH, $FeWO_4$, FeO, Fe_3O_4, and Fe_3C.
- for Ti2p3, **Table 9**, with the energetic band between 450 and 475 eV, emphasizes the local maxima from this energetic range corresponding to the following chemical compounds TiO_2, TiC, TiN, Ti_2O_3, and TiC, **Figure 16**.
- for W4f, **Table 10**, with the energetic band between 25 and 45 eV, emphasizes the local maxima from this energetic range corresponding to the following chemical compounds $Fe_2(WO_4)_3$, WO_2, WO_3, and W.

The presence of massive amounts of oxides is due to the deposition in air without a protection layer but only with the protection of the plasmatic atmosphere between cathode and. Oxygen

Chemical compound	**Fe_2O_4**	**TiO_2**	**TiNO**	**WO_3**	**Ti_2O_4**
Energetic maximum (eV)	536.7	529.4	531.1	531.1	531.1

Table 7. Local energetic maximum areas for each compound.

Chemical compound	**Fe_2O_3**	**FeOOH**	**$FeWO_4$**	**FeO**	**Fe_3C**
Energetic maximum (eV)	715.7	710.7	711.5	711.1	707.1

Table 8. Local energetic maximum areas for each compound.

Chemical compound	TiO_2	TiC	TiN	Ti_2O_3	TiC
Energetic maximum (eV)	464.9; 458.4	454.8; 460.1	454.8; 463	455.8	455.1

Table 9. Local energetic maximum areas for each compound.

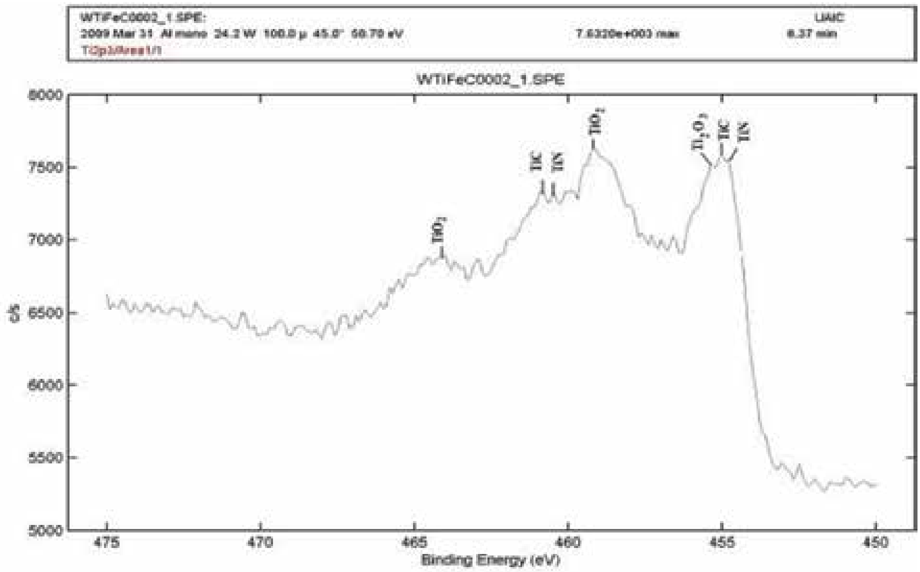

Figure 16. XPS analysis for Ti2p3 at the ferrite pearlite iron sample covered with WC/TiC/W triple layer.

Chemical compound	$Fe_2(WO_4)_3$	WO_2	WO_3	W
Energetic maximum (eV)	36.4	34.1	34.1	31.8

Table 10. Local energetic maximum areas for each compound.

and active nitrogen are also present in this atmosphere, as demonstrated by the presence of the compounds such as TiCN, WO_2, WO_3, TiO_2, FeO, Fe_2O_3, Fe_3O_4, FeOOH (rust), TiNO, and Ti_2O_3.

2.8. Thermal conductivity analysis for deposit layers

Thermal conductivity analysis for deposit layers with vibrating electrode method accomplished with Mathis TCI apparatus [29].

In case of thin layer deposition, some peculiar phenomena appear and conductivity varies in terms of deposit layer nature, deposit technology, number of deposit layer, and layer compactness. Between the properties that influence thermal conductivity, we mention besides porosity degree of the layer, deposition irregularity (drops appearance, material discontinuities, and high roughness), hardness (inverse proportional to conductivity), and thickness of the deposit layers, too, **Table 11**.

Material	Value of thermal conductivity, k (W/m K)
Base material	24.41
One-way Ti layer	18.34
Two-way Ti layer	10.59
One-way TiC layer	20.67
Two-way TiC layer	16.70

Table 11. Values of thermal conductivity for base material and all kinds of deposition.

The values for thermal conductivities, **Figure 17**, are very different, being much smaller than base material value. Thin layer depositions with Ti and TiC electrodes on base of ferritic-pearlitic gray iron create thermal barriers in the deposited piece. Thermal barrier has a positive effect because during functioning, at reduced heating, small dilatations appear, so thermal stresses with high values are not introduced in the piece and decrease the danger of deformation appearance or even thermal fatigue, which leads to piece cracking. One can meet an emphasized blockage of thermal transfer at one-way heterogeneous depositions, due to atomic lattice modification, in terms of addition materials and deposition sequence.

2.9. Hardness analysis of the deposit layers

In choosing the method for microhardness determining, it must be taken into consideration layer's structure and properties. For Ti and TiC, W and WC electrodes were made microhardness measurements with Vickers method. PMT3 microhardness machine was used. Pressing weight of the diamond indenter was 50 g (HV50), **Table 12**. The samples were grinded and polished after deposition, and microhardness measurements accomplished due to the small thickness of the deposit layer.

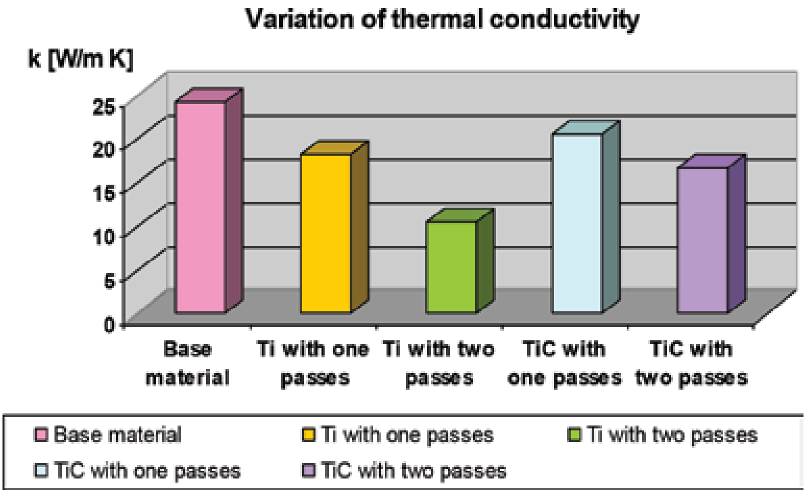

Figure 17. Graphic of thermal conductivity variation for thin layer deposition with vibrating electrode method.

Base material	400.00
One-way Ti layer	729.96
Two-way Ti layer	786.53
One-way TiC layer	773.20
Two-way TiC layer	816.32
One-way W layer	754.42
Two-way W layer	818.32
One-way WC layer	976.56
Two-way WC layer	821.54

Table 12. Values of microhardness measurements for deposit layers, HV50.

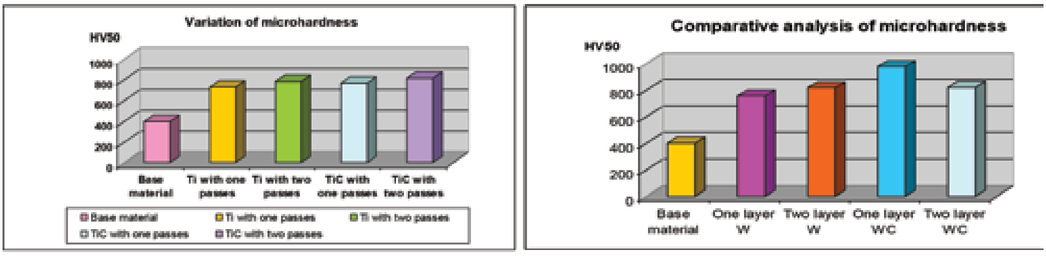

a)

b)

Figure 18. (a) Comparison analysis regarding microhardness for simple and double coatings using Ti and TiC electrodes; (b) comparison analysis regarding microhardness for simple and double coatings using W and WC electrodes.

The indenter acted on sample section, and not on deposit surface, so that values represent only the hardness of the layer and not of the base material. Analyzing **Figure 18a** notices that the microhardness values of the thin layer achieved by vibrating electrode method are close to all types of deposition, but double as value against the value of the base material (ferritic-pearlitic iron). Analyzing **Figure 18b** notices that the microhardness values of the thin layer achieved by vibrating electrode method are close to all types of deposition, but double as value against the value of the base material (ferritic-pearlitic iron).

3. Conclusions

The study of ESD deposition is useful for the wide range of application elements used and the multitude of aspects addressed (micronutrition measured in the layer section, internal stresses, roughness, conductivity, EDX analysis, and XPS analysis for the detection of types of chemical compounds obtained in postdeposition and mass and energy transfer analysis, etc.).

The chemical analysis of deposited strands using photoelectron spectroscopy reveals the presence of complex chemical compounds such as carbides, nitrides, oxides (W3C0, 375, Ti_2C, TiN, TiNO, and TiCN) in the layer, which explains the mechanical properties of the surface layer (microhardness).

The solution is multiple layers, with the advantage to obtain a greater diffusion, which leads to a better anchoring for the layer, with no effect on the surface quality.

The surface quality resulting from deposition using the pulse electric discharge method is dependent on the quality and chemical composition of the electrode. We used Ti, TiC, W, and WC electrodes, and we can conclude that Ti and TiC create much smoother surfaces than those obtained with W and WC electrodes. Titanium has a good adhesion to the surface of ferrite-perlite iron, creating compact layers, with no major bumps and few microholes. Tungsten "burns" the contact surface due to the high temperatures generated in the electric arc, does not deposit itself on the piece, but only makes superficial quenches. Titanium carbon and tungsten carbide have affinity to the ferrite base matrix creating homogeneous layers but with pronounced cracks due to the coefficient of expansion different from the base material.

It notices the influence of the chemical elements from working atmosphere (oxygen and nitrogen), leading to compound formations in the superficial layer. Thus, it notices the presence of Fe, Ti, and W oxides as well as complex nitrides and carbides.

Thermal conductivity of coated surfaces is considerable inferior from the base material. In these conditions, we can conclude that each coating is forming a thermal shield, fact that can be exploited in technical field, in case of using cast-iron for elements that must resist to thermal shocks: heating systems and burning chambers.

From metallurgical aspects point of view, for homogeneous surfaces, we can conclude that tungsten electrodes and tungsten carbide are benefic in increasing the surface hardness.

In order to obtain surfaces with superior qualities, it is possible to combine the method of deposition by impulse discharge with laser treatment or with thermal spraying treatment in order to retrieve the deposited surface in order to obtain more compact layers without cracks and with low roughness.

Author details

Petrică Vizureanu*, Manuela-Cristina Perju, Dragoş-Cristian Achiţei and Carmen Nejneru

*Address all correspondence to: peviz2002@yahoo.com

"Gheorghe Asachi" Technical University Iasi, Romania

References

[1] Wang Y, Ma H, Li X. MATEC Web of Conferences: Interface behavior of tungsten coating on stainless steel by electro spark deposition. 2015;**35**:01006. DOI: 10.1051/matecconf 20153501006

[2] Peterkin S. Electro-spark deposition machine design, physical controls and parameter effects [thesis]. Waterloo, Ontario, Canada; 2016

[3] Radek N, Sladek A. Journal of the Balkan Tribological Association: Properties of electro-spark coatings deposited on the steel substrate using the tungsten carbide-ceramic electrodes. 2016;**22**:1354-1362. DOI: WOS:000381330600026

[4] Huang QS, Chen ZG, Wei X, Wang L, Hou ZW, Yang W. China Surface Engineering: Effects of pulse energy on microstructure and properties of Mo2FeB2-based ceramet coatings prepared by electro-spark deposition. 2017;**30**:89-96. DOI: 10.11933/j.issn.1007-9289.2017 0106002

[5] Ribalko AV, Korkmaz K, Sahin O. Surface and Coating Technology: Intensification of the anodic erosion in electrospark alloying by the employment of pulse group. 2008;**202**:3591-3599. DOI: 10.1016/j.surfcoat.2007.12.037

[6] Ekmekci B. Applied Surface Science: Residual stresses and white layer in electric discharge machining (EDM). 2007;**253**:9234-9240. DOI: 10.1016/j.apsusc.2007.05.078

[7] Cadney S, Goodall G, Kim G, Moran A, Brochu M. Journal of Alloys and Compounds: The transformation of an Albased crystalline electrode material to an amorphous deposit via the electrospark welding process. 2009;**476**:147-151. DOI: 10.1016/j.jallcom.2008.09.017

[8] Cheng Y, Cai W, Li HT, Zheng YF, Zhao LC. Surface and Coating Technology: Surface characteristics and corrosion resistance properties of TiNi shape memory alloy coated with Ta. 2004;**186**:346-352. DOI: 10.1016/j.surfcoat.2004.01.012

[9] Liu DY, Gao W, Li ZW, Zhang HF, Hu ZQ. Materials Letters: Electro-spark deposition of Fe-based amorphous alloy coatings. 2007;**61**:165-167. DOI: 10.1016/j.matlet.2006.04.042

[10] Frangini S, Masci A. Surface and Coating Technology: A study on the effect of a dynamic contact force control for improving electrospark coating properties. 2010;**204**:2613-2623. DOI: 10.1016/j.surfcoat.2010.02.006

[11] Heard DW, Brochu M. Journal of Materials Processing Technology: Development of a nanostructure microstructure in the Al-Ni system using the electrospark deposition process. 2010;**210**:892-898. DOI: 10.1016/j.jmatprotec.2010.02.001

[12] Kambakas K, Tsakiropoulos P. Materials Science and Engineering A: Solidification of high-Cr white cast iron-WC particle reinforced composites. 2005;**413**:538-544. DOI: 10.1016/j.msea.2005.08.215

[13] Luo C, Xiong XA, Dong SJ. Transactions of Nonferrous Metals Society of China: TiB2/Ni coatings on surface of copper alloy electrode prepared by electrospark deposition. 2011;**21**:317-321. DOI: 10.1016/S1003-6326(11)60715-2

[14] Parkansky N, Beilis II, Boxman RL, Goldsmith S, Rosenberg Y. Surface and Coating Technology: Anode mass loss during pulsed air arc deposition. 1998;**108**:253-256. DOI: 10.1016/S0257-8972(98)00652-5

[15] Miller T, Lin JM, Pirolli L, Coquilleau L, Luharuka R, Teplyakov AV. Thin Solid Films: Investigation of thin titanium carbonitride coatings deposited onto stainless steel. 2012;**522**:193-198. DOI: 10.1016/j.tsf.2012.08.012

[16] Miller T, Pirolli L, Deng F, Ni CY, Teplyakov AV. Surface and Coating Technology: Structurally different interfaces between electrosparkdeposited titanium carbonitride and tungsten carbide films on steel. 2014;**258**:814-821. DOI: 10.1016/j.surfcoat.2014.07.076

[17] Xie YJ, Wang MC. Surface and Coating Technology: Microstructural morphology of electrospark deposition layer of a high gamma prime superalloy. 2006;**201**:691-698. DOI: 10.1016/j.surfcoat.2005.12.034

[18] Chen Z, Zhou Y. Surface and Coating Technology: Surface modification of resistance welding electrode by electrospark deposited composite coatings: Part I. Coating characterization. 2006;**201**:1503-1510. DOI: 10.1016/j.surfcoat.2006.02.015

[19] Chen Z, Zhou Y. Surface and Coating Technology: Surface modification of resistance welding electrodes by electrospark deposited composite coatings Part II. Metallurgical behavior during welding. 2006;**201**:241-243. DOI: 10.1016/j.surfcoat.2006.04.010

[20] Abboud JH, Benyounis KY, Olabi AG, Hashmi M. Journal of Materials Processing Technology: Laser surface treatments of iron-based substrates for automotive application. 2007;**182**:427-431. DOI: 10.1016/j.jmatprotec.2006.08.026

[21] Perju MC, Tugui CA, Nejneru C, Axinte M, Vizureanu P. ESD morphology deposition with WZr8 electrode on austenitic stainless steel support. In: International Conference on Innovative Research—ICIR Euroinvent; 19-20 MAY 2016; Iasi, Romania: ICIR; 2016. p. 012025

[22] Anisimov E, Khan AK, Ojo OA. Materials Characterization: Analysis of microstructure in electro-spark deposited IN718 superalloy. 2016;**119**:233-240. DOI: 10.1016/j.matchar.2016.07.025

[23] Perju MC, Găluşcă DG, Nejneru C, Agop M. Thin Layers: Impulse Discharge. Iasi, Romania: Ars Longa Publishing House; 2010. p. 339. ISBN 978-973-148-049-7

[24] Vizureanu P, Perju MC, Găluşcă DG, Nejneru C, Agop M. Metalurgia International: Mass transfer for titan and tungsten electrode coating using impulse discharge method. 2010;**12**:59-64

[25] Topala P, Slatineanu L, Dodun O, Coteata M, Pinzaru N. Materials and Manufacturing Processes: Electrospark deposition by using powder materials. 2010;**25**:932-938. DOI: 10.1080/10426910903447238

[26] Elitron 22 Installation. Republic of Moldova, Chisinau: Academy of Sciences; 1992

[27] Nejneru C, Perju MC, Axinte M. Applied Mechanics and Materials: Researches regarding Ti/W/TiC triple layers deposition on the ferritic-pearlitic cast iron support, obtained by electro-spark deposition method. 2013;**371**:363-367

[28] Perju MC, Vizureanu P. Revista de Chimie (Bucharest): Chemical compounds analysis developed on the micro alloying area of coating layers obtained by impulse discharge method. 2014;**65**:694-696. DOI: WOS:000339140400013

[29] Largeanu AE, Nejneru C, Perju MC, Galusca DG. Metalurgia International: Thermal conductivity analysis for metallic systems obtained multiple coating by electro-spark deposition method. 2011;**16**:43-46. DOI: WOS:000289606200010

Chapter 4

Surface Manufacturing of Materials by High Energy Fluxes

Stefan Valkov, Maria Ormanova and Peter Petrov

Additional information is available at the end of the chapter

http://dx.doi.org/10.5772/intechopen.79874

Abstract

This chapter aims to summarize the topics related to the application of a surface treatment by high energy fluxes (i.e., electron and laser beams) for developing of new multifunctional materials, as well as to modify their surface properties. These technologies have a large number of applications in the field of automotive and aircraft industries for manufacturing of railways, space crafts, different tools, and components. Based on the performed literature review, some examples of the use of laser and electron beams for surface manufacturing (i.e., surface alloying, cladding, and hardening) are presented. The present overview describes the relationship between electron beam and laser beam technologies, microstructure, and the obtained functional properties of the materials. The benefits of the considered techniques are extensively discussed.

Keywords: high energy fluxes, surface manufacturing, alloying, cladding, hardening

1. Introduction

In the era of exhaustion of natural resources as well as of continuous development of the modern industry, the technologies for surface treatment are becoming increasingly important. There exist a number of technologies for surface manufacturing of the materials, including electrochemical processes, electrical discharge processes, additive manufacturing, etc. [1–3].

Considering the electrochemical method, it has been used for synthesizing of nanostructures and manufacturing of advanced materials since the methods are known as cost-effective and resourceful. This technique is based on the removing of metal by electrochemical process, and it is used for treatment of extremely hard materials and materials that cannot be treated by the conventional techniques. However, some drawbacks such as long process time and too high temperature required can be mentioned. Furthermore, the formation of environmental pollution due to the use of chemicals and the need that the materials must be conductors can also be considered as limitations [1].

The electrical discharge machining process is another method which is used for manufacturing of the materials. This technique is based on the removing of the material using electrical discharge. Series of rapidly recurring current discharge between two electrodes were applied which are responsible for the removal of the material. The method is often used for prototype production and manufacturing of parts, especially for the needs of the automotive and aircraft industries. However, the slow rate of the material removal and the requirement of conductive materials that can be manufactured by the discussed method are of the major drawbacks [2].

Promising techniques for fabrication of new materials with unique properties and for modification of their structure are the additive manufacturing technologies. They are based on layer-by-layer fabrication of components [3]. The additive technologies include several techniques for materials' treatment, such as ultrasonic processes, electron beam processes, laser beam processes, etc. The ultrasonic processing is a revolutionary processing technology widely used for welding and joining. It is based on the scrubbing together with ultrasonic vibrations under controlled pressure or normal load. Nevertheless, this technique is not capable to melt the treated area and operates at a temperature significantly lower than the melting point of the manufactured materials. Thus, although the discussed technique is a revolutionary process for welding and joining, it is not suitable for processes such as surface alloying, cladding, etc. [4].

The methods of a surface treatment by high energy fluxes (HEFs), which are a part of the additive technologies, are intensively used for formation of surface alloys, as well as for modification of the surface structure of different materials. Their main advantage is the precise control of the energy input, which alloys the controlling of the structure and properties of the treated materials. Furthermore, in comparison to traditional manufacturing, some benefits of the additive technologies can be mentioned [5]:

- The use of high energy fluxes alloys manufacturing at comparatively low cost in comparison to the traditional processes.
- Single tools can be fabricated in much shorter time by using high energy flux technologies in comparison to the traditional methods.
- Materials and other products with a complex geometry can be manufactured by additive techniques, while using traditional technologies, many different parts have to be manufactured separately and after that assembled.
- High energy fluxes are useful for a surface modification and hardening and allow design changes of the surfaces. The application of the traditional technologies for these purposes is too expensive and time ineffective for the discussed purposes.

The processes used for surface manufacturing of the materials are treatment by fluxes of photons (laser radiation) or accelerated electrons (electron beam). During this process, the manufactured material is irradiated by electron or laser beam. When the flux of the photons or accelerated electrons interacts with the treated surface, the work-piece is heated and forms thermal distribution from the surface to the bulk [6–9]. After the irradiation, the sample rapidly cools down. The processes of fast heating and cooling reflect to structural transformations, changes in the chemical composition, melting of the surface, etc. According to the maximum temperature of the heating, several processes can be defined: (i) When, during the heating, the temperature is lower than the melting point of the treated specimen, the material remains in solid-state condition, but some phase and structural transformations may occur. Such technological conditions are widely used for a surface hardening of the materials [10]. (ii) When the maximum temperature is higher than the melting point of the specimen and, in the same time, lower than the boiling point, the material becomes in liquid phase condition. Such techniques are used for alloying and cladding processes [11–13]. (iii) When the temperature is higher than the boiling point of the material, the treated material is partially evaporated. Such technologies are used for a deposition of coatings (electron beam evaporation, laser deposition, etc.), laser ablation, in the field of a laser drilling [13–15].

Currently, the additive manufacturing techniques are considered for different aerospace applications, such as on-orbit constructions of space structures, a manufacturing of small multifunctional systems for astronauts for fabrication of spare parts, etc. Applying these techniques in the space, the typical pressure is up to 10^{-17} mbar. This means that for electron beam processing a vacuum chamber and the equipment are not necessary and the process can be realized directly in the space environment [5]. Also, the discussed techniques are widely used in the field of automotive and aircraft industries for manufacturing of different components and tools, for the needs of the modern medicine, for biomedical applications, and many more [5].

This chapter aims to summarize the topics related to the application of a surface treatment by high energy fluxes (i.e., electron beams and laser beams) for developing of new multifunctional materials, as well as to modify their surface properties. We present and discuss the methods and techniques for development and improvement of advanced materials by means of alloying, cladding, and hardening via electron and laser beams.

2. Technological parameters

For both types of techniques (i.e., electron and laser beam), the beam power and power density are of the important process parameters. In the case of laser beam, it can be set directly, while for e-beam it is a product of the accelerating voltage and the beam current. For example, typical values for the accelerating voltage are from 50 to 150 kV. With an increase of the beam power, the kinetic energy of the electrons also increases, which causes an increase in the penetration depth of the beam. The beam power density is an important parameter for the alloying operation since it affects the forces acting in the molten material [16].

The speed of the specimen motion during the process is also a basic parameter. As a result of this movement, the heat is transferred to the volume of the material. It is responsible for the heating and cooling rate as well as for the solidification speed. With an increase of the speed of the specimen motion, the heat input decreases. The beam power and the speed of the specimen motion are responsible for the volume of the manufactured zone, the thickness, and the width [5].

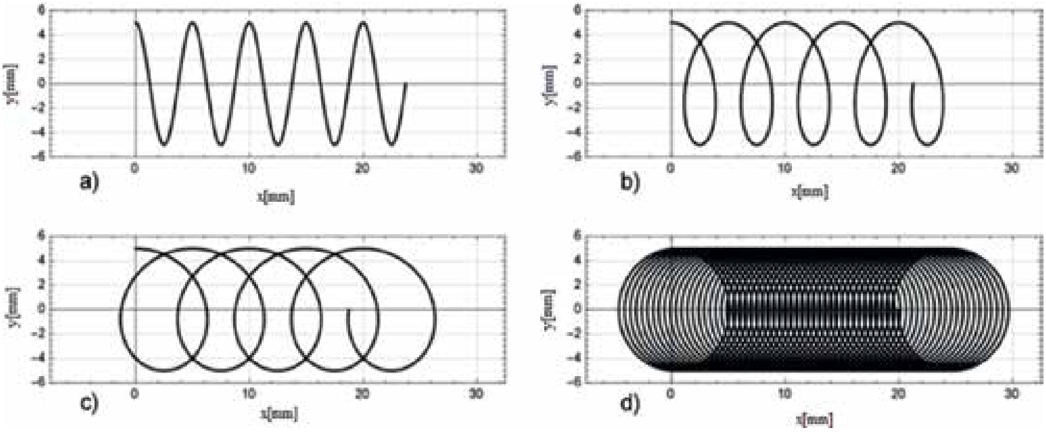

Figure 1. Different types of scanning electron beam: (a) sinusoidal dithering; (b) ellipsoidal rotating; (c) circular rotating with higher specimen movement velocity; and (d) circular rotating with slower specimen movement velocity (the figure is drawn by the authors).

The application of the electron beam for additive manufacturing has a major advantage in comparison to the laser beam, namely beam deflection. Since the electrons are charged particles, they can be deflected from the normal axis by application of electrical and electromagnetic fields. This allows a realization of different scanning approaches which affects the solidification processes and can control further the processes occurring during the abovementioned operations. For example, when applying the e-beam techniques, a scanning can be realized using regime of circular geometry. In this case, the trajectory of the beam is overlapping and maintaining the lifetime of the melt pool further. This is important for the alloying operation since the alloying elements can be distributed significantly more homogeneous [17]. Possible electron beam scanning geometries are shown in **Figure 1**.

Another difference between electron and laser beam processes is the working pressure. When applying electron beam technique, high vacuum state is absolutely required. The presence of some atoms and gas molecules on the way of the beam can result in loss of its power due to absorption and electron scattering. Typically, the pressure should be at least 5×10^{-4} mbar or lower. The laser beam processes are usually realized in atmospheric medium. In order to prevent oxidation of the manufactured area, argon is blown over the surface of the manufactured material [16, 18].

3. Heat processes

As already mentioned, the work-piece is heated on the surface and form thermal distribution. The rapid heating and cooling lead to structural transformations, changes in the chemical composition, melting the surface, etc., and therefore the rate of these processes is of major importance. There exist experimental and numerical approaches to examine the temperature field and, thus, the rates of heating and cooling, which will give us information related to the final microstructure and functional properties of the treated material. The experimental methods are time- and effort-consuming, and the results are not always reliable. For that reason, the numerical approaches are more appropriate and widely used for evaluating the thermal field and modeling the thermal processes. The heat transfer equation for the case of treatment by high energy fluxes (i.e., electron and laser beams) can be described for homogeneous and isotropic material whose thermophysical properties are temperature-independent from the following field equation of heat conduction [19–22]:

$$\frac{1}{\alpha}\frac{\partial T}{\partial t}-\nabla^2 T=\frac{f(r,t)}{\lambda} \tag{1}$$

Here, $\alpha=\frac{\lambda}{c\rho}$ is the thermal diffusivity; λ is the thermal conductivity, c is the specific heat, and ρ is the density of the specimen.

The solution *T(r,t)* of Eq. (1) for the case of three-dimensional transient, nonhomogeneous heat conduction problems can be expressed by three-dimensional Green's function:

$$T(r,t)=\frac{k}{\lambda}\int\limits_{\tau=0}^{t}d\tau\int\limits_{R}G(r,t|r',t)f(r',\tau)dv'+\int\limits_{R}G(r,t|r',\tau)\bigg|_{\tau=0}F(r')dv' \tag{2}$$

where *F(r′)* describes the initial temperature distribution. In orthogonal coordinates, the Green's function can be written as follows:

$$G(x,y,z,t|x',y',z',\tau)=G1(x,t|x',\tau)\times G2(y,t|y',\tau)\times G3(z,t|z',\tau) \tag{3}$$

In Eq. (3), each of the Green's functions (i.e., G1, G2, and G3) depends on the boundary conditions and the regions (i.e., finite, semi-infinite, or infinite). For the case of infinite region, the Green's function is the following:

$$G(x,t|x',\tau)=[4\pi\alpha(t-\tau)]^{-1/2}\exp\left(-\frac{(x-x')^2}{4\alpha(t-\tau)}\right), \tag{4}$$

and for semi-infinite, when the boundary is at z′ = 0, the Green's function is:

$$G(z,t|z',t)=[4\pi\alpha(t-\tau)]^{-1/2}\left[\exp\left(-\frac{(z-z')^2}{4\alpha(t-\tau)}\right)+\exp\left(-\frac{(z+z')^2}{4\alpha(t-\tau)}\right)\right] \tag{5}$$

By substituting G1(x,t|x′,τ) and G2(y,t|y′,τ) from Eq.(4) and G3(z,t|z′,τ) from Eq.(5) in Eq.(3), we obtain:

$$G(x,y,z,t|x',y',z'=0,\tau)=2[4\pi\alpha(t-\tau)]^{-1.5}\times\exp\left(-\frac{(x-x')^2+(y-y')^2+z^2}{4\alpha(t-\tau)}\right) \tag{6}$$

By substituting *x′ = x-r.cosθ and y′ = y-r.sinθ* and *G(r,t|r′,τ)* from Eq.(6) in Eq.(2), the distribution of the temperature is the following:

$$T(x,y,z,t) = T_0 + \frac{2\alpha}{\lambda}\int_0^t\int_{-\pi}^{\pi}\int_0^{\infty}\left[f(x-r\cos\theta, y-r\sin\theta,\tau)\times[4\pi\alpha(t-\tau)]^{-1.5}\times exp\left(-\frac{r^2+z^2}{4\alpha(t-\tau)}\right)\right] \times rdrd\theta d\tau \quad (7)$$

Here, t is the time of temperature calculating, r and θ are the polar coordinates. In Eq. (7), *f(x-r. cosθ,y-r.sinθ)* is the beam intensity distribution. For a beam with Gaussian distribution which moves along a straight line, the beam intensity is:

$$f(x-r\cos\theta, y-r\sin\theta,\tau) = \frac{3Q}{\pi r_0^2}\times\exp\left\{-3\left(\frac{(x--r\cos\theta-v\tau)^2+(y-r\sin\theta)^2}{r_0^2}\right)\right\} \quad (8)$$

In Eq. (8), r_0 is the beam radius, Q is the power transferred to the irradiated material, and *v* is the speed of the beam along moving line. For a dithering beam, the intensity distribution is the following:

$$f(x-r\cos\theta, y-r\sin\theta,\tau) = \frac{3Q}{\pi r_0^2}\exp\left(-3\frac{(x-\ \cos\theta-v\tau)^2+\left(y-r\sin\theta-l_{max}\cos\left(\frac{2\pi\tau}{\tau^*}\right)\right)^2}{r_0^2}\right) \quad (9)$$

where l_{max} is the amplitude and τ^* is the period for each cycle. In the case of rotating beam, the beam intensity is the following:

$$f(x-r\cos\theta, y-r\sin\theta,\tau) = \frac{3Q}{\pi r_0^2}\times\exp\left\{-3\left(\frac{\left(x-r\cos\theta-v\tau-a\sin\left(\frac{2\pi\tau}{\tau^*}\right)\right)^2+\left(y-r\sin\theta-l_{max}\cos\left(\frac{2\pi\tau}{\tau^*}\right)\right)^2}{r_0^2}\right)\right\} \quad (10)$$

In Eq. (10), *a* is the diameter of the rotation along the moving line.

4. Characteristics of the HEFs processes

The processes of surface modification of metals and alloys by using HEFs can be roughly divided into two groups depending on whether the HEFs act on the material in a solid (**Figure 2a**) or a liquid (**Figure 2b**) phase. Both types of techniques have found practical applications. In recent years, and in view of developing novel materials, the alloying with HEFs processing techniques has been widely used [5]. These techniques include additional alloying in the zone treated, which has a significant effect on the physical and mechanical properties of the materials processed [7–9].

4.1. Cladding and alloying

Cladding techniques are used for a coating of a substrate by different materials in order to improve the functional properties of the surface. It can be realized by two different approaches:

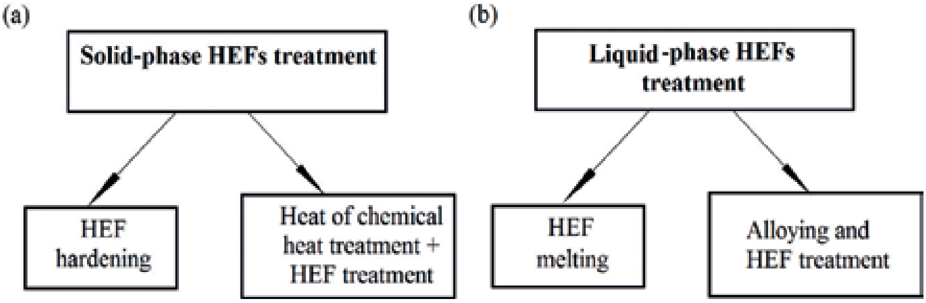

Figure 2. (a) Solid-state HEF processing of metals and alloys; (b) HEF melting and processing of metals and alloys (the figure is drawn by the authors).

by a deposition of a coating material on the substrate and subsequent treatment by laser or electron beam and by direct injection of the coating material into the melt pool. **Figure 3a** shows the cladding technique.

In the case of preliminary deposition of the coating, material is applied on the coated substrate in the form of slurry consisting of powder of the coating material mixed with a binder. The material is melted together with a thin layer of the surface substrate, and after the subsequent solidification, a clad track is formed [23]. However, this approach (a deposition of a coating material on the substrate and subsequent treatment by high energy flux) presents some drawbacks: the application of a slurry powder is taking too much time; it is too difficult to deposit a uniform film on complex surfaces. Also, this approach presents significantly lower productivity and high cost in comparison to direct injection of the coating material into the melt pool [24]. At the direct injection of the coating material, the clad track rises above the surface of the coated substrate. The injected alloying material is usually in the form of powder or wire. According to the authors of [25], at a constant beam power and scanning speed (i.e., scanned distance per second), the main parameter is the powder feed rate. Low powder feed rates correspond to lower input energy needed for melting of the incoming powder. This means that

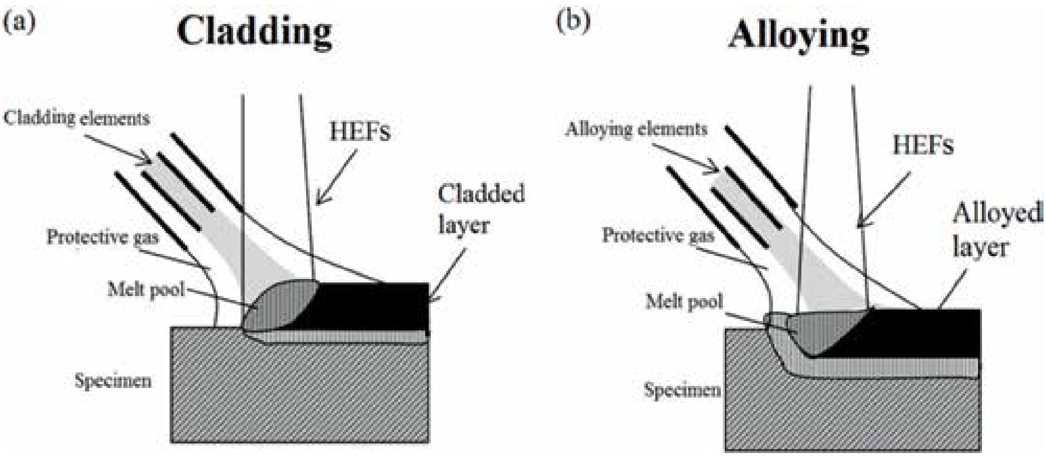

Figure 3. (a) Cladding; (b) alloying by HEFs (the figure is drawn by the authors).

the melt depth of the substrate is too high, which corresponds to low built-up material on the surface and low contact angle between the substrate surface and the tangent to the track surface at the contact edge (α) (**Figure 4**).

With an increase of the powder feed rate, the input energy needed for melting of the incoming powder also increases and the melt depth of the surface decreases. The clad height and angle α increase as well. After passing a certain value of the powder feed rate and α, the cladded material loses adherence and porosity between the tracks can be formed due to the shadowing of the substrate. The angle α is a good indicator for the quality of the cladded material. The optimal values for α are in the range from 45 to 80° [25]. By overlapping of the clad tracks, a large area can be coated. Important merits of the cladded coatings are the good adhesion between the coating and the substrate, low porosity, and absence of cracking. The typical thicknesses of the coatings formed by cladding technique are in the range from 0.5 mm to 5 mm.

For realizing of alloying mechanism (**Figure 3b**), the manufactured parts are treated by high energy fluxes and built by melting the surface, forming a melt pool. The melt pool is formed due to the energy input of the flux on the manufactured part. During the melting of the surface of the manufactured part, the alloying elements are simultaneously added into the melt pool in the form of powder or wire or are deposited onto the surface as a layer with uniform thickness. Interdiffusion processes between the substrate and the alloying elements occur. The melt pool solidifies rapidly, and after the solidification, the surface alloy is formed [6–9, 12]. The distribution of the alloying elements is based on the Marangoni convection which is caused by the high temperature gradient in the melt pool [26–28]. The influence of the convection on the homogenization process is evaluated by the surface tension number, which is given in Eq. (11):

$$S = \frac{\left(\frac{d\sigma}{dT}\right) qd}{\mu u_0 k} \tag{11}$$

In Eq. (11), S is the surface tension number; dσ/dT is the temperature coefficient of the surface tension; q is the net heat flow; d is the diameter of the beam; μ is the viscosity; u_0 is the

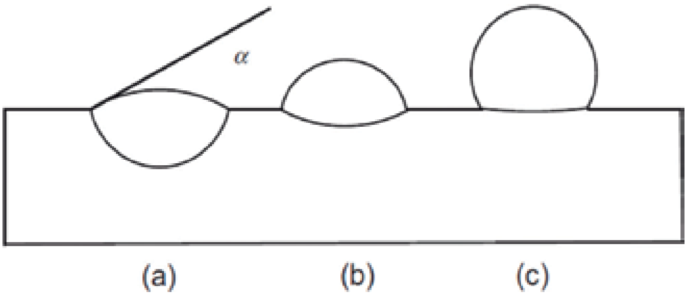

Figure 4. Cross section of cladding tracks: (a) low powder feed rate; (b) optimal powder feed rate; (c) high powder feed rate [24].

scanning speed; and k is the thermal conductivity. When the value of the surface tension number is low ($S \leq 45{,}000$ [27]), the convection is negligible and the melt homogenization will be too slow. For high values of the surface tension number, the convection takes a leading role in the transport mechanism of the melt pool. In this case, the convection speed in high, as this leads to extremely fast homogenization. Therefore, in order to obtain homogeneous surface alloys with attractive functional properties, it is very important to optimize the technological parameters, included in Eq. (1), and the amount of the alloying elements. To achieve the required characteristics of the surface alloys, the dimension and lifetime of the melt pool should be controlled accurately and kept stable during the alloying process.

4.2. Hardening

Beside for alloying and cladding technologies, the high energy fluxes are often used for a surface hardening of the materials (**Figure 5a** and **b**).

The purpose of such techniques is to increase the hardness and wear resistance of the materials as a result of the processes occurring during the heating and cooling. The hardening is a technological process, in which the metals and alloys are heated to a certain temperature, followed by a rapid cooling which results in formation of metastable structures as well as finer microstructure, leading to an increase in the hardness and wear resistance [29–34]. The high cooling rate required for the structural transformations occurring during the self-quenching process strongly depends on the thermophysical properties of the hardened material. This hardening technique has received attention only in the metallurgical industry since it offers the advantages of low hardening distortion and low energy consumption. The application of a hardening by means of high energy fluxes provides the metallurgist an additional option to conventional hardening techniques [29].

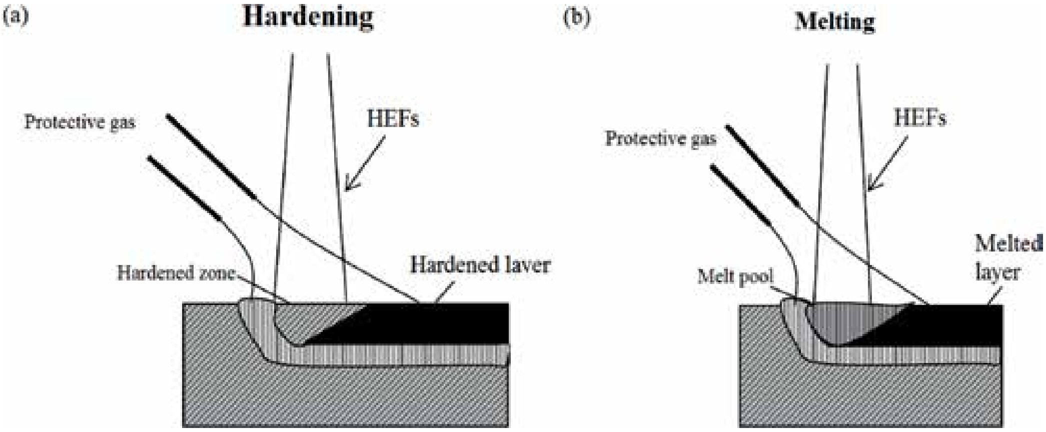

Figure 5. Surface hardening is (a) solid and (b) liquid HEFs treatment.

5. Overview of the processes

5.1. Alloying

As already mentioned, the alloying processes are based on the melting of the surface of the alloyed material and applying alloying elements into the melt pool which are dissolved into the matrix of the based material and forming surface alloys. The alloying material can be applied previously in the form of coatings by means of other techniques (e.g., magnetron sputtering, plasma spraying, etc.) or can be incorporated into the melt pool directly in the form of a powder stream or wire.

The high energy fluxes alloying techniques are widely used for fabrication of materials for the needs of the automotive and aerospace industries, for manufacturing of railway cars, space crafts, light ships, etc. Such materials are aluminum alloys due to their attractive mechanical properties and light weight. Alloying of pure aluminum with different transition metals by means of high energy fluxes is among the most promising methods for fabrication of surface alloys and for improvement of the surface properties of the materials. For that reason, many researchers are working on the formation and characterization of surface alloys by high energy fluxes.

The alloying of titanium and titanium alloys is a subject of investigations for many scientists due to the application of these materials in the field of the contemporary aviation and automotive industries, for different biomedical applications and many more.

The authors of [35] have studied a laser alloying of Ti-Si compound coating on Ti6Al4V in order to improve the bioactivity. They have reported that the microhardness increases dramatically after the alloying process. Also, the corrosion resistance of laser-alloyed Si coating is 27% improved in comparison to the base Ti6Al4V alloy. The evolution of the cell growth is the same for the case of Si alloyed layer and base Ti6Al4V materials on the first day, but in the progress, the cell growth starts to be faster on the laser-alloyed Si layer in comparison to the Ti6Al4V alloy.

Similarly, the authors of [36] have studied a laser alloying of titanium with boron and carbon. Their results show that the microstructure of the alloyed zone consists of a hard ceramic phases, namely, $TiB + TiB_2$, $TiB + TiB_2 + TiC$, or TiC. A significant increase in the hardness and wear resistance of all surface alloys has been observed in comparison to the commercially pure titanium.

As already mentioned, in addition to the laser alloying, the electron beams are also widely used for alloying processes. The authors of [37] have studied a cycling mixing of predeposited Al films onto Ti substrate by means of pulsed electron beam. The phase composition of the alloyed zone consists of TiAl and $TiAl_2$ phases. The measured nanohardness of the near-surface region is significantly greater in comparison to the base Ti substrate—11 GPa.

Similarly, Valkov et al. [38] have studied an electron beam surface alloying of pure Ti with Al films, and their results show that the alloyed zone consists of biphasic structure of Ti_3Al and TiAl, which is transformed in single phase structure of TiAl in depth. This transformation is accompanied by a decrease in the hardness from the surface to the depth. Also, Valkov and coauthors [39] have studied the conditions of alloying of pure Ti with Al and Nb and with Al and V. The results showed that the formation of an intermetallic surface alloy by means of electron beam alloying strongly depends on the input energy of the e-beam. The same authors [39] have claimed that the melting point of the materials plays a major role in the optimization of the technological parameters of a selective electron beam technology.

From the performed literature review, it is obvious that the modification of titanium with different transition metals by means of high intensity energy fluxes tends to a significant improvement in the functional properties of the discussed materials. As already mentioned, the modification of aluminum for improving of its operational characteristics is also a subject of investigations in the field of the modern materials science.

Lazarova et al. [40] have demonstrated a modification of the mechanical properties of pure Al by incorporation of TiCN nanopowder by means of electron beam alloying. Their results show that the alloyed zone has a thickness in the range of 14–33 μm and microhardness from 562 to 798 HV or the alloyed zone is 16–22 times harder than the base Al substrate.

The authors of [41] have studied the improvement in the surface properties of Al-Si cast alloy by means of laser beam surface alloying with Fe. Their results present an increase in the microhardness. Similarly, Almeida et al. [42] have studied laser beam surface alloying of Al with Cr using two-step process (alloying and remelting). The results show that an increase of the remelting speed points to an increase in the volume fraction of the intermetallic compound and the hardness, respectively. Almeida et al. [43–46] have studied an alloying of pure Al with Nb by means of laser alloying technique. The results obtained by the authors show that the distribution of the alloying element is not homogeneous and undissolved Nb particles surrounded by dendrites of Al_3Nb exist. However, the characteristics of the alloyed layers were greatly improved after a laser remelting. Most of the structural defects were eliminated, and undissolved Nb particles have not been observed. The manufactured laser beam surface alloys have been successfully formed with an Al_3Nb dendritic microstructure. The same authors [46] claimed that the microhardness increases with an increase of the scanning speed during the laser alloying technology. The reported microhardness changes from 480 to 650 HV with varying of the scanning speed from 5 to 40 mm/sec. Valkov et al. [47] have studied an alloying of pure aluminum with as-deposited Ti-Nb coatings by means of a scanning electron beam, and their results show that undissolved particles have not been observed after the alloying process, contrary to the case of laser beam alloying. The alloyed zone consists of $(Ti,Nb)Al_3$ intermetallic fractions randomly distributed in the biphasic structure of fine $(Ti,Nb)Al_3$ particles dispersed in the Al matrix. The increase of the speed of the specimen motion tends to more homogeneity distribution of the intermetallic phase in the soft Al matrix and much finer microstructure. Also, the measured microhardness reaches values of 775 HV and it does not depend on the speed of the specimen motion during the electron beam alloying process. Therefore, a significant difference between the properties and structure of the fabricated surface alloys by electron and laser beam exists. The authors of [48] have made a comparative study of electron and laser beam surface alloying of pure Al with Nb. The results reported in [48] have shown that the observed differences in the microstructure of the surface alloys formed by both techniques are explained by the different way of controlling the lifetime of the melt pool. The electron beam alloying technique can be realized in different geometries of scanning (circular, linear, etc.) since the electrons can be deflected and guided due to their nature of charged particles. When using circular scanning mode, the trajectory of the e-beam overlaps which points to longer lifetime of the melt pool. Using laser beam alloying technique, such technological conditions cannot be realized and the lifetime of the melt pool is significantly shorter [48]. The authors of [49, 50] have performed detailed investigations of the microstructure and the crystallographic structure of surface alloys fabricated by electron and laser beam alloying and explain the difference in the hardening mechanism of both kind of alloys. Vilar et al. [49] have studied the crystallographic structure of laser beam–manufactured surface alloys, and their results show that the increase of the scanning speed during the alloying process reflects to formation of a preferred crystallographic orientation while such effect of electron beam–fabricated surface alloys has not been observed [50]. According to the authors of [51, 52] the formation of a preferred crystallographic orientation can significantly affect the mechanical properties which, as mentioned in [50] can be a possible reason for the observed differences in the hardening mechanism of electron- and laser-processed surface alloys.

5.2. Cladding

The cladding technique is widely used for manufacturing of coatings for protective purposes, against adhesive wear (when two bodies with similar mechanical properties slide against each other) and abrasive wear (when hard particles or hard body slide against softer one). Such materials which can overcome these drawbacks are alloys in the system of Co-Cr-W-C due to their high strength and resistance to corrosion and wear at high temperatures [53]. These alloys are also known as stellites.

Such coatings have been applied by [54] using laser cladding of preplaced powder on stainless steel substrates, as the authors have studied the influence of the energy density of the laser beam on the degree of dilution. Their results show that an energy density of 6.4 kJ/cm^2 is needed to melt the powder and wet the substrate in order to form a good quality continuous track with less than 6% dilution. An increase in the energy density leads to significantly higher and inappropriate dilution of up to 27%. Lower energy density is capable to melt the powder without wetting the substrate. The authors of [55–57] have studied the formation of stellite coating on austenitic steel substrate as a function of the scanning speed which was in the range 1.67–167 mm/s. They have reported that coatings free of crack and pores with excellent adherence have been formed. The same authors have claimed that the microstructure of the coatings does not depend on the technological conditions of the cladding and becomes similar in the range of the scanning speed. However, the same authors [57] have mentioned that stellites can be applied without preheating of the substrate, but carbon-rich coatings have higher brittleness and are capable to crack. Therefore, the substrate must be preheated in order to avoid such defects.

The authors of [58] have studied an electron beam cladding of Cr_3C_2/Ni-Cr powder on steel substrates. The conditions for obtaining an increased thickness and modified area of still good surface layer have been investigated. The results show that the thickness and cladded area can be increased simply by increasing the number of formation passes and the beam oscillation amplitude. The measured hardness was 791 HV.

Similarly, Abe et al. [59] have studied WC12% Co- and Ni-base self-fluxing alloy powder with a mild steel substrate. Their results show good quality coatings with superior functional properties, including wear and corrosion resistance. The microhardness of the formed cladding layer reaches values of 1400 HV.

5.3. Hardening

As already mentioned, the hardening process by means of high energy fluxes is based on the irradiation of the hardened surface and formation of metastable structures as well as on the changes in the microstructure.

Such approach for improving of the functional properties of the materials has been used by the authors of [60]. They have analyzed the influence of the laser treatment of carbon steel on the changes of the microstructure and microhardness in depth. The results are compared with those obtained by conventional hardness, and it has been concluded that the laser treatment technique leads to 80% harder structure in comparison to the conventional processes. Similarly, Sarnet and coauthors [61] have conducted a surface treatment of alloyed steels by an excimer laser. As a result of the treatment, the microhardness increases with about 200%.

In study [62] the results of investigation of the electron beam surface modification of 5CrMoMn steel are shown. The beam current in the study has been varied from 6 to 8 mA with a step of 0.5 mA. The results show that surface properties of the modified specimens are greatest at a beam current of 7 mA. The microhardness reaches from 355 HV for the base material up to 656 HV and decreases with further increasing of the current above 7 mA due to the reduction of martensite and carbon content.

The authors of [63] have performed similar investigation. They have studied an electron beam surface hardening of 30CrMnSiA steel as the subject of discussion is the influence of the density of the input energy of the e-beam on the possibility of formation of hardened layers. The results show that the hardness increases dramatically, from 320 to 520 HV when the input energy density reaches a value of 1.857 kJ/cm^2. By further increasing the input energy, the hardness decreases because of the convective mixing of the melted zone, which effect becomes predominant after the discussed density of the input energy of the electron beam.

Also, electron beam surface hardening can be combined with other methods, such as physical vapor deposition [64], plasma nitriding [34, 65], etc. Grumbt et al. [64] have studied a duplex treatment $Ti_{1-x}Al_xN$ coatings with subsequent electron beam treatment of steel substrates. The results of study [64] show that the coating significantly enhanced the absorption properties, resulting to an increase in the hardened depth for the same parameters of the electron beam hardening process of coated and uncoated steel. Moreover, the hardened depth increases with an increase of Al content or the thickness of the coating. Also, it was demonstrated that the electron beam hardening of previously coated steel substrates is capable to form significantly harder surfaces in comparison to uncoated materials.

The authors of [34, 65] have studied an electron beam surface hardening of previously nitrogen-alloyed steel. Their results show a significant increase in the microhardness as well as double improvement of the wear resistance. The authors of the discussed studies [34, 65] claimed that the reasons of these improvements of the functional properties are the refined microstructure consisting of α-solid solution (nitrous martensite) and γ-solid solution (nitrous austenite) and dispersed fine nitride precipitates. Ormanova et al. [22] have presented a combined method for surface modification of tool steels, consisting of electron beam hardening followed by plasma nitriding and subsequent electron beam hardening, and the results demonstrate a hardness of 760 HV after the electron beam treatment and plasma hardening. The application of additional electron beam treatment process tends to a slight decrease in the hardness due to structural transformation and reduction of the amount of N atoms.

6. Summary

The current state of the surface manufacturing of the materials by means of high energy fluxes (electron and laser beams), including surface alloying, cladding, and hardening, has been discussed in the present book chapter. The presented data are based on our own experience as well as on the available studies in the literature. The various applications of the high energy fluxes in the field of the surface manufacturing were demonstrated with a focus on the relationship between the technological processes and the properties. It was shown that the electron and laser beams have a number of benefits as a small comparison between both techniques is provided at the discussions of each surface manufacturing process.

The area of future developments of the surface manufacturing by means of high energy fluxes will be concentrated on the optimization of the techniques, processes as well as modeling and simulations. Considering the fact that the number of the machines for high energy fluxes manufacturing, installed in the industry, extensively grows, these technologies should be rapidly incorporated in the wide range of the industry, such as aerospace, automotive, railway, biomedicine, etc.

Up to now, the materials which are extensively treated and manufactured by high energy fluxes are the steels as well as small amount of other high-performance materials, such as titanium aluminides. It can be concluded that the state of research on the applications of high energy fluxes in the field of the surface manufacturing processes is well developed and extensively introduced for different industrial applications.

Acknowledgements

The authors acknowledge the financial support of project DFNP-17-1 "Selective electron-beam surface treatment of light metals" under the Assistance for Young Scientist program of the Bulgarian Academy of Sciences.

Conflict of interest

The authors have no conflict of interest to declare.

Author details

Stefan Valkov*, Maria Ormanova and Peter Petrov

*Address all correspondence to: stsvalkov@gmail.com

Academician Emil Djakov Institute of Electronics, Bulgarian Academy of Sciences, Sofia, Bulgaria

References

[1] Todd R, Allen D, Alting L. Manufacturing Processes Reference Guide. 1st ed. New York, USA: Industrial Press Inc; 1994

[2] Jameson E. Electrical Discharge Machining. Society of Manufacturing Engineers, Dearborn, MI, USA; 2001

[3] Herzog D, Seyda V, Wycisk E, Emmelmann C. Additive manufacturing of metals. Acta Materialia. 2016;**117**:371-392

[4] Hehr A, Dapino M. Dynamics of ultrasonic additive manufacturing. Ultrasonics. 2017;**73**: 49-66

[5] Weglowski M. Electron beam rapid prototyping using wires and modification of the surface. In: Srivatsan T, Sudarshan T, Manigandan K, editors. Manufacturing Techniques for Materials: Engineering and Engineered. 1st ed. Boca Ration, FL, USA: Taylor and Francis Group; 2018. pp. 133-160

[6] Draper C, Poate J. Laser surface alloying. International Metal Reviews. 1985;**30**:85-108

[7] Petrov P. Surface modification of aluminium alloys using high intensity beams. In: Proc. NATO Advanced Study Institute. Advanced Light Alloys and Composites. Vol. 59. Zakopane: Kluwer Academic Publishers; 1998. pp. 501-505

[8] Petrov P, Dimitroff D. Electron beam treatment of aluminium alloys. In: Sossenheimer E, Eichorn F, editors. In: Proceeding of the International Beam Technologies Conference; Karlsruhe. Dusseldorf: Deutscher Verband fur Schweisstechnik; 1991. pp. 178-181

[9] Petrov P. Electron beam surface remelting and alloying of aluminium alloys. Vacuum. 1997;**48**:49-50

[10] Kou S, Sun D, Le Y. A fundamental study of laser transformation hardening. Metallurgical Transactions A. 1983;**14**:643-653

[11] Vilar R. Laser cladding. Journal of Laser Applications. 1999;**11**:64-79

[12] Vilar R. Laser alloying and laser cladding. Materials Science Forum. 1999;**301**:229-252

[13] Mackwood A, Crafer R. Thermal modeling of laser welding and related processes: A literature review. Optics and Laser Technology. 2005;**37**:99-115

[14] Hügel H, Dausinger F, Bloehs W, Grünenwald B. Basic coupling mechanisms in laser surface treatment. In: Mazumder J, Conte O, Vilar R, Steen W, editors. Laser Processing: Surface Treatment and Film Deposition. Dordrecht: Kluwer Academic Publishers; 1996. pp. 21-46

[15] Wang Z, Zhang Z. Electron beam evaporation deposition. In: Lin Y, Chen X, editors. Advanced Nano Deposition Methods. Wiley-VCH Verlag GmbH & Co. KGaA; 2016. pp. 33-58

[16] Schultz H. Electron Beam Welding. Cambridge: Abington Publishing; 1993

[17] Weglowski M, Błacha S, Phillips A. Electron beam welding—Techniques and trends—Review. Vacuum. 2016;**130**:72-92

[18] Lawler S, Clark D, Punshon C, Bagshaw N, Disney C, Powers J. Local vacuum electron beam welding for pressure vessel applications. Ironmaking & Steelmaking. 2015;**42**(10): 722-726

[19] Beck J, Haji-Sheikh A, Litkouhi B. Heat Conduction Using Greens Functions. 2nd ed. Boca Ration, FL, USA: Taylor & Francis; 2011

[20] Farrahi G, Sistaninia M. Thermal analysis of laser hardening for different moving patterns. IJE Transactions A: Basics. 2009;**22**(2):169-180

[21] Ormanova M, Angelov V, Petrov P. Investigation of thermal processes at electron-beam surface modification by means of scanning electron beam. Journal of Physics: Conference Series. 2016;**700**:012033

[22] Ormanova M, Petrov P, Kovacheva D. Electron beam surface treatment of tool steel. Vacuum. 2017;**135**:7-12

[23] Steen W, Courtney C. Hardfacing of nimonic 75 using 2 kW continuous wave CO_2 laser. Metals Technology. 1980;**7**:232-237

[24] Vilar R, Almeida A. Laser surface treatment of biomedical alloys. In: Vilar R, editor. Laser Surface Modification of Biomaterials: Techniques and Applications. Elsevier Ltd; 2016. pp. 35-75

[25] Weerasinghe V, Steen W. Laser cladding with pneumatic powder delivery. In: Soares O, Perez-Amor M, editors. Applied Laser Tooling. Dordrecht: Martinus Nijhoff Publishers; 1987. pp. 183-212

[26] Anthony T, Cline H. Surface rippling induced by surface-tension gradients during laser surface melting and alloying. Journal of Applied Physics. 1977;**48**:3888-3894

[27] Chan C, Mazumder J, Chen M. A two-dimensional transient model for convection in laser melted pool. Cambridge, MA, USA: Metallurgical Transactions A. 1984;**15**:2175-2184

[28] Chande T, Mazumder J. Two-dimensional, transient model for mass transport in laser surface alloying. Journal of Applied Physics. 1985;**57**:2226

[29] Gissler W, Jehn H, editors. Advanced Techniques for Surface Engineering. Dordrecht: Kluwer; 1992

[30] Iordanova I, Antonov V, Gurkovsky S. Changes of microstructure and mechanical properties of cold-rolled low carbon steel due to its surface treatment by Nd:glass pulsed laser. Surface and Coatings Technology. 2002;**153**:267-275

[31] Petrov P, Mladenov G. Theoretical analysis of heat flow and structural changes during electron beam irradiation of steel. Vacuum. 1991;**42**:29-32

[32] Petrov P, Dimitroff D. A computer modeling of surface electron beam transformation hardening. In: Proceedings of the 6th International Conference on Welding and Melting by Electron and Laser Beams, Toulon; 1998. pp. 101-108

[33] Petrov P. Optimization of carbon steel electron-beam hardening. Journal of Physics: Conference Series. 2010;**223**:012029

[34] Petrov P, Dimitrov D, Aprakova M, Valkanov S. Surface hardening of alloy steels using a high intensity electron beam. Materials and Manufacturing Processes. 1998;**13**:555-564

[35] Wu Y, Wang A, Zhang Z, Zheng R, Xia H, Wang Y. Laser alloying of Ti–Si compound coating on Ti–6Al–4V alloy for the improvement of bioactivity. Applied Surface Science. 2014;**305**:16-23

[36] Makuch N, Kulka M, Dziarski P, Przestacki D. Laser surface alloying of commercially pure titanium with boron and carbon. Optics and Lasers in Engineering. 2014;**57**:64-81

[37] Mei X, Fu J, Li X, Rotshtein V, Koval N, Ma T. Surface alloying of Al films/Ti substrate based on high-current pulsed electron beams irradiation. Rare Metals. 2013;**33**:155-160

[38] Valkov S, Neov D, Luytov D, Petrov P. Neutron diffraction of titanium aluminides formed by continuous electron-beam treatment. Journal of Physics: Conference Series. 2016;**700**: 012034

[39] Valkov S, Bezdushnyi R, Petrov P. Study of the influence of vanadium and niobium on the structure of Ti-Al-V and Ti-Al-Nb alloys formed by selective electron beam alloying. Journal of Physics: Conference Series. 2018;**992**:012053

[40] Lazarova R, Dimitrova R, Murdjieva Y, Valkov S, Petrov P. Layers obtained on aluminum by nanopowder deposition and subsequent electron beam scanning. Materials and Manufacturing Processes. 2018;**33**:1128-1132

[41] Pierantoni M, Wagniere J, Blank E. Improvement in the surface properties of Al-Si cast alloys by laser surface alloying. Materials Science and Engineering A. 1989;**110**:L17-L21

[42] Almeida A, Carvalho P, Vilar R. Microstructural study of Al-Cr alloys synthesised by laser alloying. SciFed Journal of Metallurgical Science. 2017;**1**:1-12

[43] Petrov P, Vilar R, Almeida A. Laser surface alloying of Al with Nb. In: Surface Modification Technologies: Proc. 8th Int. Conf. Surface Modification Technologies. Nice: The Institute of Materials; 1995. pp. 346-353

[44] Petrov P, Vilar R, Almeida A. Microstructures and properties of Al-Nb alloys produced by laser surface treatment. In: Laser Processing: Surface Treatment and Film Deposition, Proc. Seminar NATO Advanced Study Institute. Sesimbra. North Andover, MA, USA: Kluwer Academic Publishers; 1996. pp. 565-573

[45] Petrov P, Vilar R, Almeida A. A study of the mechanism of laser surface alloying aluminium with niobium. Proceedings of SPIE. 1996;**3052**:357-363

[46] Almeida A, Petrov P, Nogueira I, Vilar R. Structure and properties of Al–Nb alloys produced by laser surface alloying. Materials Science and Engineering A. 2001;**303**:273-280

[47] Valkov S, Petrov P, Lazarova R, Bezdushnyi R, Dechev D. Formation and characterization of Al-Ti-Nb alloys by electron-beam surface alloying. Applied Surface Science. 2016;**389**: 768-774

[48] Valkov S, Petrov P, Lazarova R. Comparative study of electron and laser beam surface alloying. Proceedings of SPIE. 2017;**10226**:102260I

[49] Vilar R, Conde O, Franco S. Crystallographic structure of Al_3Nb in laser-processed Al-Nb alloys. Intermetallics. 1999;**7**:1227-1233

[50] Valkov S, Neov D, Bezdushnyi R, Beskrovnyi A, Kozlenko D, Petrov P. Study of the microstructure, crystallographic structure and thermal stability of Al–Ti–Nb alloys produced by selective electron beam alloying. Journal of Surface Investigation: X-Ray, Synchrotron and Neutron Techniques. 2018;**12**:436-441

[51] Abbaschian R, Abbaschian L, Reed-Hill R. Physical Metallurgy Principles. 4th ed. Stamford, CT, USA: CL Engineering; 2008

[52] Askeland D, Haddleton F, Green P, Robertson H. The Science and Engineering of Materials. 3rd ed. US: Springer; 1996

[53] Antony K. Wear-resistant cobalt-base alloys. Journal of Metals. 1983;**35**:52-60

[54] Liu C, Humphreys M, Mason D. Effect of laser processing parameters on the formation and properties of a stellite hardfacing coating. Thin Solid Films. 1983;**107**:251-257

[55] Frenk A, Wagniere J. Laser cladding with cobalt-based hardfacing alloys. Journal de Physique IV. 1991;**01**:65-68

[56] Frenk A, Kurz W. High-speed laser cladding—Solidification conditions and microstructure of a cobalt-based alloy. Materials Science Engineering: A. 1993;**173**:339-342

[57] Frenk A, Kurz W. Microstructure formation in laser materials processing. Lasers in Engineering. 1992;**1**:193-212

[58] Morimoto J, Abe N, Kuriyama F, Tomie M. Formation of a Cr_3C_2/Ni–Cr alloy layer by an electron beam cladding method and evaluation of the layer properties. Vacuum. 2001;**62**: 203-210

[59] Abe N, Morimoto J, Tomie M, Doi C. Formation of WC-Co layers by an electron beam cladding method and evaluation of the layer properties. Vacuum. 2000;**59**:373-380

[60] Fernandez M, Fernandez E, Lique P, Cuetos J, Steel AISI. 1045: Superficial hardening by laser and tribological behaviour. In: Sudarshan TS, Jeandin M, Khor KA, editors. Surface Modification Technologies XI. London: The Institute of Materials; 1998

[61] Sarnet T, Nicolas G, Autric M. Excimer laser—Metals processing for mechanical properties improvement. In: Sudarshan TS, Jeandin M, Khor KA, editors. Surface Modification Technologies XI. London: The Institute of Materials; 1998

[62] Wei D, Wang X, Wang R, Cui H. Surface modification of 5CrMnMo steel with continuous scanning electron beam process. Vacuum. 2018;**149**:118-123

[63] Fu Y, Hu J, Shen X, Wang Y, Zhao W. Surface hardening of 30CrMnSiA steel using continuous electron beam. Nuclear Instruments and Methods in Physics Research, Section B: Beam Interactions with Materials and Atoms. 2017;**410**:207-214

[64] Grumbt G, Zenker R, Biermann H, Weigel K, Bewilogua K, Bräuer G. Duplex surface treatment–physical vapor deposition (PVD) and subsequent electron beam hardening (EBH). Advanced Engineering Materials. 2014;**16**:511-516

[65] Dimitrov D, Aprakova M, Valkanov S, Petrov P. Electron beam hardening of ion nitrided layers. Vacuum. 1998;**49**:239-246

Chapter 5

The Potential of Pyrolytic Biomass as a Sustainable Biofiller for Styrene-Butadiene Rubber

Yiran Fan and Geoff D. Fowler

Additional information is available at the end of the chapter

http://dx.doi.org/10.5772/intechopen.79994

Abstract

This chapter explains the significant potential of the pyrolytic biomass char for use as a sustainable carbon black replacement filler for rubber materials. The manufacture of rubber filler is not only energy-consuming, contributing significantly to global CO_2 emissions, but uses nonrenewable feedstock in production making it unsustainable. Ongoing work focused upon the development of carbonaceous rubber fillers based on coconut shell, a sustainable and renewable source, is presented in this chapter. A comparison between coconut char and commercial carbon black N772 demonstrates the profound potential of the pyrolytic coconut char to be used as filler. The char filler obtained was mixed with SBR and the resulting rubber product was evaluated for their technological performance, exhibiting high surface area and good tensile strength.

Keywords: rubber, reinforcing filler, carbon black, pyrolysis, biomass

1. Introduction

At present, it is seldom to see a rubber product using the polymer in an unfilled condition. Various materials are added during the rubber manufacture process. Carbon black is widely used as a rubber reinforcing filler from the third century B.C. in China. It is added to help to enhance the physical properties of the given rubber, such as hardness, tensile strength, and tear strength, etc. In 2015, the global production of carbon was about 13.9 million metric tons. It is indicated that by 2022, the production will reach 19.2 million metric tons [1]. There is no doubt that the cost of making carbon black will increase rapidly. As a result, the potential effect of the prediction may lead to an increasing demand of the fossil fuel hydrocarbon feedstock. On the other hand, the manufacture of carbon black is not only energy-intensive but also unsustainable in the long term as a feedstock due to the finite supply and the contribution to global warming.

Given the increasing pressure against using nonrenewable resources, it is essential to develop alternative materials to act as novel rubber fillers. Recently, several researches have been conducted focusing "green" fillers, which are based on the waste materials having potential "renewability" [2]. By using bio-based fillers, the dependence on fossil fuel would be improved and a sustainable material basis for rubber filler production could be established. In this chapter, the development of new type of fillers for rubber materials based on char produced during pyrolysis of biomass (coconut shell) is illustrated.

2. Rubber reinforcing filler: carbon black

Over the past century, the importance of rubber to human society has been paid more and more attentions. Several types of particulate fillers have been applied in rubber industry for different purposes, which are based on reinforcement, low material cost, and processing ease. The presence of fillers is key to achieve durable products, increase strength, and prolong life. The modulus of elasticity which is a measure of stiffness of the given materials can also be improved by fillers. Currently, carbon black is the most widely used particulate fillers, which has the ability to bond with the elastomer component enhancing the strength of vulcanized rubbers more than 10-fold as well as imparting durability to the materials [3]. Due to the incomplete combustion of fossil-origin hydrocarbon fuels during the carbon black manufacture, the process has a considerable carbon footprint. About 2.4 tons of CO_2 are estimated to be emitted per ton of carbon black, which compares to 0.8 tons of CO_2 per ton of cement for cement manufacture [4, 5].

Carbon black is usually present as types of aggregates. According to the TEM graph, its structure can be defined as partly graphitic. More graphitic structure can be observed from the outer layers than from center. Although carbon black particle aggregates are reported to work as a unit in the rubber matrix, its reinforcement ability is not determined by the aggregate units but by each individual particle within the unit. With the particle size decrease, the dispersion ability of carbon black, as well as the interface extension, can be improved, resulting in good reinforcement ability [6, 7].

Particle size, the morphology of aggregates, and the microstructure offered by carbon black can be considered as the key properties contributing to the reinforcement of elastomers. Furthermore, the surface of carbon black and its structural organization, surface area, and its chemical composition are also important. The development of a large polymer-filler interface is highly expected. The upper limit of useful specific surface area for significant reinforcement can reach 300–400 m^2/cm^3, and is determined by considerations of dispersibility, processability of the unvulcanized mix, and serious loss of rubbery characteristics of the composite [8, 9].

The surface area of carbon black is an important morphological characteristic for reinforcing. It indicates how much available surface can be accessed by rubber molecules for the interaction between the rubber and the filler surface. It is necessary to note that meso- and macropores seem to play the decisive role on the surface unlike micropores for the application of activated carbon. Since the rubber polymer chains are much larger than the micropores, the polymer cannot access these pores.

The research of the reinforcement mechanism offered by carbon black has been widely undertaken since 1960s [10]. It is widely known that the vulcanization process can only achieve resilient properties with little strength. Then, the strength properties need to be introduced by the addition of "reinforcement" fillers. After carbon blacks are added to the rubber compound, several changes occur: (1) an increase in modulus, or stress at a particular strain, (2) an increase in elongation at break for vulcanizates having a given degree of cross-linking, and (3) consequently, an increase in tensile strength [10, 11]. The improvement of stiffness and the physical properties such as tear resistance, tensile strength, and abrasion resistance are regarded as the crucial contribution of carbon black. The reinforcing ability of a filler can be demonstrated in **Figure 1**; the only difference between two SBR vulcanizates is the presence or absence of 50phr carbon black N220 in the recipe. With the addition of carbon black N220, the stress-strain curve shows a sharp rise, almost 10-fold compared with the unfilled rubber.

Large amount of literatures report about the reinforcement properties of carbon black for decades. So far, there are more than eight postulations have been wieldy applied to explain the reinforcement mechanisms, which are given in **Table 1**.

Due to the increasing price of natural rubber and other compounding ingredients, there are several concerns about the ongoing use of nonrenewable resources based carbon black feedstock.

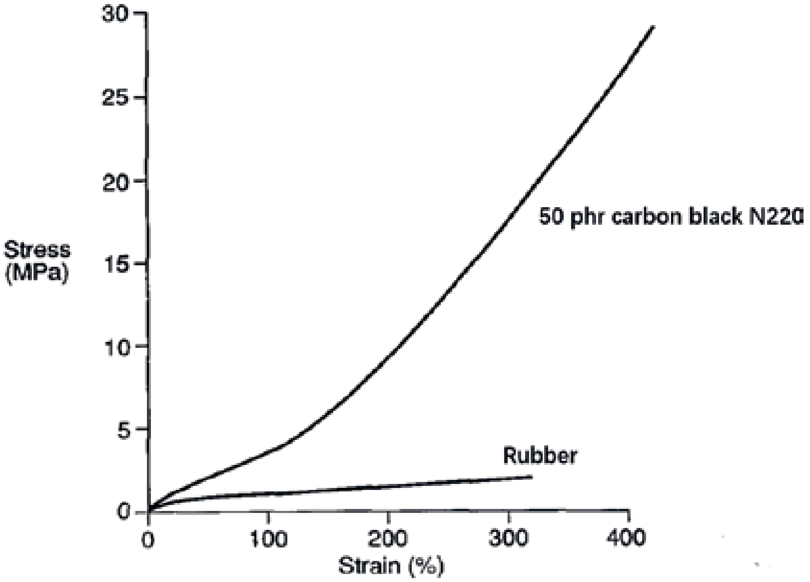

Figure 1. Comparison between filled and unfilled rubber matrix [11, 12]. (Rubber: SBR 1502, 100; zinc oxide, 3; stearic acid, 1.5; Santoflex 13, 0.5; Santoflex 77, 0.5; Sundex 8125, 3; DPG, 0.3; Santousure NS, 1.2; Sulfur, 2. Press cure: 40 min at 153°C. Same formulation with addition of 50 phr N220 carbon black).

Theories on filled elastomer	Summary	References
Small particle size	The reinforcement mechanism is attributed to an interfacial effect consequent upon small particle size. Any finely divided solid material that can be dispersed in the polymeric matrix will reinforce rubber compounds.	[12–14]
Slippage at interface	Stress can be redistributed by the slippage of molecular chains, and then helps prevent the molecular rupture. The frictional heat occurring during the relative motion between rubber molecular chains and filler can help release the strain energy so that hysteresis can be seen in the matrix instead of breakup.	[15, 16]
Chemical reaction	Functional groups on the surface of carbon black are most likely subjected to a variety of inter- and intramolecular interactions. Acid/base reaction and hydrogen bonding are probably the main reactions that may occur between the rubber matrix and the carbon black.	[17–19]
Stored energy function	Use thermodynamic concepts to study the relationship between stress and strain. The order and disorder of system correlate to the extension of the molecular chains.	[20–23]
Hydrodynamic theory	Rigid fillers typically increase the stiffness of the elastomer. The presence of the rigid fillers lead to local strains, which is greater than globally applied strains.	[24–26]
Strain amplification	Modifications to hydrodynamic model at high strains.	[19, 27, 28]
Model of weak and strong linkage	The filled rubber can be regarded to be made of strong and weak linkages. Different weak linkages can be broken by different stresses contributing to softening.	[28, 29]
The Bueche model	The fillers are connected with the molecular network chains within a filled rubber.	[30, 31]

Table 1. Eight postulations of carbon black reinforcement mechanisms [11].

Material	Short summary	References
Chicken eggshell	The eggshell calcium carbonate filled epoxidized natural rubber showed superior vulcanization characteristics (higher maximum torque and cure rate index, lower cure time, and scorch time), higher tensile properties, and lower tension set value.	[32]
Fly ash	Fly ash (up to 60 phr) can be used as a nonreinforcing filler for ESBR compounds, where abrasion resistance is not significantly required. The 300% modulus values remained unchanged with increasing loading.	[34]
Soy spent flakes	The soy spent flakes can partially replace carbon black as the reinforcement cofiller in rubber composites. The elasticity of the cofiller network structure is close to that of carbon black-filled composites.	[35]
Lignin	Reinforcing properties of lignin as filler in nitrile rubber can be improved on suitable chemical treatment for good thermal stability.	[36]
Pyrolytic tire	Chars obtained from pyrolytic tire can be successfully reused as semireinforcing fillers in rubber formulations. The physical and mechanical properties of the rubber filled with pyrolytic tire were found to be comparable to rubber containing N772 and with N772 and silica.	[4]
Waste newsprint fibers	The sodium silicate and magnesium chloride treated newsprint fiber waste at 40phr can improve the electrical and mechanical properties of the rubber composite.	[37]
Marble sludge with carbon black	Marble sludge can be used as a cofiller with carbon black in natural rubber. High tensile strength, modulus, tear strength, and hardness can be achieved.	[38]

Table 2. Novel rubber filler from green feedstock [11].

On one hand, the price of carbon black feedstock witnesses a gradual increase every year. On the other hand, severe environmental problems have been caused by the nondegradability feedstock of carbon black. Consequently, many researches have been conducted in the rubber industry to develop fillers derived from biodegradable waste feedstock, by which transforming its sourcing to a sustainable material basis. Their recyclability and utilization has become a major driving factor in their acceptance and employability, as well as low cost and abundant availability. This new class of carbon black-like feedstock includes natural sources (e.g., natural fibers), industrial by-products (e.g., saw dust, rice husk, coconut shell), and even industrial waste material (e.g., rice husk ash). This field is very attractive from both the ecological and economic point of view, since it could enable rejected material to become valuable material, which could be reused in industry [32, 33]. Some of the popular green feedstocks of novel rubber filler have been summarized in **Table 2**.

3. Process description

3.1. Feedstock and reference material

3.1.1. Feedstock: coconut shell

As a single and simple genus species, coconut is grown around the world sharing similar properties. In order to make the experiments standardized, after being crushed into to small pieces (less than 10 mm) by a laboratory-scale hammer miller (Glen Creston, UK), the small pieces of coconut shell were then dried at 105°C to constant weight, to reduce the moisture content (**Figure 2**).

3.1.2. Reference material: carbon black N772

Carbon black N772 belongs to low to semidispersion, middle-active grades of carbon black, which has the largest particle size and lowest structural and surface area among the whole

Figure 2. Dried coconut shell [11].

range of carbon black. N772 provides high elasticity, low heat-up, good aging-resistance, and superior dynamic performance to the technical rubber products or tire frames.

3.2. Pyrolysis process

Pyrolysis is a thermal treatment with limited oxygen by which organic materials are chemically decomposed by heat. It is a promising method by using waste materials such as biomass as feedstock to convert waste into energy and other valuable products. During the pyrolysis, large molecules break down into small molecules, resulting in carbonaceous materials, combustible gases, and condensable liquid hydrocarbons for renewable energy resources [39–42]. According to Sienkiewicz et al. [43], it is obvious that there is a significant potential of pyrolysis treatment based on ongoing works along with increasing cost of energy and petroleum and resources such as carbon black.

The pyrolysis of coconut shell was performed in a Carbolite 11/150 laboratory scale rotary furnace (Carbolite, Hope Valley, UK) situated in a walk-in fume cupboard. As shown in **Figure 3**, a rotatory horizontal tubular quartz vessel with the capacity of almost 5 liters is suspended by air-tight rotary fixtures inside an electrically heated box-furnace. According to several studies, the rotation rate is set as 10 ramp/min. The temperature is controlled at 600°C by the thermal system with a thermocouple in the box furnace. Nitrogen gas is introduced into the reaction vessel from the gas inlet ports at 550 ml/min flow rate [44]. The nitrogen flow maintaining in the vessel throughout the pyrolysis is to protect the char from oxidation and help to carry and remove the pyrolytic volatiles (oil and gas) toward the oil trap. At the same time, the noncondensable volatiles (gases) were vented from a small opening on the top of the oil trap to the fume cupboard.

3.3. Postpyrolysis grinding by wet TEMA milling

All the char samples after the pyrolysis were ground by wet TEMA milling using a vibratory disc mill (Tema Machinery Company Ltd., UK). Wet milling is used for the more intensive and efficient properties than dry grinding since it can break the char samples into finer

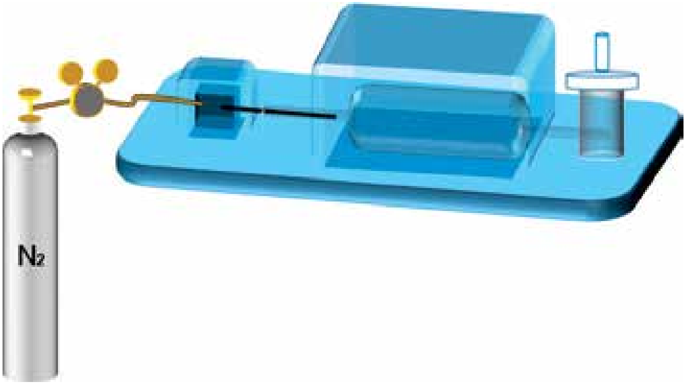

Figure 3. Illustration of rotary furnace.

particles in the micron and submicron (or nanometer) particle size. Moreover, it has been found that wet milling can cost-effectively create uniformly fine particles with limited or no contamination [45]. The optimum condition for wet TEMA milling was confirmed as 1:1 liquid and solid ratio, 1.5 min grinding time. After the milling process, the wet samples were dried at 105°C for 24 h until constant weight.

3.4. Char filler characterization

3.4.1. Textural characterization

Surface area of the samples were characterized by liquid nitrogen (at 77 K) adsorption and desorption method using the OMNISORP 100. The BET surface area can be calculated with the isotherms by using the Brunauer-Emmett-Teller equation [46]. The t-plot method was used to find the micropore volume and the combined macropore and mesopore surface area [47]. The significant surface areas were concluded from the difference between the BET surface area and the macropore and mesopore surface area and used to establish the relationship between pore size distribution and rubber uptake capacity of the fillers.

3.4.2. Toluene extraction

Toluene extraction of the char filler was test according to the ASTM D 1618-99 (Standard Test Method for Carbon Black Extractables—Transmittance of Toluene Extract) [48]. This method covers the measurement of the degree of toluene discoloration by carbon black extractables and is useful in controlling the reaction process for the production of carbon black.

3.4.3. pH value

Test Method A—Boiling Slurry of ASTM D1512-05 Standard Test Method for Carbon Black—pH value [49] was applied to obtain the pH value of the char filler. The pH value is very essential since it can affect the vulcanization of some rubber compounds.

3.4.4. Boehm titration

The oxygen surface groups on char filler were investigated by the Boehm titration [17]. This method is based on the principle that oxygen groups on surfaces have different acidities and can be neutralized by bases of different strengths. Sodium hydroxide (NaOH) is the strongest base generally used, and is assumed to neutralize all Brønsted acids, while sodium carbonate (Na_2CO_3) neutralizes carboxylic and lactonic groups and sodium bicarbonate ($NaHCO_3$) neutralizes carboxylic acids. The difference between the uptake of the bases can be used to quantify the oxygen surface groups on a char sample [50].

3.4.5. In-rubber testing

Styrene-butadiene rubber (SBR) is widely applied in tire treads. When protected by additives, excellent traction properties, good abrasion resistance, and good aging stability can be achieved [51]. It is reported that the most common use of SBR is in pneumatic tires with around 50% of car tires being made from a range of types of SBR. A widely used generic SBR

Ingredient	Parts per hundred of rubber
SBR 1502	100
Char filler	60
TDAE oil	10
Zinc oxide	5
Stearic acid	2
6PPD	1.5
TBBS	1.5
Sulfur	1.5

Table 3. SBR formulation [9, 11].

formulation is shown in **Table 3**, which was applied in the compounding process to investigate the performance of the char filler in rubber. Compounds were produced using a 60 cc Brabender mixer set at 40°C and 60 rpm.

The moving die rheometer (MDR) test was conducted based on ASTM D5289, at 160°C for 30 min. The results of the MDR were used to evaluate the cure characteristics of each compound and to allow preparation of cured sheet using a cure time of T90 + 5 min. Shore A hardness was tested according ASTM D2240. Tensile properties were determined following ASTM D412. A scanning electron microscopy (SEM) (Auriga Cross Beam, Zeiss) was applied to analyze the surface morphology of the char filler-filled rubber sample and to understand the mechanism of the char filler with the rubber matrix.

4. Results and discussion

4.1. Char characterization

The char yield, oil yield, and gas yield from the pyrolysis process are 31.6, 16.0 and 52.4%, respectively. The char yield is satisfying and encouraging in terms of the potential commercial opportunity for coconut shell to be used as a feedstock to produce a substitute carbon black. The oil yield and gas yield are both beneficial so that further implications of these two by-products have great potential.

Table 4 summarizes the transmittance of toluene extract (T%), pH value, BET surface area, T-plot surface area, and acidic groups and basic groups on the surface of both commercial carbon black N772 and the pyrolytic coconut char filler.

Toluene transmittance correlates to the amount of tarry or leachable contents in the carbon black as the leachable and unburned tarry or oil-residues on the surface of carbon black or the char can be dissolved into it. This is very important for potential applications, since the presence of a high leachable (oily) content may cause contamination during processing into rubber or other applications and present problems in the appearance and performance of the final rubber products. According to **Table 4**, the toluene transmittance of char fill is 99.95; it

	T%	pH value	BET surface area (m^2/g)	T-plot surface area (m^2/g)	Acidic groups (mmol/g)	Basic groups (mmol/g)
Char filler	99.95	9.70	373.3	315.89	0.062	0.316
CB N772	65.9	8.5	28.5	26.6	0	0.079

Table 4. Characterization of char filler and carbon black N772.

shows that the filler is quite clean and pure with little surface contamination. However, the carbon black N772 only has 65.9% of the T%, which indicates that a significant amount of leachable components exists indicating a limiting effect on the purposes.

It is widely known that pores on the surface of solids are classified into three size ranges: micropores (<2 nm width), mesopores (<2–<50 nm with), and macropores (>50 nm width). Normally, if the pores (micropores and small mesopores) are significantly smaller than the very large rubber polymer chains, then the polymer molecules cannot access to these pores. Therefore, unlike micropores present in activated carbon, meso- and macropores may play the decisive role on the filler surface. From **Table 4**, the area of all pores on N772 is 28.5 m^2/g and the area of meso- and macropores is 26.6 m^2/g. The results indicate that meso- and macropores occupied most of the surface area of carbon black, which reaffirms previous statements about the importance of these pores in carbon black's application in the rubber industry. The BET surface area of the char filler is 373.31 m^2/g, whereas the t-plot surface area is 315.86 m^2/g, which follows the same trend with N772. Moreover, the surface areas are much greater than N772. These data further support the assertion that char samples can be used as an alternative rubber filler.

The pH value of the char surface has been recognized as a foundation of the reinforcing ability of the fillers. It is reported that basic materials may accelerate vulcanization reactions, while acidic ones may delay the vulcanization time of a rubber compound [17, 48]. According to the above, a solution pH value close to 9 makes N772 suitable filler for a wide range of application with reasonable vulcanization time and ideal amount of free radicals. The pH value of the char sample was close to 9, which also supports the proposition that coconut shell could be a promising feedstock for rubber fillers. The surface chemical groups on the surface of char filler are much more plentiful than the carbon black N772, which makes char surface more active resulting in a better interaction and reinforcement from coconut shell char.

4.2. In-rubber characterization

The cure and physical properties of the rubber compounds filler with the two fillers assessed by the moving die rheometer (MDR) test are summarized in **Table 5**. At the beginning, a mixture is heated in the cavity of the rheometer under pressure. Then, the viscosity decreases

	Min (dNm)	Max (dNm)	Ts2 (mm:ss)	T90 (mm:ss)	Shore A (°)	M100% (Mpa)	M300% (Mpa)	Tensile strength (Mpa)	Elongation at break (%)
Char filler	1.16	14.42	7.04	13.48	59	1.99	2.82	5.68	653
CB N772	1.23	13.66	4.33	9.19	57	1.63	9.3	20.4	586

Table 5. Rheology and physical data of coconut shell char and N772.

and the torque exerted on the rotor drops. The lowest torque value is called moment lowest (ML), which can be used to study the stiffness of the uncured rubber compound at a given temperature, noted as "Min" in **Table 5**. After the curing process begins, the torque rises. When the torque increases 2 dNm unit above ML value, the time is recorded as Ts2. It tells about the moment the curing process actually starts. With the curing progressing, the torque

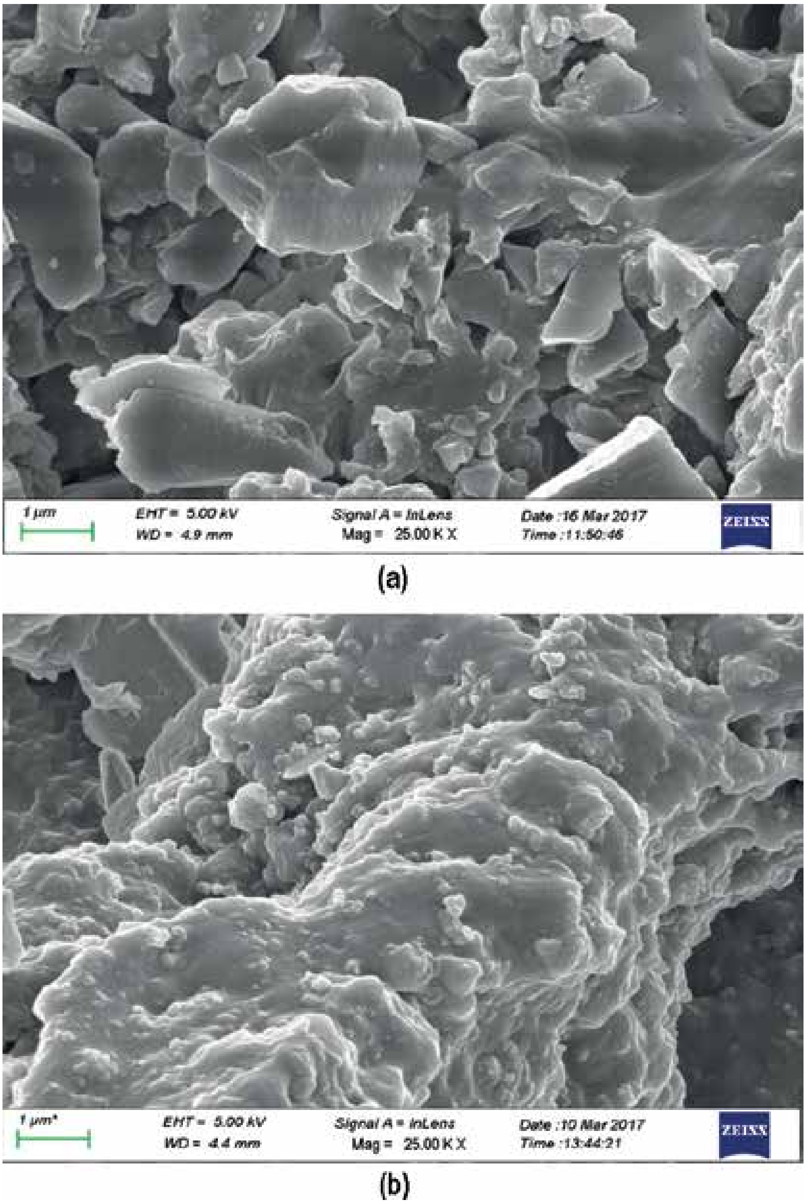

Figure 4. SEM plots of compounded rubber sheets at 25 K magnification, illustrating rubber-filler bonding system [11]. (a) SEM plot of Run 20 filled rubber sheet. (b) SEM plot of N660 filled rubber sheet.

continues increasing. After some time, the torque reaches the maximum value and a plateau appears. The highest torque is regarded as moment highest (MH), also noted as "Max" in **Table 5**. The time from the beginning of the test to the point where 90% of the MH value attained is called T90. The hardness of the filled rubber compound is tested by the Shore A with degree unit according to the ASTM D2240 standard. The M100 and M300% are the stresses required to produce an elongation of 100 and 300% of the test sample. The maximum tensile stress recorded in extending the test piece to a breaking point is shown as tensile strength; and the elongation at break is the tensile strain in the test length at breaking point [11, 52].

According to **Table 5**, the time to onset of cure (Ts2) and cure times (T90) of the coconut char filled SBR were comparable but slightly longer than conventional carbon black N772. Different surface chemistry may be the reason, since it may have some interactions with the cure package. The hardness value was slightly high than N772, also indicating that coconut shell has the potential to be used as the parent material of rubber filler. The M100% values are found to be higher than the commercial carbon black. The low tensile strength and high elongation to break values imply that there are low filler-polymer interactions and structure levels, allowing for chain slippage over the filler surface, which can be enhanced through modification of the rubber mix formulation [9]. Based on this data, the sample can be considered as a semi- to low-reinforcing filler with broadly similar cure characteristics to conventional carbon black.

The SEM plots of coconut char compounded rubber sheet and N660 (which behaves better in the rubber matrix than N772) filled rubber sheet at 25 K magnification are shown in **Figure 4**. According to the images that base layer is the rubber matrix, the small particles on the surface are fillers (char filler and N660). It can be seen from the images, the fillers are unevenly attached to the surface of the rubber, indicating that the mechanism of the interaction between char filler and rubber is similar to conventional carbon black. Particle shapes, sizes, and its distribution are the main differences between coconut char and commercial carbon black. Smaller aggregate size and more uniform size distribution of carbon black plus spheroid particles may be helpful during the vulcanization process leading to good reinforcement.

5. Conclusion

Coconut shell, as a high-volume problematic waste material, has the potential to be successfully converted into a high-quality carbon black-like char filler, and high heat value, renewable energy materials (mainly oil and some gases) at relatively small scale. Thus, global fossil fuel-derived emissions can be reduced by the help of the ability of biochar to sequester the carbon contained in the coconut shell by conversion into a stable and nonavailable form. This type of process has been regarded as popular sector with growth potential in the global carbon market with a controllable, clean, and simple manufacturing process.

High external surface area values (315.89 m^2/g), along with high levels of purity (99.95%) and suitable surface pH (9.70), can be achieved by the coconut shell char filler. The char filler produced was comparable on a physicochemical basis with the commercial semireinforcing carbon black N772. Since most of the performance testing of the rubber products was highly comparable, the semireinforcing carbon black can be partially replaced by the coconut char filler. If the level of filler-polymer interaction can be enhanced, while the current level of filler-filler interactions maintained, the char filler would have very interesting properties with regard to low energy losses, such as tire rolling resistance. Further surface modification for the char filler has been identified as a part of post-production process for further optimization, such as filler-rubber interaction. At the same time, since coconut shell char is a new type of rubber filler, the vulcanization and mixing process needs to be to be investigated for further improvement for short cure time and good tensile strength.

Acknowledgements

I would like to thank Imperial College London for the support of this research. I would like to express my gratitude to Dr. Geoff Fowler, Dr. Chris Norris, and the Avon Rubber (Artis UK) for their technical advice and help for rubber analysis. Finally, I would like to thank the Chinese Postdoctoral Science Foundation for the support.

Author details

Yiran Fan* and Geoff D. Fowler

*Address all correspondence to: yf612@mail.tsinghua.edu.cn

Department of Civil and Environmental Engineering, Imperial College London, UK

References

[1] Industry Experts. Carbon Black—A Global Market Overview. 2016. Available from: http://www.authorstream.com/Presentation/industryexperts-2711012-cp024-carbon-black-global-market-overview/ [Accessed: Jul 6, 2018]

[2] Chaudhary D, Jollands M, Cser F. Recycling rice hull ash: A filler material for polymeric composites? Advances in Polymer Technology. 2004;**23**(2):147-155. DOI: 10.1002/adv.20000

[3] Li Z, Zhang J, Chen S. Effects of carbon blacks with various structures on vulcanization and reinforcement of filled ethylene-propylene-diene rubber. Express Polymer Letters. 2008;**2**(10):695-704. DOI: 10.3144/expresspolymlett.2008.83

[4] Athanassiades E. Waste tyre pyrolysis: Sustainable recovery and reuse of a valuable resource [PhD thesis]. UK: Imperial College London; 2013

[5] International Energy Agency (IEA). Tracking Industrial Energy Efficiency and CO_2 Emissions. 2007. Available from: https://www.iea.org/publications/freepublications/publication/tracking_emissions.pdf [Accessed: Aug 3, 2017]

[6] Orion Engineered Carbons (OEC). What is Carbon Black. 2015. Available from: https://www.thecarycompany.com/media/pdf/specs/orion-what-is-carbon-black.pdf [Accessed: Jul 7, 2017]

[7] Donnet J, Bansal RC, Wang M-J. Carbon Black: Science and Technology. 2nd ed. (revised and expanded ed.) ed. New York: Dekker; 1993

[8] Maya KS. Studies on in situ precipitated silica filled rubber composites with special reference to NR, NBR and SBR [PhD thesis]. India: Cochin University of Science and Technology; 2007

[9] Fan Y, Fowler GD, Norris C. Potential of a pyrolytic coconut shell as a sustainable biofiller for styrene-butadiene rubber. Industrial and Engineering Chemistry Research. 2017; **56**(16):4779-4791. DOI: 10.1021/acs.iecr.7b00405

[10] Mark EJ, Erman B, Eirich FR. Science and Technology of Rubber. 3rd ed. San Diego; London: Elsevier Academic Press; 2005. p. 368. DOI: 10.1016/B978-0-12-464786-2.X5000-7

[11] Fan Y. The development of novel sustainable carbonaceous materials as substitutes for carbon black in rubber-based products [PhD thesis]. UK: Imperial College London; 2017

[12] Edwards D. Polymer-filler interactions in rubber reinforcement. Journal of Materials Science. 1990;**25**(10):4175-4185. DOI: 10.1007/BF00581070

[13] Gent AN, Tompkins DA. Nucleation and growth of gas bubbles in elastomers. Journal of Applied Physics. 1969;**40**(6):2520-2525. DOI: 10.1063/1.1658026

[14] Schmidt E. Effect of colloidal noncarbon pigments on elastomer properties. Industrial & Engineering Chemistry Research. 1951;**43**(3):679-683. DOI: 10.1021/ac5010794

[15] Jha V. Carbon black filler reinforcement of elastomers [PhD thesis]. UK: University of London; 2008

[16] Dannenberg EM. Molecular slippage mechanism of reinforcement. Transactions of the Institution of the Rubber Industry. 1966;**42**:26

[17] Boehm HP. Some aspects of the surface chemistry of carbon blacks and other carbons. Carbon. 1994;**32**(5):759-769. DOI: 10.1016/0008-6223(94)90031-0

[18] Mark EJ, Erman B, Roland CM. The Science and Technology of Rubber. 4th ed. Waltham: Academic Press; 2013

[19] Bueche F. Molecular basis for the mullins effect. Journal of Applied Polymer Science. 1960; **4**(10):107-114. DOI: 10.1002/app.1960.070041017

[20] Treloar LRG. The statistical length of paraffin molecules. Proceedings of the Physical Society. 1943;**55**(5):345-361

[21] Rivlin RS. In: Eirich FR, editor. Rheology. New York: Academic Press; 1956

[22] Mooney M. A theory of large elastic deformation. Journal of Applied Physics. 1940;**11**(9): 582-592. DOI: 10.1063/1.1712836

[23] Gent A, Hwang N. Internal failures in model elastomeric composites. Journal of Materials Science. 1990;**25**(12):4981-4986. DOI: 10.1007/BF00580117

[24] Guth E, Gold O. On the hydrodynamical theory of the viscosity of suspensions. Physical Review. 1938;**53**:322

[25] Guth E. Theory of Filler Reinforcement. Journal of Applied Physics. 1945;**16**(1):20-25. DOI: 10.1063/1.1707495

[26] Payne A. The dynamic properties of carbon black-loaded natural rubber vulcanizates. Part I. Journal of Applied Polymer Science. 1962;**6**(19):57-63. DOI: 10.1002/app.1962.070061906

[27] Mullins L, Tobin N. Stress softening in rubber vulcanizates. Part I. Use of a strain amplification factor to describe the elastic behavior of filler-reinforced vulcanized rubber. Journal of Applied Polymer Science. 1965;**9**(9):2993-3009. DOI: 10.1002/app.1965.070090906

[28] Blanchard A, Parkinson D. Breakage of carbon-rubber networks by applied stress. Industrial & Engineering Chemistry Research. 1952;**44**(4):799-812. DOI: 10.1021/acs.jpca.5b04889

[29] Blanchard AF, Parkinson D. Structures in rubber reinforced by carbon black. In: Second Rubber Technology Conference; Cambridge. New York: Rubber Age; 1948

[30] Bueche F. Mullins effect and rubber-filler interaction. Journal of Applied Polymer Science. 1961;**5**(15):271-281. DOI: 10.1002/app.1961.070051504

[31] Bueche F. In: Kraus G, editor. Reinforcement of Elastomer. New York: Wiley; 1965

[32] Intharapat P, Kongnoo A, Kateungngan K. The potential of chicken eggshell waste as a bio-filler filled epoxidized natural rubber (ENR) composite and its properties. Journal of Polymers and the Environment. 2013;**21**(1):245-258. DOI: 10.1007/s10924-012-0475-9

[33] Gopalan Nair K, Dufresne A. Crab shell chitin whisker reinforced natural rubber nanocomposites. 2. Mechanical behaviour. Biomacromolecules. 2003;**4**(3):666-674. DOI: 10.1021/bm02 01284

[34] Dasgupta M, Kar S, Gupta SD, Mukhopadhyay R, Bandyopadhyay A. Effect of fly ash as filler in rubber—A comprehensive study of the vulcanisate properties of styrene butadiene rubber compounds. Progress in Rubber, Plastics and Recycling Technology. 2013; **29**(3):151-168

[35] Jong L. Effect of soy spent flakes and carbon black co-filler in rubber composites. Composites: Part A Applied Science and Manufacturing. 2007;**38**(2):252-264. DOI: 10.1016/j.compositesa.2006.05.003

[36] Setua D, Shukla M, Nigam V, Singh H, Mathur G. Lignin reinforced rubber composites. Polymer Composites. 2010;**21**(6):988-995. DOI: 10.1002/pc.10252

[37] Nashar D, Abd-El-Messieh S, Basta A. Newsprint paper waste as a fiber reinforcement in rubber composites. Journal of Applied Polymer Science. 2004;**91**(1):469-478. DOI: 10.1002/app.13726

[38] Ahmed K, Nizami SS, Raza NZ. Characteristics of natural rubber hybrid composites based on marble sludge/carbon black and marble sludge/rice husk derived silica. Journal of Industrial and Engineering Chemistry. 2012;**19**(4):1169-1176. DOI: 10.1016/j.jiec.2012.12.014

[39] Mohan DU, Pittman CH Jr, Steele P. Pyrolysis of wood/biomass for bio-oil: A critical review. Energy & Fuels. 2006;**20**(3):848-889. DOI: 10.1021/ef0502397

[40] Roy C, Unsworth J. Pilot plant demonstration of used tyres vacuum pyrolysis. In: Ferrero GL, Maniatis K, Buckens A, Bridgewater AV, editors. Pyrolysis and Gasification. London: Elsevier Applied Science; 1989. pp. 180-189

[41] Cunliffe AM, Williams PT. Properties of chars and activated carbons derived from the pyrolysis of used tyres. Environmental Technology. 1998;**19**(12):1177-1190. DOI: 10.1080/09593331908616778

[42] Environment Agency. Life cycle assessment of the management options for waste tyres. In: Environment Agency R&D Report Ref. No. P1 437/TR. Bristol: Environment Agency; 2004

[43] Sienkiewicz M, Kucinska-Lipka J, Janik H, Balas A. Progress in used tyres management in the European Union: A review. Waste Management. 2012;**32**(10):1742-1751. DOI: 10.1016/j.wasman.2012.05.010

[44] Miguel SG. Activated carbon produced by pyrolysis and physical activation of waste tyres [PhD Thesis]. UK: Imperial College London; 1999

[45] Retsch. 2017. Available from: http://www.retsch.com/products/milling/disc-mills/rs-200/function-features [Accessed: Jul 7, 2017]

[46] Gregg SJ, Sing KSW. Adsorption, Surface Area and Porosity. London: Academic Press; 1982. DOI: 10.1149/1.2426447

[47] Do D. Adsorption Analysis: Equilibria and Kinetics (Series on Chemical Engineering; v. 2). London: Imperial College Press; 1998. DOI: 10.1142/9781860943829

[48] ASTM. Standard D1618-99 Standard Test Methods for Carbon Black Extractables-Transmittance of Toluene Extract. West Conshohocken: ASTM International; 2004. DOI: 10.1520/D1618-99R04

[49] ASTM. Standard D1512-05 Standard Test Methods for Carbon Black—pH Value. West Conshohocken: ASTM International; 2012. DOI: 10.1520/D1512-05R12

[50] Goertzen SL, Thériault KD, Oickle AM, Tarasuk AC, Andreas HA. Standardization of the Boehm titration. Part I. CO_2 expulsion and endpoint determination. Carbon. 2010;**48**(4):1252-1261. DOI: 10.1016/j.carbon.2009.11.050

[51] Rodgers B, Waddell W. The science of rubber compounding. In: Mark JE, Erman B, Eirich FR. (eds). Science and Technology of Rubber. 3rd ed. Burlington: Elsevier Academic Press; 2005. pp. 401-454. ISBN: 0-12-464786-3

[52] Saville BP. Physical Testing of Textiles. The Netherlands: Elsevier; 1999. pp. 116-118

Ultrafast Laser Inscription of Buried Waveguides in W-TCP Bioactive Eutectic Glasses

Daniel Sola and José I. Peña

Additional information is available at the end of the chapter

http://dx.doi.org/10.5772/intechopen.79577

Abstract

Since the first report of Davis in 1996, ultrafast laser inscription (ULI) has been widely used to fabricate buried optical devices such as active and passive waveguides inside dielectric materials. In this technique, ultra-short and ultra-intense laser pulses are tightly focused inside transparent materials leading to laser-induced nonlinear processes in the focal volume. The energy density deposited into the submicron focal volume can reach several of MJcm^{-3} and hence, may trigger dramatic changes in a strongly localized region, whereas the surrounding bulk material remains unchanged. This technique can be used from void formation to weak refractive index modification, which is the key feature to create buried optical waveguides. In this chapter, firstly, we review the fundamentals of the ultrafast laser inscription technique to produce optical waveguides inside dielectric materials such as crystals and glasses. Next, as an example, we revise the application of this technique to create buried waveguides inside bioactive glasses and specifically, inside W-TCP eutectic glasses.

Keywords: ultrafast laser inscription, optical waveguides, integrated photonic devices, rare earth-doped materials, neodymium, bioactive glass, eutectic glass

1. Introduction

Since its invention by T.H. Maiman in 1960, the laser interaction with matter has been successfully investigated to find and develop new applications in fundamental, applied, technological and industrial research [1]. Laser materials processing is a versatile tool for materials synthesis, modification and structuring involving in many cases multidisciplinary approaches. Laser technology has been studied in the search for novel applications in research fields such as optics, photonics, energy, microelectronics, aerospace and biomedicine [2–12].

The acronym "LASER" stands for "Light Amplification by Stimulated Emission of Radiation" and was first introduced in the late 1950s [13]. Essentially, a laser device is a resonator which emits coherent light originated in a stimulated emission process. A laser resonator or oscillator is usually made up of three main parts: a gain medium which amplifies light by stimulated emission, a pumping source to provide external energy to stimulate the atoms of the gain medium to its excited states, and an optical cavity which supplies feedback to the laser light. The resulting radiation, the laser light, has unique properties such as a high degree of temporal and spatial coherence, and low divergence which confers it of exceptional advantages compared to conventional light sources [14].

Along the last 50 years, laser technology has progressed based on the advances achieved in the development of new gain media, pumping sources and cavity design, leading to many different types of lasers. Attending to the gain medium, lasers can be classified as gas laser, chemical laser, excimer laser, solid-state laser, semiconductor laser, dye laser, free electron laser and metal-vapor laser. According to the laser operation wavelength, the classification can also be as ultraviolet (UV) laser, visible and infrared (IR) laser. In particular, for an operation wavelength between 700 nm and 2 μm, the laser is referred as near-infrared (NIR) laser. Also, the classification can be carried out attending to the operation mode; continuous wave (cw) and pulsed lasers [14]. The output power of a cw laser is constant, whereas for a pulsed laser, the power varies pulse-by-pulse. In this latter case, the pulse energy, E_p, and the peak power, P_p, can be calculated as:

$$E_p = {}^{P_{out}}/_{f} \tag{1}$$

$$P_p = {}^{E_p}/_{\Delta t} \tag{2}$$

where P_{out} is the output power, f is the repetition rate and Δt the pulse duration. Therefore, an appropriate combination of both repetition rate and pulse duration may allow pulsed lasers to achieve peak powers much higher than cw lasers. To date, the peak power that a pulsed laser can reach is in the range of a Petawatt with extremely high intensities, in the order of 10^{19} Wcm^{-2}, much higher than the atomic unit of intensity (3.5 10^{16} Wcm^{-2}). Hence, ultrashort pulsed lasers have recently attracted scientist's attention aiming at developing novel applications in fields such as biochemistry, spectroscopy, medicine, photonics and telecommunications due to the unique properties of the interaction between ultrashort laser pulses and matter [2–4, 14].

After the demonstration of laser action in the ruby laser by Maiman in 1960, for which pumped flash lamp produced a burst of spikes, each several nanoseconds long, that lasted several hundred microseconds, scientists focused their efforts in developing pulsed laser systems with shorter pulse duration. Q-switching was successfully applied in the early 1960s to produce single pulses 10 nanoseconds long [15]. Next, mode-locking technique was first introduced in 1964 for which pulse duration was reduced to 100 picoseconds [16], and by 1981, pulse duration had been reduced down to 100 femtoseconds using the colliding-pulse mode-locking technique [17]. Sub-6 femtosecond pulses were achieved improving passive-mode-locking and dispersion compensation [18–20].

Mode-locking is a technique in which a fixed or locked phase relationship between the longitudinal modes of the laser cavity is induced. The longitudinal modes are made to interfere with each other giving rise to the emission of a train of short pulses whose duration may range from few femtoseconds to several picoseconds [21]. The temporal separation between these pulses is the time that a pulse takes to complete one round trip in the resonator cavity. As the duration of a mode-locked laser pulse is very short, according to the time-bandwidth product, its spectrum consists of a broad wavelength range. Mode-locking technique can be active or passive. In active mode-locking, an external signal induces a modulation of the intra-cavity laser radiation by using acousto-optics modulators. Passive mode-locking is based on the introduction in the laser cavity of some elements such as saturable absorbers, dyes or solid-state media which induce self-modulation of the laser light. The most common mode-locked femtosecond lasers are the Ti:Sapphire femtosecond lasers based on the Kerr-Lens Mode-locking (KLM) mechanism, in which the Ti:Sapphire gain medium crystal placed inside the cavity acts as Kerr-effect medium [14, 21]. Nowadays, typical commercial femtosecond laser systems produce sub-100 femtoseconds.

2. Ultrafast laser inscription

The exceptional characteristics of femtosecond laser pulses have allowed the development of novel applications in the framework of femtosecond laser processing. In particular, the fabrication of two- and three-dimensional permanent structures inside transparent optical materials to be applied in the fields of optics, photonics and telecommunication as key elements such as waveguides, photonic crystals, diffraction gratings, beam splitters, and so on. Since the first report on femtosecond laser written waveguides in glass by Davis et al. [22], different types of integrated optical waveguides have been produced in a great diversity of transparent materials such as glasses, crystals, polycrystalline ceramics and polymers [23–44, 48–67].

In the ultrafast laser inscription (ULI) technique, femtosecond laser pulses are tightly focused beneath the surface. During the absorption process of ultrashort laser pulses, a high local spatial and temporal electronic and vibrational excitation densities are produced which together with the laser pulse duration, short compared to the relevant relaxation processes give rise to laser-induced nonlinear processes in the focal volume, such as two-photon or multiphoton absorption, inducing avalanche ionization in a very short time, leading to localized micro or sub-micrometric lattice damage, modifying the local refractive index and forming the so called "track" or "filament" [3].

The permanent refractive index change (Δn) induced in the focal volume has been found to be either positive or negative, depending on the processing parameters and the characteristics of the material. In addition to refractive index modification, a suitable configuration of the femtosecond laser pulses can be used to micromachine small areas by laser ablation or even to create nanovoids inside dielectric materials. The tight focalization in the focal spot can create extreme pressure and temperature conditions, with intensities significantly above the optical breakdown threshold and energy densities of several MJcm^{-3} into a submicron volume, several times higher than the strength of any material. This causes the solid to superheat yielding to the formation of a confined plasma, which explodes and generates a powerful shock wave that expands out of the focal volume and compresses the surrounding material, with pressures over 10 megabar (1 TPa) [45–47]. Therefore, an appropriate combination of the laser processing conditions in terms of numerical aperture (*NA*), diameter at the focal plane (*d*), laser wavelength (λ), pulse energy (E_p), pulse-width (Δt), repetition rate (*f*), and scanning speed (*V*) can be used to create a wide variety of laser-induced structures for waveguiding. Specifically, the energy delivered by the laser over each focal spot *d* is given by:

$$E_d = \frac{f \times d \times E_p}{V} \tag{3}$$

The repetition rate is a critical parameter since the accumulation of multiple laser pulses over the same point will result in a local temperature increase if the period between consecutive pulses (*1/f*) is shorter than the cooling time:

$$t = d^2/D \tag{4}$$

where D is the thermal diffusion coefficient. Thus, there is a critical repetition rate which determines two processing regimes; non-thermal and thermal regime for repetition rate lower and higher than the critical repetition rate [3]. For dielectric materials, thermal diffusivity is in the range of 10^{-3}cm^{2}s^{-1}. For a typical laser diameter at the focal plane of around 1 μm, the critical frequency ranges 100 kHz.

It is generally accepted the classification of waveguides structures into four categories according to the structure generated with the laser-induced filament [34]. In Type I waveguides, the laser beam generates a positive refractive index change, $\Delta n > 0$, directly in the irradiated area and the hence, the dimensions of the waveguide can be controlled by the amount of energy delivered on the focal volume. This type of waveguide can be induced in glasses since amorphous structure facilitates a positive refractive index change [3, 4, 23, 36, 37]. On the contrary, the mechanisms involved to be produced in crystals are complicated and entangled and hence, the type of refractive index change and the guiding axis cannot be envisaged. In addition, the damage created by the laser beam in the irradiated area gives rise to a non-desirable strong structural change of the material crystalline network. Furthermore, the waveguiding region is not stable with temperature, and the guidance is only supported in one polarization direction. Therefore, this type of waveguide has been reported in few crystalline materials such as $LiNbO_3$, ZnSe and $YCa_4O(BO_3)_3$ [35, 48–51].

In Type II or double-line configuration waveguides, the damage that can be produced by the laser beam in the focal volume is used to create a stress-induced region and a positive refractive index change between two close parallel tracks, normally between 15 and 30 μm. This type of configuration overcomes the drawbacks of Type I waveguide in crystalline materials so that waveguide structure is stable with temperature, the guidance can be achieved for both laser polarizations and in addition, preserves the luminescence of the bulk material.

Thus, this waveguide configuration has been widely applied in materials such as Nd:YAG, Nd:YVO_4, $LiNbO_3$, Yb:$KGd(WO_4)_2$, Yb:$KY(WO_4)_2$, and Nd:$Gd_3Ga_5O_{12}$ [29, 31, 38, 39, 50, 52, 53] and glasses [54–58].

The damage and the negative refractive index change originated by the ultra-intense and ultrashort laser radiation can be employed to surround a volume region of the bulk material. This is the origin of Type III or cladding waveguides for which the guiding core is adjusted and tailored by an appropriate position of the low-index tracks, placed few micrometers to each other to confine the light inside. The core diameter normally ranges between 25 and 150 μm so that it is possible the guidance of both monomode and multimode laser radiation for both TM and TE polarizations, from the visible to the IR region. These characteristics allow a better coupling to the waveguides, low propagation losses and a more efficient laser action in materials doped with Rare Earths (RE) [40–44, 59–62].

Finally, in Type IV, waveguide also referred as ridge waveguides, the ultra-high intensity achieved by the femtosecond laser pulses is used to ablate the surface to produce ridge waveguides on planar waveguide substrates obtained by other methods. Therefore, the guiding features strongly depend on the planar waveguide substrate [63–67].

In addition to the ULI technique, the fabrication of optical waveguides has also been reported by other processing routes. Among these techniques, it is worth noting ion exchange (IE), annealed proton exchange (APE), molecular beam epitaxy (MBE), liquid phase epitaxy (LPE), and sol-gel [68]. **Table 1** shows some examples of optical waveguides manufactured by these methods.

Nevertheless, when compared to these fabrication techniques, ULI has demonstrated to be a very powerful and robust technique due to its versatility, capable of manufacturing waveguides in a great variety of materials, from glasses to crystals, and flexible, allowing to inscribe a broad range of 3D structures and a large variety of waveguide configuration. Furthermore,

Material	Active ion	Fabrication technique	Reference
YAG	Nd^{3+}/Yb^{3+}	IE	[69]
BK7	Nd^{3+}	IE	[70]
$LiNbO_3$	Nd^{3+}	APE	[71]
$LiTaO_3$	Nd^{3+}	APE	[72]
LaF_3	Nd^{3+}	MBE	[73]
CaF_2	Er^{3+}	MBE	[74]
GGG	Nd^{3+}	LPE	[75]
$KY(WO_4)_2$	Tm^{3+}	LPE	[76]
Silicate glass	Er^{3+}	Sol-gel	[77]

Table 1. Some examples of optical waveguides manufactured by ion exchange (IE), annealed proton exchange (APE), molecular beam epitaxy (MBE), liquid phase epitaxy (LPE), and sol-gel techniques.

the fabrication of integrated photonic devices by ULI has shown to be cost-effective and efficient so that a suitable configuration of the processing parameters may lead to waveguide losses below 1 dB/cm, resulting in a low laser operation threshold.

3. Ultrashort laser interaction with dielectrics

The high power density, in the order of tens of TW/cm^2, achieved delivering laser pulses of few microjoules in short period of time, of few femtoseconds, focused beneath the surface in micron-sized areas, results in nonlinear interaction processes. Such high intensities may be manipulated to be employed for modifying the dielectric focal volume, inducing from weak refractive index changes to ultrahigh pressures which lead to void generation. These permanent structural modifications depend not only on the laser peak power but also on the focusing conditions, scanning speed, polarization and repetition rate.

The ultrashort laser-matter interaction process can be divided into three stages: generation of free carriers inside the material by non-linear processes such as multiphoton, tunnel ionization, or avalanche ionization, followed by energy relaxation processes and a subsequent modification of the material [3, 4]. The absorption process of ultrashort laser radiation for wide bandgap dielectric materials cannot be explained on the basis of linear absorption, since the photon energy of commonly used femtosecond laser pulses with wavelength between UV and NIR does not have sufficient energy to be linearly absorbed. On the contrary, multiphoton absorption can excite an electron from the valence to the conduction band as long as $m\hbar\omega > E_g$, where m is the smallest number of photons for which the overall energy surpasses the bandgap energy E_g. In addition, tunneling photoionization can also take place under an extremely strong laser electromagnetic field. This mechanism in dielectrics permits electron from the valence band to tunnel to the conduction band in a period of time shorter than the laser pulse. However, in most dielectric multiphoton, ionization dominates the excitation processes [78, 79]. On the other hand, laser photons can be sequentially absorbed by electrons excited in the conduction band by means of free carrier absorption. When the energy of an electron in the excited state exceeds the bandgap energy, the ionization of another electron from the valence band can take place, resulting in two excited electrons at the conduction band minimum. These electrons can be excited again by free carrier absorption processes, and more valence electrons can be produced by the same mechanism, leading to the electronic avalanche [3, 4]. The requirement for avalanche ionization is the existence of seed electrons in the conduction band, which can be provided by multiphoton or tunneling ionization or by thermally excited impurity or defect states.

Once the nonlinear photoionization and avalanche ionization create a free electron plasma, they transfer their energy to the lattice inducing three types of structural changes: a smooth refractive index modification for low pulse energies such as 100 nJ and 100 fs at 800 nm for 0.6 NA, a birefringent refractive index modification for pulse energies ranging 150–500 nJ and 100 fs at 800 nm for 0.6 NA, and microexplosions which result in void formation for pulse energies higher than 500 nJ and intensities greater than 100 TW/cm^2 [4, 78, 80], **Figure 1**. The

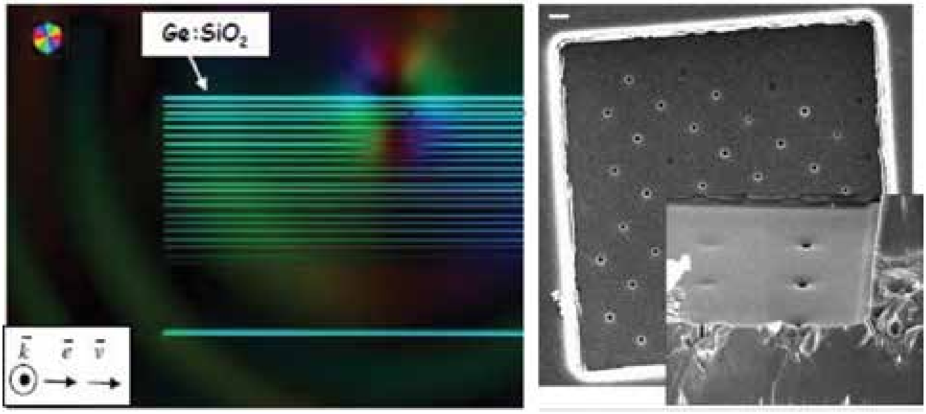

Figure 1. (Left) birefringence cartography in optical fiber Ge-doped preform core [80], and (right) nanovoids in sapphire [46].

type of structural change depends on the laser features (irradiance, repetition rate, polarization), working parameters (scanning speed, numerical aperture) and material properties (thermal conductivity, bandgap energy).

4. Bioactive glasses

Formation of glasses with improved properties and manufacturability plays an important role in many technologies. Various noncrystalline materials such as silica glasses, amorphous halides, semiconductors and metals have been used in areas for many engineering applications including biology, communications, electronics, and so on. Glass formation consists basically in avoiding crystallization by cooling from the molten state. The ability to glass formation depends on the melt composition that defines some parameters as glass transition and liquidus temperatures, on the cooling rate which has to be higher enough to avoid the nucleation and growth of the crystalline phases and also on the sample size. As the solidification technique used limits at some extent the cooling rate, the first question in the development of glasses is to determine the composition ranges in which glasses can be obtained under certain cooling conditions (quenching, directional solidification, etc.).

It is known that for multicomponent systems, a strong tendency to glass formation exists near the eutectic points because they have the lower liquidus temperature. Glass formation and its relation to eutectic growth have been investigated for different metal and ceramic alloy systems in terms of the competition between the growth of crystalline phases and the formation of the amorphous phase. The maximum growth rate of a eutectic structure with two or more phases is lower than the maximum growth rate of a single crystalline phase. Therefore, the locations of glass formation in some oxide, halide or metal systems lie near the eutectic area compositions, even though the glass formation also depends on the cooling rate. High liquidus slopes, low mutual solubility of the phases (high eutectic range $C_{\alpha\beta}$), small diffusion in the melt and large solid/liquid interfacial energies favor the glass formation in competition with the eutectic formed through cooperative growth of the crystalline phases.

Bioactive glasses capable of forming tight chemical bonds to living tissues contain silicates and some of them also phosphates, the first providing a scarcely soluble matrix that compensates for the excess solubility of the latter. The ability of bonding to bone tissue is a result of their chemical reactivity of the surface in a physiological media. The formation of SiO_2 rich layer and calcium phosphate film on the surface of a bioglass implanted in a body and bond with living bone was reported by Hench [81]. Kokubo proposed the use of artificial body fluid as a simulated body environment to estimate the bioactivity of the glasses and ceramics [82].

De Aza et al. showed that glasses and ceramics in the systems containing $CaO—P_2O_5—SiO_2$ can be designed to optimize biological and mechanical response. They have studied different microstructures in the wollastonite ($CaO.SiO_2$)-calcium phosphate TCP ($3CaO.P_2O_5$) system reporting the presence in the phase diagram of an invariant point at 1402°C and a composition of 80% mol W and 20% mol TCP [83]. It is possible to estimate the eutectic compositions from the values of melting temperature and heat of fusion of the components through the expressions [84]:

$$RT\ln X_i^l = -\Delta H_i^m\left(1-\frac{T}{T_i^m}\right) \quad i = 1,2,3,\ldots,k \tag{5}$$

$$\sum_{i=1}^{k} X_i^l = 1 \tag{6}$$

where X^l_i is the mole fraction of component *i* in the liquid and T^m_i and H^m_i are melting temperature and molar heat of fusion of component *i* in the liquid. The eutectic composition and the eutectic temperature can be calculated with the expressions indicated above if the melting temperature and heats of fusion of the components are known, as shown in **Table 2**.

On the other hand, in order to form an amorphous solid, the melt must be cooled sufficiently fast to prevent the precipitation of the competitive crystalline phases, defining a minimum cooling rate. Lu and Liu [85] used the dimensionless parameter $\gamma = Tx/(Tg + Tl)$ as an indicator of the glass-forming ability of the system, with Tx, Tg and Tl the crystallization onset, glass transition and melting temperatures, respectively. The relationship between this parameter and the critical cooling rate (Rc) for glass formation is approximately given by the expression:

$$R_c = R_o \exp.\left[\left(-\ln R_o\right)\gamma/\gamma_o\right] \tag{7}$$

where the constants R_o and γ_o are, for inorganic glasses, 8×10^{27} K/s and 0.421, respectively. Magallanes-Perdomo et al. described the devitrification and crystallization process of W-TCP eutectic glass, evidencing that the devitrification begins at 870°C with the crystallization of a Ca-deficient apatite phase [86]. Being the glass transition temperature 790°C, the γ parameter is 0.414 and the calculated critical cooling rate R_c is about 3 K/s. This rate corresponds to a solidification rate of about 100 mm/h in the Laser Floating Zone (LFZ) technique for an experimental axial thermal gradient of 10^5 K/m, in good accordance with the growth rate of

A	B	T^m_A (K)	T^m_B (K)	H^m_A (J/mol)	H^m_B (J/mol)	Calculated/Measured eutectic X_A-X_B (mol%)	Calculated/Measured T_{eut} (K)
Wollastonite	TCP	1821	1943	36.844	156.057	80.25–20.61 80–20	1670/1675

Table 2. Calculated eutectic composition and temperature in W-TCP system.

150 mm/h reported by Pardo et al. for the fabrication of a W-TCP eutectic glass rod of 3 mm in diameter [87]. A detailed description of this technique can be consulted elsewhere [88, 89].

This eutectic glass, produced by the laser floating zone technique, is chemically stable and has a high optical quality being able to be used as a matrix for luminescence active ions. This composition corresponds to an "invert" glass where the modifier content (Ca) is larger than the former content (Si + P). This term was introduced by Trapp and Stevels [90] because the traditional network forming oxides SiO_2 and P_2O_5 form continuous molecular/ionic networks in normal conditions; however, when the network modifying oxides are in majority on the molar basis, the glasses are structurally inverted compared to conventional glasses. This structural inversion is reflected in the properties of the glasses. In addition, the optical properties of this glass doped with Nd^{3+} and Er^{3+} ions have been assessed, resulting in emission cross-sections and lifetimes similar to those reported for the best commercial alkaline-silicate glasses [87]. Furthermore, the incorporation of trivalent rare-earth (RE) ions can also be used as local ordering probe due to the close relation between their spectroscopic properties and the local structure and bonding at the ion site, since the spectroscopic properties of trivalent rare-earth ions depend on the chemical composition of the glass matrix, which determines the structure and nature of the bonds, and thus spectroscopic characterization allows studying the local structure surrounding the RE ion and the covalence of the RE-O bond [91, 92]. In particular, site-selective excitation and emission of Nd- and Eu-doped W-TCP glass ceramics provided information about the differences on the spectral features of amorphous and crystalline environments in this matrix, allowing the identification by means of Raman and LIBS of crystalline phases corresponding to dicalcium silicate (Ca_2SiO_4) and apatite-like structures, both with well-known bioactive and biocompatible properties [93–95]. These results showed the potential applications of these materials obtained from the LFZ technique as luminescence bioprobes for in vitro applications and promote extended studies to other rare-earth ions, which can be used in biomedical applications such as multicolor bioprobes and biosensors among others.

5. Fabrication of photonic devices in W-TCP bioactive glasses

Both stress-induced and depressed cladding waveguides have been studied in Nd-doped $CaSiO_3$—$Ca_3(PO_4)_2$ bioactive glasses. In both cases, the guiding structures were manufactured by using the ULI technique. For this purpose, a tunable Ti:Sapphire laser emitting at the central wavelength of 795 nm with 120 fs laser pulses and 1 kHz repetition rate was used. **Figure 2** shows an example of double-line configuration and a depressed cladding waveguide obtained in this glass, (a) and (b), respectively. For the case of the stress-induced waveguide,

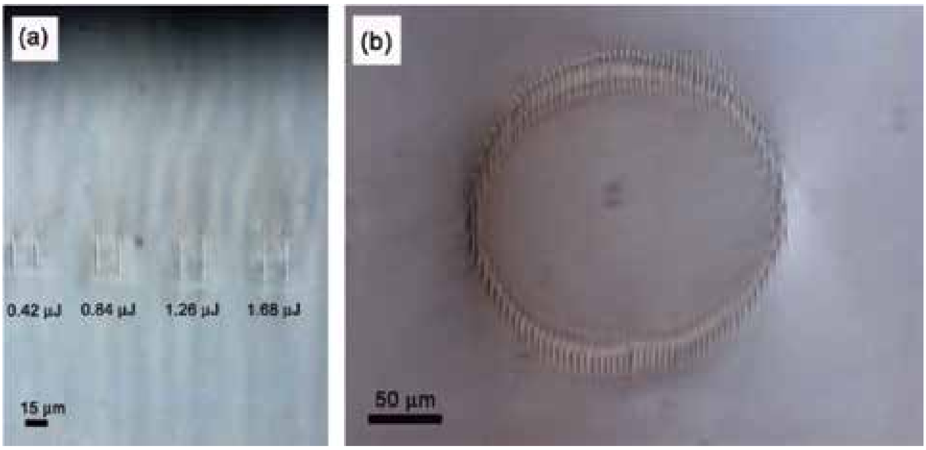

Figure 2. Double-line (a) and depressed cladding (b) waveguides produced in the W-TCP eutectic bioactive glass [56, 60].

the guiding characteristics were studied modifying the pulse energy between 0.42 and 1.68 μJ, the scanning speed at 25 and 50 μm/s and the distance between filaments at 15 and 20 μm. Also, in this case, the structures were inscribed at 150 and 250 μm beneath the surface of the sample. As shown in **Figure 2(a)**, the filament dimensions strongly depend on the energy delivered (E_d) by the laser beam, between 8.4 and 67 μJ, achieving lengths from 16 up to 40 μm. For the case of the cladding structure, both the distance between filaments and the scanning speed were set constant at 3 μm and 500 μm/s respectively, studying the guiding properties with the diameter of the core, between 20 and 150 μm, and the depth from the surface, 300 and 600 μm. Worth mentioning is the fact that the fabrication of cladding structures required lower delivered energy than in the case of double-filament waveguides, since the filaments were very close to each other and an excessive amount of energy might create cracks on the irradiated area and hence to fracture the sample. Specifically, in this case, filaments of the cladding structure were produced delivering 1.44 μJ over each focal spot. In addition, the interaction of the ultrashort laser radiation with the glass sample gave rise to an affected zone in the surroundings of the tracks, caused by the generation of color centers. It is well known that high intensity ultrashort laser pulses may modify the properties of the material at atomic scale by the photophysical and photochemical interactions which take place after the laser absorption [3]. These color centers also may affect to both the guiding and luminescence properties.

The guiding properties were assessed by characterization of the near-field intensity distribution with a continuous wave He-Ne laser at 633 nm. Both types of waveguides presented TE and TM propagation. Furthermore, all double-filament waveguides inscribed were found to be monomode, whereas only 20 μm diameter depressed cladding waveguides presented this feature. In addition, for double-filament waveguides, the width found in TE and TM modes was shorter along the x-axis than in the orthogonal one, but the modal area decreased with the pulse energy thus increasing the light confinement. Moreover, the best confinement conditions were achieved for both the shortest track distance (15 μm) and depth (150 μm), and the highest scanning speed (50 μm/s). Concerning the cladding waveguides, there were no remarkable differences depending either on the guided polarization or processing parameters. As an example, **Figure 3** shows the near-field distribution intensity of TE mode in a double-filament waveguide inscribed 150 μm beneath the surface with 15 μm between tracks (a), and cladding waveguides (b) of 20 μm (left) and 30 μm (right) diameters.

The absorption generated by color centers, appeared during the laser inscription process was reduced by means of isochronal heat treatments thus decreasing propagation losses [96–98]. This annealing process produced an improvement of up to a 29% in the transmitted power in the range of 300–350°C for the double-line waveguide, as shown in **Figure 4(a)**, whereas higher annealing temperatures led to a diminution of the stress-induced between filaments and therefore to a decrease in the refractive index change and consequently in the light confinement. In depressed cladding waveguides, the thermal treatment induced a continuous improvement of the transmitted intensity up to 650°C, based on a gradual removal of color centers and a partial recovery of the refractive index change caused by the release of the stress-induced by the ultrashort laser pulses. Annealing temperatures higher than 650°C reduced the optical barrier and the tunneling losses became non-negligible [99]. The analysis of the evolution of the modal intensity as a function of the thermal treatment temperature confirmed this mechanism, as shown in **Figure 4(b)**, revealing that the light confinement kept almost unaltered until 600°C, whereas higher temperatures enlarged the modes hindering the light transmission.

Luminescence characterization carried out in both types of waveguides revealed that spectroscopic properties were well preserved in the volume of the waveguides and that annealing treatment at high temperature recombined the damaged produced in the irradiated areas, resulting in a worsening the light confinement. Fluorescence lifetimes, around 240–250 μs, and both luminescence spectra and μL map of the $^4F_{3/2} \rightarrow {}^4I_{11/2}$ transition in the bulk and in the waveguide's volume pointed out no significant modifications, **Figure 5**.

The refractive index modification was estimated on the basis of the refractive index distribution generated by femtosecond laser pulses in double-filament waveguides [100, 101], for which:

$$\Delta n = -\Delta n_{max} \frac{1-(x/\sigma_x)^2}{1+(x/\sigma_x)^4} \exp\left(x/\sigma_y\right)^2 \tag{8}$$

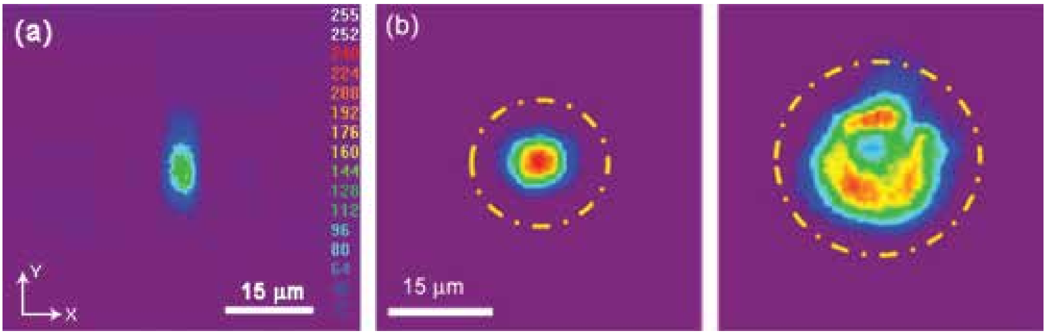

Figure 3. Near-field distribution intensity of TE mode in a double-filament waveguide with 15 μm between tracks (a) and in depressed cladding waveguides (b) 20 μm (left) and 30 μm (right) diameter produced in the W-TCP eutectic bioactive glass [56, 60].

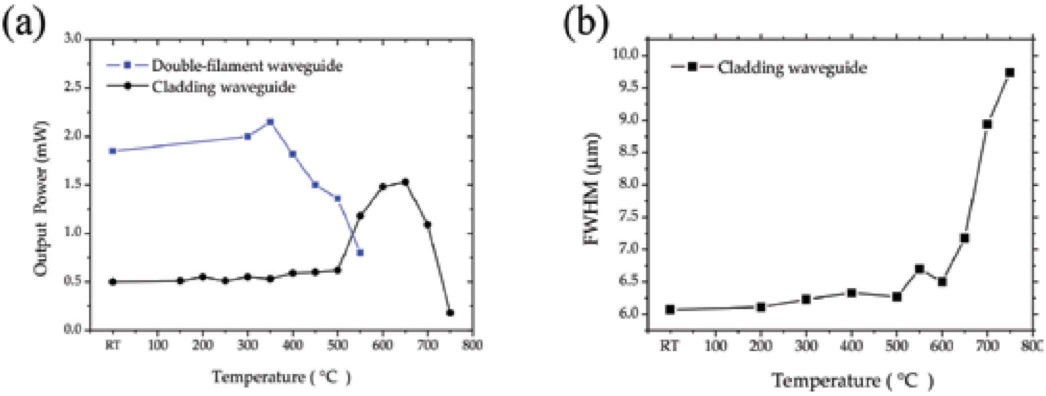

Figure 4. (a) Output power measured in double-filament and depressed cladding waveguides after isochronal heat treatment between room temperature (RT) and 750°C. (b) Evolution of the FWHM TE mode as a function of the annealing temperature between room temperature (RT) and 750°C for the 20 μm diameter cladding waveguide [56, 60].

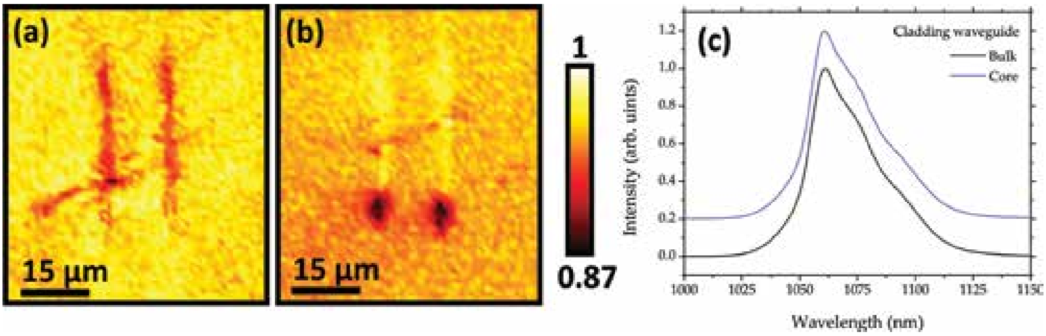

Figure 5. Spatial variation of the Nd^{3+} fluorescence intensity for a double-filament waveguide at room temperature (a) and at 550°C (b) and emission of Nd^{3+} at 1060 nm under excitation at 808 nm for a 20 μm diameter depressed cladding waveguide in the core of the waveguide and in the bulk [56, 60].

where Δn_{max} is the maximum reduction on the refractive index in the track, and σ_x and σ_y are the width of the damaged region along the horizontal and vertical directions respectively, resulting in a $\Delta n \sim 5 \times 10^{-3}$, which was found to be in the same range of previously reported for other waveguides inscribed by femtosecond laser writing, such as Nd:YAG ceramics, Nd:YVO_4 and fused-silica.

6. Conclusions

Fabrication of integrated photonic devices has been a hot topic in research since the first report on femtosecond laser written waveguides in glass by using the Ultrafast Laser Inscription Technique (ULI), in 1996. In this chapter, we have reviewed the fundamentals of this laser processing technique, describing the main configurations for waveguide fabrication achieved to date, and the materials for which they have been applied. Also, a comparison to other techniques commonly used for waveguide fabrication has been included, pointing out the principal advantages of ULI when compared to these methods. Furthermore, the basis of the interaction between ultrashort laser pulses and dielectric media which may give rise to refractive index modification and hence, to waveguide fabrication has been outlined. In addition, this chapter briefly reviews the development of bioactive glasses related to their capability of forming tight chemical bonds to living tissues. This section is particularized to the development of $CaSiO_3—Ca_3(PO_4)_2$ bioactive eutectic glass and glass ceramics, and to their potential applications as luminescence bioprobes in biomedical applications when doped with rare-earth ions. Finally, this chapter reviews the fabrication of double-filament and depressed cladding waveguides in Nd-doped $CaSiO_3—Ca_3(PO_4)_2$ bioactive eutectic glasses. Double-filament waveguides presented an increase of the refractive index in the region between damaged areas, the so-called "tracks," inscribed with the ultrashort laser pulses. In cladding waveguides, tracks were inscribed close to each other to surround a volume of bulk material. Both types of waveguides supported TE and TM polarization guiding under illumination of cw He-Ne laser radiation. In particular, only the cladding waveguide with the smallest core, 20 μm, presented monomode transmitted light. Color centers formation was observed in both types of waveguides as a consequence of the laser interaction with the glass. Isochronal thermal treatments allowed decreasing the absorption by color centers and for the highest annealing temperatures, a release of the stress-induced in the laser treated area. In addition, it was shown that spectroscopic properties were well preserved in the volume of the waveguides. Finally, the refractive index modification, Δn, was estimated in 5×10^{-3}, in the same range of previously reported works by the ULI technique.

Future work is expected to be done in the fabrication of integrated photonic devices in glasses and glass ceramics of the $CaO—P_2O_5—SiO_2—MgO$ system by the ULI technique. Glasses and glass ceramics of this system are also bioactive. Therefore, we will ascertain and assess the optimal conditions for the fabrication of optical waveguides and their possible utilization as laser sources for biomedical applications.

Acknowledgements

Dr. Daniel Sola thanks the Ministry of Economy and Competitiveness of the State General Administration under the project MINECO FIS2016-76163-R and the PIT2 program of the University of Murcia's own research plan for the financial support of his contract.

Conflict of interest

The authors declare no conflict of interest.

Author details

Daniel Sola[1]* and José I. Peña[2]

*Address all correspondence to: daniel.sola@um.es

1 Laboratorio de Optica (LO·UM), Center of Research in Optics and Nano-physics (CIOyN), University of Murcia, Murcia, Spain

2 Materials Science Institute of Aragon (ICMA), University of Zaragoza-CSIC, Zaragoza, Spain

References

[1] Maiman TH. Stimulated optical radiation in ruby. Nature. 1960;**187**:493-494. DOI: 10.1038/187493a0

[2] Bäuerle D. Laser Processing and Chemistry. 3rd ed. Berlin: Springer-Verlag; 2000. DOI: 10.1007/978-3-642-17613-5

[3] Misawa H, Juodkazis S, editors. 3D Laser Microfabrication: Principles and Applications. Weinheim: Wiley-VCH; 2006. DOI: 10.1002/352760846X.ch10

[4] Osellame R, Cerullo G, Ramponi R, editors. Femtosecond Laser Micromachining: Photonic and Microfluidic Devices in Transparent Materials. Berlin: Springer; 2012. DOI: 10.1007/978-3-642-23366-1

[5] Sola D, Peña JI. Foamy coating obtained by laser ablation of glass ceramic substrates at high temperature. Applied Surface Science. 2009;**255**:5322-5328. DOI: 10.1016/j.apsusc.2008.09.028

[6] Gurauskis J, Sola D, Peña JI, Orera VM. Laser drilling of Ni-YSZ cermets. Journal of the European Ceramic Society. 2008;**28**:2673-2680. DOI: 10.1016/j.jeurceramsoc.2008.04.012

[7] Sola D, Escartín A, Cases R, Peña JI. Crystal growth induced by Nd:YAG laser irradiation in patterning glass ceramic substrates with dots. Optical Materials. 2011;**33**:728-734. DOI: 10.1016/j.optmat.2010.11.008

[8] Sola D, Peña JI. Laser machining of Al_2O_3-ZrO_2(3%Y_2O_3) eutectic composite. Journal of the European Ceramic Society. 2012;**32**:807-814. DOI: 10.1016/j.jeurceramsoc.2011.11.007

[9] Sola D, Peña JI. Study of the wavelength dependence in laser ablation of advanced ceramics and glass-ceramic materials in the nanosecond range. Materials. 2013;**6**:5302-5313. DOI: 10.3390/ma6115302

[10] Garcia-Giron A, Sola D, Peña JI. Liquid-assisted laser ablation of advanced ceramics and glass-ceramic materials. Applied Surface Science. 2016;**363**:548-554. DOI: 10.1016/j.apsusc.2015.12.079

[11] Sola D, Grima L. Laser machining and in vitro assessment of wollastonite-tricalcium phosphate eutectic glasses and glass-ceramics. Materials. 2018;**11**:125. DOI: 10.3390/ma11010125

[12] Sola D, Lavieja C, Orera A, Clemente MJ. Direct laser interference patterning of ophthalmic polydimethylsiloxane (PDMS) polymers. Optics and Lasers in Engineering. 2018;**106**:139-146. DOI: 10.1016/j.optlaseng.2018.03.007

[13] Bromberg JL. The birth of the laser. Physics Today. 1988;**41**:26-33. DOI: 10.1063/1.881155

[14] Svelto O. Principles of Lasers. 5th ed. New York: Springer; 2010. DOI: 10.1007/978-1-4419-1302-9

[15] McClung FJ, RW, Hellwarth RW. Giant optical pulsations from ruby. Journal of Applied Physics. 1962;**33**:828. DOI: 10.1063/1.1777174

[16] Hargrove LE, Fork RL, Pollack MA. Locking of he-ne laser modes induced by synchronous intracavity modulation (diffraction by phonons in crystals E). Applied Physics Letters. 1964;**5**:4-5. DOI: 10.1063/1.1754025

[17] Fork RL, Greene BI, Shank CV. Generation of optical pulses shorter than 0.1 psec by colliding pulse mode locking. Applied Physics Letters. 1981;**38**:671-672. DOI: 10.1063/1.92500

[18] Morgner U, Kärtner FX, Cho SH, Chen Y, Haus HA, Fujimoto JG, Ippen EP. Sub-two-cycle pulses from a Kerr-lens mode-locked Ti:Sapphire laser. Optics Letters. 1999;**24**: 411-413. DOI: 10.1364/OL.24.000411

[19] Morgner U, R Ell R, Metzler G, Schibli TR, Kärtner FX, Fujimoto JG, Haus HA, Ippen EP. Nonlinear optics with phase-controlled pulses in the sub-two-cycle regime. Physical Review Letters 2001;**86**:5462-5465. DOI: 10.1103/PhysRevLett.86.5462

[20] Gallman L, Sutter DH, Matuschek N, Steinmeyer G, Keller U, Iaconis C, Walmsley IA. Characterization of sub-6-fs optical pulses with spectral phase interferometry for direct electric-field reconstruction. Optics Letters. 1999;**24**:1314-1316. DOI: 10.1364/OL.24.001314

[21] Rulliere C. Femtosecond Laser Pulses: Principles and Experiments. 2nd ed. New York: Springer; 2003. DOI: 10.1007/b137908

[22] Davis KM, Miura K, Sugimoto N, Hirao K. Writing waveguides in glass with a femtosecond laser. Optics Letters. 1996;**21**:1729-1731. DOI: 10.1364/OL.21.001729

[23] Nolte S, Will M, Burghoff J, Tuennermann A. Femtosecond waveguide writing: A new avenue to three-dimensional integrated optics. Applied Physic A. 2003;**7**:109-111. DOI: 10.1007/s00339-003-2088-6

[24] Taccheo S, Della Valle G, Osellame R, Cerullo G, Chiodo N, Laporta P, Svelto O, Killi A, Morgner U, Lederer M, Kopf D. Er:Yb-doped waveguide laser fabricated by femtosecond laser pulses. Optics Letters. 2004;**29**:2626-2628. DOI: 10.1364/OL.29.002626

[25] Zhou G, Gu M. Direct optical fabrication of three-dimensional photonic crystals in a high refractive index $LiNbO_3$ crystal. Optics Letters. 2006;**31**:2783-2785. DOI: 10.1364/OL.31.002783

[26] Thomson RR, Bookey HT, Psaila ND, Fender A, Campbell S, MacPherson WN, Barton JS, Reid DT, Kar AK. Ultrafast-laser inscription of a three dimensional fan-out device for multicore fiber coupling applications. Optics Express. 2007;**15**:11691-11697. DOI: 10.1364/OE.15.011691

[27] Psaila ND, Thomson RR, Bookey HT, Kar AK, Chiodo N, Osellame R, Cerullo G, Jha A, Shen S. Er: Yb-doped oxyfluoride silicate glass waveguide amplifier fabricated using femtosecond laser inscription. Applied Physics Letters 2007;**90**:131102. DOI: 10.1063/1.2716866

[28] Torchia GA, Rodenas A, Benayas A, Cantelar E, Roso L, Jaque D. Highly efficient laser action in femtosecond-written Nd:Yttrium aluminum garnet ceramic waveguides. Applied Physics Letters. 2008;**92**:111103. DOI: 10.1063/1.2890073

[29] Siebenmorgen J, Petermann K, Huber G, Rademaker K, Nolte S, Tünnermann A. Femtosecond laser written stress-induced Nd:$Y_3Al_5O_{12}$ (Nd:YAG) channel waveguide laser. Applied Physics B. 2009;**97**:251-255. DOI: 10.1007/s00340-009-3697-3

[30] Siebenmorgen J, Calmano T, Petermann K, Huber G. Highly efficient Yb:YAG channel waveguide laser written with a femtosecond-laser. Optics Express. 2010;**18**:16035-106041. DOI: 10.1364/OE.18.016035

[31] Silva WF, Jacinto C, Benayas A, Vazquez de Aldana JR, Torchia GA, Chen F, Tan Y, Jaque D. Femtosecond-laser-written, stress-induced Nd:YVO_4 waveguides preserving fluorescence and Raman gain. Optics Letters. 2010;**35**:916-918. DOI: 10.1364/OL.35.000916

[32] Fletcher LB, Witcher JJ, Troy N, Reis SR, Brow RK, Martinez Vazquez R, Osellame R, Krol DM. Femtosecond laser writing of waveguides in zinc phosphate glasses. Optical Materials Express. 2011;**1**:845-855. DOI: 10.1364/OME.1.000845

[33] Benayas A, Silva WF, Rodenas A, Jacinto C, Vazquez de Aldana J, Chen F, Tan Y, Thomsom RR, Psaila ND, Red DT, Torchia GA, Kar AK, Jaque D. Ultrafast laser writing of optical waveguides in ceramic Yb:YAG: A study of thermal and non-thermal regimes. Applied Physics A. 2011;**104**:301-309. DOI: 10.1007/s00339-010-6135-9

[34] Chen F, Vázquez de Aldana JR. Optical waveguides in crystalline dielectric materials produced by femtosecond-laser micromachining. Laser and Photonics Review. 2014;**8**:251-275. DOI: 10.1002/lpor.201300025

[35] Li L, Nie W, Li Z, Romero C, Rodriguez-Beltrán RI, Vázquez De Aldana JR, Chen F. Laser-writing of ring-shaped waveguides in BGO crystal for telecommunication band. Optics Express. 2017;**25**:24236-24241. DOI: 10.1364/OE.25.024236

[36] McMillen B, Zhang B, Chen KP, Benayas A, Jaque D. Ultrafast laser fabrication of low-loss waveguides in chalcogenide glass with 0.65 dB/cm loss. Optics Letters. 2012;**37**:1418-1420. DOI: 10.1364/OL.37.001418

[37] Morris JM, Mackenzie MD, Petersen CR, Demetriou G, Kar AK, Bang O, Bookey HT. $Ge_{22}As_{20}Se_{58}$ glass ultrafast laser inscribed waveguides for mid-IR integrated optics. Optical Materials Express. 2018;**8**:1001-1011. DOI: 10.1364/OME.8.001001

[38] Lv J, Cheng Y, Lu Q, Vázquez De Aldana JR, Hao X, Chen F. Femtosecond laser written optical waveguides in z-cut MgO:$LiNbO_3$ crystal: Fabrication and optical damage investigation. Optical Materials. 2016;**57**:169-173. DOI: 10.1016/j.optmat.2016.05.003

[39] Morris J, Stevenson NK, Bookey HT, Kar AK, Brown CTA, Hopkins J-M, Dawson MD, Lagatsky AA. 1.9 μm waveguide laser fabricated by ultrafast laser inscription in tm: Lu_2O_3 ceramic. Optics Express. 2017;**25**:14910-14917. DOI: 10.1364/OE.25.014910

[40] Ren Y, Zhang L, Xing H, Romero C, Vázquez de Aldana JR, Chen F. Cladding waveguide splitters fabricated by femtosecond laser inscription in Ti:Sapphire crystal. Optics and Laser Technology. 2018;**103**:82-88. DOI: 10.1016/j.optlastec.2018.01.021

[41] Li R, Nie W, Lu Q, Cheng C, Shang Z, Vázquez de Aldana JR, Chen F. Femtosecond-laser-written superficial cladding waveguides in Nd:CaF_2 crystal. Optics and Laser Technology. 2017;**92**:163-167. DOI: 10.1016/j.optlastec.2017.01.026

[42] Kifle E, Mateos X, Vázquez De Aldana JR, Ródenas A, Loiko P, Choi SY, Rotermund F, Griebner U, Petrov V, Aguiló M, Díaz F. Femtosecond-laser-written tm:$KLu(WO_4)_2$ waveguide lasers. Optics Letters. 2017;**42**:1169-1172. DOI: 10.1364/OL.42.001169

[43] Nguyen H-D, Ródenas A, De Aldana JRV, Martínez J, Chen F, Aguiló M, Pujol MC, Díaz F. Heuristic modelling of laser written mid-infrared LiNbO3 stressed-cladding waveguides. Optics Express. 2016;**24**:7777-7791. DOI: 10.1364/OE.24.007777

[44] Thorburn F, Lancaster A, McDaniel S, Cook G, Kar AK. 5.9 GHz graphene based q-switched modelocked mid-infrared monolithic waveguide laser. Optics Express. 2017;**25**:26166-26174. DOI: 10.1364/OE.25.026166

[45] Glezer E, Mazur E. Ultrafast-laser driven micro-explosions in transparent materials. Applied Physics Letters. 1997;**71**:882-884

[46] Gamaly EG, Juodkazis S, Nishimura K, Misawa H, Luther-Davis B, Hallo L, Nicolai P, Tikhonchuk V. Laser-matter interaction in the bulk of a transparent solid: Confined microexplosion and void formation. Physical Review B 2006;**73**:214101-1 214101-15.

[47] Vailionis A, Gamaly EG, Mizeikis V, Yang W, Rode AV, Juodkazis S. Evidence of superdense aluminium synthesized by ultrafast microexplosion. Nature Communications. 2011;**2**:445-451

[48] Macdonald TRR, Beecher SJ, Psaila ND, Bookey HT, Kar AK. Ultrafast laser inscription of near-infrared waveguides in polycrystalline ZnSe. Optics Letters. 2010;**35**:4036-4038. DOI: 10.1364/OL.35.004036

[49] Rodenas A, Kar AK. High-contrast step-index waveguides in borate nonlinear laser crystals by 3D laser writing. Optics Express. 2011;**19**:17820-17833. DOI: 10.1364/OE.19.017820

[50] Burghoff J, Nolte S, Tunnermann A. Origins of waveguiding in femtosecond laser-structured $LiNbO_3$. Applied Physics A. 2007;**89**:127-132. DOI: 10.1007/s00339-007-4152-0

[51] Heinrich M, Rademaker K, Nolte S. Waveguides in crystalline materials. In: Femtosecond-Laser Micromachining: Photonic and Microfluidic Devices in Transparent Materials. Berlin: Springer; 2012. pp. 295-313. DOI: 10.1007/978-3-642-23366-1

[52] Bain FM, Lagatsky AA, Thomson RR, Psaila ND, Kuleshov NV, Kar AK, Sibbett W, Brown CTA. Ultrafast laser inscribed $Yb:KGd(WO_4)_2$ and $Yb:KY(WO_4)_2$ channel waveguide lasers. Optics Express. 2009;**17**:22417-22422

[53] Zhang C, Dong N, Yang J, Chen F, Vázquez de Aldana JR, Lu Q. Channel waveguide lasers in Nd:GGG crystals fabricated by femtosecond laser inscription. Optics Express. 2011;**19**:12503-12508. DOI: 10.1364/OE.19.012503

[54] Bhardwaj VR, Corkum PB, Rayner DM, Hnatovsky C, Simova E, Taylor RS. Stress in femtosecond-laser-written waveguides in fused silica. Optics Letters. 2004;**29**:1312-1314. DOI: 10.1364/OL.29.001312

[55] Fernandes LA, Grenier JR, Herman PR, Aitchison JS, Marques PVS. Stress induced birefringence tuning in femtosecond laser fabricated waveguides in fused silica. Optics Express. 2012;**20**:24103-24114. DOI: 10.1364/OE.20.024103

[56] Sola D, de Mendibil JM, de Aldana JRV, Lifante G, Balda R, de Aza AH, Pena P, Fernandez J. Stress-induced buried waveguides in the $0.8CaSiO_3$-$0.2Ca_3(PO_4)_2$ eutectic glass doped with Nd^{3+} ions. Applied Surface Science. 2013;**278**:289-294. DOI: 10.1016/j.apsusc.2013.01.060

[57] Beresna M, Gecevičius M, Kazansky PG. Ultrafast laser direct writing and nanostructuring in transparent materials. Advances in Optics and Photonics. 2014;**6**:293-339. DOI: 10.1364/AOP.6.000293

[58] Zhang YJ, Zhang GD, Bai J, Chen CL, Stoian R, Cheng GH. Double line and tubular depressed cladding waveguides written by femtosecond laser irradiation in PTR glass. Optical Materials Express. 2017;**7**:2626-2635. DOI: 10.1364/OME.7.002626

[59] Okhrimchuk AG, Shestakov AV, Khrushchev I, Mitchell J. Depressed cladding, buried waveguide laser formed in a $YAG:Nd^{3+}$ crystal by femtosecond laser writing. Optics Letters. 2005;**30**:2248-2250. DOI: 10.1364/OL.30.002248

[60] Martínez de Mendívil J, Sola D, Vázquez de Aldana JR, Lifante G, de Aza AH, Pena P, Peña JI. Ultrafast direct laser writing of cladding waveguides in the $0.8CaSiO_3$-$0.2Ca_3(PO_4)_2$ eutectic glass doped with Nd^{3+} ions. Journal of Applied Physics. 2015;**117**:4906963. DOI: 10.1063/1.4906963

[61] Okhrimchuk A, Mezentsev V, Shestakov A, Bennion I. Low loss depressed cladding waveguide inscribed in YAG:Nd single crystal by femtosecond laser pulses. Optics Express. 2012;**20**:3832-3843. DOI: 10.1364/OE.20.003832

[62] An Q, Jia Y, Liu H, De Aldana JRV, Chen F. Ultrafast laser inscribed cladding waveguides in Nd:YAG crystal for mid-infrared wavelength. Optics and Laser Technology. 2014;**56**:382-386. DOI: 10.1016/j.optlastec.2013.09.011

[63] Li L, Nie W, Li Z, Lu Q, Romero C, Vázquez De Aldana JR, Chen F. All-laser-micromachining of ridge waveguides in $LiNbO_3$ crystal for mid-infrared band applications. Scientific Reports. 2017;**7**:7034. DOI: 10.1038/s41598-017-07587-w

[64] Martínez de Mendívil J, del Hoyo J, Solís J, Lifante G. Ridge waveguide laser in $Nd:LiNbO_3$ by Zn-diffusion and femtosecond-laser structuring. Optical Materials 2016;**62**:353-356. DOI: 10.1016/j.optmat.2016.10.008

[65] Jia Y, Dong N, Chen F, Vázquez de Aldana JR, Akhmadaliev S, Zhou S. Continuous wave ridge waveguide lasers in femtosecond laser micromachined ion irradiated Nd:YAG single crystals. Optical Materials Express. 2012;**2**:657-662. DOI: 10.1364/OME.2.000657

[66] Jia Y, Dong N, Chen F, Vázquez de Aldana JR, Akhmadaliev S, Zhou S. Ridge waveguide lasers in Nd:GGG crystals produced by swift carbon ion irradiation and femtosecond laser ablation. Optics Express. 2012;**20**:9763-9768. DOI: 10.1364/OE.20.009763

[67] Martínez De Mendívil J, Hoyo J, Solis J, Pujol MC, Aguiló M, Diaz F, Lifante G. Channel waveguide fabrication in $KY(WO_4)_2$ combining liquid-phase-epitaxy and beam-multiplexed femtosecond laser writing. Optical Materials. 2015;**45**:304-309. DOI: 10.1016/j.optmat.2015.05.046

[68] Cantelar E, Jaque D, Lifante G. Waveguide lasers based on dielectric materials. Optical Materials. 2012;**34**:555-571. DOI: 10.1016/j.optmat.2011.05.012

[69] Sugimoto N, Ohishi Y, Katoh Y, Tate A, Shimokozono M, Sudo S. A ytterbium- and neodymium-co-doped yttrium aluminum garnet–buried channel waveguide laser pumped at 0.81 μm. Applied Physics Letters. 1995;**67**:582-584. DOI: 10.1063/1.115395

[70] Hettrick SJ, Mackenzie JI, Harris RD, Wilkinson JS, Sheppherd DP, Tropper AC. Ion-exchanged tapered-waveguide laser in neodymium-doped BK7 glass. Optics Letters. 2000;**25**:1433-1435. DOI: 10.1364/OL.25.001433

[71] Lallier E, Pocholle JP, Papuchon M, He Q, De Micheli M, Ostrowsky DB, Grezes-Besset C, Pelletier E. Integrated $Nd:MgO:LiNbO_3$ FM mode-locked waveguide laser. Electronic Letters. 1991;**27**:936-937. DOI: 10.1049/el:19910585

[72] Nouh S, Baldi P, El Hadi K, De Micheli M, Monnom G, Ostrowsky DB, Lallier E, Papuchon M. Fabrication parameter optimization of a low-threshold high-efficiency proton-exchanged waveguide laser in $Nd:LiTaO_3$. Optics Letters. 1995;**20**:1468-1470. DOI: 10.1364/OL.20.001468

[73] Bhutta T, Chardon AM, Shepherd DP, Daran E, Serrano C, Muñoz-Yagüe A. Low phonon energy, $Nd:LaF_3$ channel waveguide lasers fabricated by molecular beam epitaxy. IEEE Journal of Quantum Electronics. 2001;**37**:1469-1477. DOI: 10.1109/3.958380

[74] Bausá LE, Lifante G, Daran E, Pernas PL. $CaF_2:Er^{3+}$ molecular beam epitaxial layers as optical waveguides. Applied Physics Letters. 1996;**68**:3242-3244. DOI: 10.1063/1.116561

[75] Gerhardt R, Kleine-Börger J, Beilschmidt L, Frommeyer M, Dötsch H, Gather B. Efficient channel-waveguide laser in Nd:GGG at 1.062 μm wavelength. Applied Physics Letters. 1999;**75**:1210-1212. DOI: 10.1063/1.124644

[76] Rivier S, Mateos X, Petrov V, Griebner U, Romayuk YE, Borca CN, Gardillou F, Pollnau M. Tm:KY$(WO_4)_2$ waveguide laser. Optics Express. 2007;**15**:5885-5892. DOI: 10.1364/OE.15.005885

[77] Almeida RM, Xin MD, Barbier D, Orignac X. Er^{3+}-doped multicomponent silicate glass planar waveguides prepared by sol–gel processing. Journal of Sol-Gel Science and Technology. 1999;**14**:209-216. DOI: 10.1023/A:1008794202103

[78] Mao SS, Quéré F, Guizard S, Mao X, Russo RE, Petite G, Martin P. Dynamics of femtosecon laser interactions with dielectrics. Applied Physics A. 2004;**79**:1695-1709. DOI: 10.1007/s00339-004-2684-0

[79] Schaffer CB, Brodeur A, Mazur E. Laser-induced breakdown and damage in bulk transparent materials induced by tightly focused femtosecond laser pulses. Measurement Science and Technology. 2001;**12**:1784-1794. DOI: 10.1088/0957-0233/12/11/305

[80] Lancry M, Poumellec B, Chahid-Erraji A, Beresna M, Kazansky PG. Dependence of the femtosecond laser refractive index change thresholds on the chemical composition of doped-silica glasses. Optical Materials Express. 2011;**1**:711-723. DOI: 10.1364/OME.1.000711

[81] Ogino M, Ohuchi F, Hench LL. Compositional dependence of the formation of calcium phosphate films on bioglass. Journal of Biomedical Materials Research. 1980;**14**:55-64. DOI: 10.1002/jbm.820140107

[82] Kokubo T, Takadama H. How useful is SBF in predicting in vivo bone bioactivity? Biomaterials. 2006;**27**:2907-2915. DOI: 10.1016/j.biomaterials.2006.01.017

[83] De Aza PN, Guitián F, De Aza S. A new bioactive material which transforms in situ into hydroxyapatite. Acta Materialia. 1998;**46**:2541-2549. DOI: 10.1016/S1359-6454(98)80038-4

[84] Yong D, Zhonghon J. Prediction of glass formation regions by calculation of eutectic using ideal-solution model. Journal of the Americam Ceramic Society. 1991;**74**:2295-2298. DOI: 10.1111/j.1151-2916.1991.tb08299.x

[85] Lu ZP, Liu CT. A new approach to understanding and measuring glass formation in bulk amorphous materials. Intermetallics. 2004;**12**:1035-1043. DOI: 10.1016/j.intermet.2004.04.032

[86] Magallanes-Perdomo M, Pena P, De Aza PN, Carrodeguas RG, Rodríguez MA, Turrillas X, De Aza S, De Aza AH. Devitrification studies of wollastonite–tricalcium phosphate eutectic glass. Acta Biomaterialia. 2009;**5**:3057-3066. DOI: 10.1016/j.actbio.2009.04.026

[87] Pardo JA, Peña JI, Merino RI, Cases R, Larrea A, Orera VM. Spectroscopic properties of Er^{3+} and Nd^{3+} doped glasses with 0.8CaSiO –0.2$Ca_3(PO_4)_2$ eutectic composition. Journal of Non-Crystalline Solids. 2002;**298**:23-31. DOI: 10.1016/S0022-3093(01)01043-2

[88] Arias-Egido E, Sola D, Pardo JA, Martínez JI, Cases R, Peña JI. On the control of optical transmission of aluminosilicate glasses manufactured by the laser floating zone technique. Optical Materials Express. 2016;**6**:2413-2421. DOI: 10.1364/OME.6.002413

[89] Sola D, Ester FJ, Oliete PB, Peña JI. Study of the stability of the molten zone and the stresses induced during the growth of Al_2O_3-$Y_3Al_5O_{12}$ eutectic composite by the laser floating zone technique. Journal of the European Ceramic Society. 2011;**31**:1211-1218. DOI: 10.1016/j.jeurceramsoc.2010.08.022

[90] Trapp HJL, Stevels JM. Conventional and invert glasses containing Titania, I. Physics and Chemistry of Glasses. 1960;**1**:107-118

[91] Weber MJ. Science and technology of laser glass. Journal of Non-Crystalline solids. 1990;**123**:208-222. DOI: 10.1016/0022-3093(90)90786-L

[92] Sola D, Conejos D, De Mendivil JM, SanMartín LO, Lifante G, Peña JI. Directional solidification, thermo-mechanical and optical properties of $(Mg_xCa_{1-x})_3Al_2Si_3O_{12}$ glasses doped with Nd^{3+} ions. Optics Express. 2015;**23**:26356-26368. DOI: 10.1364/OE.23.026356

[93] Sola D, Balda R, Peña JI, Fernández J. Site-selective laser spectroscopy of Nd^{3+} ions in $0.8CaSiO_3$-$0.2Ca_3(PO_4)_2$ biocompatible eutectic glass-ceramics. Optics Express. 2012;**20**:10701-10711. DOI: 10.1364/OE.20.010701

[94] Sola D, Balda R, Peña JI, Fernández J. Time-resolved fluorescence line-narrowing of Eu^{3+} in biocompatible eutectic glass-ceramics. Optics Express. 2013;**21**:6561-6571. DOI: 10.1364/OE.21.006561

[95] Sola D, Paulés D, Grima L, Anzano J. Laser-induced breakdown spectroscopy (LIBS) for monitoring the formation of hydroxyapatite porous layers. Materials. 2017;**10**:1395. DOI: 10.3390/ma10121395

[96] Dekker P, Ams M, Marshall GD, Little DJ, Withford MJ. Annealing dynamics of waveguide Bragg gratings: Evidence of femtosecond laser induced colour centres. Optics Express. 2010;**18**:3274-3283. DOI: 10.1364/OE.18.003274

[97] Benayas A, Jaque D, McMillen B, Chen KP. Thermal stability of microstructural and optical modifications induced in sapphire by ultrafast laser filamentation. Journal of Applied Physics. 2010;**107**:033522. DOI: 10.1063/1.3280029

[98] Sánchez-Morales ME, Vazquez GV, Lifante G, Cantelar E, Rickards J, Trejo-Luna R. Analysis of the absorption coefficient in carbon implanted $Nd:YVO_4$ by an annealing process. Optics and Spectroscopy. 2011;**110**:885-889. DOI: 10.1134/S0030400X11060142

[99] Townsend PD, Chandler PJ, Zhang L. Optical Effects on Ion Implantation. Cambridge: Cambridge Studies in Modern Optics; 1994. DOI: 10.1017/CBO9780511599781

[100] Ródenas A, Torchia GA, Lifante G, Cantelar E, Lamela J, Jaque F, Roso L, Jaque D. Refractive index change mechanisms in femtosecond laser written ceramic Nd:YAG waveguides: Micro-spectroscopy experiments and beam propagation calculations. Applied Physics B. 2009;**95**:85-96. DOI: 10.1007/s00340-008-3353-3

[101] Ródenas A, Maestro LM, Ramírez MO, Torchia GA, Roso L, Chen F, Jaque D. Anisotropic lattice changes in femtosecond laser inscribed $Nd^{3+}:MgO:LiNbO_3$ optical waveguides. Journal of Applied Physics. 2009;**106**:013110. DOI: 10.1063/1.3168432

Chapter 7

Surface Modification of Fe_3O_4 as Magnetic Adsorbents for Recovery of Precious Metals

Roto Roto

Additional information is available at the end of the chapter

http://dx.doi.org/10.5772/intechopen.79586

Abstract

Magnetic nanoparticles such as magnetite have been studied intensively for their unique properties that are susceptible to a magnetic field, ready to coat with silica and able to modify with a variety of functional groups. The magnetite-silica core-shell system offers flexibility for extensive modification. The magnetic core is also important in the separation by the use of a magnetic field. The shell, meanwhile, is needed for protection of the magnetic core and further modification. Functional groups at the surface shell are critical in the reaction with target precious metal ions during application. In this contribution, we will have a comprehensive look at the preparation, characterization, and use of the magnetite core-shell modified with functional groups as a magnetic adsorbent. After adsorption, the materials together with the ions can be recovered by the use of magnet before further separation and purification.

Keywords: magnetic nanoparticle, recovery, silica, precious metal, adsorption, desorption

1. Introduction

Magnetic materials that are paramagnetic, ferrimagnetic, and ferromagnetic have received much attention because of their unique properties especially ready to modify and nontoxic [1, 2]. Magnetite (Fe_3O_4), one of many magnetic materials, is widely investigated for possible magnetic resonance imaging, sensor, and adsorbent. Magnetic nanoparticles typically consist of a magnetic core, a coating, and, in some cases, surface active modifiers.

The magnetite nanoparticles have a high surface area that yields numerous active sites. However, preparation of Fe_3O_4 nanoparticles is problematic since it can agglomerate, which leads to the decrease in the active sites. Coating with organic or inorganic surfactants is one way to avoid the particle agglomeration. The organic surfactants act as capping agents, but at times, they can give bigger particle size. Inorganic capping agent such as silica (SiO_2) has exceptional physical and chemical properties. SiO_2 is chemically stable in acidic solution and tuneable for modification. Coating of Fe_3O_4 nanoparticles with SiO_2 will also avoid the agglomeration and protect them from dissolution in acidic solution. SiO_2 will cover the surface of each Fe_3O_4 nanoparticle to form Fe_3O_4/SiO_2 nanoparticle core-shell system [3].

Morel et al. have coated Fe_3O_4 particles with SiO_2 to form core-shell having nanometer scale with an average diameter of 49 nm [4]. The success of Fe_3O_4/SiO_2 core-shell nanoparticle formation depends on the size of magnetite. However, stirring with the magnetic bar during the preparation causes condensation and agglomeration of the particles. The nonmagnetic mechanical stirring method was chosen for the preparation of Fe_3O_4 nanoparticle [5].

Many researchers used thiol group as an adsorbent for $[AuCl_4]^-$ ion with a better performance [2, 3, 6–9]. We have reported on the synthesis of the Fe_3O_4/SiO_2 nanoparticle core-shell modified with a thiol group. The Fe_3O_4/SiO_2 nanoparticle core-shell preparation was performed by applying nonmagnetic stirring method. For improving adsorption capacity, modification with thiol group has been conducted. The thiol groups are of the soft bases.

On the other hand, the $[AuCl_4]^-$ ions are classified as weak acid species, thus provided specific interaction with each other based on Pearson's hard-soft acid-based concepts [10]. The adsorption kinetics, adsorption capacity, and interaction model for the adsorption of $[AuCl_4]^-$ ion in solution by Fe_3O_4/SiO_2 nanoparticle core-shell adsorbent are reported. A recent review of the matter can be found elsewhere [11].

Figure 1 shows the schematic architecture of the magnetite-silica-functional groups. The core is magnetite to function as the important part for separation. The shell is silica, which can protect the magnetite from dissolution especially when it contacts with an acidic environment. Modification of the silica surface can be realized by silanization to give functional groups having an important function to react with the metal cations. The functional group must have a strong bond with the surface via complex formation.

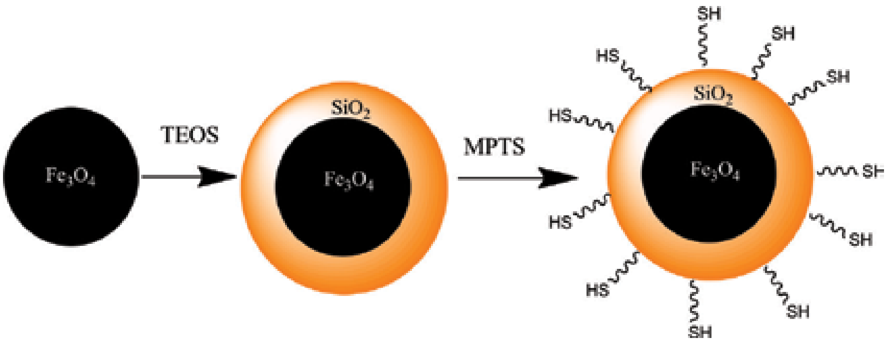

Figure 1. Step-by-step of $Fe_3O_4@SiO_2$ core-shell preparation and functionalization [3].

Figure 2. Image of simplified recovery technique of spent magnetic material after adsorption of precious metals [3].

Recovery of the magnetic material is key in the process following the adsorption. The spent adsorbent can be separated using a magnetic field. **Figure 2** shows how the used magnetic is separated by the external magnetic field. The magnetic adsorbent that has a high content of rare metals can be subject to dissolution and further separation. It is important to state that in the industrial purpose the powerful electromagnet system can be applied to do the job. In the purification, there are many possible green purification processes of metallurgy, starting from electrochemical separation to blast furnace.

2. Preparation of Fe_3O_4

Magnetite is commonly prepared by co-precipitation of Fe(II) and Fe(III) salts with suitable bases. Sodium hydroxide and ammonia are both commonly used in the preparation of magnetite. There are many bases that can be used to help control the size and the shape of the particles. Magnetite nanoparticles can be prepared in the presence of carboxylate such as laurate, palmitate, linoleate, and so on. The addition of surfactant helps reduce the particle size and control the shape. The required shape is usually spherical with a diameter of the nanoscale.

For co-precipitation methods, the size, shape, and composition of the resulting nanoparticles very much depend upon the following [12]:

a. The type of precursors' salts used, for example, chloride, sulfate, perchlorate, or nitrate

b. The Fe^{2+}/Fe^{3+} ratio

c. The mixing orders

d. The mixing rates

e. The reaction temperature

f. The pH value

g. The ionic strength of the media

The remaining issue is that magnetite nanoparticles are easily oxidized to maghemite, so this method is often used to obtain nanoparticles of magnetite and maghemite with the small size of 4–20 nm. Grüttner et al. have listed the size, coating, heating behavior, and magnetic properties of some iron oxide nanoparticles produced by this method [13]. Nanoparticles are produced by this method range in size from 4 to 45 nm. For fixed-synthesis conditions, the quality of the magnetite nanoparticles is very reproducible. Although co-precipitation is unquestionably the easiest process and highly scalable, it is not without issues. Controlling the shape is not easy, and the nanoparticles can be more varied in size than that produced in some other methods [12].

Precursors for the Fe(II) include ferrous sulfate, ferrous nitrate, and ferrous chloride. Some use ferrous acetate and ferrous oxalate. The most used precursor is ferrous sulfate. For the Fe(III), we can use ferric chloride, ferric nitrate, and so on. Ferric nitrate is used a lot. Ferric acetate and ferric oxalate are also commonly used as Fe(III) precursors.

The Fe(II) to Fe(III) molar ratio must be controlled strictly at 1:2. Therefore, the concentration of the starting material must be fixed. The oxidation of the Fe(II) ion must be contained by controlling the atmosphere by the use of inert atmosphere. During the co-precipitation, the nitrogen gas must be kept flowing to reduce possible oxidation process. Other noble gases could be used, which give a better magnetite product.

There are various ways to prepare Fe_3O_4 nanoparticles, such as hydrothermal synthesis [14], co-precipitation [15], microwave irradiation [16], oxidation of $Fe(OH)_2$ by H_2O_2 [17], and microemulsion [18]. The Fe_3O_4 nanoparticles synthesized by a hydrothermal method in the presence of sodium sulfate have a particle size of 160 nm [14]. Among various ways to prepare Fe_3O_4, hydrothermal is one of the simple methods because it gives unique characters. The shape and size of nanoparticles have a good homogeneity and high degree of crystallinity [19].

The widespread method to produce Fe_3O_4 is by co-precipitation of Fe^{2+}/Fe^{3+} solution mixture with a molar ratio of 1:2 in alkaline solution [15, 20]. The reaction for Fe_3O_4 formation by co-precipitation method is shown in chemical Eq. (1). Although this method is well known for synthesis Fe_3O_4, the molar ratio of reactant, pH, and temperature still need attention to get the proper size and morphology [15]:

$$Fe^{2+} + 2Fe^{3+} + 8OH^- \rightarrow Fe_3O_4 + 4H_2O \tag{1}$$

Microwave irradiation might be a promising method in processing materials due to its thermal and nonthermal effects. Microwave synthesis has the advantages of short reaction time, small particle size, and narrow size distribution. Aging under microwave irradiation in short period yields Fe_3O_4 nanoparticles with complete crystalline structure than those aged for 7 days at room temperature [16]. Yu et al. used H_2O_2 as an oxidizing agent to construct nano-sized superparamagnetic Fe_3O_4 powders with the size of 8–10 nm. The $Fe(OH)_2$ precipitates were partially oxidized to generate ultrafine Fe_3O_4 nanoparticles in the presence of surfactants [17]. Work on the control of the size of magnetite-silica via sol–gel method has also been reported [21].

Some researchers use capping agent to control crystal growth during Fe_3O_4 nanoparticle formation. Co-precipitation technique was used to prepare magnetite nanoparticles with diameter around 35 nm using 0.90 M NaOH solution as the precipitating agent and trisodium citrate as a capping agent. The precursors are ferric and ferrous chloride salts with predetermined Fe^{3+}/Fe^{2+} molar ratio. The diameter of silica-coated magnetite nanoparticles synthesized by Stöber method was about 50 nm. Due to an electrostatic interaction between the Fe^{3+}/Fe^{2+} ions of the Fe_3O_4 NPs and trisodium citrate surfactant, a stable magnetic fluid containing dispersed Fe_3O_4 NPs was produced [22]. A green and facile method for synthesis of magnetite nanoparticles was proposed [23]. Nano-sized polyhedral particles were synthesized by heating an aqueous solution of Fe^{2+}, Fe^{3+}, and urea at 85°C. The use of PVA in the synthesis system gives spherical magnetite nanoparticles with loose structure, unaggregated. The size of the microspheres can be tuned by changing the concentration of PVA. Upon addition of acetic acid to the system with PVA, microspheres with looser structure were produced. The size of the microspheres can further be tuned by changing the concentration of acetic acid. The co-precipitation of Fe^{2+} and Fe^{3+} in aqueous solutions under ultrasound irradiation results in smaller Fe_3O_4 NPs with a narrow size distribution (4–8 nm) than that produced without ultrasound irradiation [4]. Diethylene glycol (DEG) is also possibly used to control the particle size as reported earlier. This surfactant takes an important role in the preparation of magnetite/zinc oxide hybrid material [24].

3. Coating of Fe_3O_4 with SiO_2

The next step is coating magnetite with silica (SiO_2). It is usually performed via silanization reaction. The functional group that is ready to bond to iron oxide is methoxy silane (CH_3-O-Si-) or ethoxy silane (CH_3-CH_2-O-Si-). After the reaction, it forms a covalent bond of Fe-O-Si leaving the end group remains free. The leaving group is methane and ethane. The reaction is better to be done in an organic solvent. The silane group may have a spacer of long ethylene chain ($-CH_2^-$). The ending of the silane may be carboxylic, an amine group, hydroxyl, and so on. The surface of the silica has different accesses to the organic functional groups [25].

For example, modification by the use of 3-mercaptopropyltrimethoxysilane (3-MPTS) [3] reaction is depicted as a chemical reaction (2). For further surface modification, we can use other silanization compounds [3]:

$$\begin{aligned} &Fe_3O_4@SiO_2[(OH)_3]_n + n(CH_3O)_3Si(CH_2)_3SH \rightarrow \\ &Fe_3O_4@SiO_2[(O)_3]_nSi(CH_2)_3SH + 3nCH_3OH \end{aligned} \tag{2}$$

Iron oxide is not stable in acidic condition. After coating with silica, the magnetite core is usually stable in the acidic solution. It will come readily with a proton to give its corresponding ion either Fe^{2+} or Fe^{3+}. Dissolution of the magnetite will make the core-shell system unstable and break the bond between Fe-O-Si. To make sure that the magnetite is not dissolved in the acidic solution, we can test it by the use of an acid such as hydrochloric acid or nitric acid. The concentration of total iron as Fe^{2+} or Fe^{3+} can be an indicator if the magnetite is still strong. If high concentration of Fe^{3+} is found in the solution, we can say that the magnetite structure is collapsed and even broken down.

The visual indication can be seen from the color of the dispersion of $Fe_3O_4@SiO_2$ core-shell. The solution of Fe^{3+} in the solution is pale yellow. If the dispersion color is pale yellow, it can be concluded that magnetite does dissolve. The color is getting dark when the more magnetite dissolved in the dispersion. A combination of atomic absorption spectrometry and visual observation helps us make sure the magnetite core is still strongly intact.

Fe_3O_4/SiO_2 core-shell nanoparticles were obtained by dispersing Fe_3O_4 into the mixture solution of 80 mL of ethanol, 20 mL of deionized water, and 1.0 mL of concentrated aqueous ammonia solution (28 wt.%). After this, the mixture solution was homogenized by ultrasonication for 30 min to form a uniform dispersion. Subsequently, a certain amount of tetraethoxysilane (TEOS) was added dropwise into the solution with vigorous stirring. After stirring at room temperature for 6 h, the product was separated with a magnet bar, washed with deionized water for three times, and dried in vacuum at 50°C for 12 h. A series of $SiO_2@Fe_3O_4$ particles were prepared with 1–9% SiO_2 content [26].

The silica coating used on a core particle has several advantages. The essential advantages of the silica coating compared with another inorganic (metal or metal oxide) or organic coating are as follows: It reduces the bulk conductivity and increases the suspension stability of the core particles. Also, silica is the most chemically inert material available; it can block the core surface without interfering in the redox reaction at the core surface [27]. There are two methods for coating Fe_3O_4 with silica, by acidic hydrolysis of silicate in aqueous solutions and the modified Stöber process [4, 28].

The Stöber method consists of the alkaline hydrolysis of tetraethyl orthosilicate (TEOS) in ethanol/water mixture in the presence of Fe_3O_4 NPs [28]. The Stöber process is applied to the classic sol–gel process [29]. The Stöber synthesis has the advantage of being easy to scale up for commercial applications and the possibility to effortlessly transfer the nanoparticles into aqueous solutions [30]. Some methods that lead to the synthesis of Fe_3O_4/SiO_2 are shown in **Table 1**.

About the modification and application of magnetic materials, a coating of Fe_3O_4 by the use of various materials has been reported elsewhere. $TiO_2@Fe_3O_4$, $TiO_2@Fe_3O_4$@chitosan, and methyl pyrazolone-functionalized $TiO_2@Fe_3O_4$@chitosan were prepared for photocatalytic degradation of dyes [32]. They found that the core is important for separation and the shell is an active catalyst. The degradation of dye using these catalysts can reach up to 98–99%.

Thioctic acid-modified silica-coated magnetite nanoparticles, RS-SR-NH-$SiO_2@Fe_3O_4$, have been prepared, and its ability for the recovery of Au(III) in aqueous solutions was evaluated [31]. The Au(III) adsorption capacity of the produced adsorbent is about 25 mg/g. The possible

Core		Shell	
Method	Precursors	Method	Basic reagent
Wet chemical reaction	$FeCl_3$, N_2H_4	Sol–gel	TEOS
Wet chemical reaction	$FeCl_3$, $FeSO_4$	Hydrolysis	Na_2SiO_3
Wet chemical reaction	$FeCl_3$, $FeSO_4$	Hydrolysis	Commercial SiO_2
A chemical reaction in microemulsion	$FeCl_3$, $FeSO_4$	Sol–gel reaction in microemulsion	TEOS

Table 1. Methods for synthesis of Fe_3O_4 coated with SiO_2.

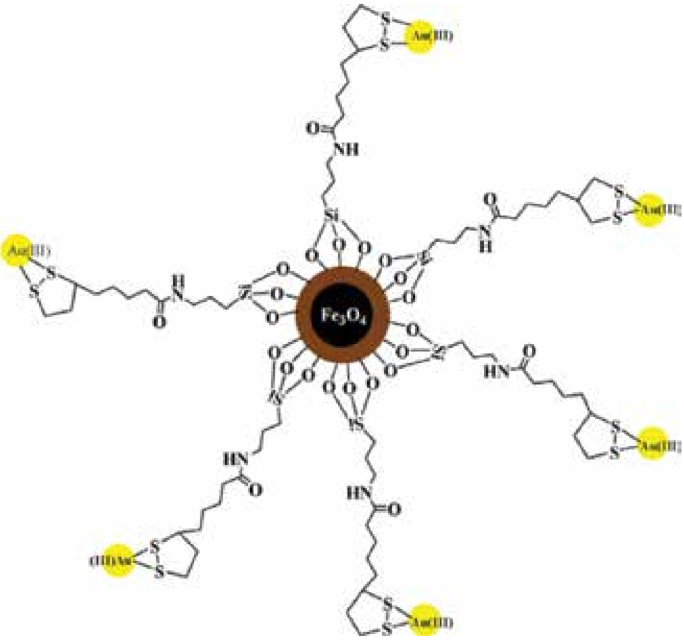

Figure 3. Possible interaction between RS-SR-NH-SiO_2@Fe_3O_4 and au(III) ions [31].

interaction is shown in **Figure 3**. Another study shows the success of recovery of gold from copper anode slime by means of magnetite nanoparticles [33]. The surface of magnetite was also modified with oleic acid, methyl methacrylate, and ethylenediamine (EDA-MMA-OA@ Fe_3O_4) giving the adsorption of indium of about 54 mg/g [34].

An interesting example of functionalization of Fe_3O_4 is by the use of dithiocarbamate, and it is applied as a magnetic nano-adsorbent for recovery of precious metal nanoparticles by contacting the nano-adsorbent with Au, Ag, Pd, or Pt hydrosols [35]. The magnetic particles are very efficient for Au due to strong affinity of sulfur-containing groups at the magnetite surfaces with this metal. Since Au colloids are used in laboratory and industrial contexts, the material could have an impact on the development of nanotechnology to recover precious metals like Au [35] and Ag. Another trial is modification using chitosan and EDTA. It shows more selective for the quasi-precious metal of Cu than Cd and Pb [36].

4. Surface functionalization of Fe_3O_4@SiO_2–X

In reaction (1), we can see the steps of surface modification of Fe_3O_4@SiO_2 core-shell to form Fe_3O_4@SiO_2–X, where X is a functional group. The layer of SiO_2 was usually coated on the surface of Fe_3O_4 using the Stöber method. The prepared Fe_3O_4 nanoparticles were used as cores and dispersed in ethanol, and it was added to a three-neck round-bottom flask in ethanol and deionized water. The solution of the concentrated ammonia solution was added. After 15 min, TEOS was added dropwise in 10 min. The mixture was allowed for mechanical stirring for 8 h to perform the silica coating. The produced Fe_3O_4@SiO_2 was separated and washed with deionized water and ethanol [37].

Direct modification by the use of organic compound is also studied, without first modification by silica. Magnetic nanoparticles modified with third-generation dendrimers followed by ethylenediaminetetraacetic acid (EDTA) were prepared and tested for their performance for recovery of precious metals that are Pd(IV), Au(III), Pd(II), and Ag(I) in the aqueous system [38]. It is interesting that high valence Pd(IV) and Au(III) exhibit relatively better adsorption efficiency than that of Pd(II) and Ag(I) with lower valence. It suggests that the adsorption of precious metals by this type of materials modified with EDTA is a function of valence. When the competing ion such as Zn(II) presents, the adsorption efficiency of the adsorbent for all four precious metals, which are Pd(IV), Au(III), Pd(II), and Ag(I), reduces much.

Magnetite nanoparticles could be directly modified with an organic compound of oleic acid. Iron oxide surface possibly bonds to carboxylic end of lauric acid [21]. However, this method of functionalization might not produce an acid-resistive magnetic adsorbent. The bond between lauric acid and magnetite could be easily damaged when the acidic solution is used. Therefore, the magnetite modified with lauric acid may find application in biological systems since both lauric acid and magnetite are biocompatible.

Silane compound such as (3-aminopropyl)trimethoxysilane (APTMS) could be used to coat magnetite nanoparticles. The product can be described as Fe_3O_4@SiO_2-CH_3-NH_2. Further surface modification by alginate gives Fe_3O_4@SiO_2-CH_3-NH_2-AA. The alginate forms the outer shell of the magnetite by electrostatic interaction with amine [39]. **Figure 1** shows a step-by-step extension of magnetite coating and functionalization. Silica coating will allow further functionalization via silanization, extension (additional of the spacer), and functional group attachment. The functional groups should be free to bond the metal ion either by an ionic or covalent coordination bond. Directed functional groups allow selective reaction with certain cation.

5. Characterization

Characterization of the magnetite can be done by at least five methods, which are vibrating sample magnetometer, powder X-ray diffraction, electron microscopy, elemental analysis, and infrared (IR) spectroscopy. The vibrating sample magnetometer (VSM) can reveal the magnetic properties of the magnetic materials. The microscopic images can be obtained commonly by the use of scanning electron microscopy (SEM), transmission electron microscopy (TEM), and atomic force microscopy (AFM). Nanomaterials are best to characterize by TEM and AFM. The IR spectroscopy is useful to detect the functional groups present on the magnetite surface. The IR spectroscopy is one of the methods to make sure that functionalization of the surface is successful.

For elemental analysis, a nondestructive energy dispersive X-ray spectrometry (EDS) can be used to estimate the chemical composition. The SEM is usually equipped with EDS system. The EDS results may lack precision and accuracy; however, it can detect the chemical composition in situ. The destructive methods such as atomic absorption spectrometry, UV–Vis spectrometry, and so forth may be used in place of EDS method. The destructive methods are usually not of choices for this type of materials.

One major analytical method in the magnetite characterization is powder X-ray diffraction. **Figure 4** shows the XRD patterns of Fe_3O_4 and Fe_3O_4/SiO_2 solid nanoparticle core-shell. The Fe_3O_4 diffraction patterns have five main peaks at 2θ values of 30.1°, 35.5°, 43.3°, 57.1°, and 62.5°. The Fe_3O_4 has a cubic system as confirmed by JCPDS Card No. 88–0315. The magnetite phase can be detected with certainty by XRD. However, when it is coated with silica, the intensity of the XRD peaks will be much diminished since silica is an amorphous solid. Further decrease in the XRD is expected after organic modification on top of the silica layer.

The FT-IR could also be useful for more characterization of magnetic materials. It can offer details of the bond between the core, the shells, and the surface modifiers. Here is the example, the FT-IR spectra of Fe_3O_4 and Fe_3O_4/SiO_2 nanoparticle core-shell are presented in **Figure 5**. Both spectra have a broad peak at 586 cm^{-1}. The peak is attributed to the Fe-O stretching mode of magnetite. The peak at 3400 cm^{-1} is due to the O-H stretching mode. The sharp peak at 1100 cm^{-1} can be attributed to the Si-O-Si stretching mode. The Si-O bending vibration

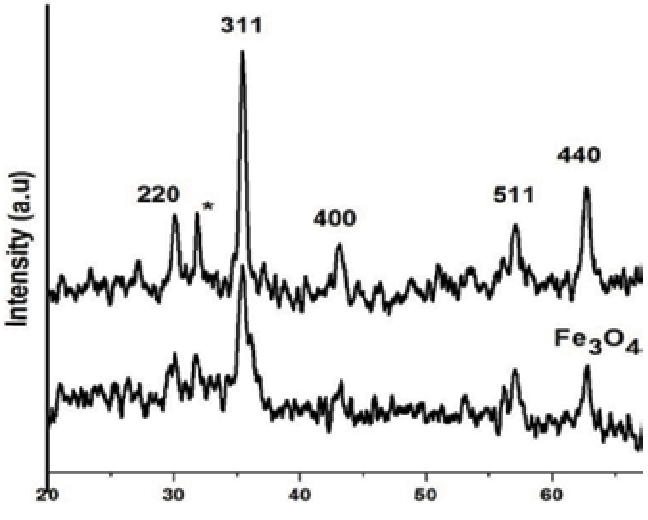

Figure 4. XRD patterns of Fe_3O_4 (top) and Fe_3O_4/SiO_2 nanoparticle core-shell modified with a thiol group (bottom) [3].

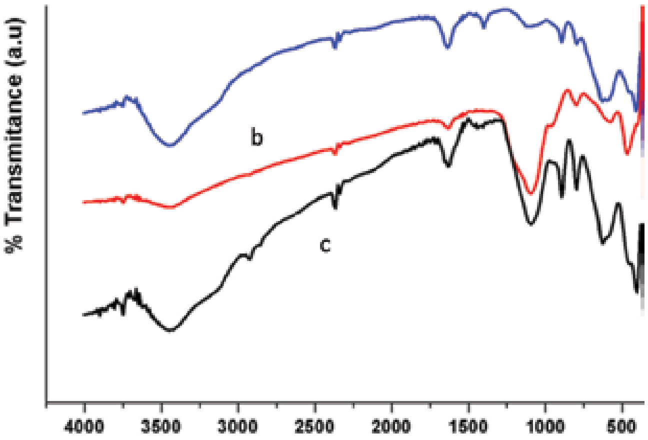

Figure 5. FT-IR spectra of resulted Fe_3O_4 (a), Fe_3O_4/SiO_2 nanoparticle core-shell (b), and Fe_3O_4/SiO_2 nanoparticle core-shell modified with a thiol group (c) [3].

mode of the silanol group is seen at 964 cm^{-1}. It indicates that the silica has coated well the outer surface of Fe_3O_4 particles [3]. The surface modification of Fe_3O_4/SiO_2 nanoparticles by thiol groups can give a better interaction with $[AuCl_4]^-$ ions in the solution. The FT-IR spectra of the Fe_3O_4/SiO_2 nanoparticle core-shell after modification with thiol group are shown in **Figure 5**. The peak at 686 cm^{-1} is attributed to the C-S bending vibration mode. The peak at near 2570–2590 cm^{-1} is attributed to the stretching vibration mode of S-H. The S-H stretching vibration mode is not usually detected [2]. The band at around 2850–2900 cm^{-1} is due to the stretching vibration of C-H of methylene. This result suggests that the surface modification of Fe_3O_4/SiO_2 nanoparticle core-shell is successful.

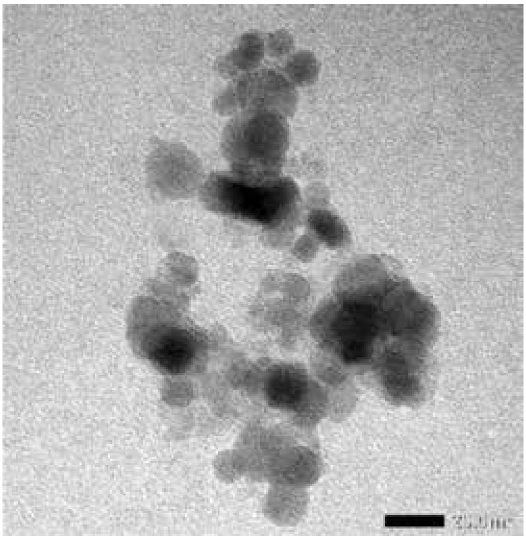

Figure 6. TEM image of Fe_3O_4/SiO_2 nanoparticle core-shell [3].

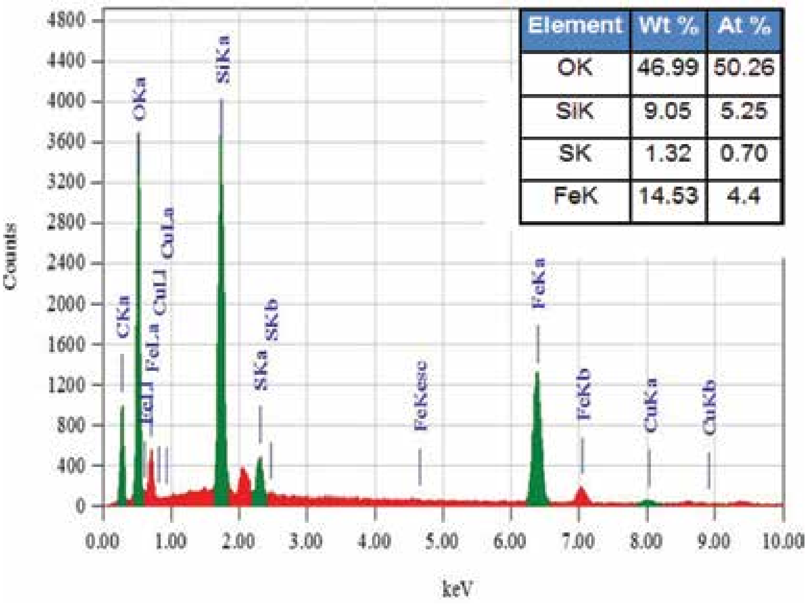

Element	Wt %	At %
OK	46.99	50.26
SiK	9.05	5.25
SK	1.32	0.70
FeK	14.53	4.4

Figure 7. EDX spectra of Fe_3O_4/SiO_2 nanoparticles modified with thiol group [3].

The covering of Fe_3O_4 nanoparticle core-shell by using silica does not only protect the magnetite core from dissolution in acid but also control the agglomeration of Fe_3O_4 particles. Silica acts as a capping agent for each Fe_3O_4 nanoparticle to form Fe_3O_4/SiO_2 core-shell. **Figure 6** shows the TEM images of Fe_3O_4/SiO_2 nanoparticle core-shell. The Fe_3O_4/SiO_2 nanoparticle core-shell has a size of approximately 10–20 nm. The size of Fe_3O_4/SiO_2 core-shell can be observed. These results prove that the synthesis of Fe_3O_4/SiO_2 nanoparticle core-shell is successful.

In situ analysis of adsorbent is preferable to understand the chemical composition of the product without a change in its nature. **Figure 7** shows the EDX spectra of modified Fe_3O_4/SiO_2 solid nanoparticle core-shell. The sulfur content is 1.32% (w/w). It suggests that thiol group is present on the surface of Fe_3O_4/SiO_2 nanoparticle core-shell material. It confirms the FT-IR spectra. The modification of Fe_3O_4/SiO_2 solid nanoparticle core-shell by 3-MPTS will give free thiol groups on the nanoparticles' surface. The thiols are expected to form covalent coordination bond with the target ion.

The EDX may also give details of atomic mapping across the sample, especially that of the functional group. For example, sulfur atom in the thiol group is mapped by the EDX method nicely. Functional groups such as amine, thiol, sulfonate, and phosphate may be better detected by EDX rather than destructive methods such as UV–Vis spectrophotometry.

6. Adsorbent performance

Table 2 shows a comparison of adsorbent performance for adsorption of precious metals especially gold and palladium [3, 38]. The first two rows show the adsorption performance of

Adsorbents	Adsorption capacity (mg/g)			Reference
	Au(III)	Pd(II)	Ag(I)	
Magnetite nanoparticles/thiolated	115	—	—	[3]
Magnetite nanoparticles/dendrimer	3.58	2.71	—	[38]
Magnetite nanoparticles/thiourea	118.5	111.6	—	[40]
Magnetite nanoparticles/chitosan	709.2	—	226.5	[41]
Magnetite nanoparticles/chitosan	59.5	—	—	[42]
Primary amine-lignin	384	40.43	—	[43]
Ethylenediamine-lignin	606.76	22.66	—	[43]

Table 2. Comparison of adsorption capacities (q_{max}) of some adsorbents for selected precious metals from aqueous solution. Data presented here are based on the Langmuir isotherm.

magnetic material modified with thiol and dendrimers. It shows that functionalization of the magnetite is very important to increase the adsorption capacity. Thiol group on the surface of magnetite produces high affinity toward Au(III). As we know, thiol can strongly react with gold to form a covalent bond. However, the adsorption capacity of magnetite is still far below that of adsorbent produced by the use of lignin as a precursor.

An adsorbent of magnetic nanoparticles modified by thiourea for effective and selective adsorption of precious metals like gold(III), palladium(II), and platinum(IV) in aqueous acid solution has also been reported. It needs contact time of less than 30 min to reach maximum capacity. Its maximum adsorption capacity of precious metals as determined by Langmuir model was 43.34, 118.46, and 111.58 mg/g for Pt(IV), Au(III), and Pd(II), respectively, at pH 2 and 25°C [40]. The adsorption is selective for Au(III) even in the presence of high concentrations of interfering ion Cu(II). The recycling was achieved by the use of a solution containing 0.7 M thiourea and 2% HCl. The result of the adsorption–desorption test shows that the adsorbent is reusable for the recovery of precious metals.

In general, the adsorption capacity of the magnetite-based adsorbent can reach up to 118.46 mg/g, which is very promising. It may still be less than that of lignin derivatives. For chitosan-modified magnetite, it even can reach the capacity for gold(III) of 707 mg/g [41]. The core-shell-modifier based adsorbent may not have such a high adsorption capacity. The modification step was done through the reaction between chitosan and polymeric Schiff's base of thiourea/glutaraldehyde in the presence of magnetite.

After adsorption test, desorption of the adsorbed cation must also be examined. Complete desorption of the adsorbed cation indicates a better adsorbent performance. In most cases, the acids can desorb adsorbed ion from the surface. The desorption process may use strong acids such as HCl, H_2SO_4, and HNO_3. The cation is believed to form complex coordination bonds with the surface, and leaching them is difficult.

On the other hand, application of concentrated acid solution may damage the structure of adsorbent. Therefore, mildly acidic solutions are usually employed to release the cation from the adsorbent's surface. People use a complexing agent to release the adsorbed metal cations. Thiourea and EDTA are of important environmentally friendly complexing agents.

Thiourea solution in 1 M HCl was employed to liberate $[AuCl_4]^-$ ions that had been adsorbed by the material [3]. Thiourea has a better affinity than that of thiol and amine groups. It can form a complex ion with $[AuCl_4]^-$ ion to dissolve back into the solution. According to the HSAB theory, both thiol and $[AuCl_4]^-$ ion are among the weak bases. A strong coordination bond forms between thiourea and $[AuCl_4]^-$ ion.

Figure 8 depicts the curve of desorption of $[AuCl_4]^-$ ion by thiourea in 1 M HCl solution at various concentrations following adsorption by the magnetite modified with a thiol group. Dilute thiourea solution can only desorb 43 mg/g $[AuCl_4]^-$ ion of initially adsorbed 68 mg/g or 60% of the total $[AuCl_4]^-$ ions bond to the surface. **Figure 9** displays schematic adsorption

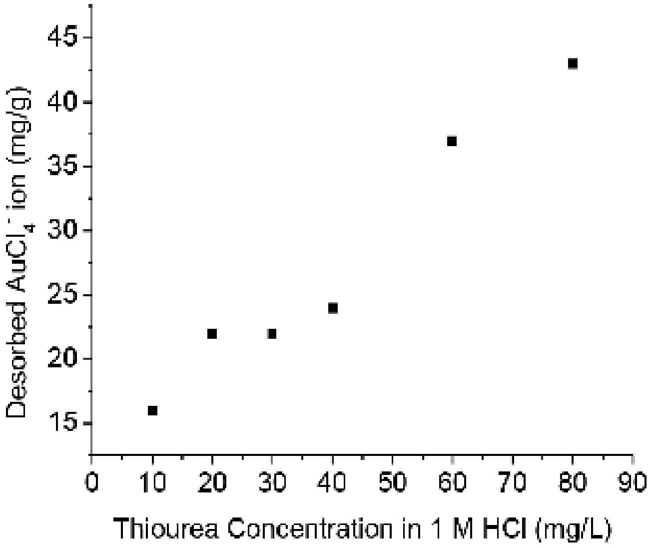

Figure 8. Profile of $[AuCl_4]^-$ ion desorption by HCl/thiourea at various concentration [3].

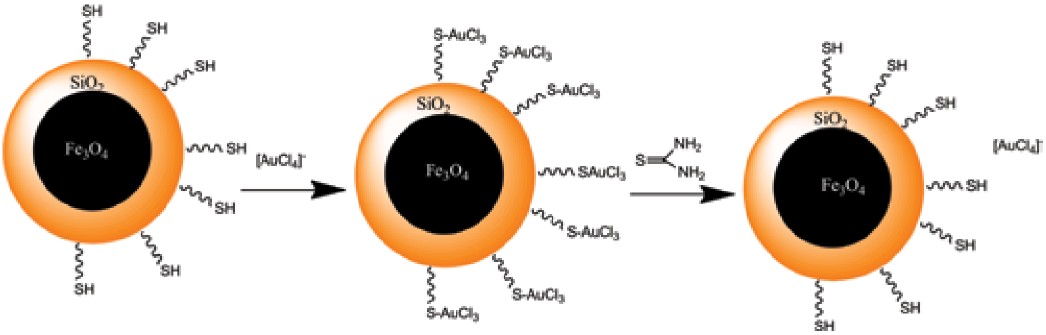

Figure 9. Adsorption and desorption of $AuCl_4^-$ ions by magnetite nanoparticles modified with a thiol group [3].

of $[AuCl_4]^-$ ion by magnetite modified with a thiol group and desorption. The desorption is done by applying thiourea in HCl solution. The concentration of the thiourea is low. The thiol group may form a covalent coordination bond with $[AuCl_4]^-$ ion on the adsorbent surface.

7. Summary

Modified magnetic adsorbents have been synthesized and used in the recovery of precious metals from aqueous solutions. Among the magnetic materials, magnetite is studied widely. Surface modification of nanoscale magnetite core is crucial to have a better adsorption capacity, stability, and turnover. The key issues of the magnetic adsorbent include size and shape of the core, choice of surface modification, adsorption capacity, stability, and recyclability. The size of the magnetite core is also better if it is in the nanoscale rather than in micron scale. It will improve the contact between pursued ions and adsorbent surface. The surface modification must have a good affinity toward certain precious metal cations. Many researchers attempt to combine adsorption capability and magnetic properties of the magnetite-based adsorbent for certain metal recovery from the solution. Selective adsorbents are also of interest for separation of precious metals from a complex system such as industrial waste. Adsorption selectivity is highly considered for complex matrices. Magnetite core has low stability in strongly acidic aqueous media. Coating with silica has two advantages, for protection against the acidic environment and a binding site for further functionalization. A suitable modification of the magnetic particles by coating or functionalization using inorganic components or organic molecules is usually needed.

The synthesis of magnetite as the core material has been established. The use of salts of Fe(II) and Fe(III) with careful stoichiometric calculation is a must. The pH of the magnetic formation should also be controlled, either by the use of sodium hydroxide or ammonia solution. In many cases, ammonia can give better homogeneous particles. It may be better to add a stabilizing agent for reducing aggregation of the magnetite nanoparticle and improve the stability of the colloid. Coating of magnetite with silica has also been well understood. TEOS and TMOS are the main choices for the outer shell of the magnetite, although sodium silicate may work. Silica is a preferable coating since it is resistant to acid and base, which will protect the magnetite core.

The final surface modification is functionalization of the silica with ligands that will strongly bind the cations. The end of the modification chain must have a special interaction with the cations, especially through coordination bonds. The functional groups could be an amine, carboxylate, thiol, sulfonate, amide, hydroxyl, and so on. Based on reagent availability, the functional groups determine the selectivity toward certain precious metal cations.

The release of the adsorbed metal cations after being concentrated in the adsorbent can be realized using acids and strong complexing agents. The acids are usually not desirable since they can cause the magnetite core to dissolve. Dissolution will damage the structure of the magnetite, which may not be possible to reuse. Complexing agents such as thiourea and EDTA can give a better option to minimize the damage to the magnetite-based adsorbents.

Purification of the recovered metals may be done through well-known processes. Electrochemical process is the best choice of metallurgy. Other methods by the use of chemical reduction could also be selected. In the large scale, we can consider blast furnace combined with a redox reaction. One important point to consider, the use of environmentally friendly reprocessing of the metals must always be prioritized.

8. Future recommendation and direction

The conventional metal reprocessing uses chemicals that are not environmentally friendly. The magnetite-based adsorbents offer technology that can reduce the application of toxic chemicals. The adsorbents give the possibility to reduce, reuse, and recycle for a few times. The magnetic core of the adsorbent is also readily synthesized with environmentally benign precursors. The coating with silica protects against acid and base media during application and recycle. The silica coating can also facilitate the attachment of the functional groups, which is critical in the modification step.

The current advanced electronic devices utilize the precious metals in their important components. The waste of electronic devices grows rapidly along with an increase in smartphone and PC use. Computer parts like processors, memories, motherboards, hard drives, and CD/DVD drives contain gold and other precious metals such as silver, palladium, and so on. The conventional gold recovery process uses cyanide ions for complex ion formation and electrolysis. The current technology attempts to recover gold and other precious metals from computers' and smartphones' components by utilizing magnetite nanoparticles. The new magnetic materials are effective yet environmentally friendly to recover precious metals. The magnetic adsorbents could also be the future of reclaiming precious metals from the waste of the other industries.

In the magnetic adsorbent development, the magnetite core could be possibly substituted with other oxides of transition metals such as manganese, cobalt, or nickel if they maintain strong magnetic characters. However, silica is the main choice for easy coating of the magnetic core, which also helps protect the magnetic core from dissolution in the acidic and basic media. The presence of the ligands on the surface of the magnetite-silica core-shell is critical for adsorption process. The environmentally safe polymers and simple molecules may be used to facilitate coordination bond with the target cations. The desorption process must be done using suitable solutions. The solution for desorption should leave the adsorbent in good shape for further reuse and turnover. The present technology available for purification of the recovered metals may apply electrochemical, chemical, and thermal processes.

Symbols and abbreviations

AFM	atomic force microscopy
APTMS	aminopropyl trimethoxysilane

DEG	diethylene glycol
EDTA	ethylenediamine tetraacetate
EDA-MMA-OA	ethylenediamine, methyl methacrylate, and oleic acid
EDX	energy dispersive X-ray spectroscopy
JCPDS	Joint Committee on Powder X-ray Diffraction Standards
MPTS	mercaptopropyltrimethoxysilane
NPs	nanoparticles
PVA	polyvinyl alcohol
q_e	maximum capacity of adsorbent (mg/g)
SEM	scanning electron microscopy
TEOS	tetraethyl orthosilicate
TEM	transmission electron microscopy
VSM	vibrating sample magnetometer

Author details

Roto Roto

Address all correspondence to: roto05@ugm.ac.id

Department of Chemistry, Faculty of Mathematics and Natural Sciences, Universitas Gadjah Mada, Yogyakarta, Indonesia

References

[1] Haw CY et al. Hydrothermal synthesis of magnetite nanoparticles as MRI contrast agents. Ceramics International. May 2010;**36**(4):1417-1422

[2] Zhang S et al. Thiol modified Fe_3O_4@SiO_2 as a robust, high effective, and recycling magnetic sorbent for mercury removal. Chemical Engineering Journal. Jun. 2013;**226**:30-38

[3] Roto R, Yusran Y, Kuncaka A. Magnetic adsorbent of Fe_3O_4@SiO_2core-shell nanoparticles modified with thiol group for chloroauric ion adsorption. Applied Surface Science. 2016;**377**:30-36

[4] Morel A et al. Sonochemical approach to the synthesis of Fe_3O_4@SiO_2 Core–Shell nanoparticles with tunable properties. ACS Nano. 2008;**2**(5):847-856

[5] El-kharrag R, Amin A, Greish YE. Low temperature synthesis of monolithic mesoporous magnetite nanoparticles. Ceramics International. Jan. 2012;**38**(1):627-634

[6] Lin J, Lai Q, Liu Y, Chen S, Le X, Zhou X. Laccase–Methacryloyl functionalized magnetic particles: Highly immobilized, reusable, and efficacious for methyl red decolourization. International Journal of Biological Macromolecules. 2017;**102**:144-152

[7] Peng L et al. Modifying Fe_3O_4 nanoparticles with humic acid for removal of Rhodamine B in water. Journal of Hazardous Materials. 2012;**209-210**:193-198

[8] Nigam S, Barick KC, Bahadur D. Development of citrate-stabilized Fe_3O_4 nanoparticles: Conjugation and release of doxorubicin for therapeutic applications. Journal of Magnetism and Magnetic Materials. 2011;**323**(2):237-243

[9] Zhang JM, Zhai SR, Zhai B, Da An Q, Tian G. Crucial factors affecting the physicochemical properties of sol-gel produced $Fe_3O_4@SiO_2\text{-}NH_2$ core-shell nanomaterials. Journal of Sol-Gel Science and Technology. 2012;**64**(2):347-357

[10] Hakami O, Zhang Y, Banks CJ. Thiol-functionalised mesoporous silica-coated magnetite nanoparticles for high efficiency removal and recovery of hg from water. Water Research. 2012;**46**(12):3913-3922

[11] Aghaei E, Alorro R, Encila A, Yoo K. Magnetic adsorbents for the recovery of precious metals from leach solutions and wastewater. Metals (Basel). 2017;**7**(12):529

[12] Narayan R editor. Nanobiomaterials: Nanostructured Materials for Biomedical Applications, Magnetic Nanoparticle Synthesis. Amsterdam: Elsevier Ltd; 2017. Chapter 8. p. 197-229

[13] Grüttner C, Müller K, Teller J, Westphal F. Synthesis and functionalisation of magnetic nanoparticles for hyperthermia applications. International Journal of Hyperthermia. 2013;**29**(8):777-789

[14] Ni S et al. Hydrothermal synthesis of Fe_3O_4 nanoparticles and its application in lithium ion battery. Materials Letters. 2009;**63**(30):2701-2703

[15] Valenzuela R et al. Influence of stirring velocity on the synthesis of magnetite nanoparticles (Fe_3O_4) by the co-precipitation method. Journal of Alloys and Compounds. Nov. 2009;**488**(1):227-231

[16] Mahmoud ME, Amira MF, Zaghloul AA, Ibrahim GAA. Microwave-enforced sorption of heavy metals from aqueous solutions on the surface of magnetic iron oxide-functionalized-3-aminopropyltriethoxysilane. Chemical Engineering Journal. 2016;**293**:200-206

[17] Yu LQ, Zheng LJ, Yang JX. Study of preparation and properties on magnetization and stability for ferromagnetic fluids. Materials Chemistry and Physics. 2000;**66**(1):6-9

[18] Zhang DE, Tong ZW, Li SZ, Zhang XB, Ying A. Fabrication and characterization of hollow Fe_3O_4 nanospheres in a microemulsion. Materials Letters. 2008;**62**(24):4053-4055

[19] Zhang H, Zhu G. One-step hydrothermal synthesis of magnetic Fe_3O_4 nanoparticles immobilized on polyamide fabric. Applied Surface Science. 2012;**258**(11):4952-4959

[20] Liao M-H, Chen D-H. Preparation and characterization of a novel magnetic nano-adsorbent. Journal of Materials Chemistry. 2002;**12**(12):3654-3659

[21] Mahdavi M et al. Synthesis, surface modification and characterisation of biocompatible magnetic iron oxide nanoparticles for biomedical applications. Molecules. 2013; **18**(7):7533-7548

[22] Khosroshahi ME, Ghazanfari L. Preparation and characterization of silica-coated iron-oxide bionanoparticles under N2 gas. Low-dimensional systems and nanostructures. 2010;**42**(6):1824-1829

[23] Yang C, Yan H. A green and facile approach for synthesis of magnetite nanoparticles with tunable sizes and morphologies. Materials Letters. 2012;**73**:129-132

[24] Feng X, Guo H, Patel K, Zhou H, Lou X. High performance, recoverable Fe_3O_4 ZnO nanoparticles for enhanced photocatalytic degradation of phenol. Chemical Engineering Journal. 2014;**244**:327-334

[25] Habila MA, Alothman ZA, El-Toni AM, Labis JP, Soylak M. Synthesis and application of Fe_3O_4@SiO_2@TiO_2 for photocatalytic decomposition of organic matrix simultaneously with magnetic solid phase extraction of heavy metals prior to ICP-MS analysis. Talanta. 2016;**154**:539-547

[26] Liu H, Jia Z, Ji S, Zheng Y, Li M, Yang H. Synthesis of TiO_2/SiO_2@Fe_3O_4 magnetic microspheres and their properties of photocatalytic degradation dyestuff. Catalysis Today. 2011;**175**(1):293-298

[27] Ghosh Chaudhuri R, Paria S. Core/shell nanoparticles: Classes, properties, synthesis mechanisms, characterization, and applications. Chemical Reviews. 2012;**112**(4):2373-2433

[28] Stober W, Fink A. Controlled growth of Monodispersed silica spheres in the Micron size range. Journal of Colloid and Interface Science. 1968;**26**:62-69

[29] Liu J et al. Extension of the stöber method to the preparation of monodisperse resorcinol-formaldehyde resin polymer and carbon spheres. Angewandte Chemie, International Edition. 2011;**50**(26):5947-5951

[30] Gholami T, Salavati-niasari M, Bazarganipour M. Superlattices and microstructures synthesis and characterization of spherical silica nanoparticles by modified Stöber process assisted by organic ligand. Superlattices and Microstructures. 2013;**61**:33-41

[31] Abd Razak NF, Shamsuddin M, Lee SL. Adsorption kinetics and thermodynamics studies of gold(III) ions using thioctic acid functionalized silica coated magnetite nanoparticles. Chemical Engineering Research and Design. 2018;**130**:18-28

[32] Abdelwahab NA, Morsy EMH. Synthesis and characterization of methyl pyrazolone functionalized magnetic chitosan composite for visible light photocatalytic degradation of methylene blue. International Journal of Biological Macromolecules. 2018;**108**:1035-1044

[33] Ranjbar R, Naderi M, Omidvar H, Amoabediny G. Gold recovery from copper anode slime by means of magnetite nanoparticles (MNPs). Hydrometallurgy. 2014;**143**:54-59

[34] Chiou CS, Chuang KJ, Chen HW, Chen YC. Magnetite modified with amine polymer to adsorb indium ions. Powder Technology. 2015;**279**:247-253

[35] Lopes JL, Marques KL, Girão AV, Pereira E, Trindade T. Functionalized magnetite particles for adsorption of colloidal noble metal nanoparticles. Journal of Colloid and Interface Science. 2016;**475**:96-103

[36] Ren Y, Abbood HA, He F, Peng H, Huang K. Magnetic EDTA-modified chitosan/SiO_2/Fe_3O_4 adsorbent: Preparation, characterization, and application in heavy metal adsorption. Chemical Engineering Journal. 2013;**226**:300-311

[37] Habila MA, Alothman ZA, El-Toni AM, Labis JP, Soylak M. Synthesis and application of Fe_3O_4@SiO_2@TiO_2 for photocatalytic decomposition of organic matrix simultaneously with magnetic solid phase extraction of heavy metals prior to ICP-MS analysis. Talanta. 2016;**154**:539-547

[38] Yen CH, Lien HL, Chung JS, Der Yeh H. Adsorption of precious metals in water by dendrimer modified magnetic nanoparticles. Journal of Hazardous Materials. 2017;**322**: 215-222

[39] Yang L et al. Modification and characterization of Fe_3O_4 nanoparticles for use in adsorption of alkaloids. Molecules. 2018;**23**:562

[40] Lin TL, Lien HL. Effective and selective recovery of precious metals by thiourea modified magnetic nanoparticles. International Journal of Molecular Sciences. 2013;**14**(5): 9834-9847

[41] Donia AM, Atia AA, Elwakeel KZ. Recovery of gold(III) and silver(I) on a chemically modified chitosan with magnetic properties. Hydrometallurgy. 2007;**87**(3-4):197-206

[42] Chang YC, Chen DH. Recovery of gold(III) ions by a chitosan coated magnetic nano-adsorbent. Gold Bulletin. 2006;**39**(3):98-102

[43] Parajuli D, Kawakita H, Inoue K, Funaoka M. Recovery of gold(III), palladium(II), and platinum(IV) by aminated lignin derivatives. Industrial and Engineering Chemistry Research. 2006;**45**(19):6405-6412

Chapter 8

Hidden Resources of Coordinated XPS and DFT Studies

Alexander R. Cholach

Additional information is available at the end of the chapter

http://dx.doi.org/10.5772/intechopen.80002

Abstract

Electronic configuration of chemically bound atoms, at the surface or in the bulk of a solid, contains the traps for energy absorption provided by the valence band electron transitions; the core-level excitation of any origin is coupled with traps forming the multichannel route for energy dissipation. This chapter displays tracing over these channels by means of X-ray photoelectron spectroscopy (XPS) and density functional theory (DFT). Conformity between energy losses in the XPS spectra and electron transitions in relevant unit cells is verified by the examples of the pristine and half fluorinated graphite C_2F, and the Br_2-embedded C_2F. Perfect XPS-DFT combination can be useful for material science providing exhaustive data on state and geometry of the atoms in a sample, regardless the field of its application. The valence band is insensitive to the energy source for its excitation. It makes the behavior of energy losses in XPS spectra of the atoms to be a descriptor of bonding between these atoms in multicomponent materials. Moreover, the state of any component can be tracked through change or invariability of satellites in the relevant XPS spectra, obtained in the course of the external influence, thus revealing a wear performance of the material.

Keywords: X-ray photoelectron spectroscopy, photoelectron energy losses, valence band, electron transitions, density functional theory

1. Introduction

Fundamental studies in the field of surface science form the grounds for the sustained development of advanced technologies and new composite materials and catalysts with the desired properties [1, 2]. The methods of electron spectroscopy are unique tools of the basic research enabling characterization of the structure, composition, and properties of solids and interfaces at the atomic-molecular level.

Key properties of a sample are often exposed in their responses to a core-level excitation. The specific responses have been discovered using the tunable synchrotron irradiation and became the basis of advanced techniques [3]. The X-ray absorption fine structure (XAFS) appears near the edge of photoionization threshold (XANES) and reveals the vacant state structure, while the XAFS beyond the absorption edge (EXAFS) exhibits the local geometry [4]. The resonant inelastic X-ray scattering (RIXS) is enabled by the energy and momentum transferred by a photon near the absorption edge and exhibits the intrinsic excitations [5]. Resonant photoemission (RPES) and Auger electron spectroscopy (RAES) disclose the local electronic structure and correlations in a system, respectively [6]. The use of the electron impact instead of the X-ray, as a source of the core-level excitation, has discovered the similar effects of the conjugate electron excitation (CEE) [7–11]. The CEE shows itself as a set of satellites in disappearance potential spectra (DAPS), which answers to valence band (VB) structures of near-surface atoms, including the adsorbed species, and plasmon excitations. Experimental evidence for the CEE phenomenon is based on DAPS spectra, obtained from various adsorbed layers and on its mechanism represented by the combination of ordinary electron transitions. For example, plasmon oscillations are often observed by means of X-ray photoelectron (XPS) and Auger electron spectroscopies (AES) [12, 13]. Ionization of the VB, of the substrate and adsorbed species, is a basis of ultraviolet photoelectron spectroscopy (UPS) [14]. Similar satellite structures, above different thresholds, in DAPS spectra confirm that the core electrons are identical with regard to CEE transitions [7, 8]. CEE phenomena represent, in whole, the multichannel route for energy dissipation within the DAPS probing depth of 2–3 monolayer (ML), which does not undermine the general concepts in the field of electron scattering.

Novel as well as advanced technologies strongly require the next generation materials in the fields of tribology [15–17], hardness [18, 19], corrosion and wear performance of the material [20], and many others [21–23]. The progress of material science in these fields is resulted, in large measure, from the fundamental studies by means of modern techniques, including the XPS as well [16, 17, 21–23]. The X-ray photoelectron spectroscopy is a powerful analytical tool; however, this method is limited by the content and charge state of the atoms, while it cannot disclose the chemical behavior and structural features of the atoms in a sample, which are urgently needed in case of the multicomponent substrate. These properties and many others are direct products of the DFT. In turn, the DFT runs give greatly different results depending on starting conditions and the operational parameters, which have to be found indirectly. A reliable intersection between the XPS and DFT outputs would help to employ the hidden resources of both techniques.

The CEE phenomenon is a true multi-channel route of energy dissipation through the VB. The identity of electronic nature of the surface and bulk atoms allows one to suggest the similarity of inelastic electron scattering mechanisms on the surface and in the bulk of a solid. Then, the CEE should also occur, under the X-ray core-level excitation, and manifest itself in the XPS spectra as energy losses. The plasmons in AES and XPS spectra correspond indeed to the collective CEE phenomena. Highest occupied molecular orbital-lowest unoccupied molecular orbital (HOMO-LUMO) transitions, which are often used for assignment the XPS, RPES and XANES spectra [24, 25], are also clear CEE manifestations. The electron energy dissipation, accompanying the core-level excitation, is the general trend of any electronic configuration.

Auger transitions are particular cases of the event resulted from filling the core hole. CEE is another route of relaxation consisting in redistribution of the photoelectron energy through the accessible valence bands.

A close attention is paid to the graphite materials as essential parts of the advanced technical devices [26]. Fluorinated graphite serves as an intermediate of the graphene synthesis, while embedded with the alkali or halogen, exhibits high chemical stability, improves the anode activity in a fuel cell, becomes the nano-reactor or the storage nano-container of volatile compounds, and so on [27–29]. We have considered highly orientated pyrolytic graphite (HOPG), half-fluorinated HOPG (C_2F), and that with the embedded Br_2 (C_2F *0.15Br) as touchstones of the following concept [30, 31]. First, inelastic electron scattering, in near-surface layer and in the bulk of a solid, follows the same regularities. Second, the X-ray core-level excitation is accompanied by the VB transitions revealing themselves as the photoelectron energy losses. Third, linking of the XPS and DFT methods via conformity between XPS spectral structures and theoretical CEE transitions justifies the other DFT products related to local geometry, chemical bonding, and states of the atoms in a sample.

2. Experimental

Inelastic electron scattering has been monitored by the elastic scattering, using the DAPS. Disappearance potential spectroscopy is based on the threshold core-level excitation by an electron beam of the time-based energy E_p [32]. Whenever the incident potential exceeds the core-level energy, a part of electrons disappears from the elastic current I and provides a dip in the dependence of $dI(E_p)/dE_p$ on E_p. The event occurs if E_p is equal to difference between the core and vacant state energy. The spectrum shape is determined by the self-convolution of vacant density of states (DOS), as the destination of interacting electrons. The adsorption of test gases over the Auger-clean Pt(100)-(1 × 1) single crystal was performed at 300 K [33]; exposures are given in Langmuir (1 L = 10^{-6} Torr s). The Fermi level (E_F) in DAPS spectra corresponds to $E_p = 314.8$ eV, which is close to the reference $Pt4d_{5/2}$ core-level energy [34]. Other experimental details and the spectrum processing can be found elsewhere [7–11].

The XPS studies were performed on a Phoibos 150 SPECS spectrometer (Germany) using monochromatized Al K_α radiation (1486.7 eV). The backgrounds of external and surface energy losses in XPS spectra have been subtracted [35]. Other experimental details, the low-temperature synthesis technique, and characterization of HOPG, pristine and fluorinated C_2F can be found elsewhere [36, 37]. The Br_2 embedding into C_2F was performed as in Ref. [38] and resulted in the $\sim C_2FBr_{0.15}$ stoichiometry.

3. Theoretical

Geometric parameters and DOS of the unit cells were calculated by the density functional theory using the Quantum ESPRESSO Software [39] and the nonlocal exchange-correlation functional in the Perdew-Burke-Ernzerhof parameterization [40]. The interactions between ionic cores and electrons were described by the projected augmented wave (PAW) method [41] with the kinetic energy cutoff $E_{cut} = 40$ Ry (320 Ry for the charge-density cutoff) for a plane-wave basis set. The Gaussian spreading for the Brillouin-zone integration was 0.02 Ry; the Marzari-Vanderbilt cold smearing was used [42], and the van der Waals (vdW) corrections were included [43].

The Pt DOS was calculated using the Perdew-Burke-Ernzerhof functional [44] and the PAW with the optimized lattice constant 3.99 Å. The kinetic energy cutoff $E_{cut} = 40$ Ry and a 12 × 12 × 12 grid of Monkhorst-Pack k-points were applied.

HOPG was modeled with a bilayer C_{24} unit cell of the Bernal and Hexagonal (*hex*) structure (**Figure 1**) and optimized lattice parameters ($a = 2.46$ Å × 3, $b = 2.46$ Å × 2) [45].

Half-fluorinated graphite, pristine and imbedded with the Br_2 molecule, was modeled with a bilayer $C_{24}F_{12}$ and $C_{24}F_{12}Br_2$ unit cell, respectively, with the optimized lattice parameters $a = 2.49$ Å × 3, $b = 2.48$ Å × 2 for the *hex* structure and $a = 2.50$ Å × 3, $b = 2.48$ Å × 2 for the Bernal structure. The F was attached to C atoms all outside and half inside and half outside a cell (**Figure 1**) with 40 Bohr space between slabs to prevent the interactions. In latter case, the entry interlayer distance d_{layer} in a $C_{24}F_{12}Br_2$ unit cell was taken larger by 2 Å than optimized d_{layer} in a $C_{24}F_{12}$ unit cell (in order to avoid unrealistic Br_2F formation or F ↔ Br_2 replacement under relaxation of the system), in line with experimental measurements [46]. All atoms were allowed to move free under an optimization of the unit cells. The Brillouin-zone integration was performed on a 20 × 20 × 1 grid of Monkhorst-Pack k-points [47]. The accuracy was verified by testing the energy convergence. The default numbers of bands were used for free bromine particles.

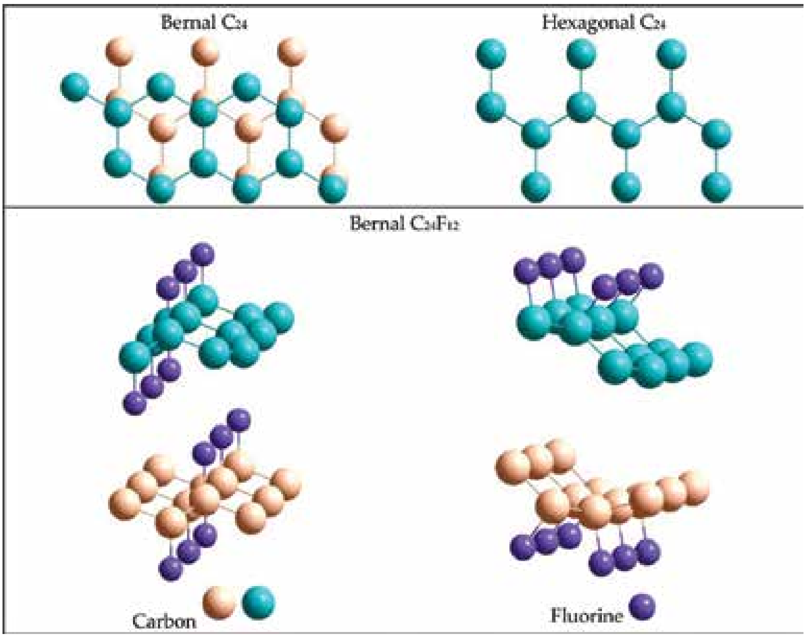

Figure 1. Unit cells C_{24} with the Bernal and *hex* structure (top panel) and unit cell $C_{24}F_{12}$ Bernal with arrangement of the F atoms half inside and half outside and all outside a cell. Adapted from [30].

4. Inelastic electron scattering in near-surface layer

DAPS theory directs core and primary electrons to nearest vacant states above E_F [32]. The larger is the vacant DOS, the larger is the spectral dip, and the lack of free DOS gives no signal. The DAPS technique discovers all channels of the elastic electron consumption, which are specifically related to CEE phenomena and consisted of shake-up and shake-off VB transitions coupled with the threshold core-level excitation of an atom. These channels are electron transitions from the ground σ_{VB} to vacant DOS σ_{Vac} and the vacuum level, whose probability $W(E)$ is in proportion to the corresponding convolution and σ_{VB}, respectively, on the absolute energy relative to E_F with a matrix element $f(E, \sigma)$:

$$\begin{aligned} W_{up}(E) &= \int_0^E f(E,\sigma)\,\sigma_{VB}(-E)\,\sigma_{Vac}(E-\varepsilon)d\varepsilon \\ W_{off}(E) &= f(E,\sigma)\,\sigma_{VB}(\varphi - E) \end{aligned} \tag{1}$$

The shake-off CEE moves σ_{VB} to free DOS at the vacuum level. According to the Rutherford relation $ds/d\Omega \sim \sin^4(\Theta/2)$, the cross-section for the nonrelativistic scattering is efficient for small angles Θ [48, 49]. The probability $W(E)_{off}$ in Eq. (1) therefore includes one-dimensional (1D) free DOS. According to Van Hove singularities, the 1D DOS is equal to 0, infinity, and $1/\sqrt{E - E_F - \varphi_{Pt}}$ at the energies below, at, and above the vacuum level, respectively [50], as shown in **Figure 2(a)** (where φ_{Pt} = 5.6 eV is the work function of Pt(100) [51]). This provides the resonant CEE behavior and multiple tracing over the adsorbed species (including hydrogen atoms and reaction intermediates) around different thresholds [8–11]. The shake-off satellite of adsorbed particle is an intense peak of the 1–2 eV base-width and coverage-proportional intensity, which is located at its ionization potential above the Pt threshold. The DAPS spectra in **Figure 2** particularly exhibit the σ state of the H_{ad} atom and 1π, 5σ, and 4σ states of the CO_{ad} molecule, which fit published UPS data in **Table 1** [52–55]. Similar accordance between the DAPS and UPS measurements has been found for the adsorbed O, N, NO, and NH species [7].

The Pt shake-off spectrum in **Figure 2(b, c)** was constructed on the basis of DFT data as follows. The VB was inverted (because the larger σ_{VB} the larger $W_{off}(E)$ in Eq. (1), and the larger the spectral dip); differentiated, and shifted to the higher energy by φ_{Pt}. Adsorbed layer makes significant contribution into the DAPS spectrum due to superior surface sensitivity of this technique, whose probing depth 2–3 ML is determined by half the electron mean free path in a solid. The Pt shake-up spectrum in **Figure 2(b)** corresponds to convolution of the occupied and vacant d states by Eq. (1). The calculated Pt shake-up and shake-off spectra in **Figure 2** are close to each other due to strongly localized vacant states at E_F and the 1D DOS at the vacuum level, respectively, and because of domination of the equal d_{zx}, d_{zy}, and d_{xy} states in total DOS [30]. An agreement between experimental and simulated spectral fragments in **Figure 2** implies regular involvement of the Pt DOS into CEE events, as well as similar matrix elements $f(E, \sigma)$ for different partial densities of states (pDOS) in Eq. (1) and no symmetry ban for CEE transitions.

Figure 2(b) demonstrates tracing over the adsorbed hydrogen atoms, which is beyond AES and XPS facilities. It is important to note that none of the satellites in the DAPS spectra was assigned to the interatomic CEE transition (from the VB of the adsorbed species to free state of

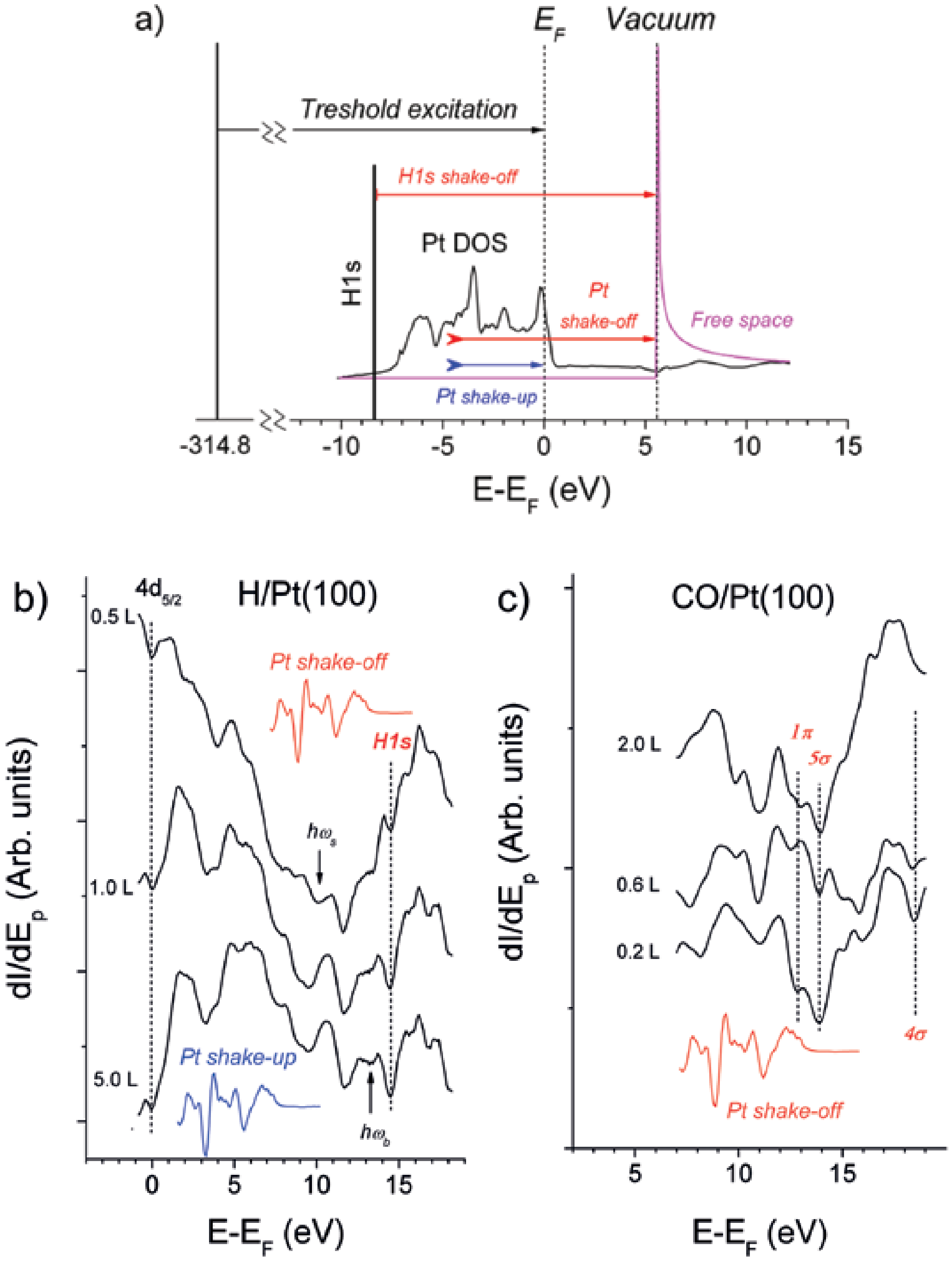

Figure 2. (a) General scheme of the CEE transitions by an example of H/Pt(100) system exposed to primary electron beam with energy above the Pt4$d_{5/2}$ threshold. (b) Difference DAPS spectra obtained after exposure of Pt(100) surface to H_2; colored curves indicate the Pt shake-up and shake-off satellites expected from (a). (c) DAPS spectra obtained after exposure of Pt(100) surface to CO; red curve shows the Pt shake-off satellites expected from (a). Adapted from [8].

Sample	O	H	CO			Source
Satellite	*O2p*	*H1s*	*1π*	*5σ*	*4σ*	
Gas	13.6	13.6	14.0	16.5	19.7	[34]
H/Pt(100)-(1 × 1)		13.7				**Figure 2a**
H/Pt(111)		12.8				[57]
CO/Pt(100)-(1 × 1)			12.7	13.7	18.3	**Figure 2c**
CO/Pt(111)			14.2	15.1	17.5	[53–55]
CO/Pt(100)-*hex*			13.4–15.8		16.4–18.0	[53]
O/Pt(100)-(1 × 1)	14.0					[10]
O/Pt(100)	12.7					[53]
O/Pt(111)	14.2					[12]
O/Pt(111)	12.1					[54, 57]

Table 1. Peak minima in the DAPS spectra as compared with the reference UPS data (eV).

the metal atom) [8, 10]. Furthermore, the surface plasmon disappears while the bulk plasmon decreases on coverage in **Figure 2(b)** because of screening by the adsorbed layer, in contrast to behavior of the VB CEE satellites [9]; multiple plasmons were also detected at relevant energy points [7]. Conformity between the calculated and experimental data in **Figure 2** indicates that the vacancies, at E_F and at the vacuum level as well, are appropriate spots of destination of the electrons under their CEE transitions. Present consideration confirms the generality of CEE phenomena under the inelastic electron scattering in the adsorbed system. The CEE control is an additional tool of electron analyzer for fingerprinting the adsorbed layer and an alternative to the RPES, which requires a tunable synchrotron irradiation and special instrumentation [6]. Besides that, the DAPS provides the vacant state structure and geometrical parameters similar to XANES and EXAFS, respectively [56].

CEE satellites of the adsorbed species accompany the threshold core-level excitation of that neighboring atom, which is bound to the above species, while core-level energies are easily distinguishable. Therefore, the CEE control empowers localization of the adsorbed species over multicomponent surface. CEE regularities in the near-surface layer can be summarized as follows:

- Shake-up transitions correspond to convolution of the occupied and unoccupied pDOS of the same atom and likely have no symmetry ban.
- Shake-off transitions are available for the substrate atom and adsorbed species as well, where the former is the energy source; the 1D DOS at the vacuum level is a common VB destination. There is no symmetry prohibition, and the satellite structure is a VB mirror-image with respect to E_F, shifted to higher energy by the work function.
- Plasmon oscillations give evidence for the collective CEE phenomenon.

5. Conjugate electron excitations in the bulk of a solid

The CEE phenomena occur with high probability in the near-surface layer of 2–3 ML [7–10]. Electronic affinity between surface and bulk atoms assumes similar channels of the inelastic electron scattering under the core-level excitation, no matter by primary electrons or X-ray irradiation. The photoelectron can partially lose its energy for the CEE transition and exhibits the VB peculiarities in fine XPS spectral structure. By analogy with the above findings, CEE phenomena in the bulk of a multicomponent material, under the nonresonant X-ray core-level excitation, can be characterized as follows:

- Shake-off transitions are available, where pDOSs must be considered due to probable difference in their matrix elements. The same ground state (VB), the common destination (the vacuum level), and enough energy excess of any of the photoelectrons should result in analogous energy losses in the XPS spectra of different components of a sample.
- Shake-up transitions are available, in which the convolution should include pDOSs of the same atom. The VB of chemically bound atoms has no preference for a photoelectron to detach its energy for the CEE transition, and so similar energy losses are also expected in the XPS spectra of different components of a sample.

This chapter focuses on the DAPS omitting the allied threshold excitation techniques of the Auger electron and soft X-ray appearance potential spectroscopies, which follow the core hole decay and are complicated, at least, by the electron-core hole interaction [32]. In contrast, the DAPS fixes origination of the core hole, when the electron–hole interaction is not yet occurred or minimal. The same is true for energy losses in the XPS spectra because the photon absorption and the CEE energy dissipation can proceed at once or shortly, thus eliminating or minimizing the electron-core hole interaction, respectively. It is worth noting that CEE events are enabled by belonging of former core and valence band electrons to the same configuration and can be hardly detectable by electron energy loss spectroscopy, while the AES spectra are usually complicated by the background.

5.1. HOPG and half-fluorinated graphite C_2F

DFT runs have revealed that density of states in **Figure 3(a)**, obtained for the C_{24} unit cells with the Bernal and *hex* structure, are similar and close to the DOS of graphite/graphene [58]. The optimized C-C bond length $d_{C\text{-}C} = 1.42$ Å and the interlayer distance $d_{\text{layer}} = 3.34$ Å in *hex* C_{24} also fit to those of the graphite. The Bernal C_{24} structure reveals the larger formation energy and smaller d_{layer} by ~0.3 Å due to stronger interaction between the layers as compared to *hex* C_{24} structure.

Conventional satellites at higher energy sides of the XPS spectra correspond indeed to the photoelectron energy consumption. The CEE approach enables complete description of the HOPG XPS C1s spectrum in **Figure 3(b)** by the combination of shake-up and shake-off CEE transitions.

The satellite ~5.5 eV in **Figure 3(b)** is assigned to a π plasmon responsible for the $\pi \rightarrow \pi^*$ transition [59], although the standard plasmon is related to the collective oscillations of free

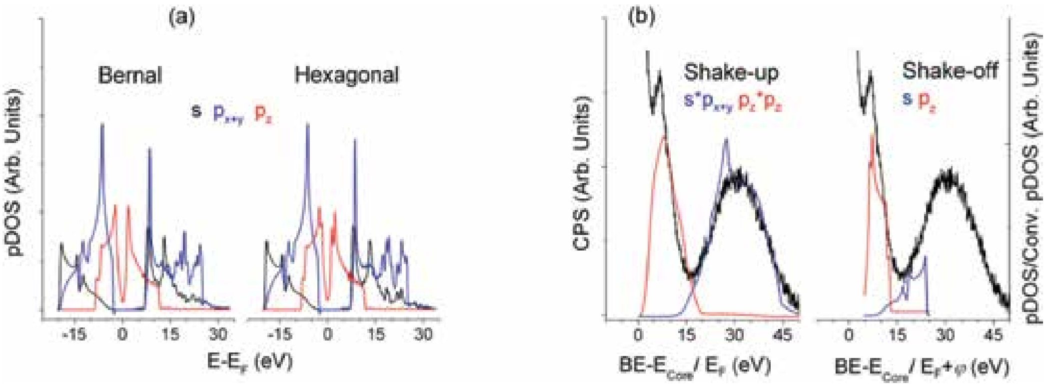

Figure 3. (a) Partial DOS for the unit cells C_{24} with the Bernal and *hex* structure ($p_x = p_y$); (b) shake-up and shake-off CEE transitions in the unit cell *hex* C_{24} as compared to energy losses above the core-level energy (284.6 eV) in the XPS C1s spectrum of HOPG. Adapted from [31].

electrons missing in HOPG [60].This satellite originates rather from the shake-off than from the shake-up p_z transition (**Figure 3(b)**).

There is expected similarity between higher energy tails of the $^{(F)}$C1s (C is bound to F) and F1s XPS spectrum in **Figure 4**, which emphasizes the indifference of the VB with respect to energy source for the CEE transition. Fine XPS spectral structures above 10 eV conform well to shake-up (**Figure 4(a)**) and shake-off (**Figure 4(b)**) CEE transitions calculated by Eq. (1). The matrix elements $f(E, \sigma)$ in Eq. (1) were accepted unity for a $W(E)$ basis set, while the Y-scale factors in **Figure 4** (a, b) evaluate $f(E, \sigma)$ and the contribution of a particular CEE transition, in total theoretical energy consumption, to fit the experimental photoelectron energy losses.

The π plasmon at ~5.4 eV in **Figure 4(a**, **b)** is assigned to the conjugated π bonds in a chain of C atoms [37]. This feature fits the shake-up Cp_z transition and accompanies the C1s spectrum, since the π bond is localized exclusively at the Csp^2 atom, not bound to F. Similar feature is exhibited in the C K- and not exhibited in F K-edge XANES spectra of C_2F [29], and the π plasmon is certainly not observed the XPS C1s spectrum under the lack of π-bonds [61]. Discovery of a similar satellite in the F1s spectrum is rather confusing because F atoms have nothing to do with the π bond between C atoms), but it is quite in line with the CEE model.

The base line shift relative to C1s = 285.1 eV in **Figure 4** (C is not bound to F) saves accordance with the DFT data and enables to make a contribution to the energy loss ~5.4 eV to the other shake-off transitions ($^{(F)}Cp_y$, Fp_y, Fp_z). The formation energy of the Bernal unit cell $C_{24}F_{12}$ is by 0.008 eV higher than that of the *hex* $C_{24}F_{12}$ cell, while pDOSs of both structures are very similar. A sizable DOS at E_F accepts plasmon oscillations that can give the energy loss at 9.1 or 12.9 eV for 1 or 2 free electrons per a C_2F fragment, respectively [30].

5.2. Br_2-embedded C_2F

XPS spectra obtained after the Br_2 intercalation into C_2F matrix reveal stoichiometry $C_2FBr_{0.15}$ and the lack of new features compared to XPS spectra of the pristine C_2F (**Figure 4**); C1s and F1s spectra are in agreement with the same CEE transitions as before the Br_2 embedding. DFT

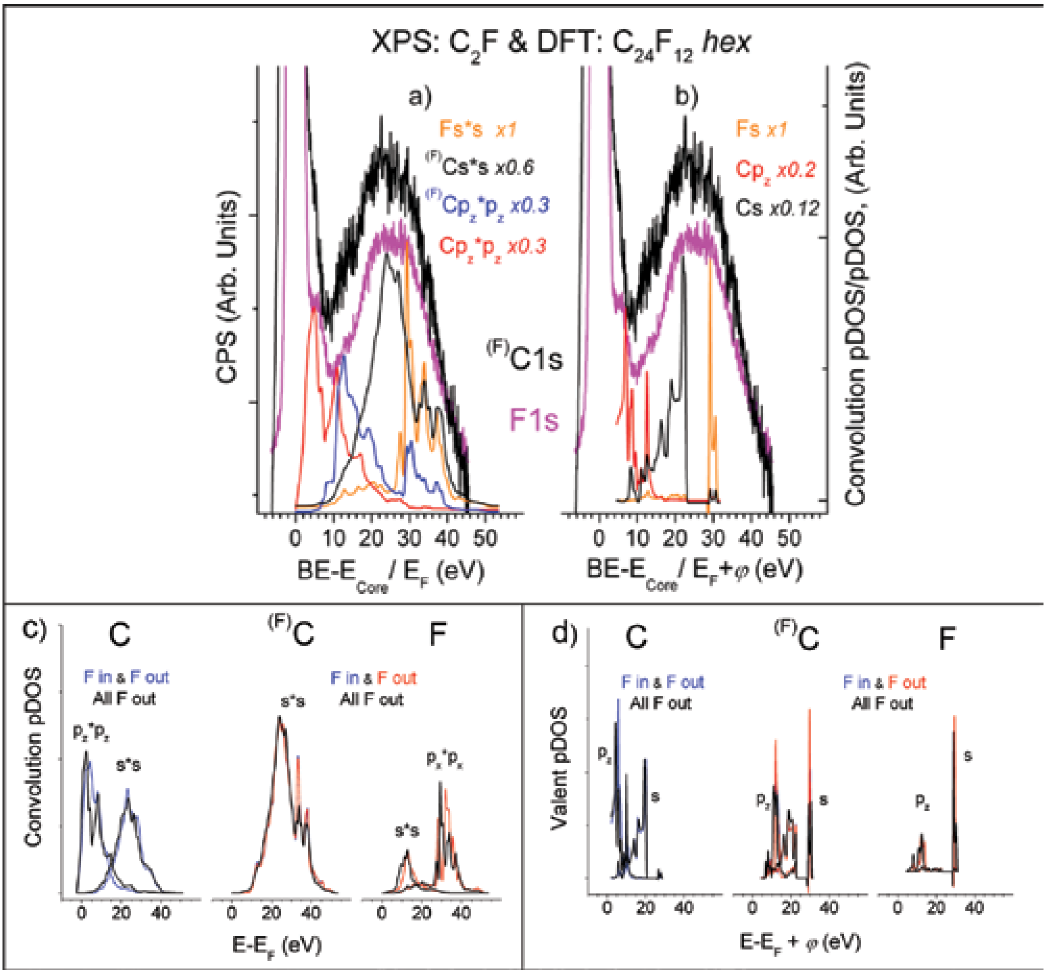

Figure 4. XPS C1s and F1s spectrum of C_2F (relative to E_{Core} = 287.6 eV and 687.4 eV, respectively; the background of external and surface energy losses are subtracted [35]) and shake-up (a) and shake-off (b) transitions of $^{(F)}C$ and F atoms forming the C-F bond in the unit cell *hex* $C_{24}F_{12}$ (all F are outside). (c) Shake-up and (d) shake-off CEE transitions for different arrangements of the F atoms (**Figure 1**). Adapted from [31].

studies were performed for the Bernal and *hex* $C_{24}F_{12}Br_2$ unit cells #1–9 in **Table 2** at the entry angles α_0 = 0 and 90° between the Br-Br axis and C planes and different arrangements of the F atoms (**Figure 1**).

DFT calculations have revealed that the Br_2 embedding enlarges the interlayer distance, but insignificantly affects the pDOS of the C, $^{(F)}C$ and F [30]. The latter conforms to chemical inertness of the pristine C_2F cell and to low Br content in the product $C_2FBr_{0.15}$ [62]. Invariant pDOS of the C and F atoms and slight change in the C1s and F1s XPS spectra, after the Br_2 embedding into $C_{24}F_{12}$ framework, restrain the correlation between XPS and DFT outputs. The novelties of XPS and DFT data, which are resulted from the Br_2 embedding, concern the bromine only and are considered in more detail.

Species/unit cell	d_{BrBr} (Å)	α (optimized)	$\Delta_{s\text{-}p}$ (eV)	Br state
Free Br_2^0	2.29	—	12.806	Molecular
Free Br_2^{-1}	2.89	—	12.061	Molecular
Free Br_1^0	—	—	12.285	Atomic
Free Br_1^{-1}	—	—	11.730	Atomic
All F out a cell (**Figure 1**)				
#1 *hex* (α_0 = 0°)	3.24	0.0°	11.66	Atomic
#2 *hex* (α_0 = 90°)	2.45	51.5°	12.06	Molecular
#3 Bernal (α_0 = 0°)	2.375	6.2°	12.32	Molecular
#4 Bernal (α_0 = 90°)	3.18	0.1°	12.68	Atomic
#5 Bernal (α_0 = 52°)	3.34	0.8°	12.61	Atomic
Half F in & half F out a cell (**Figure 1**)				
#6 *hex* (α_0 = 90°)	2.44 (nearest) 2.73 (next nearest)	17.4°	12.09	Chain type
#7 *hex* (α_0 = 0°)	2.30 (nearest) 4.96 (next nearest)	12.9°	12.82	Molecular
#8 Bernal (α_0 = 90°)	2.44 (nearest) 2.73 (next nearest)	17.2°	12.15	Chain type
#9 Bernal (α_0 = 0°)	2.29 (nearest) 4.96 (next nearest)	18.7°	12.97	Molecular

Table 2. Br-Br distance d_{BrBr}, angle α between the Br-Br axis and C-planes, and difference $\Delta_{s\text{-}p}$ between the weighted average Br *s*- and *p*- DOS in free species and unit cells $C_{24}F_{12}Br_2$.

The difference F1s spectrum in **Figure 5** exhibits a distinct structure, which conforms to shake-up transitions of the pDOS responsible for C-F bonding and which is interpreted as the C-F bond strengthening [30]. It can be the case since the Br_2 embedding weakens the interactions between carbon layers, which should be accompanied with the enrichment of the occupied DOS of C and F. Arrangement of the F atoms in a cell makes no matter for the conclusion.

DFT studies have found a set of cells $C_{24}F_{12}Br_2$ with the optimized parameters and different local geometry and the state (atomic, molecular, and chain type) of the embedded Br_2 (**Table 2**). Each of nine local structures is appropriate; no preference can be given to a particular cell from the conventional DFT study.Each of these unit cells is characterized by the specific Br pDOS structure [30]. DFT examinations of separate bromine species revealed a strong difference $\Delta_{s\text{-}p}$ = 0.2–1.3 eV between the weighted average energy $<E_{s,p}>$ of the Br *s*- and *p*- DOS, far beyond the accuracy of DFT runs ~0.01 eV (**Table 2**). The parameter $<E_{s,p}>$ was determined as E, $\sum\sigma_i E_i/\sum\sigma_i$ and middle of $\int\sigma_i d E_i$ for the Br atom with single, several localized, and diffused *s*- and *p*- DOS, respectively. In the same way, as the binding energy determines the oxidation rate in extensive XPS practice; the parameter $\Delta_{s\text{-}p}$ was taken as a descriptor of the Br state [30].

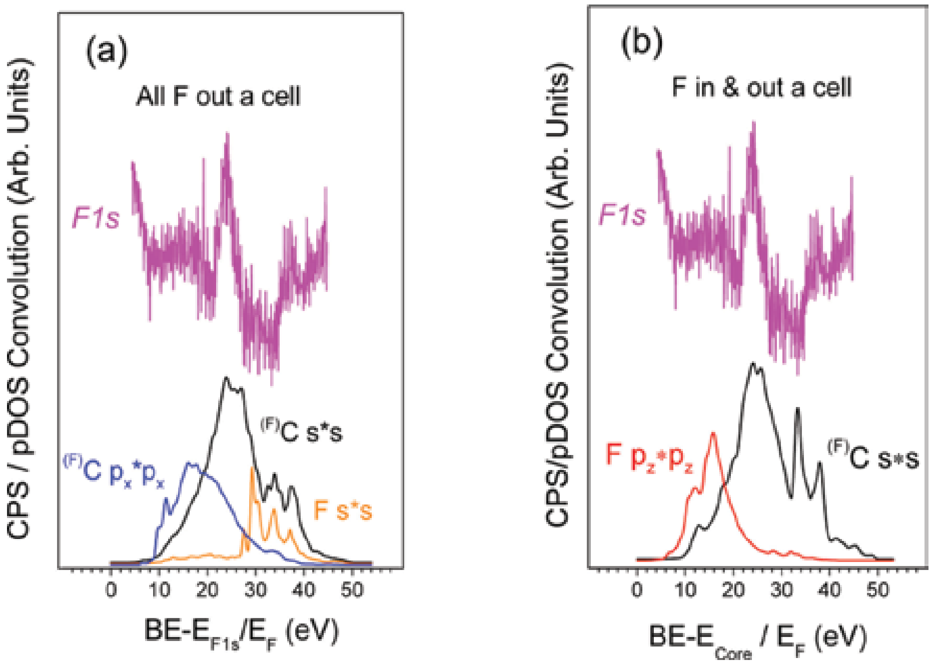

Figure 5. Difference XPS F1s spectrum (F1s C_2F was subtracted from F1s $C_2FBr_{0.15}$) as compared to shake-up VB transitions for the unit cells $C_{24}F_{12}Br_2$ (a) #2 and (b) #6 in **Table 2** with different layout of the F atoms (**Figure 1**).

For the unit cells with all F atoms outside, the minimal deviations $\Delta_{s\text{-}p}$ of 0.02, 0, and 0.04 eV make preferable the cells #1, #2, and #3, respectively (**Table 2**). Moreover, in case of the large d_{BrBr} (the Br-Br bond is lost), the difference $\Delta_{s\text{-}p}$ in a cell should be close to that of free Br_1^0. Otherwise (the Br-Br bond retains), the difference $\Delta_{s\text{-}p}$ should be close to that of the Br_2^0 species. In this case, d_{BrBr} for cell #1 (3.24 Å) and cell #2 (2.45 Å) is adequate to the lack of the Br-Br bond in Br_1^{-1} and to the eigenvalue of Br_2^0 (2.29 Å), respectively. On the contrary, the cell #3 should be ruled out, because its d_{BrBr} = 2.37 Å indicates retaining the Br-Br bond while the Br_1^0 specimen, with nearest $\Delta_{s\text{-}p}$, has no bond. Finally, the cell #2 wins the cell #1 in the formation energy (**Table 1**). Besides, the reaction $C_{24}F_{12} + Br_2 \rightarrow C_{24}F_{12}Br_2$ is endothermic for cell #1, in contrast to other cells [30].

The bromine p_z- and s- shake-off transition conforms to the nonresolved 5–12 eV fragment and ~20 eV shoulder of the Br3d spectrum in **Figure 6(a)**, respectively. The higher energy parts of the XPS Br3d, F1s and C1s spectra are similar [30], but they do not correlate with any of the Br CEE transitions. This indicates such a bonding between the Br_2 molecule and the C_2F frame that provides the Br3d photoelectron energy losses via CEE transitions of pDOS of the C and F atoms.

DFT calculations for the unit cells $C_{24}F_{12}Br_2$, with the F atoms half inside and half outside a cell, have revealed two stable Br_2 states. The first state, in cells #7 and #9, corresponds to Br_2 pairs (**Table 2**), which are separated from each other in the adjacent cells and exhibit the same Br-Br distance d_{BrBr} ~2.29 Å as in a free Br_2 molecule. The second state (cells #6 and #8) corresponds to Br arrangement as the chain, in which d_{BrBr} ~2.44 Å within a unit cell is larger than in a free

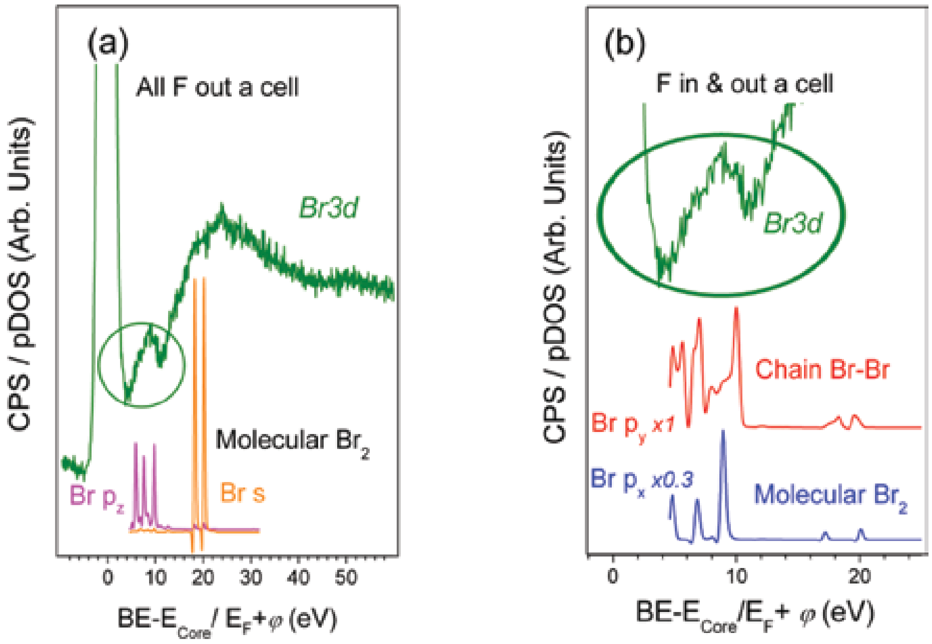

Figure 6. Br3d XPS spectrum of $C_2FBr_{0.15}$ as compared to relevant shake-off VB transitions of the Br atom in unit cells with different F layout (a) #2 (*hex*), and (b) #8 and #9 (Bernal).

Br_2, while nearest distance between the Br atoms of the adjacent cells 2.73 Å is smaller than the nearest intermolecular distance in a solid Br ~3.37 Å [63] and still enough for the vdW interaction [45]. There is no visible difference in the Br pDOS of cell #6 and #8 (chain type Br), while there is a few difference between the Br p_x and p_y states for cell #7 and #9 (molecular Br_2). Finally, the weighted average $\Delta_{s\text{-}p}$ values are line with the molecular Br state for cells #7 and #9; the state close to Br_2^{-1} for cell #6; and the intermediate, between Br_1^0 and Br_2^{-1}, Br state for cell #8 (**Table 2**).

The ~20 eV shoulder in the Br3d spectrum in **Figure 6(b)** conforms well to shake-off transition of the *s*-state in unit cells #8 and #9 with different arrangement of the Br atoms, and there is no solid reason to give preference to a particular cell. The shape and location of the 5–12 eV spectral fragment in **Figure 6(b)**, with due regard to the baseline of this energy region, are consistent with a comparable mixture of CEE transitions calculated for the unit cells #8 and #9. According to DFT data, there is a little difference between cells #6 and #8 (chain type Br) with respect to the shake-off p_y transition, while the cell #6 wins #8 by ~5% in the formation energy. On the contrary, using the cell #7 *hex* instead of #9 Bernal (molecular Br_2) results in larger discordance with the XPS data due to their specific p_x structure. Finally, the unit cell $C_{24}F_{12}Br_2$ #6, with the chain type Br layout, is preferable among others, whereas the energy losses in the Br3d XPS spectrum suggest a mixture ~1:1 of unit cells #6 and #9.

Experimental data have reported the angle α ~30° between the Br-Br axis and C-planes and the molecular Br_2 state for similar to $C_2FBr_{0.15}$ systems [38, 46]. The current combination of XPS and DFT outputs suggests possibility of the chain like bromine arrangement, which can be realized in appropriate experimental conditions. Besides, the experimental angle (~30°) is close to the weighted average (~29°) of α = 51.5, 17.4, and 18.7° in **Table 2**, which have been found for the most probable unit cells #2, #6, and #9, respectively.

6. Outlook

Any novel approach, including the CEE model, can be truly evaluated by a benefit from its practical application. By an example of the graphite based materials, the chapter has shown how a confluence of the XPS and DFT data can provide additional information on chemical behavior, local geometry and state of the embedded Br_2 molecule and of the other atoms in a sample. A similar treatment can be useful in the field of surface engineering as well, because just a deep knowledge on chemical behavior of a sample can disclose the mechanism and dynamics of its wear performance, thus facilitating the development of advanced materials. The valence band of chemically bound atoms is insensitive to a photoelectron, whose energy it uses for the CEE transition. Then, in the case of the multicomponent materials, agreement or disagreement between energy losses in the XPS spectra of some atoms can be a descriptor of the presence or absence of chemical bonding between these atoms in a sample [17, 19, 22]. Moreover, the state of any component can be traced through change or invariability of the satellites in its XPS spectra, obtained in the course of external influence, thus revealing a wear performance of the material. In case of a "simple" material, the reliable structural data can be used as starting conditions for the appropriate DFT run, which gives comprehensive information on a sample at the atomic level [16, 18]. Extensive use and practice of the XPS and DFT techniques make the CEE analysis easily accessible.

CEE control in a coordinated XPS and DFT study is characterized by the following obvious, verified, and hidden resources.

- Comparison of fine XPS spectra with the calculated CEE transitions can provide the local geometry and bond types in a sample from conventional DFT facilities. The occurrence and consequence of bonding between atoms can be also determined, because the core-level excitation of an atom is accompanied by CEE satellites of the next one only within the integrated valence band.
- The multiple CEE controls (around different XPS peaks) facilitate the data interpretation, while individual sets of the core-level energies improve studying of the multicomponent materials.
- Hydrogen tracing by the XPS, as a specific CEE satellite above the core-level energy of the other sample component, is possible without a contradiction with XPS principles.
- The CEE control is available for samples of any conductivity, because the photoelectron energy losses are linked up to the XPS peak regardless its apparent core-level energy.
- The valence band structure in the XPS spectra differs from that obtained by the nondestructive and theoretical methods. The CEE event is nondestructive as well, because the valence band absorbs only a part of the photoelectron energy for a CEE transition, omitting a destructive force of the incident X-ray impact.

7. Conclusion

Primary collecting of the extra data by a routine technique is always desirable. This chapter highlights a rational model that gives a chance to realize this desire using the conventional XPS and DFT outputs. The model is based on following statements.

- Electronic configuration of the atoms in a solid holds the traps for the energy absorption, such as valence band electron transitions; and the core-level excitation of any origin fills those traps forming the multiple channels for energy dissipation.
- These channels can be traced by the XPS, as the photoelectron energy losses, and by the DFT, as the valence band electron transitions. This pattern does not conflict with general concepts of electron-solid interaction and has been well verified in model studies of Pt and graphite-based materials.
- Intersection of the XPS and DFT outputs carries out two duties. First, it rejects those DFT results which do not conform to the fine XPS spectral structures. Second, it justifies the assignment of the refined DFT data, related to an appropriate unit cell, to a given XPS sample. As a result, the correlated XPS and DFT study discloses hidden potentialities of both techniques and provides the extra data on chemical behavior and local geometry of the atoms in a sample.
- The procedure of a coordinated XPS and DFT study being highlighted can provide a deeper insight into the mechanism of wear performance of the material, thus facilitating the development of advanced composites.

Acknowledgements

This work has been supported by the Russian Foundation for Basic Research (Grant 17-03-00049) and conducted within the framework of the budget project for Boreskov Institute of Catalysis.

Acronyms and abbreviations

AES	auger electron spectroscopy
CEE	conjugate electron excitation
DAPS	disappearance potential spectroscopy
DFT	density functional theory
DOS	density of states
pDOS	partial DOS

1D DOS	one-dimensional DOS
EXAFS	extended X-ray absorption fine structure
HOPG	highly orientated pyrolytic graphite
1 L	1 Langmuir, one second exposure of a gas at pressure of 10^{-6} Torr
ML	1 monolayer coverage of the adsorbate
PAW	projected augmented wave method of the DFT
RAES	resonant auger electron spectroscopy
RIXS	resonant inelastic X-ray scattering
RPES	resonant photoemission electron spectroscopy
Ry	Rydberg, atomic unit of energy close to 13.6 electron volts
XPS	X-ray photoelectron spectroscopy
XAFS	X-ray absorption fine structure
XANES	X-ray absorption near edge structure
UPS	ultraviolet photoelectron spectroscopy
VB	valence band
vdW	van der Waals correction, operating parameter of the DFT

Author details

Alexander R. Cholach

Address all correspondence to: cholach@catalysis.ru

Boreskov Institute of Catalysis, Novosibirsk, Russian Federation

References

[1] Bhanvase BA, Pawade VB, Dhoble SJ, Sh S, Ashokkumar HM, editors. Nanomaterials for Green Energy. 1st ed. Amsterdam: Elsevier; 2018. 500 p. ISBN: 9780128137314

[2] Busca G, editor. Heterogeneous Catalytic Materials. 1st ed. Oxford: Elsevier; 2014. 478 p. ISBN: 9780444595249

[3] Sá J, editor. High Resolution XAS/XES: Analyzing Electronic Structures of Catalysis. Boca Raton: CRC Press; 2014. 214 p. ISBN: 978-1-4665-9298-8

[4] Bunker G. Introduction to XAFS: A Practical Guide to X-ray Absorption Fine Structure Spectroscopy. Cambridge: Cambridge University Press; 2010. 260 p. ISBN: 052176775X

[5] Ament L, van Veenendaal M, Devereau T, Hill J, van den Brink J. Resonant inelastic X-ray scattering studies of elementary excitations. Reviews of Modern Physics. 2011;**83**:705. DOI: 10.1103/RevModPhys.83.705

[6] Brühwiler P, Karis O, Mårtensson N. Charge-transfer dynamics studied using resonant core spectroscopies. Reviews of Modern Physics. 2002;**74**:703. DOI: 10.1103/RevModPhys.74.703

[7] Cholach AR. Advanced power of disappearance potential spectroscopy in the adsorbed species identification. In: Hansen PW, editor. Chemical Physics Research Developments. Hauppauge, New York: Nova Science Publishers; 2011. pp. 149-173. ISBN: 978-1-61122-068-1

[8] Cholach A, Tapilin V. Specific channels for electron energy dissipation in the adsorbed system. The Journal of Chemical Physics. 2013;**138**:104201. DOI: 10.1063/1.4794141

[9] Cholach AR, Tapilin VM. Mechanism of conjugate electron transitions on the surface of a solid. Journal of Structural Chemistry. 2015;**56**:589-595. DOI: 10.1134/S0022476615030282

[10] Cholach AR, Tapilin VM. The bulk of evidence for novel electron transitions above the core level threshold. Russian Journal of Physical Chemistry A. 2015;**89**:2402-2406. DOI: 10.1134/S0036024415130105

[11] Cholach A, Tapilin V. Adsorption of small molecules on the Pt(100) single crystal surface studied by disappearance potential spectroscopy. Applied Surface Science. 2001;**180**: 173-183. DOI: 10.1016/S0169-4332(01)00332-4

[12] Briggs D, Seach M, editors. Practical Surface Analysis by Auger and X-ray Photoelectron Spectroscopy. Chichester: Wiley; 1983. 674 p. ISBN: 9780471953401

[13] Woodruff D, Delchar T, editors. Modern Techniques of Surface Science. 2nd ed. Cambridge: Cambridge University Press; 1994. 608 p. ISBN: 9780521424981

[14] Rabalais J. Principles of Ultraviolet Photoelectron Spectroscopy. NY: Wiley; 1977. 472 p. ISBN: 0471702854

[15] Chouhan A, Mungse HP, Sharma OP, Singh RK, Khatri OP. Chemically functionalized graphene for lubricant applications: Microscopic and spectroscopic studies of contact interfaces to probe the role of graphene for enhanced tribo-performance. Journal of Colloid and Interface Science. 2018;**513**:666-676. DOI: 10.1016/j.jcis.2017.11.072

[16] Rodrigues SP, Evaristo M, Carvalho S, Cavaleiro A. Fluorine-carbon doping of WS-based coatings deposited by reactive magnetron sputtering for low friction purposes. Applied Surface Science. 2018;**445**:575-585. DOI: 10.1016/j.apsusc.2018.03.113

[17] Ju H, Yu D, Yu L, Ding N, Xu J, Zhang X, Zheng Y, Yang L, He X. The influence of Ag contents on the microstructure, mechanical and tribological properties of ZrN-Ag films. Vacuum. 2018;**148**:54-61. DOI: 10.1016/j.vacuum.2017.10.029

[18] Long J, Zhang W, Wang Y, Du Y, Zhang Z, Lu B, Cheng K, Peng Y. A new type of WC-Co-Ni-Al cemented carbide: Grain size and morphology of γ'-strengthened composite binder phase. Scripta Materialia. 2017;**126**:33-36. DOI: 10.1016/j.scriptamat.2016.08.007

[19] Fernandes F, Danek M, Polcar T, Cavaleiro A. Tribological and cutting performance of TiAlCrN films with different Cr contents deposited with multilayered structure. Tribology International. 2018;**119**:345-353. DOI: 10.1016/j.triboint.2017.11.008

[20] Marchetto D, Restuccia P, Ballestrazzi A, Righi MC, Rota A, Valeri S. Surface passivation by graphene in the lubrication of iron: A comparison with bronze. Carbon. 2017;**116**: 375-380. DOI: 10.1016/j.carbon.2017.02.011

[21] Oh D-S, Kang K-H, Kim H-J, Kim J-K, Won M-S, Kim D-E. Tribological characteristics of micro-ball bearing with V-shaped grooves coated with ultra-thin protective layers. Tribology International. 2018;**119**:481-490. DOI: 10.1016/j.triboint.2017.11.014

[22] Wen X, Liang K, Tian L, Shi K, Zheng J. Al_2O_3 coating on $Li_{1.256}Ni_{0.198}Co_{0.082}Mn_{0.689}O_{2.25}$ with spinel-structure interface layer for superior performance lithium ion batteries. Electrochimica Acta. 2018;**260**:549-556. DOI: 10.1016/j.electacta.2017.12.120

[23] Liu LC, Corma A. Metal catalysts for heterogeneous catalysis: From single atoms to nanoclusters and nanoparticles. Chemical Reviews. 2018;**118**:4981-5079. DOI: 10.1021/acs.chemrev.7b00776

[24] Sedelnikova O, Bulusheva L, Asanov I, Yushina I, Okotrub A. Energy shift of collective electron excitations in highly corrugated graphitic nanostructures: Experimental and theoretical investigation. Applied Physics Letters. 2014;**104**:161905. DOI: 10.1063/1.4873123

[25] Tsuei K-D, Yuh J-Y, Tzeng C-T, Chu R-Y, Chung S-C, Tsang K-L. Photoemission and photoabsorption study of C_{60} adsorption on Cu(111) surfaces. Physical Review B. 1997; **56**:15412. DOI: 10.1103/PhysRevB.56.15412

[26] Shulga YM, Tien T-C, Huang C-C, Lo SC, Muradyan VE, Polyakova NV, Ling Y-C, Loutfy RO, Moravsky AP. XPS study of fluorinated carbon multi-walled nanotubes. Journal of Electron Spectroscopy and Related Phenomena. 2007;**160**:22-28. DOI: 10.1016/j.elspec.2007.06.002

[27] Bourlinos AB, Safarova K, Siskova K, Zbořil R. The production of chemically converted graphenes from graphite fluoride. Carbon. 2012;**50**:1425-1428. DOI: 10.1016/j.carbon.2011.10.012

[28] Nakajima T. Surface Mmodification of carbon anodes for lithium ion batteries by fluorine and chlorine. In: Nakajima T, Groult H, editors. Advanced Fluoride-Based Materials for Energy Conversion. Amsterdam: Elsevier; 2015. pp. 203-223. ISBN: 978-0-12-800679-5

[29] Asanov IP, Okotrub AV, Gusel'nikov AV, Yushina IV, Vyalikh DV, Bulusheva LG. Charge-induced formation of thin conducting layers on fluorinated graphite surface. Carbon. 2015;**82**:446-458. DOI: 10.1016/j.carbon.2014.10.088

[30] Cholach AR, Asanov IP, Bryliakova AA, Okotrub AV. Extra electronic outer-shell peculiarities accessible under a joint XPS and DFT study. Physical Chemistry Chemical Physics. 2017;**19**:15842-15848. DOI: 10.1039/c7cp00900c

[31] Cholach AR, Asanov IP, Bryliakova AA. Identification of conjugate electron transitions in X-ray photoelectron spectra. Journal of Structural Chemistry. 2017;**58**:1160-1165. DOI: 10.1134/S0022476617060130

[32] Kirschner J. Electron-excited core level spectroscopies. In: Ibach H, editor. Electron Spectroscopy for Surface Analysis. Berlin: Springer; 1977. pp. 59-115. ISBN: 978-3-642-81099-2

[33] Brodén G, Pirug G, Bonzel H. Chemisorption of CO on the unreconstructed Pt(100) surface. Surface Science. 1978;**72**:45-52. DOI: 10.1016/0039-6028(78)90376-X

[34] Lide D, editor. CRC Handbook of Chemistry and Physics. 85th ed. Boca Raton: CRC Press; 2005. 2616 p. ISBN: 9780849304859

[35] Tougaard S, Chorkendorff I. Differential inelastic electron scattering cross sections from experimental reflection electron-energy-loss spectra: Application to background removal in electron spectroscopy. Physical Review B. 1987;**35**:6570. DOI: 10.1103/PhysRevB.35.6570

[36] Shubin YV, Pinakov DV, Chekhova GN, Alferova NI, Logvinenko VA. Phase transitions of intercalation inclusion compounds $C_2F_{0.92}Br_{0.0}\cdot yCH_3CN$ in the temperature range 20-260°C. Journal of Structural Chemistry. 2006;**47**:1141-1154. DOI: 10.1007/s10947-006-0437-y

[37] Asanov I, Bulusheva L, Dubois M, Yudanov N, Alexeev A, Makarova T, Okotrub AV. Graphene nanochains and nanoislands in the layers of room-temperature fluorinated graphite. Carbon. 2013;**59**:518-529. DOI: 10.1016/j.carbon.2013.03.048

[38] Bausk N, Erenburg S, Yudanov N, Mazalov L. Geometry and orientation of molecules in a graphite fluoride matrix. Journal of Structural Chemistry. 1996;**37**:913-919. DOI: 10.1007/BF02439075

[39] Giannozzi P, Baroni S, Bonini N, Calandra M, Car R, Cavazzoni C, Ceresoli D, Chiarotti GL, Cococcioni M, Dabo I, Dal Corso A, de Gironcoli S, Fabris S, Fratesi G, Gebauer R, Gerstmann U, Gougoussis C, Kokalj A, Lazzeri M, Martin-Samos L, Marzari N, Mauri F, Mazzarello R, Paolini S, Pasquarello A, Paulatto L, Sbraccia C, Scandolo S, Sclauzero G, Seitsonen AP, Smogunov A, Umari P, Wentzcovitch RM. QUANTUM ESPRESSO: A modular and open-source software project for quantum simulations of materials. Journal of Physics: Condensed Matter. 2009;**21**:395502. DOI: 10.1088/0953-8984/21/39/395502

[40] Perdew J, Ruzsinszky A, Csonka G, Vydrov O, Scuseria G, Constantin L, Zhou X, Burke K. Restoring the density-gradient expansion for exchange in solids and surfaces. Physical Review Letters. 2008;**100**:136406. DOI: 10.1103/PhysRevLett.100.136406

[41] Blöchl P. Projector augmented-wave method. Physical Review B. 1994;**50**:17953. DOI: 10.1103/PhysRevB.50.17953

[42] Marzari N, Vanderbilt D, De Vita A, Payne M. Thermal contraction and disordering of the Al(110) surface. Physical Review Letters. 1999;**82**:3296. DOI: 10.1103/PhysRevLett.82.3296

[43] Grimme S. Semiempirical GGA-type density functional constructed with a long-range dispersion correction. Journal of Computational Chemistry. 2006;**27**:1787-1799. DOI: 10.1002/jcc.20495

[44] Perdew J, Burke K, Ernzerhof M. Generalized gradient approximation made simple. Physical Review Letters. 1996;**77**:3865. DOI: 10.1103/PhysRevLett.77.3865

[45] Hu C-H, Zhang P, Liu H-Y, Wu S-Q, Yang Y, Zhu Z-Z. Structural stability and electronic and magnetic properties of fluorinated bilayer graphene. The Journal of Physical Chemistry C. 2013;**117**:3572-3579. DOI: 10.1021/jp3103113

[46] Feldman J, Elam W, Ehrlich A, Skelton E, Dominguez D, Chung D, Lytle F. Polarized-X-ray-absorption studies of graphite intercalated-bromine compounds. Physical Review B. 1986;**33**:7961. DOI: 10.1103/PhysRevB.33.7961

[47] Monkhorst H, Pack J. Special points for Brillouin-zone integrations. Physical Review B. 1976;**13**:5188. DOI: 10.1103/PhysRevB.13.5188

[48] Rother A, Scheerschmidt K. Relativistic effects in elastic scattering of electrons in TEM. Ultramicroscopy. 2009;**109**:154-160. DOI: 10.1016/j.ultramic.2008.08.008

[49] Gingrich DM, editor. Practical Quantum Electrodynamics. NY: CRC Press; 2006. 360 p. ISBN: 9781584885429

[50] Kittel C, editor. Introduction to Solid State Physics. 8th ed. NY: Wiley; 2004. 704 p. ISBN: 9780471415268

[51] Pennemann B, Oster K, Wandelt K. Hydrogen adsorption on Pt(100) at low temperatures: Work function and thermal desorption data. Surface Science. 1991;**249**:35-43. DOI: 10.1016/0039-6028(91)90831-C

[52] Bonzel H, Fischer T. An UV photoemission study of NO and CO adsorption on Pt (100) and Ru (10-10) surfaces. Surface Science. 1975;**51**:213-227. DOI: 10.1016/0039-6028(75)90244-7

[53] Ramstad A, Strisland F, Raaen S, Borg A, Berg C. CO and O_2 adsorption on the Re/Pt(111) surface studied by photoemission and thermal desorption. Surface Science. 1999; **440**:290-300. DOI: 10.1016/S0039-6028(99)00827-4

[54] Bartram M, Koel B, Carter E. Electronic effects of surface oxygen on the bonding of NO to Pt(111). Surface Science. 1989;**219**:467-489. DOI: 10.1016/0039-6028(89)90522-0

[55] Demuth J. Ultraviolet photoemission studies of hydrogen chemisorption bonding to Ni, Pd and Pt surfaces. Surface Science. 1977;**65**:369-375. DOI: 10.1016/0039-6028(77)90317-X

[56] den Boer M, Einstein T, Elam W, Park R, Roelofs L, Laramore G. Extended appearance-potential fine-structure analysis: oxygen on Al(100). Physical Review Letters. 1980;**44**:496. DOI: 10.1103/PhysRevLett.44.496

[57] Puglia C, Nilsson A, Hernnäs B, Karis O, Bennich P, Mårtensson N. Physisorbed, chemisorbed and dissociated O_2 on Pt(111) studied by different core level spectroscopy methods. Surface Science. 1995;**342**:119-133. DOI: 10.1016/0039-6028(95)00798-9

[58] Sakai Y, Saito S, Cohen ML. Lattice matching and electronic structure of finite-layer graphene/h-BN thin films. Physical Review B. 2014;**89**:115424. DOI: 10.1103/PhysRevB.89.115424

[59] Taft E, Phillipp H. Optical properties of graphite. Physical Review. 1965;**138**:A197. DOI: 10.1103/PhysRev.138.A197

[60] Sedelnikova O, Bulusheva L, Okotrub A. Modulation of electronic density in waved graphite layers. Synthetic Metals. 2010;**160**:1848-1855. DOI: 10.1016/j.synthmet.2010.07.001

[61] Rolere S, Goulon J-F, Poncin-Epaillard F. Influence of the curing temperature on the diffusion rate of the perfluorinated alkyl chains of a modified epoxy resin. European Polymer Journal. 2017;**91**:61-69. DOI: 10.1016/j.eurpolymj.2017.03.053

[62] Bulusheva L, Tur V, Fedorovskaya E, Asanov I, Pontiroli D, Riccò M, Okotrub A. Structure and supercapacitor performance of graphene materials obtained from brominated and fluorinated graphites. Carbon. 2014;**78**:137-146. DOI: 10.1016/j.carbon.2014.06.061

[63] Powell BM, Heal KM, Torrie BH. The temperature dependence of the crystal structures of the solid halogens, bromine and chlorine. Molecular Physics. 1984;**53**:929-939. DOI: 10.1080/00268978400102741

Chapter 9

Efficient Microbial Decontamination of Translucent Liquids and Gases Using Optical Metamaterials

Nicolae Enaki, Sergiu Bizgan, Andrei Nistreanu,
Viorica Tonu, Marina Turcan, Tatiana Pislari,
Elena Starodub, Aurelia Profir,
Gianina-Florentina Popescu-Pelin, Maria Badiceanu,
Carmen-Georgeta Ristoscu and Ion N. Mihailescu

Additional information is available at the end of the chapter

http://dx.doi.org/10.5772/intechopen.80639

Abstract

An effective way of decontamination using optical metamaterials like photonic crystals consisting of glass microspheres or granulated quartz with various geometries is proposed. The efficient decontamination using the evanescent zone of metamaterials opens a new perspective in pathogen decontamination. We propose different topological structures of metamaterials to enlarge the contact surface of ultraviolet radiation with polluted translucent fluids. The approach is based upon the increased transfer of UV radiation via evanescent waves of metamaterials into contaminated translucent fluids. A series of experimental estimations of the decontamination rate of this type of metamaterials have been made. For these investigations, a decontamination core filled up with metamaterials is used through which the contaminated fluid freely flows. Experiments have conclusively proved that evanescent zone of quartz and optical fiber metamaterials can effectively inactivate *Coliform* (including *Escherichia coli*), or *Enterococcus* bacteria, as well as yeast and *Kombucha* cultures.

Keywords: metamaterials, evanescent zone, Raman excitation, decontamination, pathogen

1. Introduction

Recently, the peculiarities of metamaterials and nanoparticles are used in the construction of new devices for optoelectronics [1]. The research on photonic terahertz and microwave electromagnetic devices by using the nonlinear properties of metamaterials has been summarized. The periodicity of the building blocks of metamaterials which are smaller than the light wavelength was taken into consideration. The nanoparticle devices can be used for the localization of cavity fields, in particular surface plasmon resonance (SPR) [2]. Some of the phenomena originated by the uncommon wave dynamics in near-zero photonics and their fundamental and technological implications on different subfields of optics and metamaterials are presented in Ref. [3].

One concern in pathogen decontamination is the need of a new effective method of radiation interaction with microorganisms [4–6]. An open surface of a translucent fluid exposed to radiation cannot provide the expected solution, due to the difficulty to irradiate pathogens inside the liquid volume as an immanent self-absorption. In this case, the total contact surface in quasi-periodical structures comes to be proportional to the surface of one element multiplied by the number of elements. Accordingly, the decontamination volume increases due to the large dispersion of light in these metamaterials, being proportional to the surface of one element multiplied to their number and UV-C light penetration depth through the translucent contaminated fluid.

The use of optical metamaterials with periodical structures to act against *undesired microorganisms* (viruses, bacteria, and yeast) existing in translucent liquids and gases is proposed. Studies were devoted to the topological effect of individual metamaterial elements on the modification of UV (ultraviolet) absorption of evanescent waves dispersed in the optical contact zones, as a function of granule size and geometry. The decontamination rate also depends on the packing and optical properties of metamaterial elements, as well as on the optical properties of contaminated liquids and microorganisms inside them. Different situations were investigated, when quartz (SiO_2) or glass metamaterials with dimensions of about 0.5–3 mm are separately placed into a quartz core tube, of about 2.7 cm diameter and 90 cm length, of decontamination equipment. Quartz granules transmit UV light (240–400 nm) of the Hg lamp and ensure an efficient microbial decontamination of translucent liquids and gases. We herewith demonstrate the efficient antimicrobial action of the evanescent waves dispersed around quartz metamaterial elements inside contaminated translucent fluids.

The decontamination rate was studied in different configurations of metamaterials such as microspheres and unordered granules, with the aim to obtain an efficient contact zone of the contaminated liquids with UV radiation. This effect can be boosted by the manipulation of microorganisms along the optical fibers or around microspheres. A special trapping zone could be identified by exploration of high-density viruses and bacteria interaction with metamaterials in order to annihilate pathogens.

We herewith propose a model for structures with optical periodicity characterized by large free spaces among elements and fitting evanescent zone. This proves essential for decontamination of fluids that flow close to surface of microspheres or optical fibers. Here, one should asses the adherence of liquids to surface, evanescent field penetration depth inside contaminated fluid, and coefficient of absorption of light radiation by microorganisms.

We analyzed the contact surfaces between the contaminated fluid and optical metamaterials, like photonic crystals or unordered granules, inserted inside the "core tube" of the decontamination reactor. In this case, the dispersive optical systems connected with the liquid volume through evanescent field improve the contact zones between UV radiation and pathogens. The dynamic treatment regime of translucent liquids that flow through decontamination core tube filled up with metamaterials is discussed. Moreover, the static treatment regime is analyzed, in which the fluids filling up the free spaces between metamaterial's elements keep motionless. When increasing the dimension of metamaterial elements, the decontamination rate decreases due to the increasing of distance between elements and the weaker penetration of the radiation into the liquid.

One expects a large increase of the observed effects when passing from simple lamps to laser irradiation, that is, incoherent to coherent light sources. Also, significant improvement is expected when using optical fibers for evanescent wave generation instead of, or in parallel with, quartz microspheres. Our results prove that the energy emerging via evanescent waves from multistructures under dynamic irradiation is not in any case lost but used in this particular case for the efficient antimicrobial action. This can contribute to a positive balance of light propagation through optical metamaterials and fiber metamaterials in view of valorizing all resources with maximum efficiency.

The approach presented in this chapter proposes a new method of decontamination using metamaterials consisting of microspheres and optical fibers structures with various topologies. The proposed method secures a substantial gain in the decontamination contact surfaces between the contaminated fluid and metamaterials, inserted inside the "core tube" of the decontamination reactor during the light (UV) propagation. The efficient decontamination using the evanescent zones of metamaterials opens new perspectives, not simply for new and innovative research applications, but besides opens novel ways for fundamental studies. The cumulative effect of UV radiation in contact with contaminated liquid depends on the refractive index of metamaterial and liquid, as well as optical properties of pathogens. A decontamination complementary effect depends on the probable trapping of liquid microparticles into the evanescent zone of optical fibers or microspheres in photon crystal structures [7, 8]. In this case, throughout the wave's propagation in nanofibers, a predilection for trapping and manipulating microparticles (viruses and bacteria) along the optical fibers occurs. The trapping of dielectric particles along the fibers was observed and revealed a new perspective on the capabilities of trapping the viruses, bacteria, and other microorganisms which can be present in contaminated liquids. Several techniques are proposed in order to destroy undesirable viral or bacterial particles [9]. These methods mainly used the UV lamp radiation for sterilization, but, quite often, they induced damaging effects and issues connected with the penetration depth. For instance, the 253 nm radiation effectively disinfects the surface, but sometimes, this emission could harm not just the viral particles and bacteria, but also mammalian cells [10–14]. When the intensity of UV irradiation is increased, the decontamination is always associated with mutation and shadowing effects, or damage of the viral nucleic acids and protein shells [11–14]. In other cases, radiation of microwave origin is proposed, but the absorption is not considered efficient because the energy is mostly transferred to water and not to the viral particles [12].

These drawbacks can be overcome by solving-related problems. The first one is associated with the UV radiation penetration depth. To solve this, it is required to propose an optical system, which allows reaching large penetration of the radiation inside contaminated liquids (or gases). Second, it is needed to use the method of selective short pulse decontamination [9, 12, 13] for the estimation of the potential penetration depth in translucent liquids. For example, in Refs. [12, 13], the authors proposed a photonic approach for selective neutralization of viruses. In Ref. [12], a near-infrared (IR) ultrashort pulsed (USP) subpicoseconds fiber laser source is used instead of UV lamps to avoid IR absorption. This UPS targets only the weak links on the protein shells of viral particles. By selecting the appropriate laser parameters, the authors reveal that it is possible to damage the protein shells, conducting to their inactivation, but without affecting mammalian cells. More exactly, they demonstrated that this method can discriminate and inactivate viral particles, from nonpathogenic viruses such as M13 bacteriophage and tobacco mosaic virus (TMV) to pathogenic ones like human papillomavirus (HPV) and human immunodeficiency virus (HIV). Concomitantly, the sensitive materials, for example, human Jurkat T cells, human red blood cells, and mouse dendritic cells, keep unaffected. In Ref. [13], a mechanical model is proposed. It has a normal mode where it oscillates around its equilibrium geometry. By selecting the visible or near-IR laser pulse duration to be shorter or near to the normal oscillation period, the authors of Ref. [12] have demonstrated that a single beam excitation laser pulse can bring a macroparticle, as for example, a virus, into oscillation by impulsive stimulated Raman [14]. It is worthy to mention that similar coherent Raman effect for larger frequencies of UV pulses is used for diagnostics of the various biomolecules (e.g., lipids) with optical equipment [15, 16].

2. Nonlinear models of molecule interaction with short-pulse radiation

UV-C radiation is effective for inactivating protozoa, bacteria, viruses, and many microorganisms. According to literature [17–21], the use of UV-C radiation is especially a good, environment-friendly, and chemical-free method to inactivate dangerous pathogens in diverse condition. UV-C cannot pass through our atmosphere, so it does not contribute to DNA damage. However, it is worth to mention that UV-C lamps give effective results in killing bacteria and microbes.

The process of decontamination by UV radiation, which can cause thymine dimers of bacteria and viruses, is not yet fully understood [17]. Bactericidal mechanism of UV-C has a maximal damage to RNA and DNA. This process is accompanied by generation of pyrimidine residues in the nucleic acid strands. The consequence of this modification is a production of cyclobutane pyrimidine dimers that induces deformation of the DNA molecule. This might cause local vibration energy of the modes that may be coupled by nonharmonic, nonlinear term. For example, two vibration defects in cell replication can lead to cell death eventually (**Figure 1**).

Ref. [22] demonstrated that when exposing *E. coli* DNA to UV-C irradiation, randomly placed, dose-dependent, single-strand breaks are generated. It was proposed that the negative supercoiling strain on the DNA backbone is generated by the conformational relaxation. It has been often proved that as a result of the inactivation of bacteria and DNA viruses under UV action, thymine dimers are produced. A dose of 4.5 J/m^2 is testified to cause 50,000 pyrimidine dimers per cell [23]. It has been reported that 100 J/m^2 induces approximately

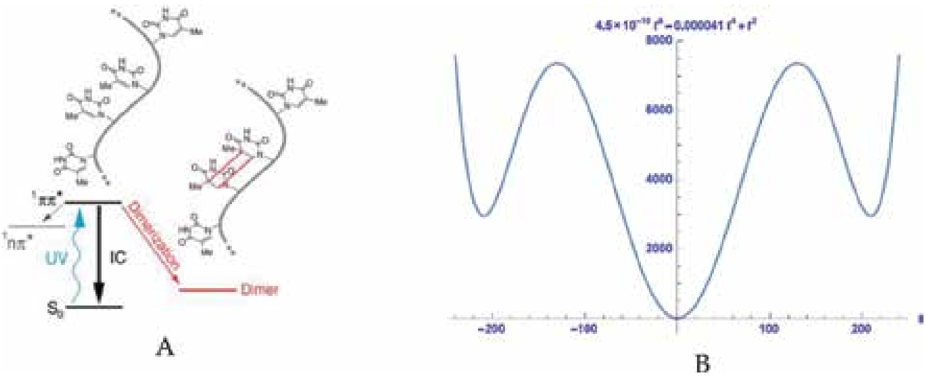

Figure 1. (A) Dimer bond generation under UV-C radiation of DNA according to Ref. [22] and (B) two-dimension potential with two minimums. First minimum corresponds to nondimer DNA and second minimum is similar to the dimer phototransformation of DNA under the UV-C radiation.

seven pyrimidine dimers per viral genome in SV40, which is sufficient to strongly inhibit viral DNA synthesis [24]. Thymine dimers formed within short pulse of UV excitation are properly oriented [19]. Only a few percent of the thymine doublets are expected to be favorably sited for reaction and dimerization at the moment of UV excitation.

a. **Figure 2(A)** explains the dimerization process for a thymine doublet having the appropriate orientation. The two most common conformations of DNA are A-DNA and B-DNA. Molecular orientations can fluctuate due to A and B conformations and vibrational or other movements of the DNA molecule. The average twist angle between consecutive base pairs varies with a few degrees only between the A and B conformations. The minor amount of conformational variation in A-DNA versus B-DNA explicates the superior resistance of A-DNA to cyclobutene pyrimidine dimer.

b. UV could induce cross-links between nonadjacent thymine besides cross-links between adjacent thymine, as illustrated in **Figure 2(B)**. Cross-linking than can be produced between the nucleotides and proteins in the viruses' capsid could damage the capsid of DNA viruses.

c. Cross-linking with cytosine and guanine requires higher energy because of three hydrogen bonds instead of two for thymine/adenine bonds. Accordingly, the thymine dimers are predominant. Thymine may also induce links with proteins, including the ones in the capsid (as is the case for viruses), as illustrated in **Figure 2(C)**. Other biological molecules with unsaturated bonds such as coenzymes, hormones, and electron carriers are prone to UV damage. In RNA (prokaryotic cells, eukaryotic cells, or viruses), uracil replaces thymine. The inactivation of RNA viruses is accompanied by cross-linking between the uracil nucleotides and the generation of uracil dimers [25]. These dimers could damage the capsid of RNA viruses, too. There exist limited quantitative data about the specific damage of DNA produced by UV absorption. Ref. [25] demonstrated that the UV exposure of mengovirus induces a fast formation of uracil dimers. This seemed to be the main source of virus inactivation. During 10 min of UV irradiation, a maximum of 9% of the total uracil dimers of the viral DNA are formed. Studies also demonstrated that irradiated viral RNA

> converts into a viral protein covalently linked. Moreover, a slow destruction process of capsid occurred and photoproducts were produced. In the virus irradiated by UV appeared a covalent linkage of viral RNA to viral polypeptides, the most probably due to close vicinity of RNA and proteins in the capsid. The protein linked covalently to the RNA does not surpass 1.5% of the total protein capsid. The authors of Ref. [26] studied Venezuelan equine encephalitis (VEE) under UV irradiation and found evidence suggesting that the formation of uracil dimers led to extensive contacts of the RNA with protein in the nucleocapsid.

Taking into consideration the important advantages of vibrational spectroscopy based on nonlinear coherent anti-Stokes generation mechanism, the new technique *coherent anti-Stokes Raman spectroscopy (CARS)* was reported by authors of Ref. [27] as an attractive tool for rapid excitation of vibrational modes. The application of USP lasers in coherent Raman scattering (CRS) or CARS opens the new possibilities in the decontamination procedures of fluids by dangerous pathogens (viruses and bacteria). In many cases for the effective inactivation procedure of pathogens on the implant surface, it is necessary to take into consideration the relative dimensions of viruses and bacteria and their possible molecular vibration symmetry [28, 29]. Most natural viruses depend upon the existence of capsids with specific geometry, protective shells of various sizes composed of protein subunits (**Figure 3**). Up to now, the general shaping capsid design is still elusive. Therefore, the correct understanding of their properties may help to realistically block the virus life cycle and, consequently, design of efficient nanoassemblies.

The authors of Ref. [30] reveal an exceptional and species-independent evolutionary pressure on virus aphids. It is based on the concept that the simplest capsid designs are the best. This holds true for all existing virus capsids. As a consequence of theories, it results a substantially significant periodic table of virus capsids that reveals strong and predominant evolutionary pressures. It also offers geometric explanations for other capsid properties (rigidity, pleomorphic, auxiliary requirements, etc.), which earlier were considered to be unique for an individual virus.

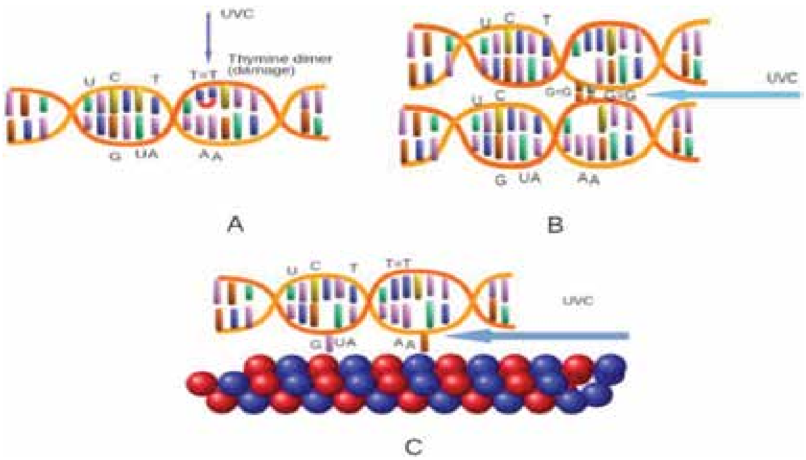

Figure 2. (A) Damage bonds and generation of dimer bonds under UV-C radiation of DNA. UV-C may also induce cross-links between nonadjacent thymine illustrated in (B). Cross-linking can occur with proteins, cytosine, and guanine (C).

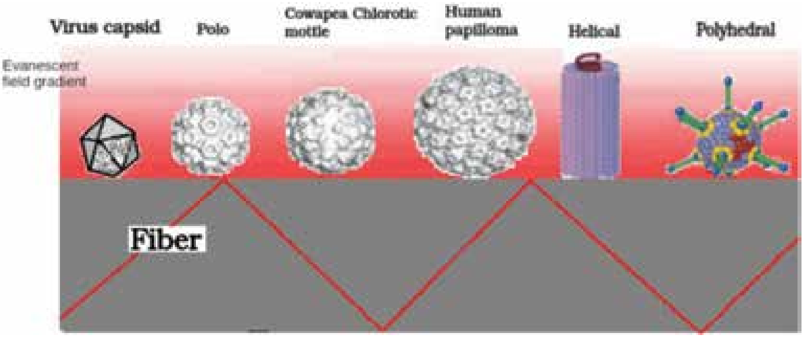

Figure 3. Relative dimension of viruses (bacteria) and their commensurability with the evanescent zone of a fiber optic. The spherical symmetry of the human papilloma, cowpea chlorotic mottle, and polo viruses. Some topological structures of polyhedral and helical viruses. Reproduced with permission from [6].

In our opinion, intrinsic topology of DNA dimmers (see **Figure 4**) may help to properly consider the symmetry vibration modes of this virus structure, such as to estimate the probable nonharmonic excitation of virus constituents by selectively annihilating them for the duration of the coherent Raman excitation. In the following, the method for exciting local vibration modes of biomolecule nanoassemblies is presented.

Most natural viruses depend upon the existence of spherical capsids: protective shells of various sizes composed of protein subunits (see **Figure 4**). Here, we must estimate the commensurability of virus dimensions with the depth of the evanescent zone of radiation around the metamaterials. So far, general evolutionary pressures shaping capsid design have remained elusive, even though an understanding of such properties may help in rationally impeding the virus life cycle and designing efficient nanoassemblies.

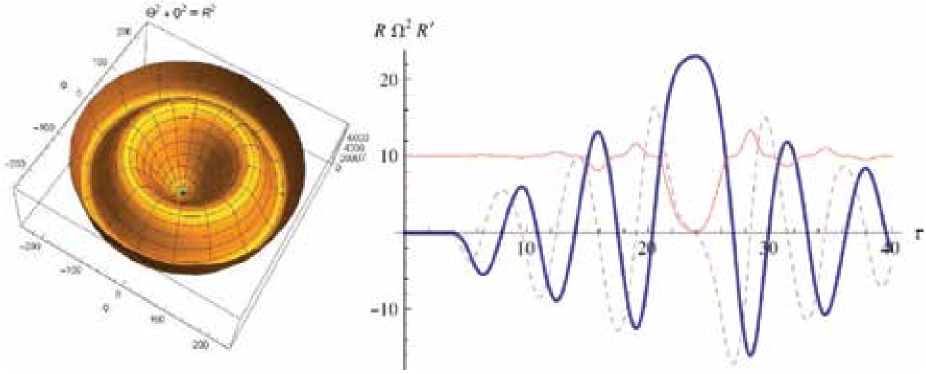

Figure 4. Two-dimensional potential with two minimums which correspond to destroy DNA schemes represented in **Figures 1** and **2**. First minimum corresponds to nondimmer DNA and second minimum to the dimerization of DNA under the UV-C radiation. In the right hand, the transfer of DNA from first minimum to the second minimum is plotted. The thick line represents the behavior of $R(t)$, the red line to nonlinear oscillatory frequency in the relative units Ω^2/Ω_0 and $\tau = t/\Omega_0$.

Local vibration energy of the modes may be coupled by nonharmonic nonlinear term. For example, two vibration modes Q and Θ can be represented as a symmetric function relative to the square value of these normal coordinates:

$$\begin{aligned} H_0 = {} & \frac{M_q}{2}\left(\frac{dQ}{dt}\right)^2 + \frac{M_\theta}{2}\left(\frac{d\Theta}{dt}\right)^2 + \frac{M_q\Omega_q^2Q^2}{2} + \frac{M_\theta\Omega_\theta^2\Theta^2}{2} - \kappa_q Q^4 - \kappa_\theta\Theta^4 \\ & - \kappa_{\theta,q}\Theta^2Q^2 + \chi_q Q^6 + \chi_\theta\Theta^6 + \chi_{q,\theta}\Theta^2Q^4 + \chi_{\theta,q}\Theta^4Q^2 \end{aligned} \tag{1}$$

Here M_i, Ω_i, and κ_i are the effective mass, frequency, and nonharmonic parameter for the vibration mode i; $\kappa_{\theta,q}$ is the nonlinear coupling of the normal modes of molecule oscillations. The nonharmonic terms present in the Hamiltonian describe the possible inactivation of pathogens at higher excitation.

Two situations of the vibration of this molecular system represented by DNA or tubulins in protein packing in the bacteria microtubule are considered. Collective nonlinear coupled modes, for example, phonons in the condensed mater [31, 32], were introduced and described by the Hamiltonian (1). Therefore, two vibration modes, Q and Θ, become aperiodic according to the theory of catastrophe [33], for higher excitation of the system with short laser pulses [13, 30] with the pulse duration $\tau_L < 1/\Omega_i$:

$$\begin{aligned} & \frac{d^2}{dt^2}Q + \left\{\Omega_q^2 - 4\tilde{\kappa}_q Q^2 + 6\tilde{\chi}_q Q^4 - 2\tilde{\kappa}_{q\theta}\Theta^2 + 2\tilde{\chi}_{\theta,q}\Theta^4 + 4\tilde{\chi}_{q,\theta}\Theta^2Q^2\right\}Q + 2\Gamma_q\frac{d}{dt}Q = F_q(t); \\ & \frac{d^2}{dt^2}\Theta + \left\{\Omega_\theta^2 - 4\tilde{\kappa}_\theta\Theta^2 + 6\tilde{\chi}_\theta\Theta^4 - 2\tilde{\kappa}_{q\theta}Q^2 + 2\tilde{\chi}_{q,\theta}Q^4 + 4\tilde{\chi}_{\theta,q}\Theta^2Q^2\right\}\Theta + 2\Gamma_\theta\frac{d}{dt}\Theta = F_\theta(t). \end{aligned} \tag{2}$$

Here, we have introduced the attenuation constant, Γ_i, of each coupling mode through nonlinear interaction, $\tilde{\chi}_{ij} = \chi_{ij}/M_i$; $\tilde{\kappa}_{q\theta} = \kappa_{\theta,q}/M_i$. The nonharmonic term of each mode is described by the nonlinear constant $\tilde{k}_i = k_i/M_i$. The first and second equations of (2) use the corresponding component for anisotropy effective masses M_q and $M\Theta$. The nonharmonic potential is described by the two-dimensional localization potential in **Figures 1** and **4**. If it is absent, the mass anisotropy and two dimensions become symmetrical and we may do the substitution $Q = R\cos\varphi$ and $\Theta = R\sin\varphi$ so that the terms $\left(M_q\Omega_q^2Q^2 + M_\theta\Omega_\theta^2\Theta^2\right)/2$, $\kappa Q^4 + \kappa\Theta^4$ $+2\kappa\Theta^2Q^2$, and $\chi Q^6 + \chi\Theta^6 + 3\chi\Theta^2Q^4 + 3\chi\Theta^4Q^2$ in Hamiltonian (1) can be substituted by $M\Omega^2R^2/2$, κR^4, and χR^6. Taking into consideration the symmetric form of the Hamiltonian,

$$H_0 = \frac{M}{2}\left[\left(\frac{dQ}{dt}\right)^2 + \left(\frac{d\Theta}{dt}\right)^2\right] + \frac{M\Omega_0^2R^2}{2} - \kappa R^4 + \chi R^6,$$

we reduce the system of Eq. (2) to a single equation for radial component of nonlinear oscillator

$$\frac{d^2}{dt^2}R + \left\{\Omega_0^2 - 4\tilde{\kappa}R^2 + 6\tilde{\chi}R^4\right\}R + 2\Gamma\frac{d}{dt}R = F(t). \tag{3}$$

Short laser pulses applied externally interact with the molecular dipole of virus components. Consequently, the Hamiltonian takes the traditional form $H_I = -(\mathbf{P}(E), \mathbf{E}(t, z))$. Following the common representation [34–36], the laser field induces the biomolecule polarization, in which components, in similar representation, have tensor character. They depend on the symmetry of excited molecules (virus' or bacteria's constituents) $P_j(E) = \alpha_{jl}E_l$. Because of the tensor character of the two oscillation modes, we can decompose the recognizability $\alpha_{jl}(Q, \Theta)$ in Taylor series relative to the normal components Q and Θ

$$\alpha_{jl} \simeq \alpha_{jl}^0 + \frac{\partial \alpha_{jl}}{\partial Q} Q + \frac{\partial \alpha_{jl}}{\partial \Theta} \Theta + \varepsilon\left(Q^2; \Theta^2; Q\Theta\right).$$

By introducing this expression in the interaction Hamiltonian, we observe that the interaction with the local vibration modes can be described by the function

$$U_I = \alpha'_{jlk} E_j E_l Q_k,$$

where $Q_1 = Q$, $Q_2 = \Theta$, and the tensor $\alpha_{jlk'} = \partial\alpha_{jl}/\partial Q_k$ must be maximally symmetrical according to the symmetry of the virus or bacteria biomolecules. Considering that laser pulses have same polarization, we represent it through the time-dependent Gaussian function $E_i = E_0 \exp\left[-\left(t/\sqrt{2}\tau_L\right)^2\right] \cos(\omega_i t)$. For this, we substitute the generalized driving forces $F_j = -\partial U_I/\partial Q_j$ in the system of Eq. (2). The numerical solution of symmetrized nonlinear Eq. (3) for the following expression of the parameters of the potential $2U/\left(|M\Omega_0^2\right) = R^2 - 4.1 \cdot 10^{-5} R^4 + 4.5 \cdot 10^{-10} R^6$ of the system is represented in **Figure 4**. Here, we have used the relative attenuation constant $2\Gamma/\Omega_0 = 10^{-3}$. In case of short laser pulses with relative intensity,

$$F(\tau)/\Omega_0^2 = \sum_1^8 \left[4.7 \cdot \exp\left[-(\tau - 5n)^2\right] \sin(\tau)\right],$$

$\omega_a - \omega_s = \Omega_0$, and $\Omega_0\tau_L = 1$ were chosen as parameters. As follows from the numerical solution of Eq. (3), in the relative time moment $\tau \sim 25$, the nonlinear oscillator achieves the local maximum potential between the wells represented in the left figure of **Figure 4**. After this relative time point ($\tau > 25$), the nonlinear oscillator relaxes in the second minimum of double well potential according to the numerical representation in **Figure 4**. This localized state corresponds to the damage situations of DNA discussed in **Figure 2**.

Let us give the analytical representation of this excitation process described by the system of nonlinear Eq. (2). According to Refs. [13, 29], we observe a same exponential dependence on the $\Omega_j\tau_L$, in the initial stage of excitation $Q_j = Q_{0j}\exp\left[-\Gamma_j t\right] \sin\left(\Omega_j t\right)$, when nonlinear frequency is approximated with linear part $\Omega_j(Q, \Theta) \approx \Omega_j$, $j = 1, 2$. Here we consider that $Q = Q_1$ and $\Theta = Q_2$. After the first pulse with duration, $\Omega_0\tau_L \ll 1$, the amplitude has the following dependence on the intensity, E_0^2, pulse duration, τ_L, and local oscillation frequency of the normal mode j, Ω_j

$$Q_{0j} = \frac{\sqrt{\pi}\tau_L E_0^2 \alpha'_j}{2\Omega_j} \exp\left[-(\Omega_j \tau_L)^2/4\right].$$

For simplicity, let us add the next square terms in the system of Eq. (2). As in Refs. [13, 29], we address the problem so as to excite the system of coupling oscillators (2). Consequently, the "nonlinear frequency" $\sqrt{\Omega_q^2 - 4\chi_q\langle Q^2\rangle - 2\chi_{q\theta}\langle\Theta^2\rangle}$ reached zero value, which equals to the termination of the local vibration mode after a finite number of short laser pulses. Let us consider a set of "n" consequent pulses generated in the time interval $T < \Gamma_j^{-1}$. The cumulative energy of the local oscillator after the precursor pulse may be used for the next excitations. For example, after the first pulse, Q and Θ amplitudes of models are described by the expression above. Introducing this expression in the system of Eq. (2), we obtain the following mean values of Q^2 and Θ^2,

$$\left\langle Q_j^2 \right\rangle = \frac{\pi\tau_L^2 E_0^4 \alpha_j'^2}{22^2\Omega_j^2} \exp\left[-(\Omega_j \tau_L)^2/2\right].$$

In other words, we obtain the new frequencies of nonlinear oscillator modes of the system of Eq. (2) described by linearized differential equations with renormalized frequencies by the first pulse

$$\begin{aligned} &\frac{d^2}{dt^2}O(t) + \left\{\Omega_q^2 - 4\chi_q\langle Q^2\rangle - 2\chi_{q\theta}\langle\Theta^2\rangle\right\}Q + 2\Gamma_q\frac{d}{dt}O(t) = F_q(t);\\ &\frac{d^2}{dt^2}\Theta(t) + \left\{\Omega_\theta^2 - 4\chi_?\langle\Theta^2\rangle - 2\chi_{\theta q}\langle Q^2\rangle\right\}\Theta + 2\Gamma_\theta\frac{d}{dt}\Theta(t) = F_\theta(t). \end{aligned} \tag{4}$$

The solutions of these equations are similar to expression (2) in which, instead of Q_{0j}, it is used by the new expression;

$$Q(t_2) = Q_{01}\exp\left[-\Gamma_q t_2\right]\sin\left(\tilde{\Omega}_q t_2\right) + Q_{02}\exp\left[-\Gamma_q t_2\right]\sin\left(\tilde{\Omega}_q t_2\right)$$

Here, the second part contains the particular solution of the excitation of oscillator after the second pulse

$$Q_{02} = \frac{\sqrt{\pi}\tau_L E_0^2 \alpha'_q}{2\tilde{\Omega}_q} \exp\left[-\left(\tilde{\Omega}_q \tau_L\right)^2/4\right],$$

where $\tilde{\Omega}_q = \sqrt{\Omega_q^2 - 4\chi_q\langle Q^2\rangle - 2\chi_{q\theta}\langle\Theta^2\rangle}$. This procedure to excite a nonlinear oscillator may continue till one of the amplitudes of oscillation attains the maximal separation line of nonlinear potential function $U_0(Q,\Theta)$, as represented in **Figure 5**. It corresponds to the case when the frequency achieves the zero value after "n" short pulses

$$\Omega_q^2 - 4\chi_q\langle Q_n^2\rangle - 2\chi_{q\theta}\langle\Theta_n^2\rangle = 0;$$

or

$$\Omega_\theta^2 - 4\chi_q\langle\Theta_n^2\rangle - 2\chi_{\theta q}\langle Q_n^2\rangle = 0.$$

In fact, this effect may be observed in a single pulse excitation of nonlinear system of Eq. (2).

The above-described excitation method depends on the condition imputed for applied pulse duration relative to the vibration frequency of biomolecules $\Omega\tau_L < 1$. The local molecular oscillator is described by nonlinear equations; therefore the local frequency depends on the excited energy of such biomolecule. To surpass this difficulty, it is better to consider a longer laser pulse $\Omega\Gamma^{-1} > \Omega\tau_L > 1$, so that during the excitation to apply for selective excitations of virus and bacteria (see **Figure 5**). This excitation method is alike to the diagnostics of molecular systems suggested in Refs. [14–16]. The method attracted many specialists in CARS diagnostics and studies of molecular and cellular subsystem design. According to this theory, the strength product [5] of two possible fields through the Stokes and anti-Stokes generation components is introduced:

$$\begin{aligned}\Pi^-(t,z) &= E_p^+(z,t)E_a^-(z,t) + E_s^+(z,t)E_p^-(z,t)\\ &= G(k_p,k_a)\hat{b}\hat{a}^\dagger\exp\left[i\Omega_0 t - i(k_a-k_p)z\right] + G(k_s,k_p)\hat{s}\hat{b}^\dagger\exp\left[i\Omega_0 t - i(k_p-k_s)z\right],\end{aligned} \tag{5}$$

Here, $E_p^+(z,t)$, $E_s^+(z,t)$, and $E_a^+(z,t)$ are the positively defined pump, Stokes, and anti-Stokes strength components of Raman process, expressed by the generation of photon operators in each mode $\hat{b}^\dagger$, $\hat{s}^\dagger$, and $\hat{a}^\dagger$, respectively. The related negative field component expressed by the annihilation operators is introduced in expression (5). The frequency $\Omega_0 = \omega_p - \omega_s = \omega_a - \omega_p$ is approximately equal to local vibration mode of the biomolecule Ω. Accordingly, the interaction Hamiltonian with the local nonlinear mode of viruses or bacteria may be described by:

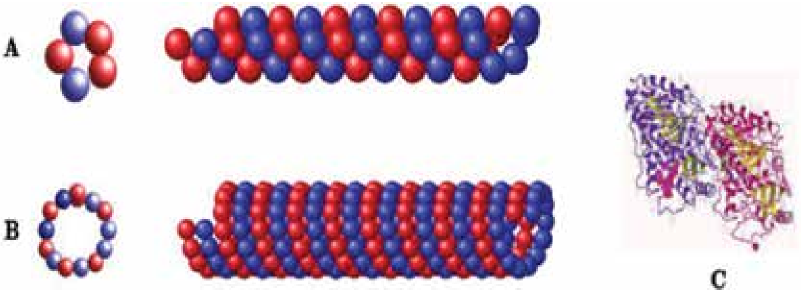

Figure 5. Comparison of 5-protofilament bacterial microtubule architectures. (A) α and β tubulins are represented in blue and red, respectively. (B) Representation of a 13-protofilament eukaryotic microtubule: α—tubulin in red; and β—tubulin in blue. Seams and start-helices are indicated in green and red, respectively. (C) The biomolecular structure of α and β tubulins is indicated.

$$\hat{H}_I = -\hat{\Phi}^+(t, z)\hat{\Pi}^-(t, z) + H.c., \tag{6}$$

The operator $\hat{\Phi}^+(t, z)$ is proportional to the displacement of local oscillator mode from the equilibrium position, $\hat{P}(t, z) \sim \hat{Q}(t, z) \sim |e><g| + |g><e|$. The two-mode Raman transitions from the first excited to the ground states of the local oscillator are given in **Figure 6**.

Bistable excitation process of nonlinear oscillator in external biharmonic field was in the center of attention in many papers (see, e.g. [34, 37]). Following the ideas of Ref. [37], we simplify the local vibration system (2) to single vibration mode Q described by the nonlinear Hamiltonian:

$$\hat{H}_0 = \hbar\Omega\hat{q}^\dagger\hat{q} - \hbar\kappa\left(\hat{q}^\dagger\right)^2(\hat{q})^2 \tag{7}$$

Introducing the new excitations, $\hat{D}^+ = \hat{q}^\dagger\sqrt{\Omega_0/\kappa - \hat{q}^\dagger\hat{q}}$, and de-excitation, $\hat{D}^- = \sqrt{\Omega_0/\kappa - \hat{q}^\dagger\hat{q}\hat{q}}$ operators in the vibration mode of the nonlinear Hamiltonian (6) [38], we observe that their commutation relation $\left[\hat{D}^+, \hat{D}^-\right] = 2\hat{D}_z$. For biomolecules with a positive nonharmonic parameter $\kappa > 0$, we observe that the inversion $\hat{D}_z = -\Omega_0/(2\kappa) + \hat{q}^\dagger\hat{q}$, together with two x and y polarization components, $\hat{D}_x = \left(\hat{D}^+ + \hat{D}^-\right)/2$ and $\hat{D}_x = \left(\hat{D}^+ - \hat{D}^-\right)/2i$, forms the square pseudovector $\hat{D}^2 = \hat{D}_z^2 + \hat{D}_x^2 + \hat{D}_y^2$, which is conserved during the excitations. These operators are similar to angular momentum generators in quantum mechanics and belong to $SU(2)$ algebra. Similar operators can be introduced for bimodal field in Raman scattering (7), $\hat{L}_z = \hat{a}^\dagger\hat{a} - \hat{s}^\dagger\hat{s}$; $\hat{L}^- = \sqrt{2}\left(\hat{b}\hat{s}^\dagger + \hat{a}\hat{b}^\dagger\right)$; $\hat{L}^+ = \sqrt{2}\left(\hat{s}\hat{b}^\dagger + \hat{b}\hat{a}^\dagger\right)$. Here, in rotating wave approximation, we obtain the following symmetrical form of the Hamiltonian:

$$\hat{H} = \hbar\Delta\hat{D}_z - \hbar\kappa\hat{D}^+\hat{D}^- - \hbar g\left\{\hat{L}^-\hat{D}^+ + \hat{D}^-\hat{L}^+\right\}, \tag{8}$$

which describes the interaction of three discrete modes of microcavity (or nanofiber) with nonlinear vibration of biomolecule with conservation of total number of photons and two pseudovectors, D^2 and $L^2 = \hat{L}_z^2 + \hat{L}_y^2 + \hat{L}_x^2$. In the Hamiltonian (8), we have $\Delta = \Omega - \Omega_0$, which is the detuning from resonance to the frequency of bimodal vector of Raman field, Ω_0, and the frequency of local oscillator, Ω. κ is the nonharmonic parameter, which drastically reduces the distance between the level of harmonic vibrations of the molecular system. The coupling constant $\hbar g$ describes the biharmonic coupling between the vibrational mode of biomolecules and Stokes, pump, and anti-Stokes modes of the electromagnetic field. Let us study the case when $\Omega\tau_L > 1$ and the damping rate of excited oscillator is lesser than life time of Stokes, anti-Stokes, and pump photons in nanofibers. Here, the operators of electromagnetic field in the density matrix of the system might be adiabatically eliminated. If we consider that the photons are organized in the anti-Stokes mode, we obtain a master equation, which characterizes the dynamic behavior of biomolecule nonlinear oscillators:

$$\frac{\partial}{\partial t}\hat{W}(t) = -i\left[\Delta\hat{D}_z,\hat{W}(t)\right] + i\kappa\left[\hat{D}^+\hat{D}^-,\hat{W}(t)\right] + \left\{i\Omega_R\left[\hat{D}^+\hat{W}(t)\right] + \left[\hat{D}^-\hat{W}(t),\hat{D}^+\right] + H.c.\right\}, \tag{9}$$

Here $\Omega_R \simeq g\sqrt{2n_a n_p}$ and $\gamma \approx 2g^2 n_a \varepsilon/\left(\Delta^2+\varepsilon^2\right)$ are the two-photon Rabbi frequency and the coherent scattering rate of the applied anti-Stokes field component, while n_a and n_p are the numbers of photons in the anti-Stokes and pump modes. When detuning Δ is positive, the excitation of nonlinear oscillator is compensated by the nonharmonic term in the master Eq. (9), which is proportional to the nonlinear parameter, κ. This excitation is complemented by the improving of resonance between the excited vibration levels of molecular oscillator. It may be defined as a jump of the number of excitations with increasing of the external field intensity. Using the solution of the equation, the number of excitations of the nonlinear oscillator can be given as a function of intensity of applied field Ω_R, nonlinear parameter κ, and detuning from resonance Δ:

$$n = \frac{N}{2} - \sum_{n=0}^{N} n\frac{\Gamma(N+n)}{\Gamma(2n)\Gamma(2j-n)}\left\{\frac{\left|\Gamma\left(1+i\tilde{\delta}+n\right)\right|^2}{\tilde{v}^{2n}\left|\Gamma\left(1+i\tilde{\delta}\right)\right|^2}\right\}\frac{1}{2A}. \tag{10}$$

The normalized constant is

$$A = \sum_{n=0}^{N}\left\{\left|\frac{\Gamma\left(1+i\tilde{\delta}+n\right)\right|^2}{\tilde{v}2n\left|\Gamma\left(1+i\tilde{\delta}\right)\right|^2}\right\}\frac{\Gamma(N+n)}{\Gamma(2n)\Gamma(2j-n)}. \tag{11}$$

Here, $\tilde{\delta} = \delta(1+i\chi)/\left(1+\chi^2\right)$; $\tilde{v} = v/(1+i\chi)$, where the new parameters represent the relative values of the detuning $\delta = \Delta/\gamma$; nonlinear parameter $\chi = \kappa/\gamma$, and the intensity of the field $v = \Omega_R/\gamma$.

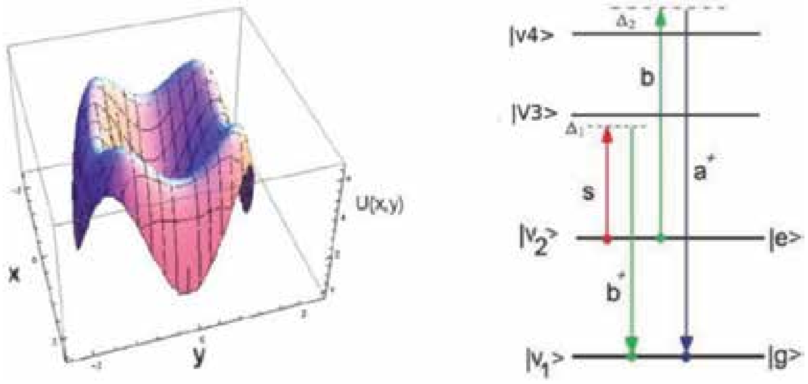

Figure 6. The dependence of the potential energy of the nonlinear oscillator on two normalized modes $x = \sqrt{M/2}\Omega Q$ and $y = \sqrt{M/2}\Omega\Theta$, energy scheme for such nonlinear potential with possible Raman excitation. Reproduced with permission from [6].

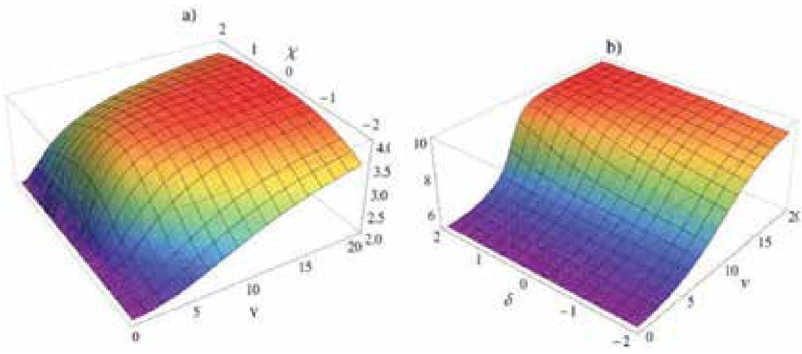

Figure 7. The dependence of number of excitation n as function of (a) coherent excitation, ν, and nonlinearity, χ, for constant detuning, $\delta = 2$, and (b) coherent excitation, ν, and detuning, δ, for the constant nonlinearity, $\chi = 2$. Here, the total number of excitation is $N = 10$. Reproduced with permission from [6].

The number of excitations for a nonlinear oscillator is defined by the ratio $N = \Omega/\kappa$. Following the solutions (10) presented in literature in various publications (see, e.g. Ref. [37]), we displayed in **Figure 7** the mean number of excitations as a function of the intensity and nonlinearity of applied field or as a function of excited field and detuning. This phase transition is typically described by a bistable behavior of the nonlinear oscillator. Taking into account other nonlinear terms (e.g., Q^6) in the Hamiltonian (1), we may terminate the nonharmonic oscillator moved to other metastable position.

3. Decontamination volume estimated for different metamaterials

Latest investigations consider the geometry of metamaterial elements for different applications [38–43]. Conical metallic nanoparticles in an array configuration could be used for localization of SPR [38]. The geometry of nanoparticles and their arrangement improve the biochemical sensing and detection for drug delivery, heating therapy, etc. Ref. [40] describes a similar localized SPR. An electromagnetic sensor made of nonspherical gold nanoparticles deposited on a silica substrate having a matrix configuration with the interparticle distance much smaller than the incident wavelength is proposed. Other applications of the different geometry of elements of metamaterials are related with optical proprieties of each element. Explicitly, the cylindrical elements of metamaterials could be used as a performing resonator in the optical cloaking [41]. The authors of Ref. [42] mentioned that macroscopic characteristics depend not only on molecular structure but also on specific geometry. Advances and potential applications of optical electromagnetic metamaterials and metasurfaces for refractive index sensing and sensing light properties are presented in Ref. [43]. These metamaterials can be simply integrated with several electronic devices.

Here, we give a clear explanation for the increasing of the penetration depth of UV-C radiation inside the decontamination core. It is due to multiple refractions and reflections of radiation on the spherical and conical structures of metamaterials. If the light enters into the translucent liquid through a circular surface, the decontamination volume may be proportional to the surface of the circle multiplied by the attenuation depth of the radiation inside the contaminated liquid (see **Figure 8**). Conversely, if the light penetrates the liquid through the base of a quartz semisphere, the contact surface increases two times, becoming $2\pi R^2$. The decontamination volume also increases, becoming equal to the surface of semisphere multiplied by attenuation depth. If the light is introduced inside the cone through its base, a considerable increase of the contact surface metamaterial (liquid) occurs. Here, the multiple refractions of UV-C radiation inside the cone improve the contact surface between the quartz cone and the translucent liquid. It increases significantly when the cone generator is larger than the cone radius. The multiple optical contacts between metamaterial elements (spheres, granules, conic elements, fibers) lead to a drastically dispersed light inside the contaminated fluid that flows between these elements.

Let us analyze the liquid decontamination by traditional method, which makes use of UV-C pulsed light (see **Figure 9(a)**). If the contaminated liquid flows inside a cylinder and it is irradiated from all directions with UV radiation, the total decontamination surface is $S = 2\pi R(L + R)$. The first term designates the lateral surface, the last term the surface of the bases, R the radius of the base, while L is the length of the cylinder. Using classical decontamination, a large volume, V_{con}, of infected liquid remains contaminated:

$$V_{cl} = \pi 2\pi R(L + R)d_p;$$
$$V_{con} = \pi R^2 L - V_{cl} \gg V_{cl},$$

where V_{cl} represents the efficient decontamination volume and $d_p \sim \lambda$ is the UV radiation penetration depth into liquid. Further down, we suggest a decontamination method making use of metamaterials in order to increase the decontamination volume.

Sensing properties are anticipated to be related to nanoscale system dimensions. In a first step, the contact surface of flowing gas or liquid is estimated. To increase the contact surface of the contaminated liquid, we examined the UV radiation propagation in two types of metamaterials: type A corresponds to the packing of photonic crystal fibers (PCFs) and type B to the photonic crystals (PCs) (see **Figure 9(b** and **c)**). Both metamaterials are transparent in UV region.

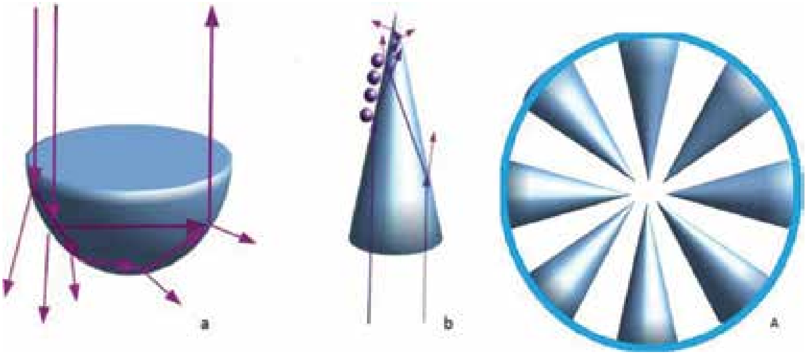

Figure 8. The multiple reflection and refractions of the UV light passing through the bases of semispherical (a) and conical (b) elements of metamaterial. Figure A represents the decontamination core filled up with conical structures. The radiation of six UV lamps is guided inside the center of decontamination tube through the bases of such conical structures where the nontransparent contaminated liquid has the maximal flow velocity.

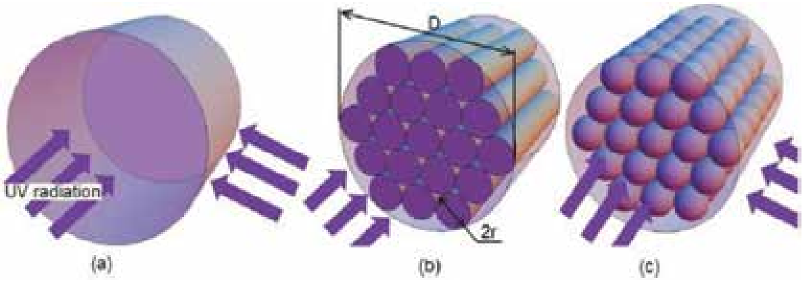

Figure 9. Methods of decontamination: (a) traditional decontamination; (b) decontamination using photonic crystal fibers in the hexagonal packed bundle; (c) metamaterial like photon crystal. Reproduced with permission from [6].

When the PCF system is positioned in a cylinder containing contaminated liquid (see **Figure 9(b)**), this liquid will fill completely the space between fibers. Therefore, the decontamination surface grows substantially

$$S_d = \pi r(r + 2rLN), \tag{12}$$

where N is the number of fibers from PCF and r is the radius of one fiber. Last term stands for the fibers' lateral surface. It is assumed that the UV radiation is introduced by fibers in the cylinder. The UV radiation penetration depth (evanescent field) is influenced by the relative refractive indexes of fibers and contaminated liquid. The evanescent field intensity is given by:

$$I = I_0 \exp\left[-z/d\right], \tag{13}$$

where I is the intensity of evanescent zone at distance z from fiber and d is characteristic exponential decay depth expressed as:

$$d = \frac{\lambda}{4\pi n_2}\sqrt{\frac{\sin^2(\theta_c)}{\sin^2(\theta) - \sin^2(\theta_c)}}.$$

Here, θ_c represents the critical angle of incidence $\sin\theta_c = n_2/n_1$, θ is the angle of incidence, $\theta > \theta_c$; n_1 is refractive index of the fibers, n_2 is refractive index of the liquid medium, while λ is the wavelength of UV radiation. In order to connect this approach with the classical decontamination method, it is necessary to indicate the decontamination area through the number of fibers. The estimates show that the small radius of fiber r is proportional to $r \sim R/\sqrt{N}$. If r is introduced in relation (12), the decontamination area of N cylindrical fibers is obtained:

$$S_d \sim 2\pi RL\sqrt{N}. \tag{14}$$

According to (14), the decontamination surface is proportional to the square root of N, number of fibers. Here, we consider negligibly the small surfaces of cylinder base as compared with the lateral surface of the fibers. Eqs. (13) and (14) demonstrate that decontamination volume of liquid is, in this case, proportional to

$$V_d \sim 2\pi RLd\sqrt{N} \tag{15}$$

It is obvious also that the decontamination volume is proportional to $\sqrt{N}$ ($V_d/V_{cl} \sim \sqrt{N}$). But it is yet not clear what happens with the free volume of liquid flowing between fibers, which is placed at a bigger distance in comparison with $\lambda/2$. This volume may be implicated in the contamination zone if the thickness of the fiber is decreased.

Using a standard hexagonal packed bundle symbolized in **Figure 9(b)**, it is possible to estimate the free volume between three fibers $v_f = r^2\left(\sqrt{3} - \pi/2\right)L = 0.18r^2L$. In this case, the free volume in the big bundle does not depend on the diameter of the fiber and is equal to $V_f = \pi R^2 L\left(\sqrt{3} - \pi/2\right)$. The unused volume may be expressed as $V_a = \pi RL\left(0.18R - \sqrt{N}\lambda\right)$. When this expression reaches zero value, the whole volume between the fibers can be used for fluid decontamination. Consequently, the fiber radius is $r \sim R/\sqrt{N} \sim \lambda/0.18$. A similar expression can be obtained for other types of fiber packing. Using the same method, we have estimated the decontamination surfaces of metamaterials like PC (see **Figure 9(c)**).

$$S_d = 4\pi r^2 N \sim \pi L^2 N^{1/3},$$

where L is the edge length of the cube, r is the radius of one microsphere, and N is the number of microspheres of the metamaterial. The liquid fills the space between microspheres and the decontamination volume can be expressed as

$$V_d \sim dS_d = 4\pi d R^2 N^{1/3} \tag{16}$$

We mention here that the increase of decontamination volume depends on the number of microspheres, described by a $N^{1/3}$ dependence.

At a first glance, it appears that the decontamination volume is smaller than in PCF, but this is just an illusion. Because the number of microspheres in a PC-like metamaterial is much larger than the number of fibers in PCF, decontamination volume is much higher in the second case. Another priority of last metamaterial consists in the fact that this works in all directions symmetrically, in comparison with PCF.

The free volume between spheres in a PC can be expressed as $v_{fr} = (2r)^3 - 4\left(\pi r^3/3\right) = 8r^3$ $(1 - \pi/6) \sim 0.48v_c$. The free volume between large cubes with dimension L have the same proportion $V_{fr} = 0.48V$. In this case, the difference $V_{fr} - V_d$ is proportional to $V[0.1/3/(2L)]$. When $L < \pi N^{1/3}/0.98$, a further increase of surface becomes impossible and therefore the classical aspect of evanescent zone is not acceptable. Consequently, the volume between the spheres may be considered a decontamination zone.

Metamaterials, as optical fibers or periodic photonic structures, open new possibilities to manipulate and annihilate viruses and bacteria in contaminated areas of liquids or organic tissue. For example, a good contact area between the implant and cells can be obtained if such metamaterials will cover the surface. The UV radiation guided along the surface of the implant ensures the best medical support against potential viruses or bacteria.

The depth and the volume of the evanescent zone of periodical waveguide structures influence UV action against bacteria and viruses. In **Figure 10**, we represent a periodical structure (containing fibers and spherical metamaterials), which is introduced in a cylinder inside the contaminated fluid flows. Using Eqs. (12), (15), and (16) (arrangements (b) and (c) in **Figure 9**), the relative decontamination coefficient is introduced:

$$\rho = \frac{V_d}{V_c}.$$

Since the cylinder has a lateral surface larger than that of the bases, the relative decontamination coefficient is $\rho \sim d\sqrt{N}/d_p$. A similar expression can be written for PC-like metamaterials if the cylinder is filled up with SiO_2 periodical bubbles. For this, the relative decontamination coefficient is $\rho \sim dN^{1/3}/d_p$. The classical decontamination volume is considered to be the penetration of radiation into the spherical elementary volume $4\pi R^2 d_p$ with the width $\Delta R \sim d_p$. Periodical fiber structures and periodical spherical materials were proposed for carrying out the preliminary measurements in decontamination procedures as a function of the intensity and pulse duration of UV pulses.

Taking this dependence into consideration, we used a funnel filled with 400 fibers. The relative coefficient, ρ, of contaminated liquid, which flows through the funnel filled up with fibers and a funnel without fibers for the same flowing volume, is calculated. This coefficient becomes 20 times larger for the same volume of liquid flowing inside the cylindrical part of the funnel filled with fibers (relative to funnel without fibers), when the penetration depth is comparable with the depth of the evanescent field $d \sim d_p$, where $d \sim 100$ nm. A similar equipment for SiO_2 cylinder filled with SiO_2 spherical bubbles through which contaminated liquid flows under the intense UV irradiation delivered by six lamps (see **Figure 10**) is proposed and preliminary tested. The decontamination rate is proportional to $N^{1/2}$ for PCF and to $N^{1/3}$ for PC, respectively.

Our previous studies [4] were devoted to the research of chemical reactions, which are produced in the microorganisms under UV pulse action. Here, one should consider the quantified structure of a quasiparticle energy transmitted from one DNA segment to another, or connected to protein microtubule. These vibration structures are analogous with two-dimensional phonon flows,

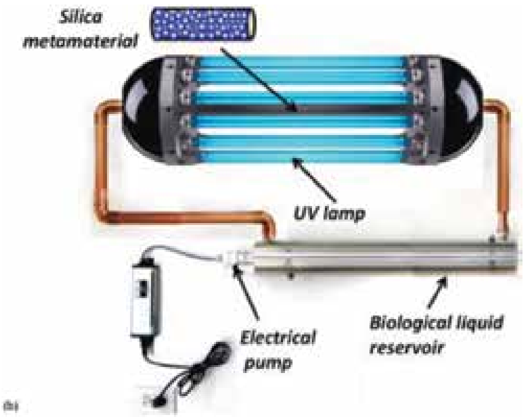

Figure 10. Experimental schemes proposed for the improvement of UV radiation contacts with fluids in the periodic optical SiO_2 structures in interacting with the contaminated liquids. Reproduced with permission from [6].

which are studied in graphene, boron nitride, or planar superlattices [31]. During decontamination process, the trapping of pathogen particles (viruses and bacteria) near the surface of fibers (or spheres) can occur. This effect was also described in literature [44]. It involves the attractive force acting on the particles presenting higher refractive indexes relative to the refraction index of liquid. This force occurs as a consequence of the large gradient of electromagnetic field (EMF) in the evanescent zone nearby the fiber (sphere).

In the next section, the contact area between the radiation propagating through the metamaterial elements and contaminated translucent fluids is increased. The decontamination rate is proportional to periodical spherical structures (N stands for the number of metamaterial elements) [4–6]. The efficiency of UV-C action on microorganisms present in contaminated fluids depends on the depth and volume of the evanescent zone of periodical waveguide structures.

4. Experimental decontamination equipment with metamaterials

For the decontamination of translucent liquids by UV-C radiation, we proposed the equipment in **Figure 11**, formed from a UV-C transparent core tube, which can be filled with metamaterials. As was estimated in Section 3, the decontamination rate is influenced by the packing and optical properties of metamaterial elements. Two types of metamaterials were used: (a) quartz (SiO_2) unordered granules with dimension around 1–5 mm and (b) transmission spectrum in UV region 240–260 nm (**Figure 11(a** and **b)**) spheres of glass material with diameter of 2 mm and transmission at 300 nm. The comparative analysis of the decontamination rate for these metamaterials is performed. Optical metamaterials can disperse UV-C light inside the fluid volume and improve the contact zone between radiation and contaminated fluids. In **Figure 11(a)**, the UV-C core tube used for the decontamination of translucent fluids is shown, while **Figure 11(b)** presents the decontamination equipment for dynamic treatment regime. The decontamination equipment consists of six low-pressure Hg UV-C lamps (30 W) with 90 cm length and about 2.7 cm diameter. These lamps surrounding the decontamination core tube (**Figure 10**) are placed in the center of a reflecting aluminum cylinder (with a diameter of about 30 cm). The UV-C radiation (with Gaussian distribution) is focused along the axis, i.e., in the decontamination area. The core tube can be filled up with optical metamaterials, while polluted fluids can freely circulate between elements, in interaction with evanescent waves.

The radiation penetration into the core tube offers a significant yield of the contact surface between the flowing fluid and UV radiation in a volume of $\sim 0.9 \times 10^{-4}$ m^3. The fluid circulating through the decontamination zone changes arbitrarily the optical frontiers among metamaterial elements and fluid, in function of pathogen concentration and optical properties. Consequently, the decontamination efficiency depends on the contact surface between the contaminated fluid and periodical optical metamaterial, and it is proportional to the number of elements of metamaterial. The penetration of light radiation into translucent fluids flowing through elements of metamaterials increases due to the optical evanescent field around each element. For the dynamic treatment regime, the core tube is connected to an external reservoir through which the polluted biological fluid flows. The circulation of the fluid is conducted by an electrical pump device. The working principle of the installation can be described as follows. The UV-C irradiation

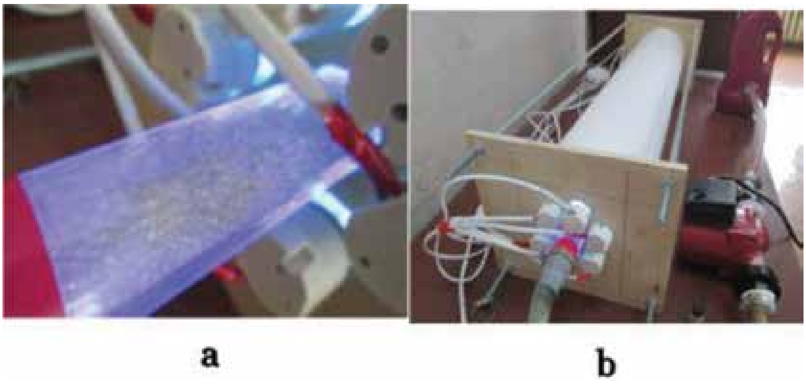

Figure 11. (a) Optical metamaterial used for decontamination and (b) decontamination equipment used for dynamic treatment regime.

of six germicidal lamps is concentrated in the quartz core tube and propagates inside the whole volume through UV transparent metamaterial elements. When using quartz metamaterials, the decontamination volume can be increased by the evanescent zone of UV light radiation forming around each element of the metamaterial.

The microorganism decontamination is achieved in the evanescent area, which can improve the contact zone between radiation and contaminated fluids. The optical force produced by electromagnetic radiation acts as a tweezer, attracting microparticles at the EMF regions with the highest intensity. Microorganisms located in the evanescent zone of metamaterials can be efficiently annihilated. It is worthy to mention that such a UV-C decontamination equipment can be used, as for example, in water distribution system of a city or directly in water pipes of apartments, in order to prevent the biological risk. Moreover, UV-C decontamination reactors can be used for gases (air) decontamination in hazardous situations.

5. Decontamination in dynamic treatment regime

Contaminated water samples collected from metropolitan "Valea Morilor" Lake from Chisinau and sweetened beer yeast solutions were tested. Experiments confirmed that the proposed optical metamaterials effectively disperse the UV radiation inside the liquid volume, improving the contact surfaces between the radiation and liquid. The packing symmetry and optical properties of the metamaterial elements, as well as the optical properties of contaminated liquids influence the decontamination rate.

5.1. Bacteria and fungi inactivation during a dynamic treatment regime

A series of experiments for decontamination of polluted water samples were carried out. The collected lake water samples, contaminated with *Coliform* (including *Escherichia coli*) and *Enterococcus* bacteria, were treated in a dynamic regime for 5 and 10 min. The contaminated water for testing was pumped by an electrical device to continuously circulate through the core tube filled up with optical metamaterials (glass spherical bubbles). As follows from experimental results (**Table 1**), *E. coli, Enterococcus*, and *Coliform* bacteria were totally inactivated from a volume of 1 L of contaminated water after 10 min of UV-C irradiation in the presence of glass spheres. This keeps valid after 5 min of treatment, as the bacterial colonies of *Coliform* and *Enterococcus* were also annihilated. Nevertheless, an insignificant part of *Coliform* bacteria survived after 5 min irradiation in dynamic treatment (**Figure 12**) (see also **Table 1**). The individual numerical values of the control and treated water samples are collected in **Table 1**.

In **Figure 12**, images of Petri dishes with bacteria colonies after 48 h of incubation are given. Bacteria in the contaminated water that flows in-between the metamaterial elements in the core tube (glass spheres) are periodically collapsed on the evanescent zone of each element.

As can be observed from **Figure 12** and **Table 1**, the *Coliform* (including *E. coli*) and *Enterococcus* bacteria from a volume of 1 L contaminated water were totally inactivated after 10 min of treatment under UV-C irradiation in dynamic regime, in the presence of glass spheres. The contaminated water is penetrated by UV-C radiation via evanescent field around spheres inside the quartz tube cylinder. The decontamination effect is significant in all cases, leading after 10 min to the eradication of all bacterial strains (*B. coliform, E. coli*, and *Enterococcus*).

5.2. Yeast inactivation by dynamic treatment regime

Next experiments were conducted with beer yeast fermentation. The yeast species transforms by fermentation carbohydrates to carbon dioxide and alcohols [45]. The fermentation was used to estimate the decontamination rate efficiency of the UV-C equipment (**Figure 13**).

About 50 g of fresh yeast were dissolved into 1 L of warm (40°C) sweetened water (20%). After 1 h of observation, the fermentation is still active in the untreated solution (**Figure 13B)**, while

Bacterial strain	Results [CFU/100 cm^3]
Polluted lake water—control samples	
B. coliform	482
E. coli	3
Enterococcus	11
Lake water UV irradiated for 5 min in the core tube filled up with glass spheres	
B. coliform	5
E. coli	0
Enterococcus	0
Lake water UV irradiated for 10 min in the core tube filled up with glass spheres	
B. coliform	0
E. coli	0
Enterococcus	0

Table 1. Characteristic numerical values of untreated (control) and treated water samples in dynamic regime for 5 and 10 min.

in the irradiated one (1 L), during 15 min of circulation through the core tube filled up by unordered granulated quartz (transparent to 254 nm), the fermentation is completely stopped (**Figure 13A)**. These experiments demonstrated that yeast solution treated for 15 min in dynamic regime was efficiently inactivated. Only 5 min irradiation of yeast solution using unordered granulated SiO_2 induced the partial stopping of bubbling in the treated solution, relative to the control samples.

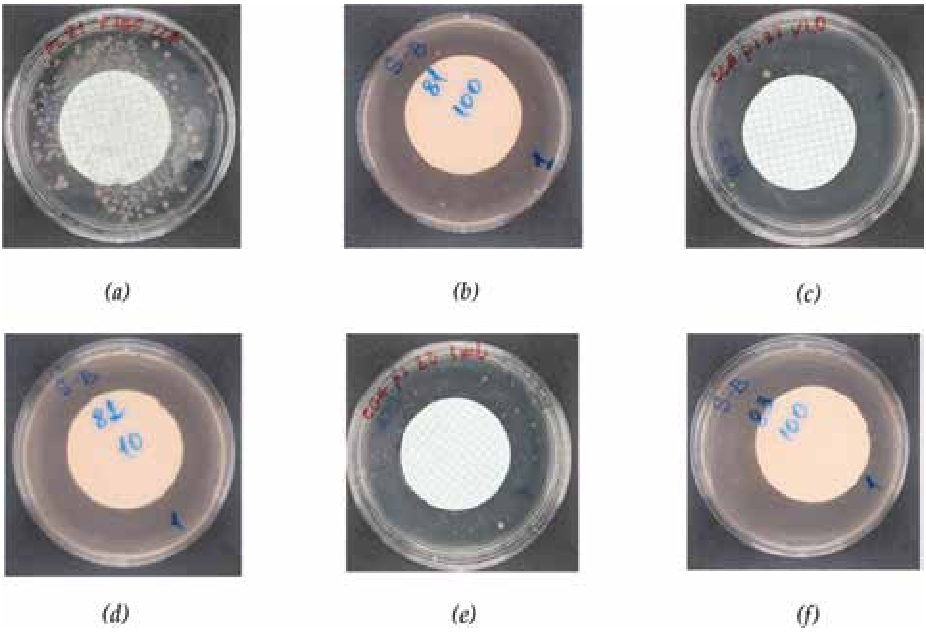

Figure 12. *Coliform bacteria* (inclusively *E. coli*) (a) and *Enterococcus* (b)—control samples, at 48 h growth without UV treatment, irradiated for 5 min (c and d) and irradiated for 10 min (e and f).

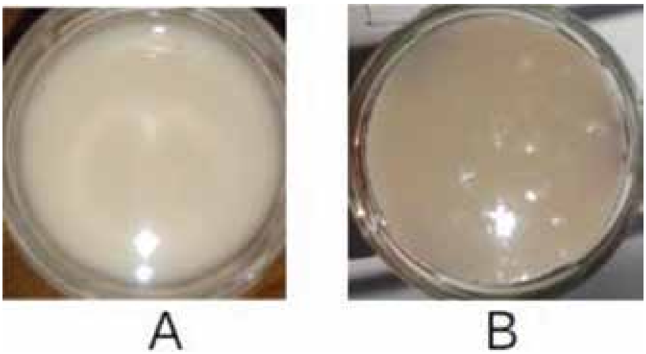

Figure 13. After 1 h, it was observed the stopping of bubbling in the yeast-treated solution (A), while in the untreated solution, the fermentation continued to be active (B).

The fermentation is, however, more active when glass bubbles (approximately 2 mm in diameter) were used in the decontamination equipment. After 5 min exposure, a substantial inhibition of the fermentation was not observed when using glass metamaterials (nontransparent to either UV or visible light).

6. Decontamination in static treatment regime

In order to distinguish between fluid dynamical effects produced as an effect of the acceleration and rotation of microorganisms in polluted fluids, some tests were conducted in static decontamination regime. For this purpose, the decontamination equipment was placed in vertical position. The liquid is motionless in the core tube. The contaminated liquid was UV-C irradiated and crossed by the evanescent field of each element of metamaterial placed in the quartz cylinder. Two dedicated series of experiments were performed in static treatment regime of decontamination: (i) one devoted to annihilation of *E. coli* bacteria in water samples prepared in the Laboratory of Sanitary Microbiology at the National Center of Public Health, Republic of Moldova, and (ii) another to the prevention of mat formation in *Kombucha* culture.

6.1. *E. coli* inactivation in static treatment regime

Water samples contaminated with *E. coli* were treated in static regime by UV-C radiation for 1, 1.5, and 2 min. In **Table 2**, the characteristic numerical values of the nonirradiated (infected with *E. coli*) and irradiated water samples in static regime are collected.

The infected water with *E. coli* was poured in the decontamination "core tube" and was UV-C irradiated for 1 min. In **Figure 14**, the experimental results for decontamination of water samples in static treatment regime using quartz granules in the core tube (**Figure 14B**) and in absence of metamaterials are presented (**Figure 14C**)—corresponding to the traditional decontamination method, see Section 3). For reference, in **Figure 14M**, the photo of Petri dish of the control (untreated) sample is shown.

Nr.	Tested samples, experimental results	Measurement units	
		CFU/ml	**CFU/100 ml**
***E. coli* ATCC 25922 with the concentration 10^2 UFC/ml (sample nr. 1)**			
1.	Control sample—untreated water contaminated with *E. coli* (reg. nr. 137)	1.9×10^2 CFU/ml	1.9×10^4 CFU/100 ml
2.	Sample nr. 1 water contaminated with *E. coli* treated without metamaterials (reg. nr. 144)	0 CFU/ml	1.6×10^1 CFU / 100 ml
3.	Sample nr. 2 water infected by *E. coli* treated with quartz unordered granules (reg. nr. 143)	0 CFU/ml	0 CFU/ml

Table 2. Characteristic numerical values of the untreated water samples (1) prepared in Laboratory of Sanitary Microbiology at the National Center of Public Health, Republic of Moldova, and the treated water samples without metamaterials (2) and with metamaterials (quartz unordered granules) (3).

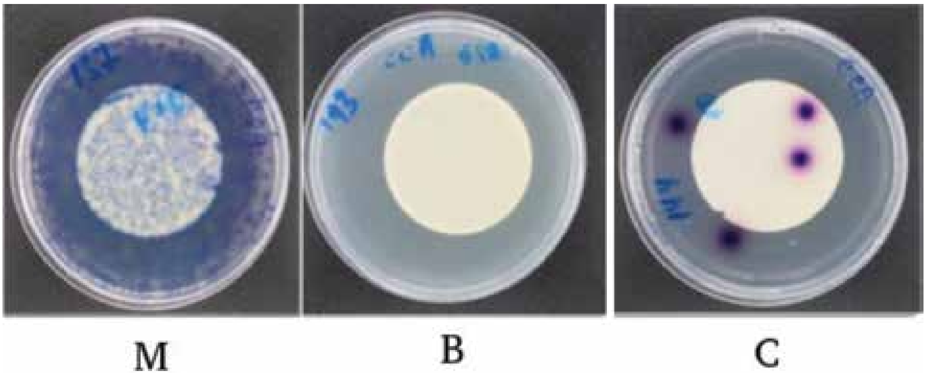

Figure 14. Specially prepared *E. coli* contaminated samples. (M) control sample; (B) sample after static treatment using quartz unordered granules in the core tube; (C) sample after static treatment without metamaterials.

It is observed that *E. coli* bacteria in the samples treated using metamaterials consisting of quartz unordered granules were completely inactivated. On the other hand, for the samples treated without metamaterials, the bacteria were not completely inhibited (**Figure 14**C). In this case, some *E. coli* colonies are still present in the decontaminated liquid. This convincingly demonstrates the key role of quartz metamaterials in liquid decontamination under UV-C irradiation.

6.2. Inactivation of Kombucha tea under static treatment regime

Static decontamination regime was applied to examine samples of *Kombucha* tea, *Medusomyces gisevii* [46]—symbiotic culture of acetic acid—producing bacteria and yeast (Symbiotic Community Of Bacteria and Yeast—SCOBY). They contain one or several species of bacteria and yeast, which form a zoogloeal mat [47], known as "mother" [46]. After a storage period at a temperature higher than 20°C for about 3 weeks, a microbial biofilm is appearing onto the surface of the fermented *Kombucha* tea. It usually has the aspect of a giant oily pellicle. This dense microbial mat is fused together by cellulose produced by bacteria primarily responsible for the glued community. Yeast living in biofilm uses tea sugars to produce alcohol, which is then consumed by neighboring bacteria to produce acetic acid. The yeasts that can form a *Kombucha* culture are *Saccharomyces cerevisiae*, *Brettanomyces bruxellensis*, *Candida stellata*, *Schizosaccharomyces pombe*, and *Zygosaccharomyces bailli* [48]. The bacterial component of *Kombucha* consists of several species but always includes *Gluconacetobacter xylinus* (*G. xylinus*, formerly *Acetobacter xylinus*). *Kombucha*-fermented tea samples were prepared as follows: sugar (10%) is added to the fresh black tea and then a 1:1 quantity to 1-month-fermented *Kombucha* tea, which presents already a dense microbial biofilm on the surface. The UV-C irradiation time was set at 5, 7, 9, or 11 min. The core tube of the decontamination equipment was filled out with (1) granular unordered quartz of 1–5 mm transparent to 254 nm or (2) glass spheres nontransmitting at 254 nm. In the third case, the core tube was kept empty, without metamaterials—the case that models the traditional decontamination method (see Section 3). In *Kombucha* black tea at room temperature, colonies of bacteria (15×10^3 CFU/mL) and yeast (7×10^3 CFU/mL) have been observed [49]. It was also

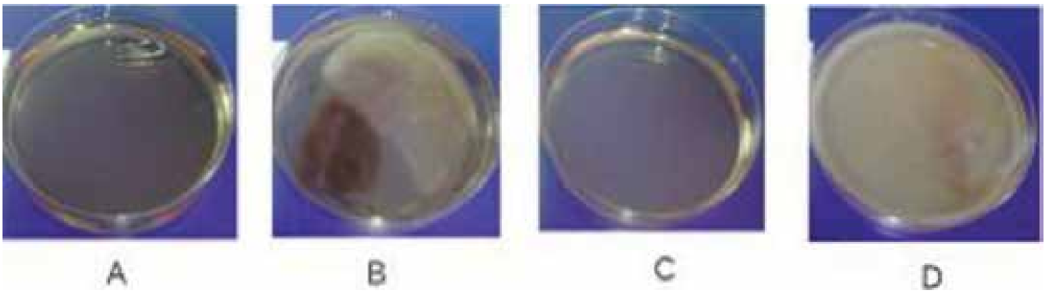

Figure 15. *Kombucha* culture after 7 min irradiation: (A) in the presence of quartz granules, a biofilm on the surface of the liquid is not observable; (B) mat becomes visible when using glass spheres; (C) without metamaterials in the core tube, the mat becomes also visible; (D) the control sample.

revealed that heat treatment is an efficient method to annihilate microorganisms from *Kombucha* tea. For this reason, during experiments, the liquid temperature was preserved below 40°C. Therefore, a thermal inactivation of *Kombucha* microorganisms was ruled out. When *Kombucha* tea is kept at temperatures higher than 20°C, the fungal microbes contribute to biofilm formation (mat). The mat can be therefore inhibited during the storage period by inactivation or removal of the microbes in *Kombucha* tea. The prevention of mat formation is an indication of microorganisms' inactivation during UV-C irradiation. Mat formation was analyzed after 4 days of storage at room temperature. The changes in the rate of microorganisms' inactivation on the metamaterial type were also studied. A more efficient microorganism inactivation was observed for shorter irradiation times when using quartz granules, than in case of irradiation without metamaterials or using glass spheres.

Kombucha culture was inactivated after 7 min irradiation using quartz metamaterials, while mat formation contracted, in direct relation with the irradiation dose. When using quartz granules, the microorganism inactivation is amplified than in the case of glass spheres. After 7 min irradiation in the presence of quartz granules (**Figure 15A**), a mat on the surface of the liquid is not observable. It becomes visible when using glass spheres (**Figure 15B**) or when no metamaterials are present in the core tube (**Figure 15C**). The control sample is presented in **Figure 15D**.

7. Conclusions

A method of annihilation of pathogens using optical metamaterials consisting of microspheres and fiber optical structures having various geometries is suggested. It is proved that using optical metamaterials, like photonic crystal, we get a substantial gain in the decontamination contact surface during the propagation of the contaminated translucent liquid (by viruses and bacteria) through the space between the microspheres (or optical fibers) of metamaterials. The increase of the surface contact of the UV radiation with contaminated liquid strongly depends on the refractive index of metamaterial, liquid volume, and optical properties of viruses and bacteria. We investigated the possibility to trap the viruses and bacteria using an efficient UV decontamination method.

The advancement of nonlinear models based on UV-C interaction with microorganisms opens novel possibilities for the decontamination and diagnosis of different collective processes, which can occur in viruses, bacteria, or other cellular structures under the action of external UV pulses. The possibility to select the UV radiation, which acts on microorganisms with minimal effects, was studied and presented herewith.

The efficient antimicrobial action of the evanescent wave acting around quartz granules in a circulating contaminated translucent liquid when submitted to UV-C irradiation was demonstrated. The treated liquids were polluted water from a natural source, yeast solution, or *Kombucha* fermented tea, while the radiation was generated by 6 UV-C 30 W lamps. Glass microspheres of 1–3 mm diameter were used in experiments, in comparison with quartz unordered granules.

1. Dynamic treatment regime: The complete annihilation of *E. coli* and *Enterococcus* bacteria was observed after 5 min of irradiation; the total elimination of *Coliform* bacteria was achieved after 10 min of irradiation.

   The fermentation of the liquid containing yeast fungi was completely stopped after 15 min UV-C irradiation in the presence of quartz granules. To the contrary, normal fermentation continues after 20 min of irradiation in the absence of optical metamaterials—the case that corresponds to the traditional decontamination method.

2. Static treatment regime: *E. coli* bacteria were completely inactivated in the presence of quartz granules after 1 min irradiation, while in the absence of the quartz metamaterials, some colonies were still present inside the analyzed liquid. This convincingly demonstrates the key role of the quartz metamaterial in fluid decontamination under UV-C irradiation.

   Kombucha-fermented tea microorganisms were completely inactivated after 7 min of treatment using quartz unordered metamaterials. After 7 min of treatment in the presence of glass metamaterials, a thin biofilm may still be observed on the sample surface. Therefore, when using quartz granules, the microorganism inactivation is considerably augmented than in the case of using glass spheres. The biofilm formation on the surface of the liquid after 7 min of treatment becomes visible when using glass spheres, or without metamaterials in the core tube. Mat formation contracted in direct relation with irradiation dose.

   One expects a large increase of the observed effects when passing from simple lamps to laser irradiation, that is, from incoherent to coherent light sources. Also, a significant improvement is expected when using optical fibers for evanescent wave generation instead, or in tandem with, quartz granules.

   Our results prove that the energy emerging via evanescent waves from multistructures submitted to dynamic irradiation is not in any case lost but efficiently used for antimicrobial action. This can contribute to a positive balance of light propagation through PC and PCF metamaterials in view of using light sources with maximum efficiency.

Acknowledgements

This paper was supported by the NATO EAP SFPP 984890, STCU 6140, and 43 NATO/2017 projects.

Author details

Nicolae Enaki[1], Sergiu Bizgan[1], Andrei Nistreanu[1], Viorica Tonu[1,2], Marina Turcan[1], Tatiana Pislari[1], Elena Starodub[1], Aurelia Profir[1], Gianina-Florentina Popescu-Pelin[3], Maria Badiceanu[3,4], Carmen-Georgeta Ristoscu[3] and Ion N. Mihailescu[3]*

*Address all correspondence to: ion.mihailescu@inflpr.ro

1 Quantum Optics and Kinetic Processes Lab, Institute of Applied Physics, Academy of Sciences of Moldova, Chisinau, Republic of Moldova

2 Department of Human Physiology and Biophysics, State University of Medicine and Pharmacy "Nicolae Testemitanu", Chisinau, Moldova

3 "Laser-Surface-Plasma Interactions" Laboratory, National Institute for Lasers, Plasma and Radiation Physics (INFLPR), Magurele, Ilfov, Romania

4 Physics Department, University of Bucharest, Magurele, Ilfov, Romania

References

[1] Zheludev NI, Kivshar YS. From metamaterials to metadevices. Nature Materials. 2012;**11**: 917-924

[2] Iovine R, La Spada L, Vegni L. Nanoparticle device for biomedical and optoelectronics applications. COMPEL. 2013;**32**(5):1596-1608

[3] Liberal I, Engheta N. Near-zero refractive index photonics. Nature Photonics. 2017;**11**:149-158

[4] Bazgan S, Ristoscu C, Negut I, Hapenciuc C, Turcan M, Ciobanu N, et al. Propagation of UV radiation through meta-materials and its application in bio decontamination. Romanian Reports in Physics. 2015;**67**(4):1602-1607

[5] Enaki N, Profir A, Bazgan S, Paslari T, Ristoscu C, Mihailescu CN, et al. Metamaterials for antimicrobial biofilm applications: Photon-crystals of microspheres and fiber optics for decontamination of liquids and gases. In: Tiwari A, editor. Handbook of Anti-Microbial Coatings. Amsterdam NL, Oxford UK, Cambridge MA USA: Elsevier Inc; 2018. pp. 257-282

[6] Enaki NA, Bazgan S, Ciobanu N, Turcan M, Paslari T, Ristoscu C, et al. Improvement in ultraviolet based decontamination rate using meta-materials. Applied Surface Science. 2017;**417**:40-47

[7] Ashkin A, Dziedzic JM. Optical trapping and manipulation of viruses and bacteria. Science. 1987;**235**(4795):1517-1520

[8] Morrissey MJ, Deasy K, Wu Y, Chakrabarti S, Nic Chormaic S. Tapered optical fibres as tools for probing magneto-optical trap characteristics. Review of Scientific Instruments. 2009;**80**(5):053102

[9] Rowan NJ, MacGregor SJ, Anderson JG, Fouracre RA, McIlvaney L, Farish O. Pulsed-light inactivation of food-related microorganisms. Applied and Environmental Microbiology. 1999;**65**(3):1312-1315

[10] Rosenheck K, Doty P. The far ultraviolet absorption spectra of polypeptide and protein solutions and their dependence on conformation. Proceedings of the National Academy of Sciences. 1961;**47**(11):1775-1785

[11] Sutherland JC, Griffin KP. Absorption spectrum of DNA for wavelengths greater than 300 nm. Radiation Research. 1981;**86**(3):399-410

[12] Tsen KT, Tsen SW, Wu TC, Kibler K, Jacobs B. Selective destruction of viruses with ultrashort pulsed lasers. SPIE Newsroom. 2009:3. DOI: 10.1117/2.1200911.1845

[13] Tsen SW, Wu TC, Kiang JG, Tsen KT. Prospects for a novel ultrashort pulsed laser technology for pathogen inactivation. Journal of Biomedical Science. 2012;**19**(1):62

[14] Zhang C, Li J, Lan L, Cheng JX. Quantification of lipid metabolism in living cells through the dynamics of lipid droplets measured by stimulated Raman scattering imaging. Analytical Chemistry. 2017;**89**(8):4502-4507

[15] Palonpon AF, Ando J, Yamakoshi H, Dodo K, Sodeoka M, Kawata S, et al. Raman and SERS microscopy for molecular imaging of live cells. Nature Protocols. 2013;**8**(4):677

[16] Yamakoshi H, Dodo K, Okada M, Ando J, Palonpon A, Fujita K, et al. Imaging of EdU, an alkyne-tagged cell proliferation probe, by Raman microscopy. Journal of the American Chemical Society. 2011;**133**(16):6102-6105

[17] Kowalski W. UVGI disinfection theory. In: Kowalski W, editor. Ultraviolet Germicidal Irradiation Handbook. Berlin, Heidelberg: Springer; 2009. pp. 17-50. DOI: 10.1007/978-3-642-01999-9_2

[18] Rastogi RP, Kumar A, Tyagi MB, Sinha RP. Molecular mechanisms of ultraviolet radiation-induced DNA damage and repair. Journal of Nucleic Acids. 2010;**2010**:592980. DOI: 10.4061/2010/592980

[19] Schreier WJ, Schrader TE, Koller FO, Gilch P, Crespo-Hernández CE, Swaminathan VN, et al. Thymine dimerization in DNA is an ultrafast photoreaction. Science. 2007;**315**(5812):625-629

[20] Buonanno M, Ponnaiya B, Welch D, Stanislauskas M, Randers-Pehrson G, Smilenov L, et al. Germicidal efficacy and mammalian skin safety of 222-nm UV light. Radiation Research. 2017;**187**(4):493-501

[21] Stein BE, Rahmsdorf HJ, Steffen AN, Litfin MA, Herrlich PE. UV-induced DNA damage is an intermediate step in UV-induced expression of human immunodeficiency virus type 1, collagenase, c-fos, and metallothionein. Molecular and Cellular Biology. 1989;**9**(11):5169-5181

[22] Bhattacharjee C, Sharan RN. UV-C radiation induced conformational relaxation of pMTa4 DNA in *Escherichia coli* may be the cause of single strand breaks. International Journal of Radiation Biology. 2005;**81**(12):919-927

[23] Rothman RH, Setlow RB. An action spectrum for cell killing and pyrimidine dimer formation in Chinese hamster v-79 cells. Photochemistry and Photobiology. 1979;**29**(1):57-61

[24] Sarasin AR, Hanawalt PC. Replication of ultraviolet-irradiated simian virus 40 in monkey kidney cells. Journal of Molecular Biology. 1980;**138**(2):299-319

[25] Miller RL, Plagemann PG. Effect of ultraviolet light on mengovirus: Formation of uracil dimers, instability and degradation of capsid, and covalent linkage of protein to viral RNA. Journal of Virology. 1974;**13**(3):729-739

[26] Smirnov YA, Kapitulez SP, Kaverin NV. Effects of UV-irradiation upon Venezuelan equine encephalomyelitis virus. Virus Research. 1992;**22**(2):151-158

[27] Begley RF, Harvey AB, Byer RL. Coherent anti-Stokes Raman spectroscopy. Applied Physics Letters. 1974;**25**(7):387-390

[28] Bloembergen N. Nonlinear optics. Singapore, New Jersey, London, Hong Kong: World Scientific; 1996. 188 p. DOI: 10.1142/3046

[29] Yan YX, Gamble EB Jr, Nelson KA. Impulsive stimulated scattering: General importance in femtosecond laser pulse interactions with matter, and spectroscopic applications. The Journal of Chemical Physics. 1985;**83**(11):5391-5399

[30] Mannige RV, Brooks CL III. Periodic table of virus capsids: Implications for natural selection and design. PLoS One. 2010;**5**(3):e9423

[31] Zhu T, Ertekin E. Phonon transport on two-dimensional graphene/boron nitride superlattices. Physical Review B. 2014;**90**(19):195209

[32] Zhu T, Ertekin E. Resolving anomalous strain effects on two-dimensional phonon flows: The cases of graphene, boron nitride, and planar superlattices. Physical Review B. 2015; **91**(20):205429

[33] Gilmore R. Catastrophe Theory for Scientists and Engineers. New York: Courier Corporation, Dover Publications Inc; 1993. 666 p

[34] Loudon R. The Quantum Theory of Light. Oxford UK: Oxford University Press; 2000. 448 p

[35] Enaki NA. Non-linear Cooperative Effects in Open Quantum Systems. NY: Nova Science Publishers; 2015. 355 p

[36] Schubert M, Wilhelmi B. Nonlinear Optics and Quantum Electronics. New York: Wiley-Interscience; 1986. 744 p

[37] Enaki N, Colun S. Nonlinear effects in the theory of superconductivity. Journal of Physics: Conference Series. 2012;**338**:012006

[38] La Spada L, Iovine R, Tarparelli R, Vegni L. Conical nanoparticles for blood disease detection. Advances in Nanoparticles. 2013;**2**(3):259-265

[39] Liu Y, Hao Y, Li K, Gong S. Radar cross section reduction of a microstrip antenna based on polarization conversion metamaterial. IEEE Antennas and Wireless Propagation Letters. 2016;**15**:80-83

[40] Iovine R, La Spada L, Vegni L. Nanoplasmonic sensor for chemical measurements. Proceedings of SPIE (Optical Sensors 2013). 2013;**8774**:877411

[41] Cai W, Chettiar UK, Kildishev AV, Shalaev VM. Optical cloaking with metamaterials. Nature Photonics. 2007;**1**:224-227

[42] La Spada L, Bilotti F, Vegni L. Metamaterial resonator arrays for organic and inorganic compound sensing. Proceedings of SPIE (Photonics, Devices, and Systems V). 2011;**8306**: 83060I

[43] Lee Y, Kim S-J, Park H, Lee B. Metamaterials and metasurfaces for sensor applications. Sensors. 2017;**17**:1726

[44] Gusachenko I, Truong VG, Frawley MC, Nic Chormaic S. Optical nano-fibre integrated into optical tweezers for in situ fibre probing and optical binding studies. Photonics. 2015; **2**(3):795-807

[45] Legras JL, Merdinoglu D, Cornuet JM, Karst F. Bread, beer and wine: *Saccharomyces cerevisiae* diversity reflects human history. Molecular Ecology. 2007;**16**(10):2091-2102

[46] Jayabalan R, Malbaša RV, Lončar ES, Vitas JS, Sathishkumar M. A review on kombucha tea—Microbiology, composition, fermentation, beneficial effects, toxicity, and tea fungus. Comprehensive Reviews in Food Science and Food Safety. 2014;**13**(4):538-550

[47] Jonas R, Farah LF. Production and application of microbial cellulose. Polymer Degradation and Stability. 1998;**59**(1–3):101-106

[48] Blanc PJ. Characterization of the tea fungus metabolites. Biotechnology Letters. 1996;**18**(2): 139-142

[49] Jayabalan R, Marimuthu S, Thangaraj P, Sathishkumar M, Binupriya AR, Swaminathan K, et al. Preservation of Kombucha tea effect of temperature on tea components and free radical scavenging properties. Journal of Agricultural and Food Chemistry. 2008;**56**(19): 9064-9071

Chapter 10

Advanced Surface Treatments for Improving the Biocompatibility of Prosthesis and Medical Implants

José A. García, Pedro J. Rivero, Rocío Ortiz,
Iban Quintana and Rafael J. Rodríguez

Additional information is available at the end of the chapter

http://dx.doi.org/10.5772/intechopen.79532

Abstract

During the last two decades, numerous surface treatments have been developed to improve the biocompatibility of different types of prosthesis and other medical implants. Some of these devices are subject to demanding loading and friction conditions (e.g., hip, knee, and spine prosthesis). However, for other implants, there are more specific requirements as it happens for coronary stents or pacemaker electrodes. The materials used for the manufacture of the aforementioned devices are subjected to very high restrictions in terms of biocompatibility, in particular on chemical composition, corrosion resistance, or ion release. As a consequence, most of prosthesis and other implants are made of a limited number of materials such as titanium alloys, stainless steels, cobalt-chromium alloys, UHMWPE, or PEEK. Unfortunately, from a strict point of view, none of these materials meet all the requirements that would be desirable in terms of durability and prevention of infections and inflammatory processes. Coatings and other surface treatments have been developed to solve these problems and to improve biocompatibility. In this chapter, we present an updated review of the most used surface engineering technologies for biomaterials, like novel PVD coatings, ion implantation, and other plasma spray treatments, as well as a critical review of the characterization techniques. This study is completed with an insight into the future of the field.

Keywords: surface engineering, biomaterials, biocompatibility, plasma spraying, PVD coatings, ion implantation

1. Introduction

Since the first prosthetics were placed in patients in 1890, the evolution of materials and superficial treatments has been in continuous evolution [1]. Currently, prostheses are used in different areas of the body ranging from scaffolds, coronary stents, and heart valves to hip and knee prostheses [2–5]. Although there are characteristics common to all the different prostheses such as resistance to corrosion and biocompatibility (they should not "harm" the patient), the requirements of each of them are in many cases very different [6]. A replacement plate of a cranial bone or a hip prosthesis inserted into the femur should have a good capacity for osseointegration. However, a coronary stent should prevent cell growth in its internal part [7]. This differentiation occurs not only between different prostheses but also between different zones in the same prosthesis. This determines that different materials are used not only for different prostheses but also in different areas of the same prosthesis; for instance, hip prostheses have a basal titanium alloy, with a femoral head of CoCr or ceramic that rotates on a high-density polyethylene cup.

Although the development of materials and treatments has allowed the durability and performance of these devices to be very high, there are still several problems associated with the prosthesis [8]. The most known are premature wear and dislocation in hip and knee prostheses, infection and rejection in dental prostheses, restenosis and heavy metal release in coronary stents, among others. In this way, infections are frequent complications in hospitals with dramatic consequences. It has been estimated that 80% of the infections in hospitals involve bacterial biofilms that have up to 1000 times higher resistance to antimicrobials than bacteria in the planktonic form [9, 10].

In this context, advanced surface treatments are playing an essential role in improving performance and increasing the life of prostheses. The treatments of thermal projection of hydroxyapatite (HA) are an extended solution to increase the capacity of growth of the cells of the bone on alloys of titanium and stainless steels. Physical vapor deposition (PVD) treatments, both ceramic and diamond like carbon (DLC), are an effective tool for increasing wear resistance. Ionic implantation is a method used to decrease the migration of heavy ions to the body, and laser texturing is being effectively used to obtain antimicrobial surfaces in an effective strategy to interrupt infections. This work includes a review of the state of the art and industrial implementation of some of the most used surface treatment techniques for the improvement of the different types of prostheses, paying special attention to the most used solutions and the future possibilities of advanced surface treatment techniques.

2. Plasma-sprayed hydroxyapatite coating

One of the ongoing research fields in the scientific community is the design of novel materials which can stimulate the bone regenerative process because the bone regeneration is a constant and continuous process in our lives, although the resultant regeneration speed shows a decreased tendency as a function of the age [11]. In addition, several studies indicate that every year over 2 million people worldwide require bone grafting surgery in order to repair large bone defects which are a very common problem in orthopedic surgery, being the main alternatives to repair these defects the use of autologous bone grafts, allografts, or biocompatible synthetic materials [12, 13].

Bones as well as other calcified tissues are considered as natural anisotropic composites consisting of biominerals embedded in a protein matrix, other organic materials, and water [14]. More specifically, the biomineral phase can be one or more types of calcium phosphates (CP) salts which vary in the resultant chemical formula and solubility value, respectively. Among all the known CP salts, hydroxyapatite (HA) stands out because it is the main calcium phosphate phase constituent of bones, comprising around 70% in comparison with water (10%) and organic phase (collagen) which constitutes the remaining part (around 20%), providing elastic resistance [15]. Due to this, multiple works can be found in the bibliography related to a wide variety of chemical methods (dry, wet, or high-temperature processes) for the fabrication of synthetic HA for biomedical applications (bone scaffold, bone filler, implant coating, or drug delivery systems) [14, 16, 17]. It has been demonstrated that synthetic HA shows a wide number of advantages such as an excellent biocompatibility, bioactivity, noninflammatory, affinity to biopolymers, and high-osteoconductive as well as osteointegrative properties without causing any systemic toxicity, rejection, or foreign body response [18–20]. A representative example can be observed in **Figure 1** where the in vivo bone repair experiments demonstrate that a new type of porous scaffold such as poly (γ-benzyl-L-glutamate)-modified hydroxyapatite/(poly (L-lactic acid) (PBLG-g-HA/PLLA) induced higher levels of new bone formation (rat femur defect) in comparison with blank (control), poly (L-lactic acid) (PLLA), and hydroxyapatite/poly (L-lactic acid) (HA/PLLA), respectively. These results indicate the potential applications for bone tissue engineering by demonstrating favorable osteogenic properties [21].

Other aspect of great relevance is that the presence of hydroxyapatite particles can be also employed for the inhibition growth of different types of cancer cells [22–24]. In this sense, it is well documented that the use of nanosized hydroxyapatite particles can significantly increase the biocompatibility and bioactivity of man-made materials [25, 26]. A clear example can be found in [26] where a highly biocompatible hydroxyapatite nanopowder (known as GoHAP) has been successfully synthesized in a very short of period of time (range of 90 s). These GoHAP nanoparticles showed excellent biocompatibility properties (confirmed by in vitro tests) because no vacuolization or cell membrane lysis was found on the surface and the resultant cells presented a correctly flattened phenotype, maintaining morphology typical for bone cells. The experimental results clearly indicate that GoHAP could be a promising material for resorbable bone implant fabrication.

One of the most important applications is that as coatings deposited onto bioinert metallic implants can promote early bonding of bones with an increase of biological fixation. In this sense, it has to be mentioned that as coatings, they are not intended to substitute existing materials, although these HA coatings are used for an enhancement of a fully functional implant. Due to this, different deposition techniques such as sol-gel process [27–29], pulsed laser deposition [30–32], electrospinning [33, 34], sputtering [35–37], or plasma spray [38] can be found in the bibliography related to design of optimal HA coatings onto the surface of metallic implants. Among all these fabrication methodologies, it has to be mentioned that plasma spray technique is the only process which has been approved by US Food and Drug Administration (FDA) for coating implants with biocompatible materials [39]. The plasma

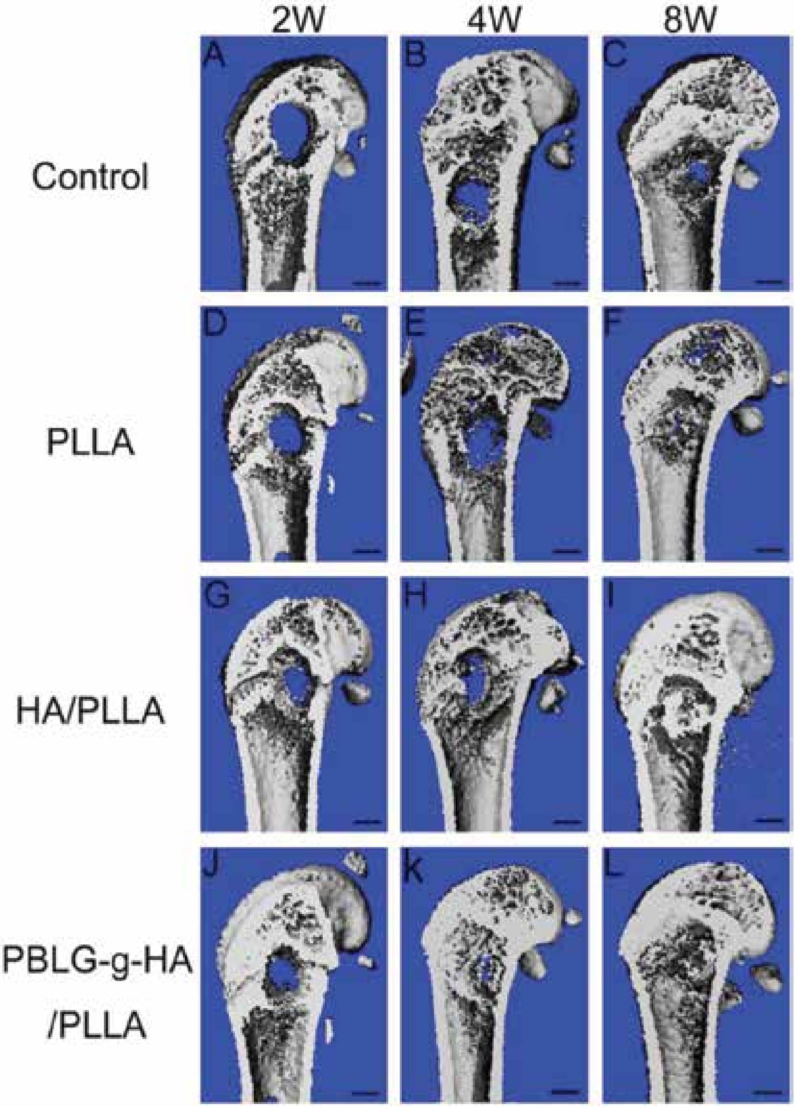

Figure 1. In vivo bone formation assessed by microcomputerized tomography (μ- CT) of control (A–C), poly (L-lactic acid) (PLLA) (D–F), HA/PLLA (G–I), and poly (γ-benzyl-L-glutamate)-modified hydroxyapatite/(poly (L-lactic acid) (PBLG-g-HA/PLLA) (J–L) scaffolds at 2, 4, and 8 weeks postimplantation. Reprinted with permission of [21].

spray process demands a control of several parameters for the design of optimal coatings (particle size range, distance between gun and substrate, arc current, power setting, particle morphology, plasma gas mixture, postspray treatment, etc.) [40]. A schematic representation of plasma spray torch is shown in **Figure 2**.

A novel study about the physical and chemical characterization of bioactive ceramic-coated plateau root form implant surface by using plasma-sprayed hydroxyapatite (PSHA) is presented in [41]. The surface characterization of the PSHA coatings has been performed by

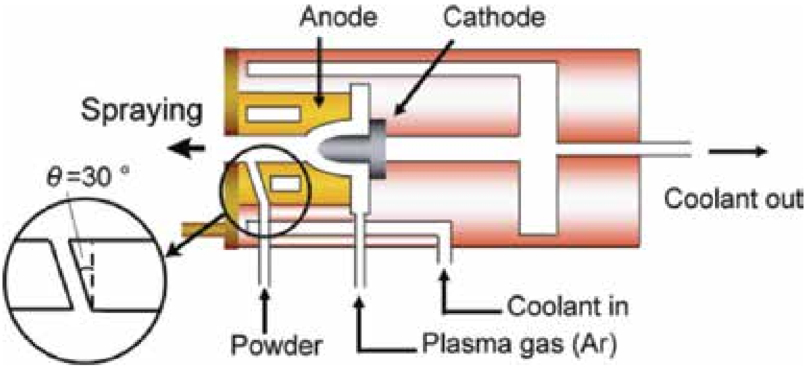

Figure 2. Schematic diagram (cross section) of plasma spray torch. Reprinted with permission of [40].

scanning electron microscopy (SEM), whereas the determination of the roughness has been performed by optical interferometry (IFM), as it can be observed in **Figure 3**. The experimental results indicate that lamellar bone formation in close contact with implant surfaces has been observed.

A consideration related to the material concerned (HA) is that it reacts strongly to rapid solidification following the plasma spray, yielding the formation of amorphous or metastable phases. According to this, the presence of an amorphous phase is undesirable because the natural bone is crystalline, being the integrity of the bone-implant compromised [42]. In this sense, an ideal HA coating for biomedical implants should have low porosity, high cohesive strength, a good adhesion to the substrate, high degree of crystallinity, high chemical purity, and phase stability [43]. According to this, the optimization of the coating properties by just varying the plasma spray parameters is a concern for obtaining a coating with the desired characteristics. An interesting work can be found in [44] where several steps are recommended in order to produce stable and adherent HA coatings.

However, mechanical tests indicate that the resultant HA coatings suffer poor mechanical properties (tensile strength, wear resistance, hardness, toughness, or fatigue), limiting its long-term application due to the relative movement between the implant and human bone, respectively. In order to overcome these mechanical limitations of HA coatings, the addition of different bioinert ceramic materials into HA matrix for reinforcement such as aluminum oxide [45, 46], zirconia [45], mixture of titania and zirconia [47], yttria-stabilized zirconium [48], or nanodiamond particles [49] have been evaluated. A representative example can be found in [45] where two reinforced HA coatings with alumina (Al_2O_3) and zirconia (ZrO_2), respectively, have been analyzed in order to investigate the microstructure, phase formation, and mechanical properties (hardness and tensile bond strength) as a function of as-sprayed coating and after postthermal treatment at 700°C for 1 h. The results indicate that after postcoating heat treatment, a dual effect has been observed such as an increase in the crystallinity and a decrease in the resultant porosity. This heat treatment enables an enhancement in cross-sectional hardness, although a decrease in bond strength has been also observed.

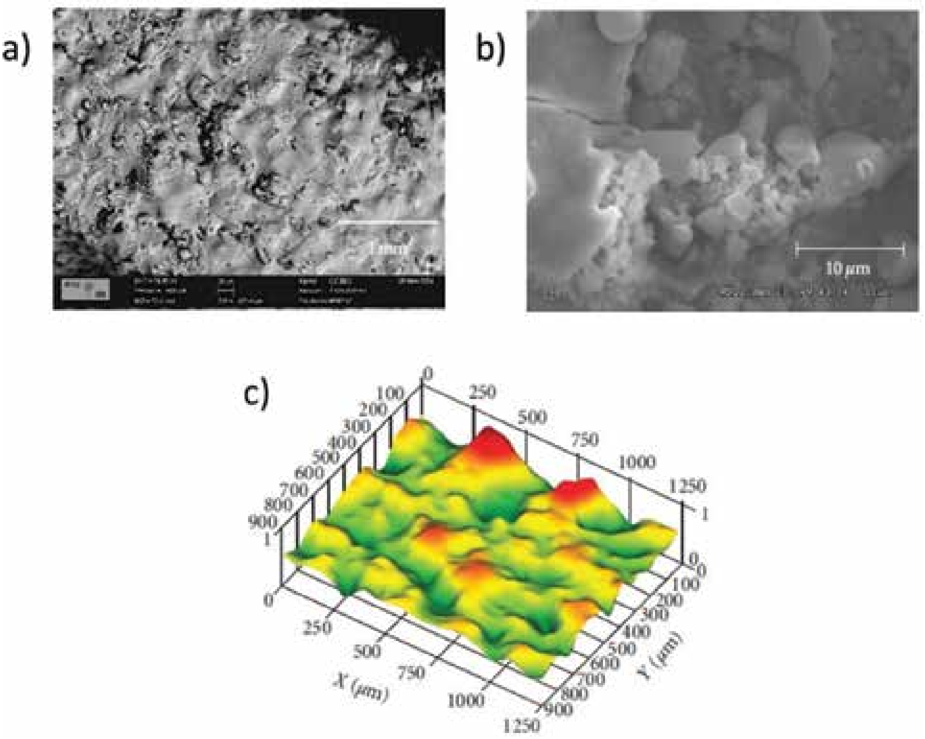

Figure 3. SEM intermediate micrograph (a) high magnification micrograph (b) and IFM three-dimensional reconstruction for PSHA coatings (c). Reprinted with permission of [41].

3. Physical vapor deposition coatings

The acronym PVD comes from the English expression Physical Vapor Deposition, knowing by this name a wide range of coating techniques that have in common the use of physical methods to obtain some of the components of the deposited layer. PVD coatings are made in high-vacuum chambers (10–50 mbar), working with average process temperatures in the range of 450°C to room temperature. By using this deposition technique, films from very thin thickness (10 nm) up to several microns with controllable composition can be perfectly obtained. In **Figure 4**, a schematic representation of PVD chamber is presented.

Basically, the PVD coatings are formed as follows. Firstly, a material is evaporated starting from a solid source (Ti, TiAl, Cr) by means of different physical methods as a function of the deposition technique employed which are electron beam evaporation or arc electric, pulverization (sputtering) by ionic bombardment, etc. The atmosphere of the treatment chamber consists of high vacuum in which there are partial pressures of controlled gases (mostly nitrogen and argon). The evaporated metal and the reactive gas of the chamber react condensing on the surface of the components to be coated. According to this process, the most known PVD coatings of typical industrial use are TiN, TiAlN, TiCN, or CrN, among others [50–55].

Concerning to the PVD processes, there are three main methods that are more widespread such as the electron beam (EB), the cathodic arc (CA), and the magnetron sputtering (MS), respectively. On the other hand, new concept in magnetron sputtering systems has been developed using high-power pulses (HIPIMS), making possible a significant increase in plasma ionization, and as a result, a considerable enhancement in the resultant adhesion of the coatings has been obtained [56, 57]. In **Figure 5**, a comparison between high-power impulse magnetron sputtering (HIPIMS), direct current magnetron sputtering (DCMS), and modulated pulsed power magnetron sputtering (MPPMS) is presented as function of power and time, respectively.

One of the research lines where PVD coatings have shown a high degree of novelty is in the protection against joint wear. The first experiences date back to the decade of the 1980s of the last century where TiN in total join arthroplasty was used as well as clinical trials were started in the 1990s in knee and hip arthroplasty [58, 59].

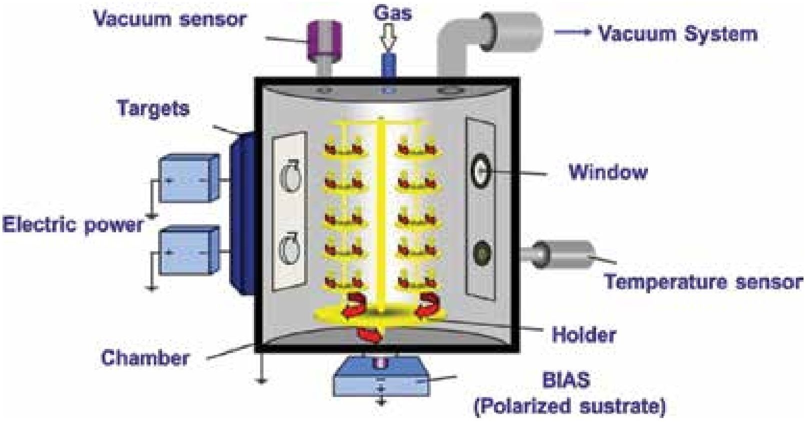

Figure 4. Scheme of the Metaplas Ionon MZR 323 arc evaporation PVD system. Courtesy of AIN.

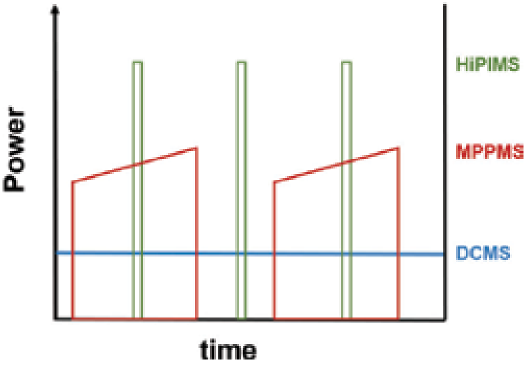

Figure 5. Power versus time in direct current magnetron sputtering (DCMS), high-power impulse magnetron sputtering (HIPIMS), and modulated pulsed power magnetron sputtering (MPPMS), respectively.

Subsequently, diamond-like carbon (DLC) coatings were introduced, following the strategy of favoring sliding with very low coefficients of friction (0.1), maintaining relatively high hardness (H > 15 GPa). Although these specific coatings showed high efficacy in laboratory tests, the clinical tests performed to date for hip and knee prostheses showed undesirable results, being the decohesion of the layers and the subsequent localized corrosion the main cause of the failure.

On the other hand, TiN and DLC coatings showed very good biocompatibility so they are being marketed in other types of prostheses such as dental implants and heart valves. For these specific purposes, the absence of high loads which can delaminate the coating as it happened in the case of hip and knee prosthesis enables its introduction into the market. In **Figure 6**, two representative examples of Ti dental implants obtained which are coated by TiN (left) or DLC (right) magnetron sputtering can be clearly appreciated.

However, one of the main problems concerned to this type of coatings is the adhesion and corrosion behavior, being one of the hot topics in the community scientific their implementation and introduction of them in a massive way in the market of hip and knee prostheses. One of the most promising approaches is the use of the aforementioned HIPIMS. This PVD technology allows obtaining layers of much greater adhesion and density, giving excellent results in terms of corrosion and wear resistance. A representative example is shown in **Figures 7** and **8**, respectively. In **Figure 7** is shown a cross section of a sample coated with TaN DC magnetron sputtering (left), where a columnar growth with micron-sized grains can be appreciated. On the other hand, the photograph on the right shows a layer of TaN coating by HIPIMS where a greater density and compactness can be observed. The corrosion resistance in terms of polarization resistance as a function of time (4, 24, and 168 h, respectively) is shown in **Figure 8**.

Another research line which is showing promoting results is ceramic coatings doped with bactericidal elements (mostly Ag or Cu) in the form of nanoparticles embedded in the TiN or CrN. The controlled release of Cu or Ag ions provides a bactericidal effect which makes possible the prevention of infections due to bacterial proliferation on the surfaces of the prostheses. Doped metal nitrides and carbonitrides deposited by pulsed magnetron sputtering are widely tested [60, 61]. In addition, Cu and Ag concentrations between 5 and 25% have been shown to be highly efficient, avoiding the proliferation of different contagious types of bacteria such as *S. aureus*, *P. aeruginosa*, and *S. epidermis*, increasing bactericidal efficacy with increased concentration of Ag and Cu, respectively. Finally, another extended solution is the coatings of diamond-like carbon(DLC) doped with Ag because the experimental results of depositing these layers by means of magnetron sputtering point to the fact that silver segregates in the form of nanoparticles (order of 3 nm), and in high concentrations appear nanofibers of Ag on the surface, showing very good antibacterial behavior [62].

Figure 6. TiN magnetron sputtering coating (left) and diamond-like carbon (DLC) magnetron sputtering coating (right) on Ti dental implant. Courtesy of the commercial company Flubetech.

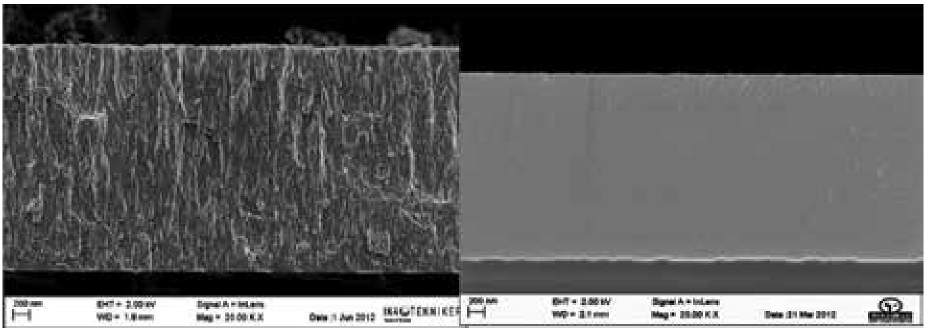

Figure 7. Cross-sectional SEM images of TaN DC magnetron sputtering (left) and TaN HIPIMS coating (right), respectively. Courtesy of IK4-TEKNIKER.

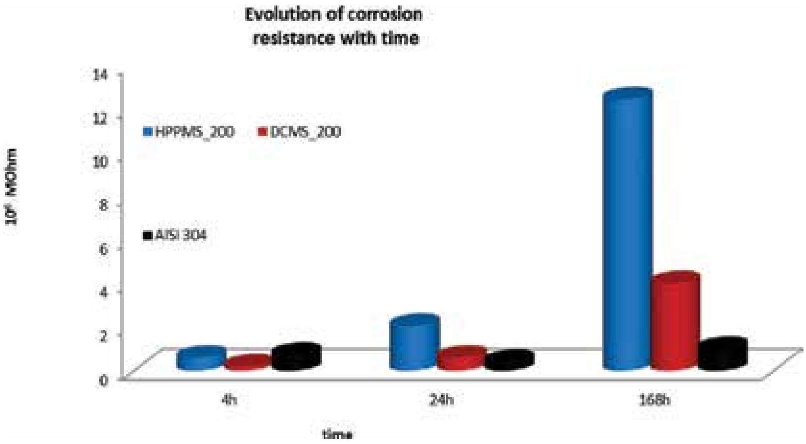

Figure 8. Evolution of corrosion resistance for TaN HIPIMS sample (blue color), TaN DCMS (red color), and pristine sample (AISI 304, black color), respectively. Courtesy of IK4-TEKNIKER.

4. Ion implantation techniques

Ion implantation techniques consist in the superficial modification of materials by ion bombardment. By means of these techniques is possible to improve surface properties of different materials [63, 64]. Although these techniques have their origin in the nuclear industry [65, 66], the first works on semiconductor applications appeared in Bell Laboratories in 1948 when Kingsbury and Ohl carried out studies of implantation of light ions on wafers of Si [67, 68]. Metallurgical application of ion implantation was firstly reported simultaneity in the 1970s by Harwell laboratory (UK), and Naval Research Laboratory (USA). These early works were mainly focused on nitrogen implantation of steels. From these first results up to today ion implantation techniques have been introduced in many different industrial applications (mostly in aeronautical or biomedical sector).

Ion implanters equipment consists of a series of characteristic elements (see **Figure 9**) such as a source of ions (capable of producing sufficient quantities of certain types of ions), one or two acceleration stages (potential differences of the order of 100,000 V), a mass separator magnet, and a thermal chamber (high-vacuum chamber where the samples whose surface is to be treated) are placed. The whole process of generation, acceleration, and implantation is carried out in high vacuum, of the order of 10^{-5}–10^{-6} mbar to ensure that the average travels of the ions far surpass the distance that separates the source of the whites to implant. In addition, ion implantation process is performed in an approximate range of energies of 25–300 KeV, although most of the studies are carried out to energies between 50 and 200 keV. The relevant parameters of these treatments are the type of ion, the implanted dose, the implantation energy, and the temperature of the process, which in the most cases is kept deliberately below a certain level (being able to talk about temperature environment), as it can be observed in **Figure 9**. By a properly selection of all these parameters, physical-chemical properties of the surface of the implanted samples can be perfectly controlled [69].

In **Figure 10**, a schematic diagram of the used plasma immersion ion implantation-enhanced deposition (PIIIeD) processing system is shown. For this figure, the process chamber is similar to a conventional plasma immersion ion implantation (PIII) combined with an RF magnetron sputtering and a glow discharge (GD) plasma source. In this system, thin films are deposited simultaneously with 3-D implantation of argon ions, improving film adhesion and relaxing film stress. As metal ions are rare in a magnetron discharge, the auxiliary electrode for glow discharge plasma helps to ionize some metal neutrals which are also implanted into the substrate during the high-voltage pulses.

The basic difference between ion beam implantation (II) and plasma immersion ion implantation (PIII) consist in PIII the target is an active part of the system, and it is biased at pulsed high voltage. On the other hand, in II, the target is isolated from the ion beam generation (it is not active part of electric circuit), and both treatments have relevant differences as it can be shown in **Table 1** [71].

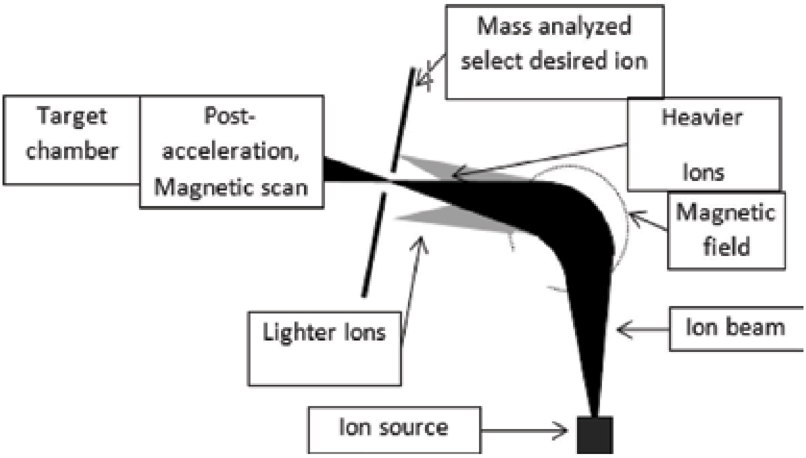

Figure 9. Scheme of a mass separation ion implanter. Ion implantation, the invisible shield. Courtesy of R. Rodríguez, T. Tate & N. Mikkelsen, SPRINT RA372 project.

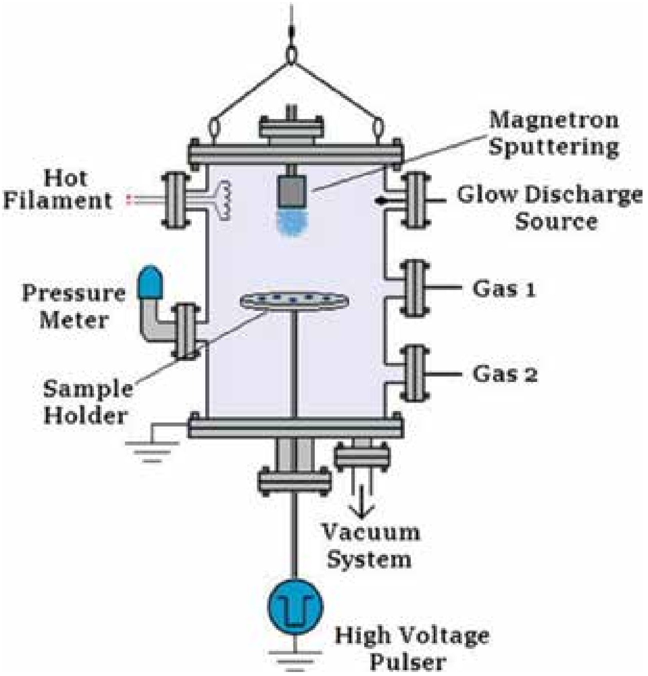

Figure 10. Schematic diagram of the used plasma immersion ion implantation-enhanced deposition (PIIIeD) processing system. The process chamber is similar to a conventional PIII combined with an RF magnetron sputtering and a glow discharge (GD) plasma source. Reprinted with permission of [70].

Conventional ion implantation is a ballistic process where kinetic energy from ions promotes ion implantation in the target. Plasma immersion ion implantation (PIII) is a combined process where temperature and voltage were defined to obtain an implantation profile. According to this, the temperature is an important parameter in PIII, dominating in many cases the final implantation characteristics. In addition, ion energy is the other key parameter in ion implantation, much more important in II where is the most relevant parameter affecting implantation profile. However, the temperature is not considered a key factor in plasma immersion ion implantation, being the typical implantation energies from a few KV up to no more of 30 kV.

The most extended applications of ion implantation technologies have been in biomedical devices. There are different functionalities that ion implantation can achieve in hip, knee, and other prosthesis. One of the first applications was the implantation of Ca and P to obtain a surface with characteristics similar to hydroxyapatite [72]. As in the case of PVD, this solution has not been incorporated into the market due to the good performance of the hydroxyapatite grown by plasma spraying. In this way, ion implantation has been more relevant in the strategies aimed at increasing the hardness and wear resistance of the prostheses. Conventional ion implantation was the first attempt to apply on different alloys of titanium and CoCr in order to reduce the wear of the prosthesis. The results obtained were not satisfactory due mainly to the low thickness of the modified layer (typically around 0.1 microns) [71]. In order to overcome the problem of the low thickness of the conventional ionic implantation, low energy-high temperature implantation techniques [73], and plasma immersion ion implantation techniques have been performed [74]. By using these techniques, the resultant implantation profiles of more than 1 micron have been achieved (see figure GDOS profile of **Figure 11**), increasing the hardness and wear resistance.

Although the experimental results indicate an enhancement in the wear resistance, it has been also observed the precipitation of part of the chromium of the stainless steels, or of the alloys of CoCr, due to an increase in the temperature produced a decrease in the corrosion resistance, even at temperatures where carbides are not appreciated [74], as it can be appreciated

	Ion implantation	**Plasma immersion**
Geometry	Line of sight	Conformal
Temperature	Room temperature	400°C
Thickness	0.1 micron	0.05–10 microns
Batch time	10–100 h	0.1–2 h
Ion energy	10–1000 kV	0.1–100 kV
Ion current	1–100 mA	100–1000 mA
Industrial scaling	Low	Medium

Table 1. A comparative scheme of the different parameters (geometry, temperature, thickness, batch time, ion energy, ion current, or industrial scaling) between plasma immersion ion implantation and ion beam implantation, respectively. Reprinted with permission of [71].

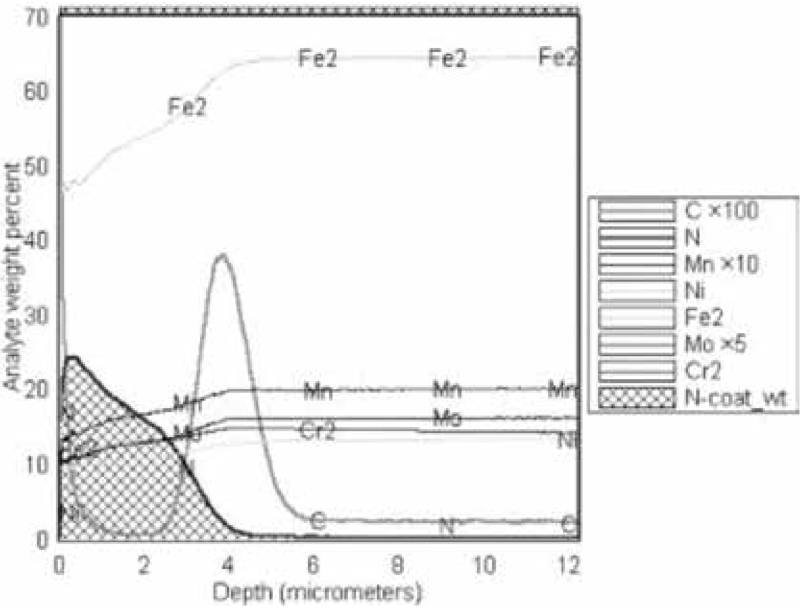

Figure 11. Glow discharge optical spectroscopy (GDOS) depth profiles of nitrogen after implantation at 400°C (ion energy 1.2 keV, current density 1 mA/cm^2 and fluence 3.5 × 10^{19} cm^{-2}) for AISI 316. Reprinted with permission of [73].

in the polarization curves (Tafel plots) of **Figure 12**. However, this problem can be solved through the implantation of oxygen, obtaining for these specific cases an important increases of the corrosion resistance [75], as it can be observed in **Figure 13**.

Another application of interest for implantation by immersion in oxygen plasma is the reduction of the release of heavy ions to the blood flow observed in cardiovascular devices. The implantation of oxygen in stainless steels "pushes" the ions such as Ni and Cr into the surface, and as a promoting result, a significant decrease in the release of these ions have been obtained with an improvement in biocompatibility [71]. By means of oxygen implantation, heavy ions (Ni, Mo, and Cr) go deeper into the material as shown in **Figure 14**, where it is

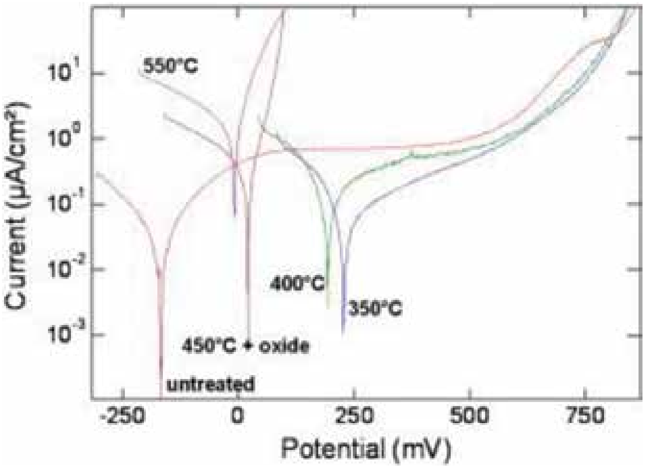

Figure 12. Polarization curves for different samples in Ringer solution at 37.2°C. Reprinted with permission of [74].

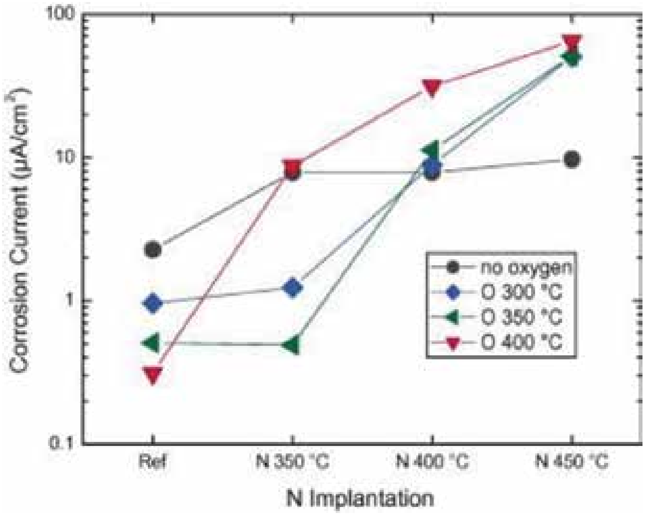

Figure 13. Corrosion rates calculated from the polarization curves as function of nitrogen and oxygen implantation temperature. The samples labeled as "ref" are either only implanted with oxygen (with indicated temperature) or a sample from untreated base material (circle). Reprinted with permission of [75].

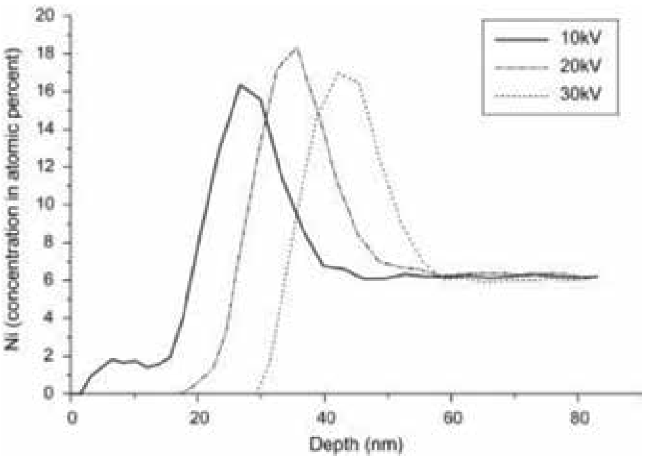

Figure 14. Compositional profiles for oxygen implanted into stainless steel at energies of 10, 20, and 30 keV. Reprinted with permission of [71].

possible to observe atomic concentration of Ni after oxygen implantation. As a consequence of this, migration tests show a reduction of the concentration of these ions in blood of more than 50%.

Finally, interesting approaches for the design and implementation of multifunctional layers (bactericides, wear resistance, and anticorrosion) have been tested by using combined treatment techniques. As a representative example, ionic implantation of Ag on ceramic layers previously deposited by PVD is a novel approach that allows to have a better control of the distribution of the Ag, solving potential problems of cytotoxicity by the excessive release of silver cations [76].

5. Summary

Since the first implant was made in the nineteenth century, different prostheses have achieved significant improvements in terms of durability and performance. In addition to the improvements in the design, result of the better knowledge of the biomechanical processes, the development of new materials, and the superficial treatments have been decisive. Hundreds of different materials and dozens of surface treatments which have been studied in a rigorous and systematic way to be used as part of the different types of prostheses. Among all these vast set of materials and treatments, the solutions applied in each type of prosthesis are considerably reduced, as a result of all the research carried out.

In this work, we have reviewed some of the most widespread solutions and have the best results and perspectives of implantation. The thermal injection of HA is currently an extended solution that is applied in different types of implants to significantly increase the osseointegration capacity. PVD coatings by conventional magnetron sputtering techniques are being used to increase corrosion and wear resistance in heart valves and dental implants. In this line, the appearance of improved PVD techniques (HIPIMS) has achieved levels of adhesion and layer density that augur a wide use in other types of implants. Ion implantation and fundamentally the immersion in plasma are very effective tools to increase the wear resistance, maintaining the corrosion resistance of stainless steels and titanium and CoCr alloys.

Although all these techniques, and some more like plasma electrooxidation (PEO), have allowed significant advances already introduced in the market, there are still problems to be solved and challenges to be addressed within the surface treatments and design of novel materials. New manufacturing techniques such as additive manufacturing and social aspects such as the increase in life expectancy, determine that a continuous research is necessary to develop new materials and treatments compatible with this new framework. Probably one of the most promising ways of research is the use of combined treatment techniques within materials and customized designs for each patient.

Nomenclature

HA	hydroxyapatite
PVD	physical vapor deposition
DLC	diamond-like carbon
CP	calcium phosphates
PBLG-g-HA	poly (γ-benzyl-L-glutamate) modified hydroxyapatite
PLLA	poly (L-lactic acid)
FDA	food and drug administration
PSHA	plasma sprayed hydroxyapatite
SEM	scanning electron microscopy
IFM	interferometry
EB	electron beam (EB)
CA	cathodic arc
MS	magnetron sputtering
HIPIMS	high power impulse magnetron sputtering
DCMS	direct current magnetron sputtering
MPPMS	modulated pulsed power magnetron sputtering
PIII	plasma immersion ion implantation

GDOS	glow discharge optical spectroscopy
II	ion beam implantation (II)
PIIIeD	plasma immersion ion implantation-enhanced deposition

Author details

José A. García[1]*, Pedro J. Rivero[1,2], Rocío Ortiz[3], Iban Quintana[3] and Rafael J. Rodríguez[1,2]

*Address all correspondence to: joseantonio.garcia@unavarra.es

1 Materials Engineering Laboratory, Department of Mechanical, Energy and Materials Engineering, Public University of Navarre, Pamplona, Spain

2 Institute for Advanced Materials (INAMAT), Public University of Navarre, Pamplona, Spain

3 IK4-TEKNIKER, Ignacio Goenaga, EIBAR, Gipuzkoa, Spain

References

[1] Eynon-Lewis NJ, Ferry D, Pearse MF. Themistocles Gluck: An unrecognised genius. British Medical Journal. 1992;**305**:1534-1536

[2] Roseti L, Parisi V, Petretta M, Cavallo C, Desando G, Bartolotti I, Grigolo B. Scaffolds for bone tissue engineering: State of the art and new perspectives. Materials Science and Engineering: C. 2017;**78**:1246-1262

[3] Abu-Omar Y, Ratnatunga CP. Prosthetic heart valves. Surgery (GBR). 2008;**26**:496-500

[4] Aslam AK, Aslam AF, Vasavada BC, Khan IA. Prosthetic heart valves: Types and echocardiographic evaluation. International Journal of Cardiology. 2007;**122**:99-110

[5] Tan C, Schatz RA. The history of coronary stenting. Interventional Cardiology Clinics. 2016;**5**:271-280

[6] Pezzotti G, Yamamoto K. Advances in artificial joint materials. Journal of the Mechanical Behavior of Biomedical Materials. 2014;**31**:1-2

[7] Manam NS, Harun WSW, Shri DNA, Ghani SAC, Kurniawan T, Ismail MH, Ibrahim MHI. Study of corrosion in biocompatible metals for implants: A review. Journal of Alloys and Compounds. 2017;**701**:698-715

[8] Goodman SB, Barrena EG, Takagi M, Konttinen YT. Biocompatibility of total joint replacements: A review, Journal of Biomedical Materials Research Part A. 2009;**90**:603-618

[9] Hall-Stoodley L, Costerton JW, Stoodley P. Bacterial biofilms: From the natural environment to infectious diseases. Nature Reviews. Microbiology. 2004;**2**:95-108

[10] Costerton JW, Stewart PS, Greenberg EP. Bacterial biofilms: A common cause of persistent infections. Science. 1999;**284**:1318-1322

[11] Stevens MM. Biomaterials for bone tissue engineering, Materials Today. 2008;**11**:18-25

[12] Engstrand T, Kihlström L, Neovius E, Skogh A-D, Lundgren TK, Jacobsson H, Bohlin J, Åberg J, Engqvist H. Development of a bioactive implant for repair and potential healing of cranial defects: Technical note. Journal of Neurosurgery. 2014;**120**:273-277

[13] Neovius E, Engstrand T. Craniofacial reconstruction with bone and biomaterials: Review over the last 11 years. Journal of Plastic, Reconstructive and Aesthetic Surgery. 2010;**63**: 1615-1623

[14] Sadat-Shojai M, Khorasani M, Dinpanah-Khoshdargi E, Jamshidi A. Synthesis methods for nanosized hydroxyapatite with diverse structures. Acta Biomaterialia. 2013;**9**: 7591-7621

[15] Batchelar DL, Davidson MTM, Dabrowski W, Cunningham IA. Bone-composition imaging using coherent-scatter computed tomography: Assessing bone health beyond bone mineral density. Medical Physics. 2006;**33**:904-915

[16] Szczes A, Holysz L, Chibowski E. Synthesis of hydroxyapatite for biomedical applications. Advances in Colloid and Interface Science. 2017;**249**:321-330

[17] Fragal EH, Cellet TSP, Fragal VH, Companhoni MVP, Ueda-Nakamura T, Muniz EC, Silva R, Rubira AF. Hybrid materials for bone tissue engineering from biomimetic growth of hydroxiapatite on cellulose nanowhiskers. Carbohydrate Polymers. 2016;**152**:734-746

[18] Chen L, Mccrate JM, Lee JC, Li H. The role of surface charge on the uptake and biocompatibility of hydroxyapatite nanoparticles with osteoblast cells. Nanotechnology. 2011;**22**:1-20

[19] Pelin IM, Maier SS, Chitanu GC, Bulacovschi V. Preparation and characterization of a hydroxyapatite-collagen composite as component for injectable bone substitute. Materials Science and Engineering: C. 2009;**29**:2188-2194

[20] He M, Chang C, Peng N, Zhang L. Structure and properties of hydroxyapatite/cellulose nanocomposite films. Carbohydrate Polymers. 2012;**87**:2512-2518

[21] Liao L, Yang S, Miron RJ, Wei J, Zhang Y, Zhang M. Osteogenic properties of PBLG-g-HA/PLLA nanocomposites. PLoS One. 2014;**9**:1-8

[22] Hou C, Hou S, Hsueh Y, Lin J, Wu H, Lin F. The in vivo performance of biomagnetic hydroxyapatite nanoparticles in cancer hyperthermia therapy. Biomaterials. 2009;**30**: 3956-3960

[23] Tampieri A, D'Alessandro T, Sandri M, Sprio S, Landi E, Bertinetti L, Panseri S, Pepponi G, Goettlicher J, Bañobre-López M, Rivas J. Intrinsic magnetism and hyperthermia in bioactive Fe-doped hydroxyapatite. Acta Biomaterialia. 2012;**8**:843-851

[24] Yuan Y, Liu C, Qian J, Wang J, Zhang Y. Size-mediated cytotoxicity and apoptosis of hydroxyapatite nanoparticles in human hepatoma HepG2 cells. Biomaterials. 2010;**31**: 730-740

[25] Walmsley GG, McArdle A, Tevlin R, Momeni A, Atashroo D, Hu MS, Feroze AH, Wong VW, Lorenz PH, Longaker MT, Wan DC. Nanotechnology in bone tissue engineering. Nanomedicine: Nanotechnology, Biology and Medicine. 2015;**11**:1253-1263

[26] Smolen D, Chudoba T, Malka I, Kedzierska A, Lojkowski W, Swieszkowski W, Kurzydlowski KJ, Kolodziejczyk-Mierzynska M, Lewandowska-Szumiel M. Highly biocompatible, nanocrystalline hydroxyapatite synthesized in a solvothermal process driven by high energy density microwave radiation. International Journal of Nanomedicine. 2013;**8**:653-668

[27] Domínguez-Trujillo C, Peón E, Chicardi E, Pérez H, Rodríguez-Ortiz JA, Pavón JJ, García-Couce J, Galván JC, García-Moreno F, Torres Y. Sol-gel deposition of hydroxyapatite coatings on porous titanium for biomedical applications. Surface and Coating Technology. 2018;**333**:158-162

[28] Manso M, Langlet M, Jiménez C, Martínez-Duart JM. Microstructural study of aerosol-gel derived hydroxyapatite coatings. Biomolecular Engineering. 2002;**19**:63-66

[29] Vijayalakshmi U, Prabakaran K, Rajeswari S. Preparation and characterization of sol-gel hydroxyapatite and its electrochemical evaluation for biomedical applications. Journal of Biomedial Materials Research Part A. 2008;**87**:739-749

[30] Ismail RA, Salim ET, Hamoudi WK. Characterization of nanostructured hydroxyapatite prepared by Nd:YAG laser deposition. Materials Science and Engineering: C. 2013; **33**:47-52

[31] Pereiro I, Rodríguez-Valencia C, Serra C, Solla EL, Serra J, González P. Pulsed laser deposition of strontium-substituted hydroxyapatite coatings. Applied Surface Science. 2012;**258**:9192-9197

[32] Rajesh P, Muraleedharan CV, Komath M, Varma H. Pulsed laser deposition of hydroxyapatite on titanium substrate with Titania interlayer. Journal of Materials Science. Materials in Medicine. 2011;**22**:497-505

[33] Zhong Z, Qin J, Ma J. Cellulose acetate/hydroxyapatite/chitosan coatings for improved corrosion resistance and bioactivity. Materials Science and Engineering: C. 2015;**49**: 251-255

[34] Abdal-Hay A, Hasan A, Lee MH, Hamdy AS, Khalil KA. Biocorrosion behavior of biodegradable nanocomposite fibers coated layer-by-layer on AM50 magnesium implant. Materials Science and Engineering C. 2016;**58**:1232-1241

[35] López EO, Rossi AL, Archanjo BS, Ospina RO, Mello A, Rossi AM. Crystalline nanocoatings of fluorine-substituted hydroxyapatite produced by magnetron sputtering with high plasma confinement. Surface and Coating Technology. 2015;**264**:163-174

[36] Molagic A. Structural characterization of TiN/HAp and ZrO_2/HAp thin films deposited onto Ti-6Al-4V alloy by magnetron sputtering. UPB Scientific Bulletin, Series B. 2010; **72**:187-194

[37] Urquia Edreira ER, Wolke JGC, Aldosari AA, Al-Johany SS, Anil S, Jansen JA, Van Den Beucken JJJP. Effects of calcium phosphate composition in sputter coatings on in vitro and in vivo performance. Journal of Biomedial Materials Research Part A. 2015;**103**:300-310

[38] De Groot K, Geesink R, Klein CPAT, Serekian P. Plasma sprayed coatings of hydroxylapatite. Journal of Biomedical Materials Research. 1987;**21**:1375-1381

[39] Balani K, Chen Y, Harimkar SP, Dahotre NB, Agarwal A. Tribological behavior of plasma-sprayed carbon nanotube-reinforced hydroxyapatite coating in physiological solution. Acta Biomaterialia. 2007;**3**:944-951

[40] Takahashi Y, Shibata Y, Maeda M, Miyano Y, Murai K, Ohmori A. Plasma-spraying synthesis of high-performance photocatalytic TiO_2 coatings. In: IOP Conference Series: Materials Science and Engineering. 2014;**61**:012039:1-10

[41] Bonfante EA, Witek L, Tovar N, Suzuki M, Marin C, Granato R, Coelho PG. Physicochemical characterization and in vivo evaluation of amorphous and partially crystalline calcium phosphate coatings fabricated on Ti-6Al-4V implants by the plasma spray method. International Journal of Biomaterials. 2012:603826

[42] Cheang P, Khor KA. Addressing processing problems associated with plasma spraying of hydroxyapatite coatings. Biomaterials. 1996;**17**:537-544

[43] Tsui YC, Doyle C, Clyne TW. Plasma sprayed hydroxyapatite coatings on titanium substrates. Part 1: Mechanical properties and residual stress levels. Biomaterials. 1998;**19**: 2015-2029

[44] Tsui YC, Doyle C, Clyne TW. Plasma sprayed hydroxyapatite coatings on titanium substrates. Part 2: Optimisation of coating properties. Biomaterials. 1998;**19**:2031-2043

[45] Mittal M, Nath SK, Prakash S. Improvement in mechanical properties of plasma sprayed hydroxyapatite coatings by Al_2O_3 reinforcement. Materials Science and Engineering: C. 2013;**33**:2838-2845

[46] Singh A, Singh G, Chawla V. Characterization of vacuum plasma sprayed reinforced hydroxyapatite coatings on Ti-6Al-4V alloy. Transactions of the Indian Institute of Metals. 2017;**70**:2609-2628

[47] Kumari R, Majumdar JD. Studies on corrosion resistance and bio-activity of plasma spray deposited Hydroxylapatite (HA) based $TiO_2$and ZrO_2dispersed composite coatings on titanium alloy (Ti-6Al-4V) and the same after post spray heat treatment. Applied Surface Science. 2017;**420**:935-943

[48] Gu YW, Khor KA, Pan D, Cheang P. Activity of plasma sprayed Yttria stabilized zirconia reinforced hydroxyapatite/Ti-6Al-4V composite coatings in simulated body fluid. Biomaterials. 2004;**25**:3177-3185

[49] Chen X, Zhang B, Gong Y, Zhou P, Li H. Mechanical properties of nanodiamond-reinforced hydroxyapatite composite coatings deposited by suspension plasma spraying. Applied Surface Science. 2018;**439**:60-65

[50] Rodríguez RJ, García JA, Medrano A, Rico M, Sánchez R, Martínez R, Labrugère C, Lahaye M, Guette A. Tribological behaviour of hard coatings deposited by arc-evaporation PVD. Vacuum. 2002;**67**:559-566

[51] Román E, de Segovia JL, Alberdi A, Calvo J, Laucirica J. Comparative study of the interface composition of TiN and TiCN hard coatings on high speed steel substrates obtained by arc discharge. Materials Science and Engineering A. 1993;**163**:197-200

[52] Guu YY, Lin JF, Ai C. The tribological characteristics of titanium nitride, titanium carbonitride and titanium carbide coatings. Thin Solid Films. 1997;**302**:193-200

[53] Byeli AV, Minevich AA, Stepanenko AV, Gick LA, Kholodilov OV. Wear resistance and structure of (Ti,Al)N coatings. Journal of Physics D. 1992;**25**:A292-A296

[54] Vetter J. Vacuum arc coatings for tools: Potential and application. Surface and Coating Technology. 1995;**76-77**:719-724

[55] de Damborenea J, Navas C, García JA, Arenas MA, Conde A. Corrosion-erosion of TiN-PVD coatings in collagen and cellulose meat casing. Surface and Coating Technology. 2007;**201**:5751-5757

[56] Kaufman HR. Technology of ion beam sources used in sputtering. Journal of Vacuum Science and Technology. 1978;**15**:272-276

[57] Sarakinos K, Alami J, Konstantinidis S. High power pulsed magnetron sputtering: A review on scientific and engineering state of the art. Surface and Coating Technology. 2010;**204**:1661-1684

[58] Coll BF, Jacquot P. Surface modification of medical implants and surgical devices using TiN layers. Surface and Coating Technology. 1988;**36**:867-878

[59] Buechel FF, Helbig TE, Pappas MJ. 31 year evolution of the rotating-platform total knee replacment: Coping with "spinout" and wear. Journal of ASTM International. 2012;**9**:1-14

[60] Kelly PJ, Li H, Benson PS, Whitehead KA, Verran J, Arnell RD, Iordanova I. Comparison of the tribological and antimicrobial properties of CrN/Ag, ZrN/Ag, TiN/Ag, and TiN/Cu nanocomposite coatings. Surface and Coating Technology. 2010;**205**:1606-1610

[61] Carvalho I, Henriques M, Oliveira JC, Alves CFA, Piedade AP, Carvalho S. Influence of surface features on the adhesion of staphylococcus epidermidis to Ag-TiCN thin films. Science and Technology of Advanced Materials. 2013;**14**:1-10

[62] Manninen NK, Galindo RE, Carvalho S, Cavaleiro A. Silver surface segregation in Ag-DLC nanocomposite coatings. Surface and Coating Technology. 2015;**267**:90-97

[63] Ziegler J, editor. Handbook of Ion Implantation Technology. North-Holland: Elsevier; 1992. ISBN: 0444897

[64] Anders A. Handbook of Plasma Immersion Ion Implantation and Deposition. John Willey and Son; 2000. ISBN: 0471246980

[65] Davies JA. Early ion implantation history (or "how I met Jim Mayer – and Högsted Phim!"). Materials Chemistry and Physics. 1996;**46**:111-117

[66] Moffatt S. Ion implantation from the past and into the future. Nuclear Instruments and Methods in Physics Research Section B. 1995;**96**:1-6

[67] Kingsbury EF, Ohl RS. Photoelectric properties of Ionically bombarded silicon. Bell Labs Technical Journal. 1952;**31**:802-815

[68] Ohl RS. Properties of ionic bombarded silicon. Bell Labs Technical Journal. 1952;**31**:104-121

[69] McHargue CJ. Ion implantation in metals and ceramics. International Metals Reviews. 1986;**31**:49-76

[70] Mello CB, Ueda M, Oliveira RM, Garcia JA. Corrosion effects of plasma immersion ion implantation-enhanced Cr deposition on SAE 1070 carbon steel. Surface and Coating Technology. 2011;**205**:S151-S156

[71] García JA, Rodríguez RJ. Ion implantation techniques for non-electronic applications. Vacuum. 2011;**85**:1125-1129

[72] Rautray TR, Narayanan R, Kwon T, Kim K. Accelerator based synthesis of hydroxyapatite by MeV ion implantation. Thin Solid Films. 2010;**518**:3160-3163

[73] Rivière JP, Méheust P, García JA, Martínez R, Sánchez R, Rodríguez R. Tribological properties of Fe and Ni base alloys after low energy nitrogen bombardment. Surface and Coating Technology. 2002;**158-159**:295-300

[74] Lutz J, Díaz C, García JA, Blawert C, Mändl S. Corrosion behaviour of medical CoCr alloy after nitrogen plasma immersion ion implantation. Surface and Coating Technology. 2011;**205**:3043-3049

[75] Mändl S, Díaz C, Gerlach JW, García JA. Near surface analysis of duplex PIII treated CoCr alloys. Nuclear Instruments and Methods in Physics Research Section B. 2013;**307**:305-309

[76] Osés J, Palacio JF, Kulkarni S, Medrano A, García JA, Rodríguez R. Antibacterial PVD coatings doped with silver by ion implantation. Applied Surface Science. 2014;**310**:56-61

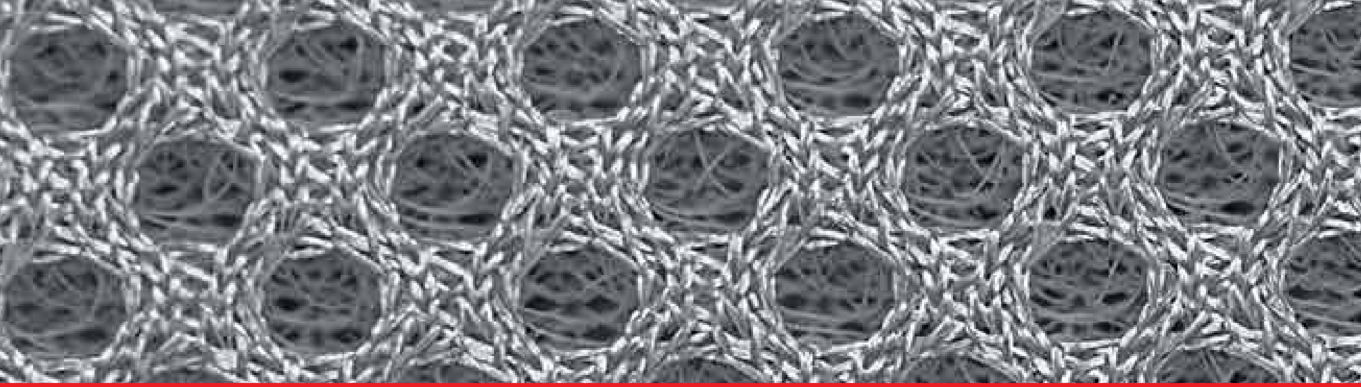

Edited by Mohammad Asaduzzaman Chowdhury

Surface engineering has rapidly expanded in recent years as the demand for improved materials has increased. Surface engineering is a valuable tool for conceiving both surface and bulk properties, which cannot be achieved simultaneously either by the coating material or by the substrate material alone. The book is written on the current trends of surface engineering and relevant research. The applied and basic research as well as some worthy concepts of materials related to this area is explained clearly to understand the need for surface engineering in industrial applications. The different surface modification processes, properties, and their characterizations are discussed elaborately for future research and as a text book. Modification of surface properties by films or coatings is used in industrial applications. This is an area of interest to numerous fields: fabrication of parts, mechanics, transport, catalysis, energy, production, microelectronics, optoelectronics, the leisure industry, etc. The properties are considered for protection against corrosion, oxidation or wear, biocompatibility, wetting, adhesion, durability, catalytic activity, and toughness. The modern concept of engineering is discussed to ensure that the contributions of this subject minimize energy consumption. The book will be used as a state of the art for present and future researchers, industrial components design, and control.

Published in London, UK

IntechOpen

ISBN 978-1-83881-827-2
9 781838 818272